1 OF 3

PB

297480

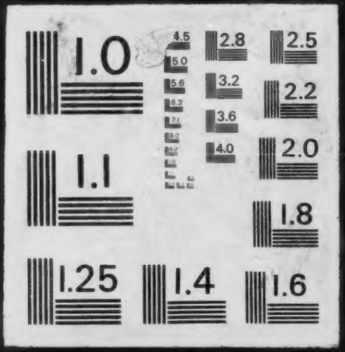

U.S. DEPARTMENT OF COMMERCE
National Technical Information Service

PB-297 480

# Smog Chamber Validation Using Lagrangian Atmospheric Data

North Carolina Univ at Chapel Hill

Prepared for

Environmental Sciences Research Lab, Research Triangle Park, NC

May 79

## TECHNICAL REPORT DATA
*(Please read Instructions on the reverse before completing)*

1. REPORT NO. EPA-600/3-79-050

2\.

3. RECIPIENT'S ACCESSION NO. PB297480

4. TITLE AND SUBTITLE
SMOG CHAMBER VALIDATION USING LAGRANGIAN ATMOSPHERIC DATA

5. REPORT DATE May 1979

6. PERFORMING ORGANIZATION CODE

7. AUTHOR(S)
Charles Eugene Feigley, Harvey E. Jeffries, and Myra A. Carpenter

8. PERFORMING ORGANIZATION REPORT NO.

9. PERFORMING ORGANIZATION NAME AND ADDRESS
Department of Environmental Sciences and Engineering
University of North Carolina at Chapel Hill
Chapel Hill, North Carolina 27514

10. PROGRAM ELEMENT NO. 1AA603 AC-005 (FY-78)

11. CONTRACT/GRANT NO. Grant No. 800916

12. SPONSORING AGENCY NAME AND ADDRESS
Environmental Sciences Research Laboratory-RTP, NC
Office of Research and Development
U.S. Environmental Protection Agency
Research Triangle Park, North Carolina 27711

13. TYPE OF REPORT AND PERIOD COVERED Interim

14. SPONSORING AGENCY CODE EPA/600/09

15. SUPPLEMENTARY NOTES

16. ABSTRACT

A method was developed for validating outdoor smog chamber experiments as a means of determining the relationships between oxidant concentrations and its precursors - hydrocarbons and nitrogen oxides. When chamber experiments were performed in a manner that simulated relevant meteorological processes and precursor concentrations, the validation method showed that photochemical smog reactions observed in the smog chamber generally agreed with data from the Los Angeles Reactive Pollutant Program (LARPP). The LARPP data consist of detailed airborne and ground level pollutant and meteorological measurements.

17. KEY WORDS AND DOCUMENT ANALYSIS

| a. DESCRIPTORS | b. IDENTIFIERS/OPEN ENDED TERMS | c. COSATI Field/Group |
|---|---|---|
| * Air pollution<br>* Ozone<br>* Hydrocarbons<br>* Nitrogen oxides<br>* Chemical reactions<br>Test chambers<br>* Mathematical models<br>* Computer simulation | | 13B<br>07B<br>076<br>07D<br>14B<br>12A<br>09B |

| | | |
|---|---|---|
| 18. DISTRIBUTION STATEMENT<br>RELEASE TO PUBLIC | 19. SECURITY CLASS *(This Report)*<br>UNCLASSIFIED | 21. NO. OF PAGES<br>272 |
| | 20. SECURITY CLASS *(This page)*<br>UNCLASSIFIED | 22. PRICE<br>PC A12 / MF A01 |

EPA Form 2220-1 (9-73)

United States
Environmental Protection
Agency

Environmental Sciences Research
Laboratory
Research Triangle Park NC 27711

EPA-600/3-79-050
May 1979

Research and Development

PB 297480

EPA

# Smog Chamber Validation Using Lagrangian Atmospheric Data

REPRODUCED BY
NATIONAL TECHNICAL
INFORMATION SERVICE
U.S. DEPARTMENT OF COMMERCE
SPRINGFIELD, VA. 22161

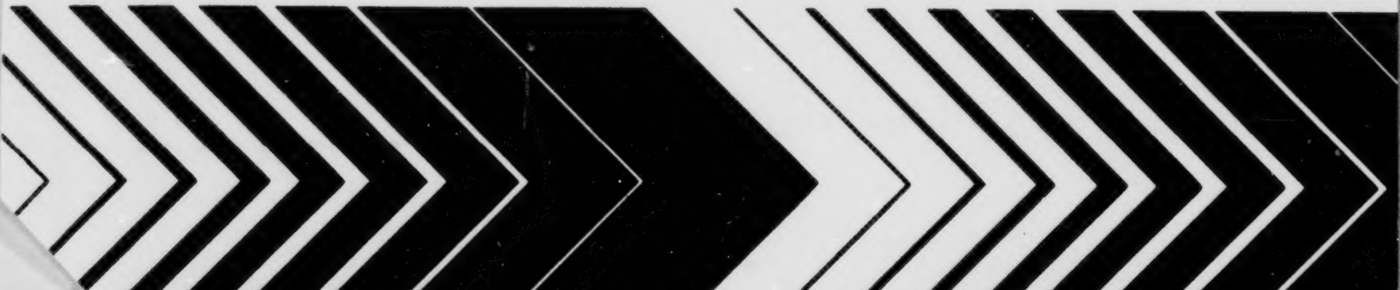

## RESEARCH REPORTING SERIES

Research reports of the Office of Research and Development, U.S. Environmental Protection Agency, have been grouped into nine series. These nine broad categories were established to facilitate further development and application of environmental technology. Elimination of traditional grouping was consciously planned to foster technology transfer and a maximum interface in related fields. The nine series are:

1. Environmental Health Effects Research
2. Environmental Protection Technology
3. Ecological Research
4. Environmental Monitoring
5. Socioeconomic Environmental Studies
6. Scientific and Technical Assessment Reports (STAR)
7. Interagency Energy-Environment Research and Development
8. "Special" Reports
9. Miscellaneous Reports

This report has been assigned to the ECOLOGICAL RESEARCH series. This series describes research on the effects of pollution on humans, plant and animal species, and materials. Problems are assessed for their long- and short-term influences. Investigations include formation, transport, and pathway studies to determine the fate of pollutants and their effects. This work provides the technical basis for setting standards to minimize undesirable changes in living organisms in the aquatic, terrestrial, and atmospheric environments.

This document is available to the public through the National Technical Information Service, Springfield, Virginia 22161.

EPA-600/3-79-050
May 1979

# SMOG CHAMBER VALIDATION USING LAGRANGIAN ATMOSPHERIC DATA

by

Charles Eugene Feigley
Harvey E. Jeffries, and
Myra A. Carpenter

Department of Environmental Sciences and Engineering
University of North Carolina at Chapel Hill
Chapel Hill, North Carolina 27514

Grant Number 800916

Project Officer

Bruce W. Gay, Jr.
Atmospheric Chemistry and Physics Division
Environmental Sciences Research Laboratory
U.S. Environmental Protection Agency
Research Triangle Park, North Carolina 27711

ENVIRONMENTAL SCIENCES RESEARCH LABORATORY
OFFICE OF RESEARCH AND DEVELOPMENT
U.S. ENVIRONMENTAL PROTECTION AGENCY
RESEARCH TRIANGLE PARK, NORTH CAROLINA 27711

# DISCLAIMER

This report has been reviewed by the U.S. Environmental Protection Agency, and approved for publication. Approval does not signify that the contents necessarily reflect the views and policies of the U.S. Environmental Protection Agency, nor does mention of trade names or commercial products constitute endorsement or recommendations for use.

# ABSTRACT

A method was developed for validating outdoor smog chamber experiments as a means of determining the relationships between oxidant concentrations and its precursors - hydrocarbons and nitrogen oxides. When chamber experiments were performed in a manner that simulated relevant meteorological processes and precursor concentrations, the validation method showed that photochemical smog reactions observed in the smog chamber generally agreed with data from the Los Angeles Reactive Pollutant Program (LARPP). The LARPP data consist of detailed airborne and ground level pollutant and meteorological measurements.

# CONTENTS

Abstract . . . . . . . . . . . . . . . . . . . . . . . . . . . . iii
Figures . . . . . . . . . . . . . . . . . . . . . . . . . . . . vii
Tables . . . . . . . . . . . . . . . . . . . . . . . . . . . . xiv
Abbreviations and Symbols . . . . . . . . . . . . . . . . . . xvi
Acknowledgments . . . . . . . . . . . . . . . . . . . . . . . xvii

1. Introduction . . . . . . . . . . . . . . . . . . . . . . . 1
    Photochemical smog chemistry . . . . . . . . . . . . 3
    Trends of photochemical pollutants in the atmosphere . . . . . . . . . . . . . . . . . 11
2. Conclusions . . . . . . . . . . . . . . . . . . . . . . . 16
3. Recommendations . . . . . . . . . . . . . . . . . . . . . 22
    Precursor central requirements . . . . . . . . . . . 22
    Further experimental simulations of Operation 33. . 22
    Numerical modeling . . . . . . . . . . . . . . . . . 23
    Field studies . . . . . . . . . . . . . . . . . . . 23
4. Methods of Relating Oxidant to Precursors. . . . . . . . 24
    The EPA assessment of control requirements . . . . 25
    Other methods of assessing the effects of controlling oxidant precursor emissions . . . . . 32
    Conclusions . . . . . . . . . . . . . . . . . . . . 45
5. The Los Angeles Reactive Pollutant Program . . . . . . . 47
    General description . . . . . . . . . . . . . . . . 47
    Analysis of Operation 33 . . . . . . . . . . . . . . 48
    Method of comparison of smog chamber results with LARPP data . . . . . . . . . . . . . . . . . . 93
6. Experimental Methods and Results . . . . . . . . . . . . 123
    Methods . . . . . . . . . . . . . . . . . . . . . . 123
    Results . . . . . . . . . . . . . . . . . . . . . . 133
7. Discussion . . . . . . . . . . . . . . . . . . . . . . . 181
    Solar radiation . . . . . . . . . . . . . . . . . . 181
    Atmospheric inhomogeneity . . . . . . . . . . . . . 184
    Temperature . . . . . . . . . . . . . . . . . . . . 196
    Discussion of Comparisons . . . . . . . . . . . . . 199

References . . . . . . . . . . . . . . . . . . . . . . . . . . 211

Preceding page blank

Appendices

A. Flag field messages for Operation 33. . . . . . . . . . 220
B. Source reconciliation and associated calculations . . . 223
C. Numerical computation of vertical flux along a LARPP trajectory. . . . . . . . . . . . . . . . . . . . . . . 226
D. Calculation of $k_1$ from theory . . . . . . . . . . . . . 233
E. The interactive effects of inhomogeneity and atmospheric processes on photostationary state income . 237
F. Correction of data for the dark reaction of NO and $O_3$ during sampling . . . . . . . . . . . . . . . . . . . . . 250

# FIGURES

| Number | | Page |
|---|---|---|
| 1 | Important reaction cycles in photochemical smog. . . . . | 10 |
| 2 | A typical diurnal pattern of photochemical smog constituents at a stationary monitoring site . . . . . . | 11 |
| 3 | Freeway and non-freeway emissions. . . . . . . . . . . . | 14 |
| 4 | Annual trends of photochemical oxidant in three U.S. cities . . . . . . . . . . . . . . . . . . . . . . . . . | 15 |
| 5 | Maximum smog chamber oxidant corresponding to observed and projected NMHC, 1960-1990. . . . . . . . . . . . . . | 35 |
| 6 | Oxidant/$O_3$ isopleths derived from combined use of smog chamber and photochemical modeling techniques. . . . . . | 43 |
| 7 | Typical LARPP helicopter pattern from (a) Lagrangian (moving with mean wind) viewpoint, and from (b) Eulerian (fixed point and ground) viewpoint, in a 1.5 m. $sec^{-1}$ mean wind. . . . . . . . . . . . . . . . . . . . . . | 49 |
| 8 | Tetroon trajectories for LARPP Operation 33. . . . . . . | 50 |
| 9 | Tetroon altitude above ground level versus time. . . . . | 52 |
| 10 | Example of concentration-position figure for carbon monoxide . . . . . . . . . . . . . . . . . . . . . . . | 61 |
| 11 | Concentration-position figures for Operation 33 carbon monoxide before 1030 PST . . . . . . . . . . . . . . . . | 63 |
| 12 | Concentration-position figure for Operation 33 carbon monoxide after 1030 PST. . . . . . . . . . . . . . . . . | 64 |
| 13 | Concentration-position figures for Operation 33 nitrogen oxides before 1030 PST . . . . . . . . . . . . . . . . . | 65 |
| 14 | Concentration-position figures for Operation 33 nitrogen oxides after 1030 PST. . . . . . . . . . . . . . . . . . | 66 |

Number Page

15 Concentration-position figures for Operation 33 nitric oxide before 1030 PST. . . . . . . . . . . . . . . . . 67

16 Concentration-position figures for Operation 33 nitric oxide after 1030 PST . . . . . . . . . . . . . . . . . 68

17 Concentration-position figures for Operation 33 ozone before 1030 PST. . . . . . . . . . . . . . . . . . . . 69

18 Concentration-position figures for Operation 33 ozone after 1030 PST . . . . . . . . . . . . . . . . . . . . 70

19 Helicopter pattern average nitric oxide concentrations for Operation 33 . . . . . . . . . . . . . . . . . . . 73

20 Helicopter pattern average nitrogen oxides concentrations for Operation 33 . . . . . . . . . . . . . . . . 74

21 Helicopter pattern average scattering coefficients for Operation 33 . . . . . . . . . . . . . . . . . . . . . 75

22 Helicopter pattern average carbon monoxide concentration for Operation 33. . . . . . . . . . . . . . . . 76

23 Helicopter pattern average temperatures for Operation 33 . . . . . . . . . . . . . . . . . . . . . . . . . 77

24 Helicopter pattern average dew points for Operation 33 78

25 Helicopter pattern average nonmethane hydrocarbon concentrations for Operation 33 . . . . . . . . . . . . 79

26 Helicopter pattern average methane concentrations for Operation 33 . . . . . . . . . . . . . . . . . . . . 80

27 Helicopter pattern average ozone concentrations for Operation 33 . . . . . . . . . . . . . . . . . . . . . 81

28 Helicopter pattern standard deviation of nitric oxide concentration. . . . . . . . . . . . . . . . . . . . . 84

29 Helicopter pattern relative standard deviation of nitrogen oxides concentrations . . . . . . . . . . . . 85

30 Helicopter pattern relative standard deviations of scattering coefficients. . . . . . . . . . . . . . . . . 86

31 Helicopter pattern relative standard deviations of carbon monoxide concentrations . . . . . . . . . . . . 87

Number Page

32 Helicopter pattern relative standard deviations of temperatures . . . . . . . . . . . . . . . . . . . . . . 88

33 Helicopter pattern relative standard deviations of dew points . . . . . . . . . . . . . . . . . . . . . . . 89

34 Helicopter pattern relative standard deviations of nonmethane hydrocarbon concentrations. . . . . . . . . 90

35 Helicopter pattern relative standard deviations of methane concentrations . . . . . . . . . . . . . . . . 91

36 Helicopter pattern relative standard deviations of ozone concentrations . . . . . . . . . . . . . . . . . 92

37 Mixing depth estimated for the LARPP Operation 33 trajectory . . . . . . . . . . . . . . . . . . . . . . 105

38 Carbon monoxide vertical concentration profiles for Operation 33 at one-hour intervals estimated by numerical solution . . . . . . . . . . . . . . . . . . 106

39 Estimated carbon monoxide flux at altitudes of 150 feet and half the mixing depths from numerical solution . . . . . . . . . . . . . . . . . . . . . . . 107

40 Zero gradient nonmethane hydrocarbon concentrations in the absence of reaction as estimated from source reconciliation results and regression line . . . . . . . 110

41 Comparison of nonmethane hydrocarbon. Concentration line from source reconciliation and nonmethane hydrocarbon concentration as measured by environmental chromatograph. . . . . . . . . . . . . . . . . . . . . 111

42 Nonmethane hydrocarbon vertical concentration profiles for Operation 33 at one-hour intervals estimated by numerical solution . . . . . . . . . . . . . . . . . . 113

43 Estimated nonmethane hydrocarbon flux at altitudes of 150 feet and half the mixing depth from numerical solution . . . . . . . . . . . . . . . . . . . . . . . 114

44 Logic for calculating injection and dilution rates from flux and mixing height estimates. . . . . . . . . 117

45 Nonmethane hydrocarbon injection rates for simulation ofLARPP Operation 33. . . . . . . . . . . . . . . . . . 119

Number Page

46 Chamber dilution rates for simulation of LARPP Operation 33 . . . . . . . . . . . . . . . . . . . . . . . 120

47 Cumulative nonmethane hydrocarbon injection rates for simulation of LARPP Operation 33 . . . . . . . . . . . 121

48 Cumulative dilution volume for simulation of LARPP Operation 33 . . . . . . . . . . . . . . . . . . . . . . . 122

49 Schematic diagram of UNC outdoor smog chamber dilution and exhaust system . . . . . . . . . . . . . . . . . . 129

50 NO, $NO_2$, and $O_3$ profiles from static experiment of September 1, 1976. . . . . . . . . . . . . . . . . . . . 135

51 Solar radiation and ultraviolet radiation for September 1, 1976. . . . . . . . . . . . . . . . . . . . 136

52 NO, $NO_2$, and $O_3$ profiles from simulation experiment of September 6, 1976. . . . . . . . . . . . . . . . . . . . 138

53 NO, $NO_2$, and $O_3$ profiles from static experiment of September 6, 1976. . . . . . . . . . . . . . . . . . . . 139

54 Solar radiation and ultraviolet radiation from September 6, 1976. . . . . . . . . . . . . . . . . . . . 140

55 NO, $NO_2$, and $O_3$ profiles from simulation experiment of September 25, 1976 . . . . . . . . . . . . . . . . . . . 142

56 NO, $NO_2$, and $O_3$ profiles from static experiment of September 25, 1976 . . . . . . . . . . . . . . . . . . . 143

57 Solar radiation and ultraviolet radiation from September 25, 1976 . . . . . . . . . . . . . . . . . . . 144

58 NO, $NO_2$, and $O_3$ profiles from static experiment of October 4, 1976. . . . . . . . . . . . . . . . . . . . 146

59 NO, $NO_2$, and $O_3$ profiles from static experiment of October 4, 1976. . . . . . . . . . . . . . . . . . . . 147

60 Solar radiation, ultraviolet radiation, and $NO_2$ photolysis rate constant from October 4, 1976. . . . . 148

61 NO, $NO_2$, and $O_3$ profiles from simulation experiment of October 6, 1976. . . . . . . . . . . . . . . . . . . . 150

62 NO, $NO_2$, and $O_3$ profiles from static experiment of October 6, 1976. . . . . . . . . . . . . . . . . . . . 151

Number Page

63 Solar radiation, ultraviolet radiation, and $NO_2$ photolysis rate constant from October 6, 1976. . . . . 152

64 NO, $NO_2$, and $O_3$ profiles from static experiment of October 11, 1976 . . . . . . . . . . . . . . . . . . 154

65 Solar radiation, ultraviolet radiation, and $NO_2$ photolysis rate constant from October 11, 1976. . . . . 155

66 NO, $NO_2$, and $O_3$ profiles from simulation experiment of October 12, 1976 . . . . . . . . . . . . . . . . . . 157

67 NO, $NO_2$, and $O_3$ profiles from static experiment of October 12, 1976 . . . . . . . . . . . . . . . . . . 158

68 Solar radiation, ultraviolet radiation, and $NO_2$ photolysis rate constant from October 12, 1976. . . . . 159

69 NO, $NO_2$, and $O_3$ profiles from simulation experiment of October 13, 1976 . . . . . . . . . . . . . . . . . . 161

70 NO, $NO_2$, and $O_3$ profiles from static experiment of October 13, 1976 . . . . . . . . . . . . . . . . . . 162

71 Solar radiation, ultraviolet radiation, and $NO_2$ photolysis rate constant from October 13, 1976. . . . . 163

72 NO, $NO_2$, and $O_3$ profiles from static experiments of October 15, 1976 . . . . . . . . . . . . . . . . . . 165

73 NO, $NO_2$, and $O_3$ profiles for simulation experiment of October 16, 1976 . . . . . . . . . . . . . . . . . . 167

74 NO, $NO_2$, and $O_3$ profiles for October 16, 1976, red side . . . . . . . . . . . . . . . . . . . . . . . 168

75 Solar radiation and ultraviolet radiation for October 16, 1976 . . . . . . . . . . . . . . . . . . . . . . 169

76 Comparisons of NO, $NO_2$, and $O_3$ profiles for October 12 simulation and LARPP zero-gradient region. . . . . . . 175

77 Comparison of NO, $NO_2$, and $O_3$ profiles for October 13 simulation and LARPP zero-gradient region. . . . . . . 176

78 Comparison of NMHC source reconciliation regression line with NMHC mix concentrations estimated from n-pentane peak for simulations of October 12 and 13. . 177

| Number |  | Page |
|---|---|---|
| 79 | $O_3$ concentrations at 1400 hours and maximum produced versus initial NMHC concentration during static experiments on clear days . . . . . . . . . . . . . . . . . | 180 |
| 80 | Comparison of Mt. Disappointment UV radiometer measurements with theoretical calculation of UV radiation from 290 to 390 nm above the boundary layer in Los Angeles on November 5, 1973. . . . . . . . . . . . . . | 183 |
| 81 | Theoretical estimates of $k_1$, the rate constant of $NO_2$ photolysis at four altitudes above ground level in Los Angeles on November 5, 1973. . . . . . . . . . . . . | 188 |
| 82 | Theoretical estimates of $k_1/k_3$, the ratio of the $NO_2$ photolysis rate constant to the rate constant of the $NO\text{-}O_3$ reaction at four altitudes above ground level in Los Angeles on November 5, 1973. . . . . . . . . . . . | 186 |
| 83 | Two hypothetical parcels of air at photostationary state at $k_1/k_3 = 0.016$ ppm . . . . . . . . . . . . . . | 188 |
| 84 | Estimated helicopter pattern average covariance of NO and $O_3$ from Operation 33 . . . . . . . . . . . . . . . . | 193 |
| 85 | Estimated helicopter pattern average ratio of covariance of NO and $O_3$ to the NO concentration. . . . . . . | 195 |
| 86 | Comparison of NO, $NO_2$, and $O_3$ profiles from static propylene experiments in UNC outdoor chamber . . . . . | 198 |
| 87 | PKSS model of 0.22 ppm $NO_x$, 2.00 ppmC HC mix for three temperature profiles . . . . . . . . . . . . . . . . . | 200 |
| 88 | NO, $NO_2$, and $O_3$ helicopter pattern average concentrations from LARPP Operation 33. . . . . . . . . . . . . | 202 |
| 89 | Comparison of ratio of $NO_2$ photolysis rate constant to $NO\text{-}O_3$ reaction rate constant . . . . . . . . . . . . . . | 204 |
| 90 | Comparison of the chamber temperatures on October 12 and 13 with range of helicopter pattern average temperatures from LARPP Operation 33 . . . . . . . . . . . | 207 |
| C-1 | Region of solution . . . . . . . . . . . . . . . . . . | 226 |
| C-2 | Solution-space indexing. . . . . . . . . . . . . . . . | 228 |
| E-1 | Data for example E-1 and summary . . . . . . . . . . . | 238 |

Number Page

F-1 Measured and corrected ozone for October 12 simulation 252

F-2 Measured and corrected NO for simulation of October 12 253

F-3 Measured and corrected $NO_2$ for October 12 simulation . 254

## TABLES

| Number | | Page |
|---|---|---|
| 1 | Reactions and Rate Constants for the System $NO-NO_2-N_2-O_2$ in Sunlight. . . . . . . . . . . . . . . . . | 5 |
| 2 | Selected Reactions of the $NO_x-H_2O$-CO-Air Photochemical System . . . . . . . . . . . . . . . . . . . | 6 |
| 3 | Other Methods of Relating Oxidants to Precursors and the Sources of Data for Each Method . . . . . . . . . . | 33 |
| 4 | Files Produced by Program UNMERGE and the Number of Records Transferred from the Operation 33 Archive to Each File Type. . . . . . . . . . . . . . . . . . . . | 54 |
| 5 | Some Programs Developed for Examination of LARPP Data . | 56 |
| 6 | Contents of Helicopter Data Records and Sources of Data | 57 |
| 7 | Weight Fractions of Tracer Species in Major Hydrocarbon Sources in the Los Angeles Area . . . . . . . . . . . . | 98 |
| 8 | Nonmethane Hydrocarbon Distributions for Automotive Exhaust, Gasoline, Gasoline Vapor, Commercial Natural Gas, and Geogenic Natural Gas . . . . . . . . . . . . . | 99 |
| 9 | Bag Sample Time and Altitude Estimated Weight Fraction of NMHC from Each Source Category and $R^2$ from Source Reconciliation. . . . . . . . . . . . . . . . . . . . . | 101 |
| 10 | Comparison of CO Flux Estimates from Panofsky and from Numerical Flux Computation. . . . . . . . . . . . . . . . | 108 |
| 11 | Pollutant Injection Data. . . . . . . . . . . . . . . . | 127 |
| 12 | Hydrocarbon Mix Composition Concentration of Compound, ppmC. . . . . . . . . . . . . . . . . . . . . . . . | 128 |
| 13 | Summary of Conditions and Results of Static Runs. . . . | 178 |

Number Page

14 Estimates of $NO_2/NO$ Ratio for Simulations of October 12 and 13 and the Effective $NO_2/NO$ Ratio for the LARPP Data Corrected and Uncorrected for Inhomogeneity. . . . 209

A-1 SMOG 2 Data Flag Messages for Operation 33. . . . . . . 221

A-2 SMOG 3 Data Flag Messages for Operation 33. . . . . . . 222

C-1 Comparison of Flux Calculations Using Different Time and Altitude Grid Spacing . . . . . . . . . . . . . . . . 232

E-1 Results of Various Approaches to Estimate Photostationary State $O_3$ and $k_1/k_3$ . . . . . . . . . . . . . 242

# LIST OF ABBREVIATIONS AND SYMBOLS

## ABBREVIATIONS

A -- angstroms
CAMP -- Continuous Air Monitoring Program
hr -- hour
in. -- inch
lpm -- liter(s) per minute
LAAPCD -- Los Angeles Air Pollution Control District
LARPP -- Los Angeles Reactive Pollutant Program
m -- meter(s)
min -- minute(s)
ml -- milliliter(s)
mm -- millimeter(s)
nm -- nanometer(s)
$O(^1D)$ -- single activated state of atomic oxygen
$O(^3P)$ -- triplet activated state of atomic oxygen
PAN -- peroxyacetyl nitrate
ppb -- parts per billion
pphm -- parts per hundred million
ppm -- parts per million
ppmC -- parts per million carbon
sec -- second(s)

## SYMBOLS

$CH_3$ -- methylene radical
$CH_4$ -- methane
$CH_2O$ -- formaldehyde
H -- hydrogen radical
HC -- generalized hydrocarbon
HCO -- formyl radical
$HCOO_2$ -- peroxyformyl radical
$HNO_2$ -- nitrous acid
$HNO_3$ -- nitric acid
HO -- hydroxyl radical
$HO_2$ -- hydroperoxy radical
HONO -- nitrous acid
$HONO_2$ -- pernitric acid
$HOONO_2$ -- pernitric acid
$H_2O$ -- water
$h\nu$ -- Planck's constant times the wave length of light
NMHC -- nonmethane hydrocarbon
NO -- nitric oxide
$NO_2$ -- nitrogen dioxide
$NO_3$ -- nitrogen trioxide
$NO_x$ -- oxides of nitrogen
$N_2O_5$ -- nitrogen pentoxide
$O_2$ -- oxygen
$O_3$ -- ozone
$RCO_3$ -- generalized peroxyacyl radical
RCHO -- generalized aldehyde

# ACKNOWLEDGEMENTS

Thanks are extended to Dr. Donald Fox for helping define this project initially and for his support through the final stages of this research. Special thanks also are expressed to Dr. Basil Dimitriades, Dr. Larry Kupper, Dr. Parker Reist, and Dr. Lyman Ripperton, and to Richard Kamens for his help with the experimental work.

Also acknowledged is the assistance of the staff of the School of Public Health, in particular, Mr. Frank Malcolm and his shop staff; Dr. Robin Baker for his programming help; Ms. Laura Alexander; Ms. Cynthia Crossen for her keypunching; and to Ms. Shirley Milton for typing the final copy.

## SECTION 1

## INTRODUCTION

Until the late 1940s, most polluted air was characterized by a chemical reducing power because of its sulfur dioxide content. The sulfur dioxide was released to the air mainly as a consequence of burning sulfur-bearing fossil fuels. It was indeed surprising then that Los Angeles air was found to contain materials with oxidizing ability. The first hint of this property was the rapid cracking of rubber products such as automobile tires. Ozone ($O_3$) was known to cause a similar cracking of stressed rubber. Ozone concentrations in ambient air were measured by rubber cracking ability, but there was no known source of ozone which might account for the concentrations found.

In 1953, Haagen-Smit et al. (1) demonstrated that synthetic mixtures of hydrocarbons and nitrogen dioxide in oxygen could crack rubber upon irradiation with natural and simulated solar radiation. This was the initial step toward understanding the mechanism of formation of oxidants in polluted air. Soon after, Stephens et al. in 1956 (2) confirmed the presence of ozone in irradiated mixtures of nitrogen dioxide ($NO_2$) and hydrocarbons in air, as well as in ambient southern California air, by long-path infrared spectroscopy. Since then the mechanisms of oxidant synthesis in polluted atmospheres have been discussed in detail: Leighton (3); Wayne (4); Haagen-Smit and Wayne (5); Pitts (6); Altshuller and Bufalini (7); and Demerjian, Kerr and Calvert (8).

In the past three decades, certain very obvious effects of smog have been noted: (1) eye irritation and lacrimation probably due to the formation of species such as acrolein, peroxyacetyl nitrate (PAN), and peroxybenzoyl nitrate; (2) the phytotoxicity of ozone, $NO_2$, PAN, and aldehydes; (3) rubber cracking caused by $O_3$; (4) reduced visibility due to $NO_2$ and photochemically produced aerosols.

The Clean Air Act, as amended in 1967, required the Administrator of the Environmental Protection Agency to prepare air quality criteria documents for certain pollutants. These documents were intended to explore the relationship between the presence of a pollutant in the air and any identifiable effects on health and welfare, based on the latest scientific knowledge. The Administrator was allowed up to one year and 30 days after enactment (of the Act) to prepare the criteria documents. Then, based on these criteria, national ambient air quality standards were promulgated (9). Primary standards "are those which, in the judgment of the Administrator, based on the air quality criteria and allowing an adequate margin of safety, are requisite to protect the public welfare from any known or anticipated adverse effects associated with the presence of air pollutants in the ambient air" (9).

The air quality standards for photochemical oxidants, both primary and secondary were set at 0.08 parts per million (ppm): a 1-hr average concentration not to be exceeded more than once per year. This is essentially a standard for $O_3$ since the "reference" method for measuring photochemical oxidants is the ethylene chemiluminescent technique which is specific for $O_3$. The standard for non-methane hydrocarbons (NMHC) was set at 0.24 ppm: an average from 6:00 to 9:00 a.m. not to be exceeded more than once per year. The hydrocarbon standard is not based on direct effects on health or welfare, but it is intended "for use as a guide in devising implementation plans to achieve oxidant standards" (9).

The methods used to arrive at the NMHC standard and the emission reductions required to meet the standard have been criticized from many quarters. It has been suggested that other methods or sources of data be utilized to reevaluate the standard. One such source of data is laboratory experimentation (smog chamber work) which simulates the formation of smog. Use of this data base for developing a quantitative relationship between oxidant and its precursors for control purposes is just beginning since the extent to which these data were influenced by the artificial experimental conditions was not known. Nor could the magnitude of these influences be determined because, until recently, there was no data from the ambient air with which to compare smog chamber data.

The purpose of this research was to study the suitability of data from the Los Angeles Reactive Pollutant Program (LARPP) for use in validating smog chambers. More specifically, the purpose was to perform chamber validation experiments in the UNC outdoor smog chamber.

## PHOTOCHEMICAL SMOG CHEMISTRY

### General Discussion

Tropospheric $O_3$ is formed by a reaction cycle involving mainly nitrogen oxides, hydrocarbons, and atmospheric oxygen. The chemical species emitted directly to the atmosphere from a source are known as primary pollutants, while those formed by reaction in the atmosphere are known as secondary pollutants. Relative to other tropospheric constituents, $NO_2$ is an extremely efficient absorber of light at wavelengths reaching the lower troposphere (290 to 415 nm). One possible consequence of the absorption of a photon is the rupture of the $NO_2$ molecule to form nitric oxide (NO) and atomic oxygen ($O_2$). Most of the extremely reactive oxygen atoms combine with molecular oxygen to form $O_3$ because of the high concentration of oxygen compared with the other possible reactants such as NO, $NO_2$, $O_3$, or hydrocarbons. Most of the $O_3$ produced reacts with NO to regenerate $NO_2$.

$$NO_2 + h\nu \rightarrow NO + O \tag{1}$$

$$O + O_2 + M \rightarrow O_3 + M \tag{2}$$

$$O_3 + NO \rightarrow NO_2 + O_2 \tag{3}$$

The specific rate of reaction 1, $k_1$, depends mainly on the intensity and wavelength of light. Without reactions 2 and 3 to regenerate $NO_2$, Leighton (3) calculated that the half-life of $NO_2$ in typical sunlight would be about 2 mins. While $NO_2$ absorbs light over most of the ultraviolet and visible portions of the solar spectrum, not all absorbed photons are sufficiently energetic to photodissociate the molecule. The quantum yield of photolysis is near one at wavelengths less than 3660 angstroms (A), continuously decreasing between 3800 A and 4047 A to near zero at wavelengths greater than 4358 A. Non-dissociative absorption by $NO_2$ results mainly in thermal quenching back to the ground state, but some singlet molecular oxygen may be created by energy transfer during collision between excited $NO_2$ and ground state oxygen molecules.

Reaction 2 may be thought of as a two-step process: the formation of a high-energy $O_3$ molecule and the collisional loss of energy which stabilizes the $O_3$ molecule. "M" is any third body which absorbs the energy of reaction. This reaction is extremely fast; the half-life of the oxygen atom in air is about $10^{-5}$ sec. (10).

Reaction 3 is also rather rapid ($k_3$ is 24.2 $ppm^{-1}$ $min^{-1}$ at $298^{o}K$) such that $O_3$ reaches a steady-state concentration in several minutes under constant light intensity. When this steady state is reached in the absence of other slower reactions there is a continuous conversion of light into heat with no change in concentrations.

Of course a great many more reactions actually take place. Demerjian, Kerr and Calvert (8) listed 101 reactions which involve only inorganic species. Nevertheless, reactions 1, 2, and 3 are so rapid that they control the $O_3$ concentration. Some of the more important reactions of the NO - $NO_2$ - air system are shown in Table 1 (11).

The calculation of a steady state $O_3$ concentration based on the rates of reaction and the nitrogen oxides emitted into ambient air yields $O_3$ levels well below those observed. The enhanced $O_3$ concentrations of the troposphere are primarily the result of hydrocarbon reactions which oxidize NO to $NO_2$ without consuming $O_3$. The steady-state $O_3$ concentration is given by

$$[O_3] = k_1[NO_2]/k_3[NO].$$

The effect of oxidizing NO to $NO_2$ without removing $O_3$ is to raise the $NO_2$-to-NO ratio and to increase the steady-state $O_3$ concentration. Thus, to explain high observed $O_3$ levels in an active photochemical

TABLE 1. REACTIONS AND RATE CONSTANTS FOR THE SYSTEM $NO\text{-}NO_2\text{-}N_2\text{-}O_2$ IN SUNLIGHT (11)

| Reaction Number | Reaction | Rate Constant at 298° K |
|---|---|---|
| 1 | $NO_2 + h\nu \rightarrow NO + O$ | depends on light |
| 2 | $O + O_2 + M \rightarrow O_3 + M$ | $2.33 \times 10^{-5}$ ppm$^{-2}$ min$^{-1}$ |
| 3 | $O_3 + NO \rightarrow NO_2 + O_2$ | $2.95 \times 10^{1}$ ppm$^{-1}$ min$^{-1}$ |
| 4 | $O + NO_2 \rightarrow NO + O_2$ | $1.38 \times 10^{4}$ ppm$^{-1}$ min$^{-1}$ |
| 5 | $O + NO_2 + M \rightarrow NO_3 + M$ | $4.50 \times 10^{-3}$ ppm$^{-2}$ min$^{-1}$ |
| 6 | $NO_3 + NO \rightarrow 2NO_2$ | $1.48 \times 10^{4}$ ppm$^{-1}$ min$^{-1}$ |
| 7 | $O + NO + M \rightarrow NO_2 + M$ | $2.34 \times 10^{-3}$ ppm$^{-2}$ min$^{-1}$ |
| 8 | $2NO + O_2 \rightarrow 2NO_2$ | $7.62 \times 10^{-10}$ ppm$^{-2}$ min$^{-1}$ |
| 9 | $NO_3 + NO_2 \rightarrow N_2O_5$ | $4.43 \times 10^{3}$ ppm$^{-1}$ min$^{-1}$ |
| 10 | $N_2O_5 \rightarrow NO_3 + NO_2$ | $1.38 \times 10^{1}$ min$^{-1}$ |
| 11 | $NO_2 + O_3 \rightarrow NO_3 + O_2$ | $4.6 \times 10^{-2}$ ppm$^{-1}$ min$^{-1}$ |

system, one must explain the conversion of NO to $NO_2$ which is necessary for $O_3$ buildup.

## The Air-$H_2O$-CO System

If, in addition to NO and $NO_2$, the air contains water ($H_2O$) vapor and carbon monoxide (CO), other reactions become possible which may partially explain the oxidation of NO. While many reaction pathways are possible, the most important have four steps in common: (1) the formation of hydroxyl radical, HO; (2) reaction of HO to form $HO_2$, the hydroperoxy radical; (3) oxidation of NO to $NO_2$ with regeneration of HO; and (4) recombination and other termination reactions.

HO, unlike many atoms, hydrocarbon and alkoxy radicals, does not react with molecular oxygen; and thus its concentration may rise high

TABLE 2. SELECTION REACTIONS OF THE $NO_x$-$H_2O$-CO-AIR PHOTOCHEMICAL SYSTEM (8)

| Reaction Number | Reaction |
|---|---|
| | Initial Formation of HO |
| 12 | $O_3 + h\nu\ (2900\ A^o \leq \lambda \leq 3500\ A^o) \rightarrow O(^1D) + O_2$ |
| 13 | $O(^1D) + H_2O \rightarrow 2OH$ |
| 14 | $NO_2 + NO + H_2O \rightarrow 2HONO$ |
| 15 | $HONO + h\nu\ (\lambda < 4000A^o) \rightarrow HO + NO$ |
| 16 | $N_2O_5 + H_2O \rightleftarrows 2HONO_2$ |
| 17 | $HONO_3 + h\nu\ (\lambda < 3300A^o) \rightarrow HO + NO_2$ |
| | Initial Formation of $HO_2$ |
| 18 | $HO + HO + M \rightarrow H_2O_2 + M$ |
| 19 | $HO + H_2O_2 \rightarrow H_2O + HO_2$ |
| 20 | $NO_3 + H_2O_2 \rightarrow HONO_2 + HO_2$ |
| 21 | $HO + CO \rightarrow CO_2 + H$ |
| 22 | $H + O_2 + M \rightarrow HO_2 + M$ |
| | Oxidation of NO |
| 23 | $HO_2 + NO \rightarrow NO_2 + HO$ |
| | Recombination and Termination Reactions |
| 24 | $HO + NO_2 + M \rightarrow HONO_2 + M$ |
| 25 | $HO + HO + M \rightarrow H_2O_2 + M$ |
| 26 | $HO + HO \rightarrow H_2O + O$ |
| 27 | $HO_2 + NO_3 \rightarrow O_2 + HONO_3$ |
| 28 | $HO_2 + O_3 \rightarrow HO + 2O_2$ |
| 29 | $HO_2 + HO_2 \rightarrow H_2O_2 + O_2$ |
| 30 | $HO_2 + OH \rightarrow H_2O + O_2$ |

enough to react with other trace gases. The rates of reactions involving nitrous and nitric acid, reactions 14 and 16, may be affected by a significant heterogeneous contribution, thus the rate constants used for these reactions in modeling smog chamber data are often considered to be adjustable parameters.

Demerjian, Kerr, and Calvert (8) ran simulations at various initial concentrations of $H_2O$ and CO. In a simulated system initially containing 5 parts per hundred million (pphm) of NO and 5 pphm $NO_2$ the major reactions of HO after 60 min are with NO (62.9 percent) and $NO_2$ (34.2 percent) to form HONO and $HONO_2$. When CO is added, the significance of reaction 21 increases drastically over a range of initial CO concentrations from 1 to 100 ppm. The $O_3$ produced after 151.6 min by these systems also increases: from 0.40 pphm to 7.49 pphm with 100 percent relative humidity and from 0.42 pphm to 6.88 pphm at 50 percent relative humidity. Without CO, the 100 percent and 50 percent simulations produced 0.17 pphm and 0.24 pphm of $O_3$. The concentration of various intermediates was also greatly influenced by increasing initial CO. Over the range considered, $[O(^3P)]$ and $[O(^1D)]$ increased by an order of magnitude; $[NO_3]$ increased by a factor of 500; $[HO_2]$ increased by a factor of $10^7$ and [HO] was reduced by a factor of 10. Thus, in inorganic systems, carbon monoxide's ability to serve as an electron donor to the hydroxyl oxygen leads to the formation of $HO_2$, the oxidation of NO, and the increased photostationary-state $O_3$ concentration. In the atmosphere, however, CO concentrations are not sufficient for reactions 21 and 22 to account for the $O_3$ concentrations observed. It is necessary to consider the effect of hydrocarbon reactions for such an explanation.

## The Role of Hydrocarbons

From examination of the structure of hydrocarbons commonly found in urban air, it may be inferred that in general they are more vulnerable to electrophilic attack than CO. The rate constant for the reaction of HO with CO is about 250 $ppm^{-1}$ $min^{-1}$, the rate constants of studied reactions of HO with atmospheric hydrocarbons are all higher than the CO rate constant with the exception of the methane rate constant. The rate constants for some typical alkanes, olefins, aldehydes, and acetylene were listed by Seinfeld (12). The reactivity of alkanes with OH generally increases with molecular weight and complexity: methane, 16.4 $ppm^{-1}$ $min^{-1}$; ethane, 443 $ppm^{-1}$ $min^{-1}$; n-butane, 1500 $ppm^{-1}$ $min^{-1}$; cyclohexane, 12,000 $ppm^{-1}$ $min^{-1}$. Most rate constants for alkenes and aldehydes are about $2 \times 10^4$ to $3 \times 10^4$ $ppm^{-1}$ $min^{-1}$. The rate constant for acetylene is 1470 $ppm^{-1}$ $min^{-1}$. Hampson and Garvin (13) cite rate constants for the reaction of HO with two aromatics, benzene and toluene; they are greater than $10^3$ $ppm^{-1}$ $min^{-1}$. Thus, in numerical simulations of urban atmospheres most of the HO reacts with hydrocarbons rather than CO or other organic species. The most significant result of the oxidation of hydrocarbons by HO is the formation of organic radicals which may directly oxidize NO to $NO_2$, and/or produce $HO_2$ radicals. $HO_2$ may then, in turn, oxidize NO and regenerate the hydroxyl via reaction 23. Such a sequence of cyclical reactions is known as a free radical chain reaction. HO is called a chain carrier. Individual reactions involved in chain reactions may be grouped according to their function in the overall system. The three typical functions in a chain reaction are initiation, propagation, and termination.

The hydrocarbon free radical chain may be initiated by reactions which form HO or $HO_2$, such as reactions 12 through 22 in Table 2. In the presence of organics the following reactions are among those that may initiate the chain:

$$O_3 + \text{olefins} \rightarrow nHO_2 + \text{other products} \qquad (31)$$

$$CH_2O + h\nu \rightarrow H + HCO \qquad (32)$$

$$HCO + O_2 \rightarrow CO + HO_2 \qquad (33)$$

$$H + O_2 + M \rightarrow HO_2 + M \qquad (34)$$

$$RCHO + h\nu \rightarrow R\cdot + HCO \qquad (35)$$

where R represents an arbitrary organic carbon-hydrogen group.

After the cycle has been initiated, propagation reactions oxidize hydrocarbons and NO. The major reaction cycles in photochemical smog are shown in Figure 1 (14). A characteristic of propagation reactions is that for each HO molecule reacting with hydrocarbons more than one molecule of $HO_2$ may be produced. As shown in Figure 1, $HO_2$ may then oxidize NO and regenerate HO. The concentrations of $HO_2$ and HO increase very rapidly after initiation. They would increase to rather high levels if not for consumption by termination reactions such as 24 through 30 in Table 2 that result in the formation of more stable chemical species. In addition to mediating the propagation of the chain, termination reactions form several of the secondary species which are characteristic of photochemical smog such as peroxyacyl nitrates (PAN) and nitric acid.

$$RCO_3 + NO_2 \rightarrow PAN \tag{36}$$

$$OH + NO_2 \rightarrow HNO_3 \tag{37}$$

## Gas-to-Particle Conversion

Another aspect of [illegible] chemistry is the formation and growth of aerosol in photochemical smog. This area is not as well understood as the gas-phase reactions discussed above; however, much has been learned in recent years. About one half the particulate mass during periods of moderate and heavy smog in Los Angeles is secondary material, i.e., the result of gas-to-particle conversion processes (15). The particle mass loading increases during the day, and distribution of material on a number basis shifts toward larger particle sizes in the ambient air (15) and in experimental studies (16). Hasar et al. (17) have demonstrated that coagulation cannot account for observed distribution shifts from smaller to larger particle sizes. Thus, particle growth by gas-to-particle conversion must be postulated (15, 17, 18).

In the work of Hasar et al. (17), homogeneous nucleation was observed in filtered Pasadena air exposed to sunlight, indicating the formation of secondary, condensable substances. Heisler (18) found that the growth of existing aerosol in a system of ambient Pasadena air with added NO, $NO_2$, and an organic could only be explained by a mechanism of formation of secondary materials in the gas phase and subsequent diffusion to the aerosol surface. The aerosol growth was found to be

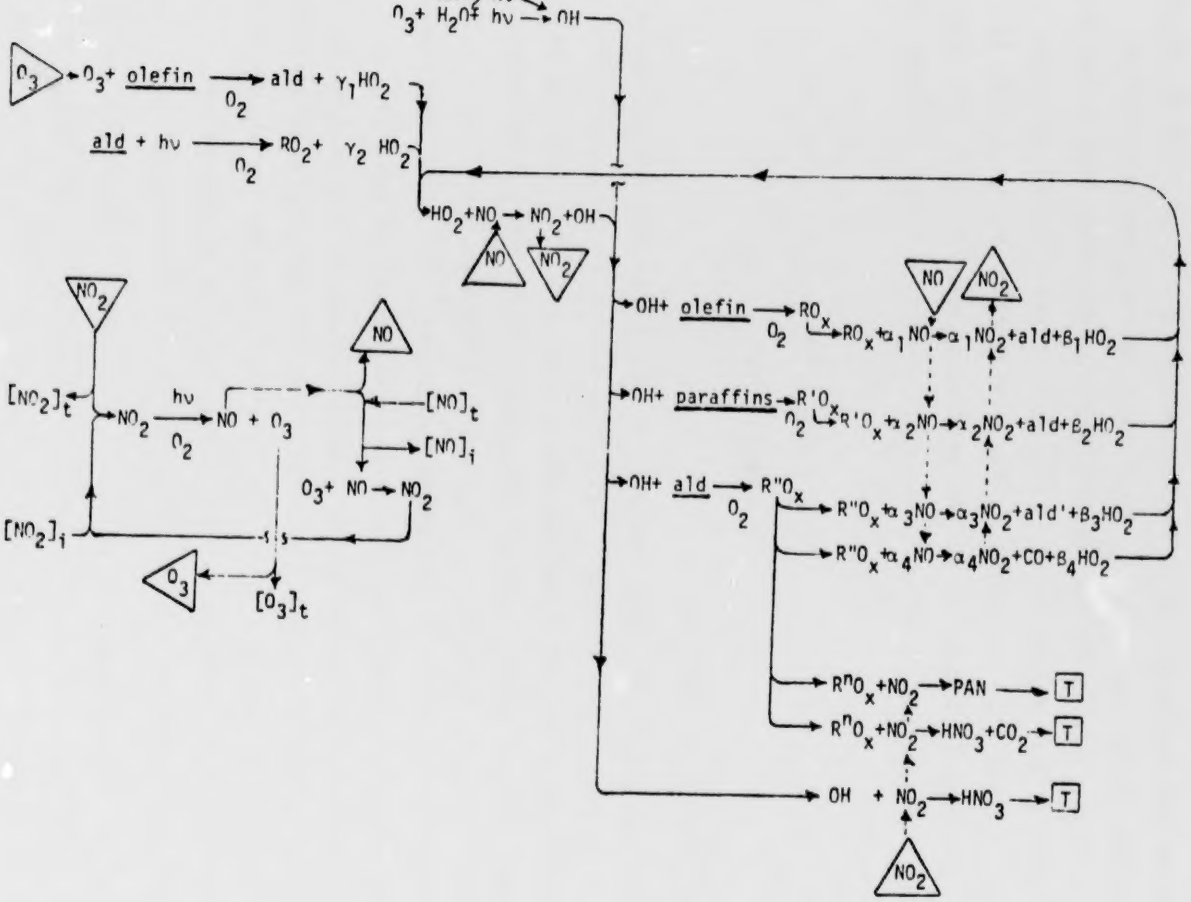

Figure 1. Important reaction cycles in photochemical smog (14).

controlled by the diffusion of a number of organic species to the particles. The organics identified in the condensed phase from olefin experiments were carbon-hydrogen chains oxygenated on both ends of the molecules. The functional groups found were acids, aldehydes, alcohols, and nitrates. When dienes were studied, molecules were found in the aerosol with the oxygenated functional groups on one end and a double bond on the other end.

## TRENDS OF PHOTOCHEMICAL POLLUTANTS IN THE ATMOSPHERE

### Interpreting the Diurnal Pattern of a Fixed Monitoring Site

The diurnal pattern of the concentrations of both primary and secondary pollutants as observed in polluted air is a readily recognizable characteristic of photochemical smog. It is the result of the combined trends of primary pollutant emissions and meteorological factors, such as sunlight, dispersion, and advection. An example of this diurnal pattern is shown in Figure 2 as observed from a stationary monitoring site in downtown Los Angeles.

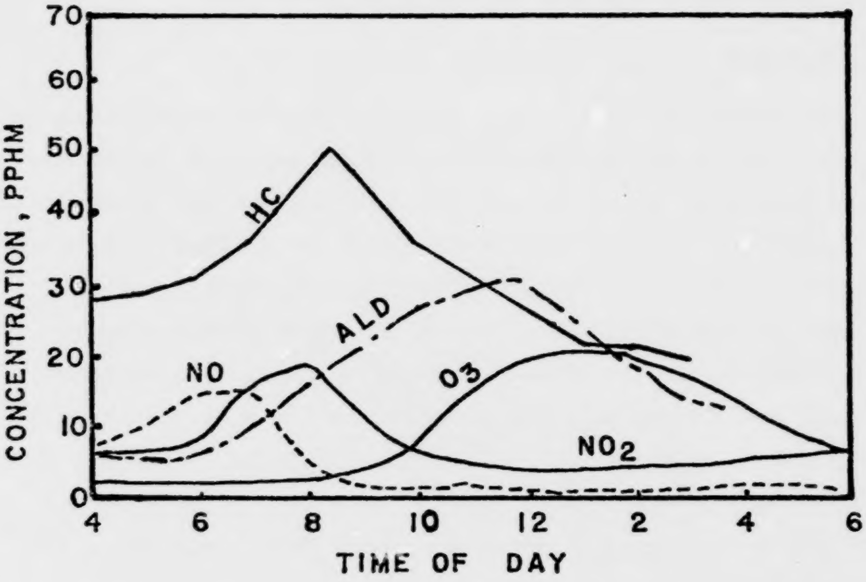

Figure 2. A typical diurnal pattern of photochemical smog constituents at a stationary monitoring site.

In order to interpret data from a fixed location, it must be recognized that air arriving at the station at any particular time has a unique history of emission, dilution, and extent of reaction. Attempts to explain fixed-station data as if the air surrounding the station were more or less homogeneous can lead to misconceptions about the processes at work. At a fixed location in downtown Los Angeles it is known that the mixing depth generally increases with time by turbulent entrainment during daylight hours. The boundary layer turbulence is a result of buoyancy which is, in turn, due to a positive surface heat flux. The rate of entrainment is dependent upon the intensity of turbulent convection (19). Also, emissions are greatest during the morning rush hour. Given these two basic facts, it is tempting to accept them plus some loss by reaction as a total explanation of the behavior of hydrocarbons and nitrous oxides in Figure 2. Both these primary pollutants reach a peak early in the morning and taper off rapidly afterward. From a Lagrangian viewpoint the concentration of a pollutant observed at a fixed station is some complex function of the emission rates along the trajectory, the windspeed as a function of time, the dilution due to increase in mixing depth, and chemical processes.

## Meteorological Trends in the Los Angeles Basin

During the warmer months--roughly April to October--the climate of the California coast is dominated by a major high pressure system centered several hundred miles offshore. The anticyclonic air movements result in prevailing south-easterly winds along the southern California coast. The subsidence associated with the high, and cooling at the ocean's surface by upwelling currents near the shore produces very stable lapse rates within the planetary boundary layer. In addition, turbulence near the air-sea interface humidifies the air, forming a "marine layer" which is about 1800 m deep near Honolulu and tapers to an average of 450 m at the California coast. Thus, air moving onshore generally consists of a humid lower layer capped by a temperature inversion, with extremely dry air above the inversion base.

Effects of the local topography are also quite important in the Los Angeles basin. In the night and early morning, cooling on the slopes of the Santa Monica, San Gabriel, and Santa Ana Mountains and the Palos Verdes and Puente Hills sets up a flow generally toward the southwestern quadrant; wind speeds are quite low and direction is variable. A convergence zone is created at coastal areas since the nocturnal mountain-valley and land-sea breezes are in opposition to the frontal circulation. Roughly two hours after sunrise the flow regime is reversed with marine air moving in over land. The marine layer is deepened and diluted with dry air along its land trajectory. Wind speeds increase until late afternoon reaching an average of 2-3 m $sec^{-1}$.

Edinger (20) studied the modification of this air as it is affected by wind speed, heat input, and position in the Los Angeles basin. His observations are summarized as follows: the marine layer during daylight hours (1) is shallow at the coast and deep inland, at any time; (2) increases in depth early in the day and then becomes progressively shallower during the afternoon at a fixed location; and (3) reaches its maximum depth first along the coast and later inland. At any location and time, the mixing depth and thus the depth of the marine layer is a function of three variables: (1) convergence or divergence of the horizontal wind averaged throughout the marine layer and over the coastal plain; (2) convective mixing which modifies the temperature profile; and (3) advection which determines how long the air has been over land. (The mixing depth may not correspond exactly with the depth of the marine layer, although they are usually nearly equal. Edinger (21) described the interaction of marine air and the temperature inversion in a developing boundary layer above the Santa Clara valley.)

Roth et al. (22) studied the temporal trends of motor vehicle emissions. The percentage of the total daily traffic for each hour is shown in Figure 3 (23). Note that the emissions at noon are only about 20 percent less than the rush-hour peaks.

Data from a fixed station in downtown Los Angeles as in Figure 2, shows the air reaching the station 2 to 3 hours after sunrise probably contains mostly local emissions and the mixing depth is quite low since surface heat flux is not large. As the heat flux goes up, the sea breeze reverses direction bringing clean air onshore. Nevertheless, the

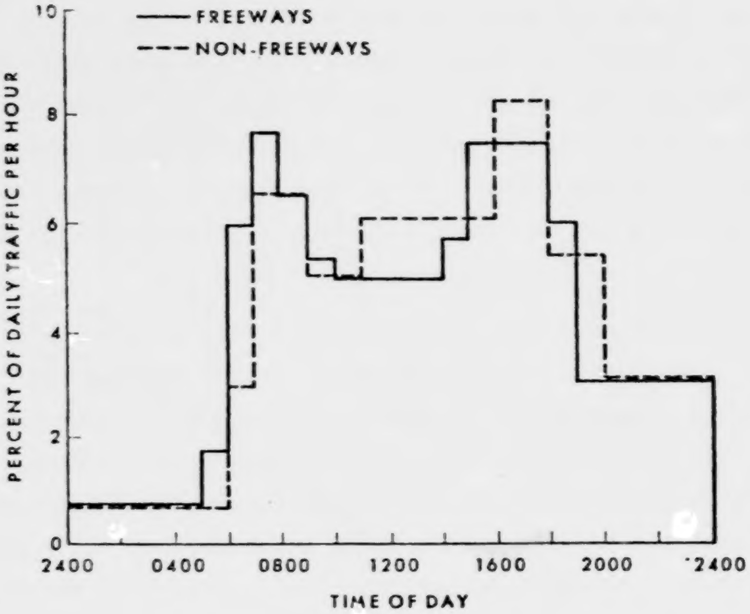

Figure 3. Freeway and non-freeway emissions.

low wind speed provides substantial time over source areas before the air reaches the station. In the later morning, wind speed is increasing, source strengths decreasing, and the mixing height nearing its maximum for that location; thus, primary pollutant concentrations are dropping off. For reactive species, the chemical consumption should also be significant by this time. After 1200, the concentrations continue to drop due to the increasing wind speed and consumption by reaction. As wind speed increases the amount of time spent over source areas decreases, as does the amount of time for photochemical reaction. Thus, in late afternoon the $O_3$ concentration is almost always higher at the eastern reaches of the basin than in the downtown area.

Oxidants in polluted atmospheres often show annual trends that are directly related to the seasonal variability of meteorological parameters. Figure 4 shows typical annual cycles for Los Angeles, Denver, and Phoenix (24). Maximum concentrations are found in the summer and fall months.

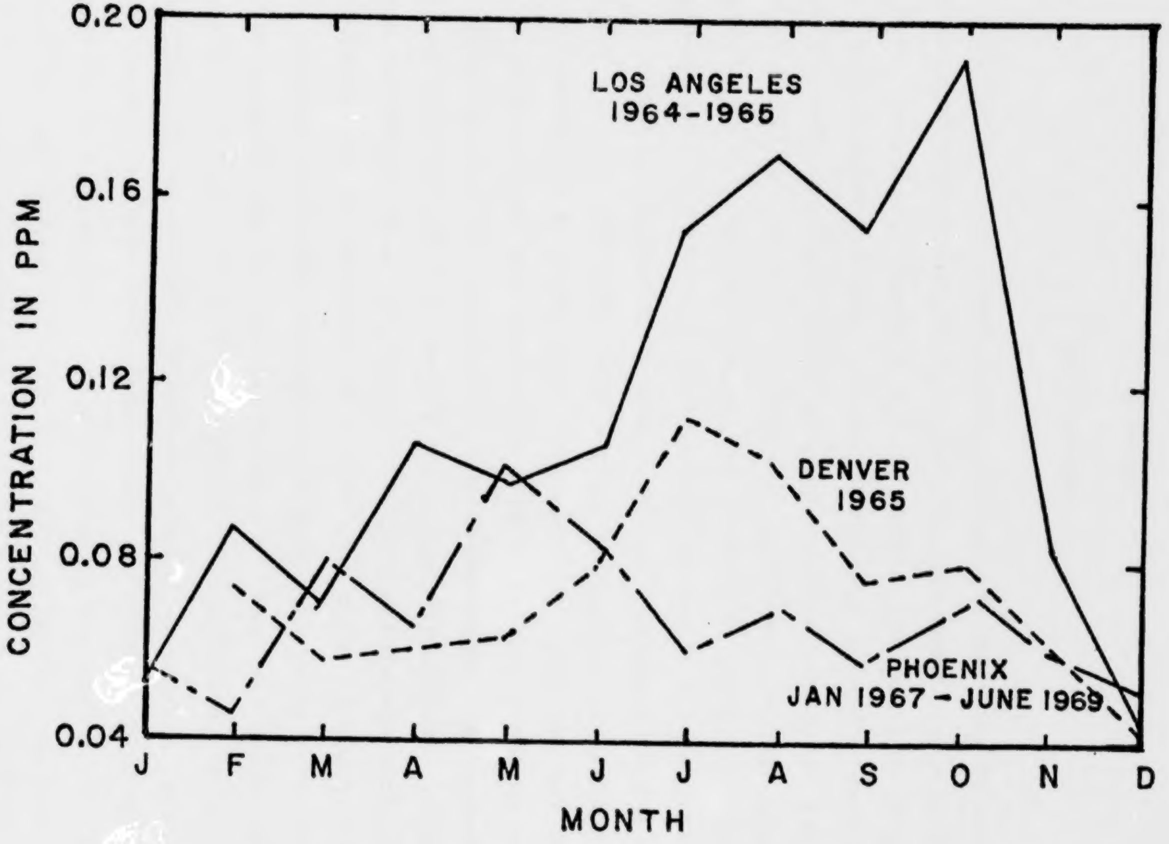

Figure 4. Annual trends of photochemical oxidant in three U.S. cities.

## SECTION 2

## CONCLUSIONS

Photochemical smog results from an extremely complex system of reactions in the ambient air. Primary pollutants, mainly nonmethane hydrocarbons and nitrogen oxides, in the presence of adequate sunlight react to form secondary pollutant species. Oxidant (measured as $O_3$ only) and $NO_2$ are two secondary species for which EPA has promulgated national ambient air quality standards. The control of $O_3$ and $NO_2$ must be based on reducing emissions of primary pollutants. One of the most difficult and controversial problems in implementing controls for these pollutants has been the determination of the degree of emissions reduction of primary pollutants required to assure compliance with the air quality standards for oxidant. The many techniques employed to relate precursor emissions to the resulting oxidant concentrations fall, in general, into three categories: cause-and-effect, correlative (or statistical), and mechanistic. Correlative techniques suffer from the reliance on present-day data; for determining control requirements, such techniques must be extrapolated beyond their data base. The mechanistic, or modeling, approaches have great promise for control strategy applications. Their major difficulty has been the great complexity of the chemical and meteorological processes, forcing the use of many simplifying assumptions. Also, kinetic mechanisms require validation and the only source of data for validation is cause-and-effect type studies. Cause-and-effect relationships are those that result from observation of reaction systems from the initial introduction of precursors to the formation of oxidant or other products, and they are the only conceptually valid means of relating oxidant to precursors at this time.

Two sources of cause-and-effect data are Lagrangian monitoring studies and smog chamber experiments. Both of these sources have certain practical difficulties. Lagrangian monitoring is expensive and the turbulent diffusion of material must be accounted for. Smog chamber experiments may be affected by the processes occurring on chamber walls, by the spectral distribution of the light source, and by the absence of a diurnal light profile, in some cases. One method of relating oxidants to precursors, that of Dimitriades, uses cause-and-effect smog chamber data but avoids some of the problems by assuming that the atmosphere's ozone isopleths on the $NO_x$-NMHC plane are proportional to $O_3$ isopleths from the chamber modified to reflect conditions of the ambient air. Both modeling and smog chamber methods require that the reactions in the smog chamber are not greatly different from those in the atmosphere. Validation of kinetic mechanisms for use in smog models depends in a quantitative fashion on the ability of the smog chamber to simulate ambient reactions. Modelers often include processes in modeling chamber results, such as the formation of nitrous and nitric acid and hydrocarbon desorption from walls, which are either eliminated or greatly decreased for application to the atmosphere. There is a great deal of uncertainty, however, concerning these adjustments.

Given the importance of smog chamber data in oxidant control decisions, it was decided to explore available atmospheric data in order to develop a data base for smog chamber validation and to attempt to validate the UNC outdoor smog chamber by simulating observed atmospheric data. Lagrangian monitoring is the only means of obtaining cause-and-effect data from the atmosphere for validation, and the Los Angeles Reactive Pollutant Program (LARPP) was judged to be the best available collection of Lagrangian data on reactive pollutants. Operation 33 (November 5, 1973) was selected for study on the recommendation of those who collected the data and because of the large number of complete helicopter patterns.

All the available data for operation 33 were examined from listings. The helicopter data were then analyzed in detail to gain an understanding of the processes affecting the concentrations of oxidant and precursors. A graphic technique was developed for displaying large numbers of individual concentration measurements and their spatial positions on a helicopter flight pattern. A three-dimensional figure was constructed for each helicopter pattern: the bottom outline of a figure represents the helicopter's flight path in geographical coordinates and the height of a figure represents the scaled pollutant concentration at the geographical position. It was possible using this technique to assess the extent of inhomogeneity in a qualitative fashion, to identify patterns with erroneous data, and to note the temporal trends of concentration at four altitude levels. It may be concluded that this representation of data is excellent for both screening data and for elucidating meteorological and chemical processes. The effects of mixing height elevation and $O_3$ generation in the morning inversion were noted.

While the concentration-position figures emphasize the inhomogeneity and random variability, consideration of helicopter pattern average concentrations revealed an overlying order to what on a small scale appeared chaotic. A region of the atmosphere was found with zero average vertical gradient for pollutants emitted at the ground. During the early morning, when concentration measurements extended to the inversion base, it was noted (as pointed out by Panofsky (25)) that this region extends from an altitude of 50 m to one-half the mixing depth. On theoretical grounds, the ratio between the upper limit of this region and the mixing depth should not have changed greatly later in the day. This region represents a much greater mass of air than does the surface layer (i.e., below 50 m for operation 33). Indeed, ground level concentrations differ from the concentrations in the zero-gradient region only to the extent that they are altered by local sources. Simulation of the zero-gradient region concentrations is probably more important than simulation of the concentration profiles at a single ground station, since the data at the ground may be influenced to a large extent by local sources. Thus, it was decided to analyze the zero-gradient region to obtain information necessary for simulation.

Since hydrocarbons are not a conservative species in the ambient air, it was necessary to calculate the total NMHC concentration which would be present in the absence of reaction based on the observed concentrations of relatively unreactive species.

Next an algorithm for determining vertical flux at the top and bottom of the zero-gradient region was developed and tested using CO data. The general agreement of the estimates of CO flux in the morning with estimates of Panofsky (25) and the greater sophistication of calculations used in this study lends credence to the early flux estimates. The validity of later flux estimates is based primarily on boundary layer theory. It should be noted that zero-gradient region concentration changes were assumed to be due to vertical transport; changes which occurred as a result of horizontal diffusion were incorporated in the vertical flux estimates. Horizontal diffusion was not treated explicitly because oxidant precursors near the operation 33 trajectory are primarily emitted from area sources, and there was not enough cross-wind data for an accurate estimate of this effect.

The fluxes of NMHC were then determined using the regression line through source reconciliation points as the lower boundary condition for the numerical solution. An analogy was drawn between the zero-gradient region and a variable volume batch reactor by means of Equation 1 below:

$$\frac{dC}{dt} = \frac{F_b}{H} - \frac{F_t}{H} - \frac{C}{H}\frac{dH}{dt} \qquad (1)$$

where C is the concentration of a conservative species, $F_b$ is the vertical flux at the bottom of the zero-gradient region, $F_t$ is the vertical flux at the top of the zero-gradient region, and H is the vertical extent of the zero-gradient region. The terms of this equation were equated with the terms in the mass balance for the smog chamber (a completely mixed flow reactor) by a logical scheme that assured that the NMHC concentration in the smog chamber would follow the concentration in the zero-gradient region if no reactions affected NMHC concentrations in either regime. Injections of $NO_x$ were kept at a constant ratio with NMHC injections based on the early morning LARPP NMHC/$NO_x$ ratio. For reactive species, differences in the LARPP and chamber concentrations can result from several sources.

(1) Failure to correctly represent emissions and meteorology is one source of discrepancy. While great effort was expended to simulate these processes, there are nevertheless some simplifications which may affect the comparison, for example, (a) the use of constant NMHC/$NO_x$ injections; (b) the use of a constant composition hydrocarbon mix; (c) the use of six source categories to represent the myriad hydrocarbon sources in Los Angeles; and (d) numerical computation of flux at altitudes for which no data exist.

(2) Differences between LARPP and the smog chamber in factors which are not under control in this experimental setting also cause differences in results. These factors include solar radiation, atmospheric inhomogeneity, and temperature. The magnitude of these effects has been discussed, as well as the effects of instrumental error.

(3) Basic differences between the chemical processes in the atmosphere and in the smog chamber are another source of discrepancy. The principal aim of this work was to explore the extent of differences between chamber and atmospheric chemical characteristics.

Simulations were performed during September and October, 1976. The two best experiments with respect to execution of the experimental procedure and weather conditions were those of October 12 and 13. After consideration of the factors which may cause differences in the pollutant profiles, it may be concluded that the atmospheric reaction processes were well simulated by the chamber reaction processes. The differences in $O_3$ between the LARPP trajectory and the experiments seem to be primarily due to very small differences in the NO concentrations. The chamber NO concentration did not reach concentrations as low as the atmosphere. This difference in NO could be explained as either too great an injection of NO or lower oxidizing radical concentrations in the chamber. Excess NO could have resulted from the simplification of maintaining a constant NMHC/$NO_x$ injection ratio. A lower oxidizing capacity of the chamber reaction system could easily be due to the use of acetaldehyde to represent all exhaust aldehyde emissions, or the down-mixing of second-day photochemical systems from above the inversion base in operation 33.

Examination of the factors affecting photostationary state $O_3$ in the atmosphere revealed much interesting information. A disagreement between $k_1/k_3$ estimated at the four altitude levels along the LARPP trajectory with $[O_3][NO]/[NO_2]$ was attributed to atmospheric inhomogeneities as Calvert (26) suggested. Beyond Calvert's analysis, the equation for photostationary state $O_3$ in an inhomogeneous medium was derived, for single measurement values and for helicopter pattern averages. Using the estimated $k_1/k_3$ and the pattern average $NO_2/NO$ ratios, it was possible to obtain estimates of the covariance of NO and $O_3$. This is the first time this value has been estimated for the atmosphere.

Inhomogeneity contributed an average of 2 pphm to the spatial average atmospheric $O_3$ concentration in the zero-gradient region on a day that produced only 15 pphm at 1400 PST. In the morning, near and above the inversion base, the contribution of inhomogeneity was as great as 6 pphm. The effects of some atmospheric processes on the covariance and on photostationary state $O_3$ were also discussed.

# SECTION 3

# RECOMMENDATIONS

The recommendations for work beyond that presented here may be divided into several categories, but they are to some extent interrelated.

## PRECURSOR CENTRAL REQUIREMENTS

Of the methods discussed in Chapter II, the Dimitriades method is the only one to use cause-and-effect data to relate oxidant to precursor levels in a manner that takes into account the differences between static chamber experiments and sample atmospheric processes. There are, however, several assumptions which require further examination. The principal one is that the $O_3$ isopleths in the atmosphere are proportional to the $O_3$ isopleths from a smog chamber adjusted by kinetic modeling to represent the atmosphere. One use of the data from the simulation experiments may be to validate the adjustment of chamber isopleths by modeling. A kinetic mechanism which has been validated against static hydrocarbon mix experiments may be run under the conditions of the simulation and the results compared with that of the smog chamber. Also, analysis of other LARPP trajectories in a cursory fashion could lead to the establishment of a set of $O_3$-NMHC-$NO_x$ points against which the assumption of proportionality may be checked.

## FURTHER EXPERIMENTAL SIMULATIONS OF OPERATION 33

Several refinements in the simulation of operation 33 may lead to even greater agreement with the LARPP concentration profiles. It is believed that major improvement would result by injection of formaldehyde in the appropriate quantities to simulate exhaust emissions.

Beyond this a more representative hydrocarbon mix could be developed although the mix employed was not greatly different from that predicted by source reconciliation. Another refinement would be to vary the NMHC/$NO_x$ injection ratio and the $NO_2/NO_x$ injection ratio. Information on the NMHC and $NO_x$ emissions along the trajectory could be used to determine the proper ratio-time profile.

## NUMERICAL MODELING

The modeling of chamber simulation results would have been a more sophisticated method of investigating the effect of light and temperature differences between the chamber and operation 33. Also, modeling of operation 33 itself would be an excellent test for a trajectory model, especially if the flux estimates of this work are used to specify emissions.

## FIELD STUDIES

The information obtained in LARPP may be used to design future field programs. Because the concentration of precursors was not known between the zero-gradient region and the inversion base, it was necessary in this analysis to develop a numerical method for estimating the vertical concentration profile of NMHC. Future field programs should obtain data up to and into the inversion.

This analysis assumed that horizontal dispersion was negligible. Future field studies should obtain data for estimating cross-wind dispersion, as well as vertical dispersion.

# SECTION 4

# METHODS OF RELATING OXIDANT TO PRECURSORS

In order to control a secondary pollutant such as $O_3$, it is necessary to know quantitatively how precursor emissions affect the amount of $O_3$ formed. The methods for obtaining an oxidant-precursor relationship may be divided into three categories:

1. Cause-and-effect relationships are those that result from observation of reaction systems from the initial emission or injection of primary pollutants to the formation of oxidant and other products, for example, smog chambers, or Lagrangian air monitoring data.
2. Correlative or statistical relationships are those obtained from observation of ambient air with no assurance that the precursors observed gave rise to the oxidant measured at some later time. The EPA upper limit curve (to be discussed later) is an example of this type.
3. Mechanistic relationships are those obtained from knowledge of the individual reactions in the photochemical smog complex such as any of the numerical kinetic models, e.g., Hecht and Seinfeld (27) or Wayne et al. (28).

There are problems with all approaches for use as the basis of a control strategy, or for standard setting. Correlative, or statistical approaches are derived from data collected at present-day emission levels. The effect of emissions controls on the relationship cannot be known when extrapolating beyond the emission ranges giving rise to the aerometric data base. The mechanistic approaches must be "validated," i.e., its predictions must be compared with observations in the ambient air. Also, it is not known how far the model may be extrapolated beyond the conditions of validation because arbitrary adjustments of rate constants are often necessary to get a "good fit." No model has yet been developed which provides good prediction of oxidant levels from a hydrocarbon mixture typical of urban air. Cause-and-effect relationships from smog chambers are questionable due to the possible effects of surface characteristics, background reactivity, and simulated radiation. Thus, smog chambers must also be validated. Cause-and-effect relationships derived from monitoring ambient air along a trajectory are very expensive and conditions cannot be controlled. Nevertheless, Lagrangian monitoring is the only theoretically perfect source of data for validation of a smog chamber or a kinetic mechanism. The precursor concentrations measured in the morning along a trajectory are the cause of the oxidant formation later in the day. Of course, it is necessary to collect sufficient information to evaluate the effects of meteorology along the trajectory.

Some of the individual methods of obtaining oxidant-precursor relationships will now be described and evaluated. Mechanistic methods (models) will not be considered because of their great complexity and their continuous development and improvement.

## THE EPA ASSESSMENT OF CONTROL REQUIREMENTS

The promulgation of a hydrocarbon standard represents a considerable simplification of the complex relationship between hydrocarbon emissions and oxidant level. Essentially, a day is divided into a time for build-up of primary pollutants and a time for reaction, although in reality emissions and reactions occur throughout the day. It implicitly asserts that hydrocarbon may be treated as an inert pollutant until 9:00 a.m.; emissions after 9:00 a.m. are assumed to have negligible effect on oxidant.

Since the Federal method of assessing the effects of hydrocarbon emission, and thus the efficacy of hydrocarbon control, has caused such controversy it will be considered first.

## The Upper Limit Curve

The relationship between the morning concentration of nonmethane hydrocarbons and the maximum 1-hr oxidant concentration was obtained by analysis of air monitoring data from CAMP (Continuous Air Monitoring Program) stations. The daily maximum 1-hr average oxidant concentrations were plotted versus the corresponding 6:00 to 9:00 a.m. average nonmethane hydrocarbon concentrations. Then, a curve was drawn such that, at almost all hydrocarbon concentrations, the largest observed oxidant was somewhere below the curve (29). It was reasoned that oxidant read from this curve represented the highest oxidant which could be expected from the corresponding nonmethane hydrocarbon concentration. Thus, if oxidant was to be prevented from exceeding 0.08 ppm more than once per year, the 6:00 to 9:00 a.m. nonmethane hydrocarbon concentration must not exceed the corresponding value, 0.24 parts per million carbon (ppmC), more than once per year. This is known as the "upper limit" or "umbrella" curve.

Heuss, Nebel, and Colucci (30) presented six criticisms of the upper limit curve. First, they contended that this model includes an excessively large probability factor. That is, they state that maximum oxidant potential is reached less than one percent of the time. (They give no reference.) Thus, that on the single allowable day each year which exceeds the 0.24 ppmC hydrocarbon standard, the probability of exceeding the oxidant standard is less than 0.01. Further, they conclude that "the combined probability of exceeding the oxidant standard is only once in 100 years." This assertion may be considered as a simple statement of probability. If event A is defined as exceeding 0.24 ppmC 6-9 am NMHC, and event B is defined as reaching maximum oxidant forming potential, then the probability of exceeding the oxidant standard is $P(A \cap B)$, the probability of A intersection B. The probability statement of Heuss, Nebel, and Colucci is then:

$$P(A \cap B) = P(A) \cdot P(B) \tag{2}$$

where P(A) and P(B) are the probability of events A and B respectively. This equality is only true when events A and B are stochastically independent. Since it is likely that the meteorological factors which cause the NMHC standard to be exceeded, viz., poor atmospheric dispersion, are also a prerequisite for maximum oxidant forming potential, the assumption of independence cannot be made. Therefore, $P(A \cap B)$ is probably much greater tha $P(A) \cdot P(B)$; this criticism is then a great exaggeration.

The second criticism was that the EPA model does not account for the great change in the ratio of hydrocarbon to nitrogen oxides which should result from control of these pollutants. This is certainly a valid objection. There was only a small quantity of data available with which to assess the effects of $NO_x$ and NMHC/$NO_x$ ratio on oxidant from the CAMP stations (31) when the NMHC standard was promulgated.

The third criticism was that the often large error in nonmethane hydrocarbon measurements may have caused considerable underestimation of the actual NMHC of the data point defining the upper limit curve. This would, of course, lead to an unrealistically high assessment of control required to achieve compliance with the oxidant standard. It is not clear how closely this was considered in the analysis by EPA, but in general the data were very meticulously selected for producing the upper limit curve.

Heuss, Nebel, and Colucci (30) pointed out in their fourth objection that the upper-limit curve relies heavily on weekend data. This is suspect because emissions on weekends are only 5 to 10 percent of the weekday emissions from 6:00 to 9:00 a.m., but nearly equal to weekday emissions from 9:00 to 12:00 a.m. Thus, the selection of the 6:00 to 9:00 a.m. average NMHC to characterize the chemical potential for oxidant formation is seriously questioned.

Their fifth criticism was that the model does not properly account for situations of increasing stability during the day. Again, they conclude that the 6:00 to 9:00 a.m. average is not a good indicator of the potential to form oxidant, since the NMHC maximum concentration may occur after 9:00 a.m. under increasingly stable conditions. There may be certain days on which this is valid; however, the meteorological factors which cause the lower atmosphere to become more stable after sunrise do not favor the formation of oxidants. Two such meteorological factors are: (1) very cloudy weather and (2) frontal inversion (advection of a cold front below a warmer air mass).

The sixth objection was that sampling location factors are not adequately treated in the model. Heuss, Nebel, and Colucci (30) maintain that the oxidant precursor concentrations measured at a particular monitoring site are determined by local sources, while the oxidant measured later that day is characteristic of a much larger area since there has been sufficient time for mixing in an air basin. This is perhaps a much more important point than was thought: not only is the influence of local sources unquestionable in measuring precursors, but there is recent evidence that mixing within an air basin during the day may be much less than was originally supposed (29). Angell, Dickson, and Hoecker (32) reported the results of following a triad of simultaneously-launched constant-density tetroons in the Los Angeles area. Their work, performed as part of the Los Angeles Reactive Pollutant Program (LARPP), showed limited horizontal mixing.

The National Academy of Sciences Committee on Motor Vehicle Emissions (33) based its criticisms of the NMHC standard primarily on the smog chamber work of Dimitriades (34). Since it was not possible to state that the smog chamber duplicates the behavior of the atmosphere, it was not possible to validate this criticism. Dimitriades (34) states, "Considering the difference between the experimental system of this study and the natural atmosphere, it would be of interest to compare smog levels observed in this study with smog levels in the atmosphere for similar mixtures of pollutants. For such comparison, atmospheric data not readily attainable must be used; for example, HC and $NO_x$ levels in an air parcel during early morning hours and levels of smog in the same air parcel after several hours of sun irradiation."

The Los Angeles Air Pollution Control District (LAAPCD) also criticized the NMHC standard because it does not consider the role of nitrogen oxides (35-36). Their alternative approach, which will be discussed in more detail later, is based on smog chamber experimentation and an empirical equation for relating chamber oxidant to atmospheric oxidant.

Since the initial flurry of criticism, other problems with the upper-limit curve have been identified. One principal difficulty with this approach is that most of the variation in hydrocarbon concentration resulted from meteorological variation rather than changes in emissions. There is some experimental evidence that systems which are diluted with clean air may produce more $O_3$ than an undiluted system under certain conditions, even though the initial hydrocarbon concentrations were the same (37). The data were not available when the standard was promulgated, and thus the significance of this problem was not known. Considering this effect alone, it indicates that reduction of emissions may be more effective in controlling oxidants than is indicated by the upper-limit curve.

A second problem in applying the upper-limit curve is that it assumes that the stationary-site monitoring data are representative of the concentrations over a large urban area. That is, it assumes that the parcels of air which contain the maximum 1-hr oxidant at a fixed station had approximately the same NMHC as was measured at the station several hours before (from 6:00 to 9:00 a.m.). This approach was justified in the Hydrocarbon Criteria document by pointing to the good correlation between various stations in the Los Angeles area (38).

Regardless of such correlations, it would be desirable to know the concentration of hydrocarbons (and $NO_x$) which truly gave rise to the maximum oxidant. This is necessary to obtain a valid cause-and-effect relationship, as opposed to a relationship based on correlation. Also, more recent studies (39-41) emphasize and attempt to explain the spatial variation of photochemical pollutants in the Los Angeles basin. In order to obtain a causative relationship in the ambient air, it is necessary to tag and follow parcels of air as they traverse an air basin, measuring the relevant chemical species. Of course, experimental techniques which employ a captive air parcel, smog chamber experiments, produce relationships which are valid with respect to their cause-and-effect character. There may be other factors which cause differences between the ambient and the experimental air parcels.

## The Rollback Model

In the two-part EPA model for relating emissions of precursors to oxidants, the first step was to establish a NMHC standard which would assure compliance with the oxidant standard. The remaining step was to determine what degree of emission reduction would be needed to comply with the NMHC standard. This was done by means of the "proportional," or "rollback" model (42). This approach is based on the assumption that a particular percentage reduction in emissions of a pollutant will result in equal percentage reduction in the ambient concentration corrected for natural background.

Obviously, the only circumstances under which concentration displays a nearly linear relationship with emissions are on rather long averaging times, such as a year. On shorter time intervals, the meteorological factors which affect pollutant dispersion are likely to introduce considerable variation around the straight concentration-emission line. The variation of pollutant concentration for a wide range of averaging times has been shown to be approximated by a log-normal distribution (43-44). (That is, the logs of concentrations appear to exhibit normal distributions.)

The distribution results from variations in both emissions and meteorological factors. For nonmethane hydrocarbons between 6:00 and 9:00 a.m., it is felt that the major part of concentration variations is due to changes in meteorological conditions, although emissions at this time of day do show some day-of-the-week effects. One study found that only 20 percent of the variation in NMHC could be explained by changes in emissions; the total range of hydrocarbons and oxidant values varied as much as 200 percent (29). Thus, the Federal model for control is a straight-line, concentration-emission relationship with the residuals about the line exhibiting a log-normal distribution at any particular emission level.

Also, the calculations of the required percentage reduction of hydrocarbons failed to take into account a very important point. It was assumed that emission reduction has the effect of simply translating the distribution of concentrations to produce a lower geometric mean value without changing the spread of the distribution. This is not reasonable on common-sense grounds. In simple dispersion models, concentration is directly proportional to source strength. Thus, if the source strength is reduced and the distribution of meteorological variables remains unchanged, the standard deviation of the distribution would also be reduced. The significance of this is uncertain now, but it bears further consideration.

Another problem with the rollback model is that the concentration-emission line may not be straight if atmospheric reactions are important. There may be interactions that have severe effects on the control requirements. The $NO_2$ air quality standard and the emissions standard for nitrogen oxides are based on the avoidance of adverse health effects from $NO_2$ with no consideration of the effects on the production of oxidant. There is evidence that reduction of NO concentrations can produce increased maximum oxidant at the concentration ranges of precursors projected for Los Angeles air (34, 45). Thus, this should be considered in setting emission standards for $NO_x$.

Conversely, control by hydrocarbons may affect the dosage of $NO_2$. In chamber experiments, the rate of $NO_2$ formation up to the $NO_2$ peak is proportional or a little less than directly proportional to the initial hydrocarbon concentration under constant light intensity (34, 46). In outdoor smog chamber experiments, Kamens et al. (47) found that reductions of initial NMHC concentrations of 50 percent to 85 percent from a concentration of 2.9 ppmC (at the same initial $NO_x$) resulted in high nighttime $NO_2$ concentrations. In these experiments it was noted that combinations of hydrocarbons and meteorological variables which were sufficient to convert NO to $NO_2$, yet slow enough that a low maximum daily $O_3$ concentration was produced, gave rise to high $NO_2$ concentrations during the night. The observed effect of NMHC concentration reduction was to reduce oxidant concentrations, and maximum $NO_2$ concentrations, while increasing $NO_2$ average concentration over a 22-hr period.

The possibility of such interactions, as described above, points up the need to consider the hydrocarbon-$NO_x$-oxidant system as opposed to separate handling of $NO_2$ when setting standards.

## OTHER METHODS OF ASSESSING THE EFFECTS OF CONTROLLING OXIDANT PRECURSOR EMISSIONS

There are numerous approaches to relate oxidants to precursors, other than the method used by EPA. These approaches have several things in common. They are, for the most part, well-thought-out uses of available data and of present scientific understanding of the problems. Also, they all are attempts to use data from present-day air to predict the effects of future events on future air quality. Thus, they are all, in this respect, extrapolations, and contain various degrees of uncertainty. The present approaches may be categorized in many ways; one way of interest is the source or type of information utilized. The types of information utilized by most of the published methods are presented in Table 3. It should be noted that most of these methods depend to some extent on stationary monitoring data to define the oxidant-precursor relationship. Such approaches cannot yield valid cause-and-effect relationships between precursors and products because an air parcel passing by a monitoring site has a different trajectory and emission history from the air that passed that site sometime before. The methods enumerated in Table 3 will now be summarized and critically evaluated, except the upper-limit curve which has already been considered. The method developed by the Los Angeles Air Pollution Control District (LAAPCD) is considered first and in considerable detail because it has caused much controversy.

### The LAAPCD Method

LAAPCD (35) has criticized the EPA method of assessing the effects of precursor emissions on the following grounds. (1) The very important ratio between NMHC and $NO_x$ has not been considered. (2) Reduction of stationary-source emissions is not necessary since the air into which these pollutants are emitted lacks either the NMHC or the $NO_x$ to form smog. That is, these emissions are not mixed with emissions from

TABLE 3. OTHER METHODS OF RELATING OXIDANTS TO PRECURSORS AND THE SOURCES OF DATA FOR EACH METHOD

| Type/ Approaches | Stationary Monitoring Data | Emission Inventory | Smog Chamber | Deterministic Models | Meteorology |
|---|---|---|---|---|---|
| 1. Upper limit curve | CAMP data | | | | |
| 2. Kent Wilson | 17 L.A. and S.D. monitoring sites | Geocoded emission a 2000'x2000' gird (at nodes) (RAND & SAI) | | | |
| 3. Texaco | 86 station years from 15 cities (includes CAMP) | | | | |
| 4. Trijonis | APCD data | APCD Profile (1971) | Dimitriades (BOM) | | surface wind direction for monitoring data |
| 5. Hamming LAAPCD | LAAPCD data | | LAAPCD chamber data | | (gross assumptions |
| 6. Chevron | | | | | |
| 7. Stephens | his own | Emissions directly determined | | | very basic |
| 8. Dimitriades | only to establish present oxidant levels | not necessary | Dimitriades (BOM) | Model of chamber data | worst case conditions assumed in model run |

automobiles to any appreciable extent. LAAPCD contends that only automobile emissions are important in forming high oxidant levels. (3) The reductions of emissions by transportation controls suggested by EPA will have minimal effect since it cannot affect the NMHC/$NO_x$ ratio.

The alternative method of assessment is based on several assumptions. (1) Maximum emissions occur in downtown Los Angeles and maximum oxidant concentrations are observed in outlying areas, such as Pasadena and Azusa, thus the emission in the downtown area shows its effects in outlying areas. (2) "Wind-flow patterns show that characteristic patterns of transport for related source area-effect area combinations are separate and parallel, not mixing or joining. Each source area has its own "reaction pipeline" to its own effect area or areas. Generally wind flow follows the same route on all smoggy days." (3) Since the emissions of a particular area are assumed to remain segregated, the reactions occur in a batch mode similar to smog chamber operation. (4) The effects of NMHC and $NO_x$ control cannot be seen in the ambient air, it must be studied in a smog chamber and the chamber results related to the ambient air.

The maximum smog chamber oxidant corresponding to observed and projected NMHC and $NO_x$ levels for the years 1960 to 1990 is shown in Figure 5 (35). The maximum atmospheric $O_3$ can then be calculated from maximum chamber ozone by the "Hamming transformation" equation.

This equation deserves further discussion. It is an equation whose form is completely empirically determined, but it is presented in a reply to EPA questions (36) as if it were a physical or deterministic model. The derivation begins with the equation:

$$\text{Conc. } O_{3_{\text{air}}} = \frac{k_1 \text{ Conc. } O_{3_{\text{ch.}}} + k_2 \text{ Conc. } O_{3_{\text{ch.}}}}{D_f} \qquad (3)$$

where $k_1$ is a "constant intended to represent the constant rate of loss of pollutants associated with test chamber experiments due to both instrument sampling and leakage from the chamber during six hours or more of constant irradiation." The term $k_2$ is related "to the additional ozone that is formed from additional HC and $NO_x$ introduced into

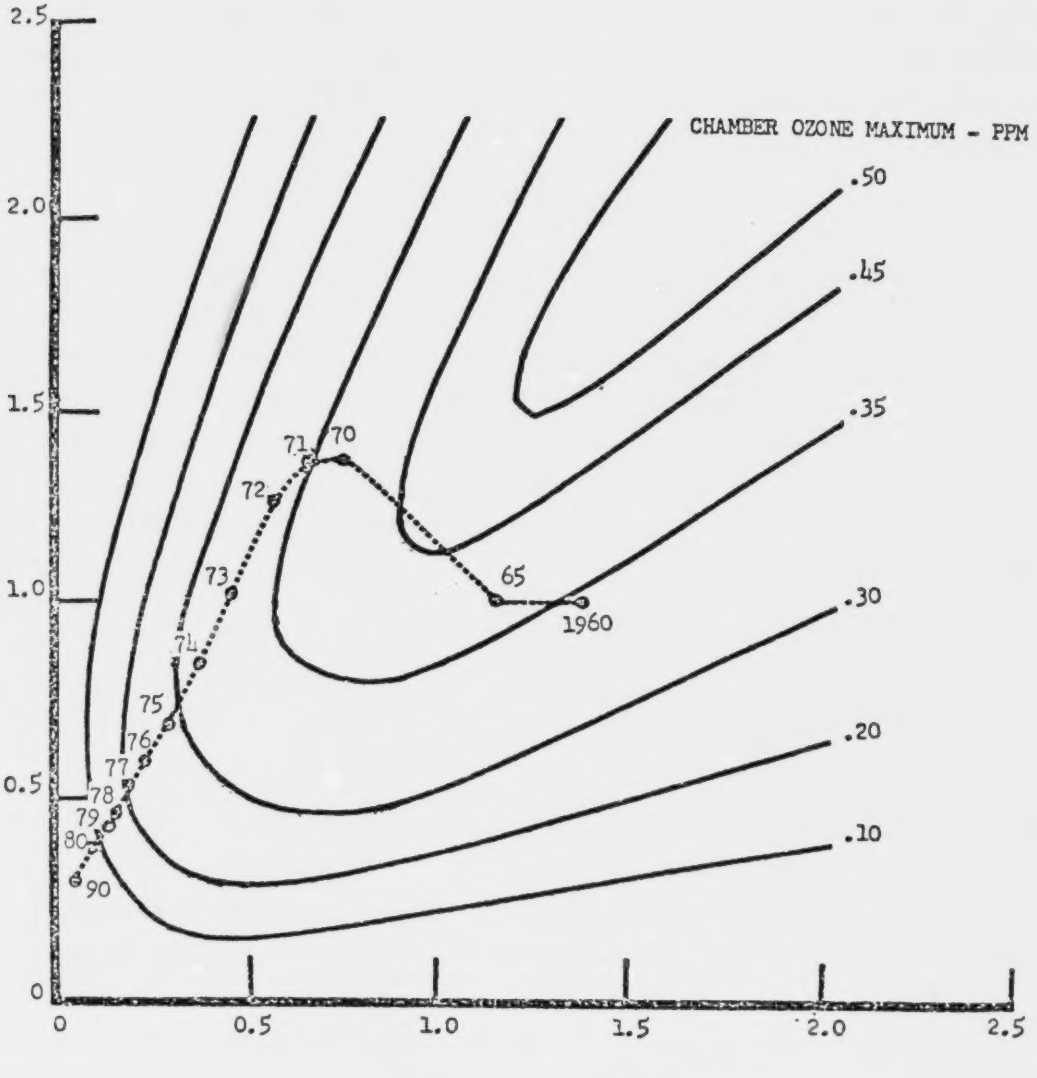

Figure 5. Maximum smog chamber oxidant corresponding to observed and projected NMHC, 1960-1990 (35).

the 'pipeline' by sources, predominantly traffic, along the path traveled by the air moving from a central source area in the morning...," "$D_f$ defines the minimum diffusion and dilution coefficient; that which produces the maximum ozone." This equation then assumes that minimum dilution produces maximum ozone. As shown by Fox, Kamens, and Jeffries (37), this is not necessarily true with low reactivity systems such as at hydrocarbon concentrations near the NMHC standard. The term $D_f$ is not a constant, but is some function of the time over which dilution processes take place. The form

$$D_f = k_4 \, (NO_x)^m \, (T_r)^n \tag{4}$$

was presented without corroborating data concerning goodness-of-fit. $NO_x$ is "the amount of $NO_x$ in the air parcel" and $T_r$ is the time between the NO peak and the $NO_2$ peak. It is difficult to examine this expression since $D_f$ is not measurable, and no data is presented. "Conc. $O_{3_{ch.}}$" is the maximum $O_3$ concentration which would result from a chamber irradiation of NMHC and $NO_x$ levels observed in the atmosphere. "Conc. $O_{3_{air}}$" is the concentration $O_3$ would reach under the very bad meteorological conditions.

Equations 3 and 4 were then combined:

$$R = \frac{\text{Conc. } O_{3_{air}}}{\text{Conc. } O_{3_{ch.}}} = \frac{k_1 + k_2}{D_f} = \frac{K}{(NO_x)^m \, (T_r)^n} \tag{5}$$

The exponents m and n were estimated from data on the years 1960, 1965, 1969, 1970, 1972, and 1973. The "Conc. $O_{3_{ch.}}$" used to calculate R for each of these years was the $O_3$ corresponding to the maximum NMHC and $NO_x$ observed during the year. The source of $NO_x$ and $T_r$ used in the estimation is not clear, nor is the estimation algorithm described. These particular years were selected because they were the years which cluster at the highest level of R; 1971, the year with the greatest R, was excluded from the estimation procedure. The exponent estimates were $m = -0.222$ and $n = 0.106$.

After the exponents were obtained, the values for K were calculated for each year. (It was not explained how m and n could be estimated without some value of K either known or assumed.) 1971 had the highest K value, or 1.50 was used; no explanation of the 80 percent figure was given.

Further adjustment of maximum $O_{3_{air}}$ is made since the oxidant standard allows the 0.08 ppm level to be exceeded once per year. Thus, the mean ratio between highest oxidant value each year and the second highest oxidant for several years (1.094) is divided into the oxidant predicted from Equation 5.

This approach is similar to the EPA method in that it treated precursors as inert material which accumulate early in the morning to some starting concentrations analogous to the initial concentrations in a smog chamber. The EPA approach assumes that the air basin is fairly homogeneous, and thus a single CAMP station can characterize the entire air basin; LAAPCD rejects this but assumes that a stationary monitoring site in downtown Los Angeles will measure the highest levels of precursors emitted and that the stations in Pasadena and Azusa will measure the highest resulting oxidant. Both these assumptions are rather simplistic and greatly limit the reliability of the methods.

The LAAPCD method has numerous other difficulties. One problem is the use of the maximum observed NMHC and $NO_x$ concentrations during any year to calculate "Max. $O_{3_{ch.}}$" seems to violate their own strong assertion that the ratio $HC/NO_x$ is very important. They do this because they believe that only automotive emissions are important in oxidant production, and, thus, the ratio is nearly fixed in any year by the extent of HC and $NO_x$ control in the vehicle population. There is evidence that the ratio is not fixed. Trijonis (48) presented data on summer morning $NO_x$ and HC concentrations (730 - 930 PST) measured at the downtown LA APCD station from 1966-70. Most of the HC-$NO_x$ pairs have ratios which fall between 40 and 9; within this range their distribution is fairly uniform (with respect to ratio). Even if the fixed-ratio assumption is accepted, there is a possibility that the maximum $NO_x$ during a year may have been the result of stationary source emissions, while the highest HC occurring at some other time was the result of mobile-source emissions. One must also be rather skeptical concerning the "Hamming transformation" operation. The form of this model has never been justified either from basic physical and chemical principles or from its ability to fit data (35-36, 45, 49).

The good points of the LAACCD method are that it makes an attempt to account for the role of $NO_x$ in smog formation and it recognizes that transport of pollutants must be considered.

### The Wilson Method

Wilson (50) has developed a statistical model which is purported to assess the effects hydrocarbon emissions have on an index of photochemical air quality. The index chosen was the number of days per year that a given region exceeds the oxidant air quality standard of 0.08 ppm. Input to the model during its calibration included reactive hydrocarbon emission inventory at each node of a 2000 by 2000 foot grid, most probable wind paths for Los Angeles and San Diego, and the number of days per year that the oxidant standard is exceeded for seventeen monitoring stations. In the Los Angeles region, air quality index data 1968, 1969, and 1970 were used with emissions data from 1970. For each monitoring station the emissions in a 4.5 mile-wide strip along the most probable wind path were integrated. These values were then plotted versus the air quality index (the mean index for the three year span, if data were available for three years) for each monitoring station. Also, at each station a "roll-back" analysis was performed to determine the emission level at which the expected highest 1-hr $O_3$ concentration would equal 0.08 ppm. The average emission level for compliance was used as the intercept with the horizontal axis. A second-order least-squares fit to this data was obtained. The curve appears to have been forced through the emission axis intercept. From inspection of the plot, it is difficult to believe that the second-order coefficient in such a fit could be statistically significant since the scatter around the line is considerable; in fact the statistical significance of the first-order coefficient is in doubt.

The Wilson approach is quite good in its spatial resolution, but the treatment of smog chemistry is extremely primitive. The role of $NO_x$ is ignored, emissions at different times of the day are treated as though they have the same effect, and the "roll-back" method is used on a non-linear process. The use of "most probable paths" to approximate the often meandering trajectories (32) of the South Coast air basin is not detailed enough for many purposes. The equation relating emissions to air quality index does not fit the data well at all, thus its predictive capabilities must be called into question.

## The Trijonis Method

Trijonis (48, 51) developed a means of assessing the effects of reduced NMHC and $NO_x$ emissions as part of his economic analysis of photochemical air pollution control in Los Angeles County. Like Wilson, Trijonis used an index of air quality as opposed to actual concentration. The following assumptions are made. (1) Emission reduction of NMHC and $NO_x$ occur homogeneously in space and time. (2) Emissions of precursors accumulate in the morning without reacting to produce final morning concentrations and, thus, precursor concentrations are proportional to their emissions. (3) Accumulation stops and meteorological factors act on precursors to produce the maximum oxidant level. (4) The weather variables which affect the oxidant level produced are statistically independent of the distribution of maximum oxidant later in the day. These last two assumptions are rather difficult to justify, but steps have been taken in selection of data to increase their validity.

The actual analysis proceeded by obtaining the joint frequency distribution for NMHC and $NO_x$ from five years of data (1966-1970) at the downtown Los Angeles APCD station. The average maximum 1-hr oxidant values between 11:00 a.m. and 1:00 p.m. for the downtown, Burbank, and Pasadena stations, weighted according to wind speed and direction, were used to develop the probability for exceeding the oxidant standard as a function of NMHC and $NO_x$ concentrations. By assumptions (1) and (2), the probability distribution of precursors can be determined for any emission level if it is known for a fixed level. And, by assumptions (3) and (4), the oxidant probability as a function of precursor concentrations does not change with emissions. Thus, the number of days per year expected to exceed the oxidant standard is plotted as isopleths on a graph of $NO_x$ emissions versus NMHC emissions.

This method has a great deal of appeal since a direct relationship is obtained between emissions and air quality. Also, it is presented clearly with nearly all assumptions stated and defended. Nevertheless, it is marred by the same flaw as the "upper limit curve:" the relationship between oxidant and precursor concentrations reflects the effect of variable atmospheric dilution on precursors, not the effect of reduced emissions. If assumption (4) were absolutely correct, this would not matter, but it is by no means completely true. As mentioned earlier, lowering precursor concentration by dilution may not have the same effect on oxidant as lowering by cutting emissions, especially at low concentrations. This is intended as an air basin model, thus spatial resolution is not great. Assumption (3) is another weak spot: emissions after 9:30 a.m., while not as great as the rush-hour emissions, can have significant effects on oxidant maxima as indicated by mathematical modeling efforts at UNC (52).

## Stephens Method

The work of Stephens (53) at the University of California at Riverside is not a well-developed method for assessing the effect of changes in emission levels as the methods discussed above. Only a very small amount of data has been analyzed by Stephens' technique. The concepts developed by Stephens could be used for such a purpose if its present problems can be resolved.

By measuring tracer compounds in air with high oxidant concentrations, Stephens has attempted to estimate the total emissions of hydrocarbons into the air parcel in which the oxidant was measured. Acetylene was used as an indication of automobile emissions, and ethane and propane, as indicators of natural gas emissions. The ratio of propane to ethene is used as a measure of the extent of reaction. This ratio measured in the air parcel was compared with the ratio calculated for both batch and stirred-tank reactors using the first-order removal rates of the two olefins as observed in a smog chamber. A major problem with this approach is that the batch and stirred-tank regimes do not represent the full range of reactant contacting schemes--it is a definite mistake to assume that the ratio in the air must fall between the lines representing these regimes on the ratio versus time axes. In addition, the equation used by Stephens to compute the concentrations in a continuous-flow, stirred-tank reactor as a function of time is in error. Also, it is not possible using this method to obtain a good estimate of $NO_x$ emissions (23). Thus, much work is needed prior to application of this technique.

## Texaco and Chevron Models

Both the Texaco (54) and the Chevron (51) models are based on regression analysis of stationary-site monitoring data. Texaco used data from fifteen U.S. cities, including eighty-six station-years of data. The second highest annual oxidant measurements were related to the means and standard deviations of the yearly distributions of oxidant, hydrocarbon, and nitrogen oxides. The Chevron technique uses step-wise regression to relate the 1-hr maximum oxidant to NMHX and $NO_x$ concentrations at a single, stationary, monitoring site in Los Angeles. Both these methods rely on single-site data in each city examined, thus transport is not considered. Another drawback similar to the "upper limit curve" approach is that the range of hydrocarbon and $NO_x$ values considered mainly results from meteorological variations rather than reduced emissions. Thus, these approaches are not applicable to the assessment of control requirements.

## Dimitriades Method

Recently, a method was proposed by Dimitriades (34) as an alternative to the current Federal method of relating oxidants to precursors. It is similar to the current EPA method (Appendix J approach) in that it treats the emission of precursors to produce early morning concentrations as separate from the dependence of oxidant on morning NMHC and $NO_x$ concentrations. The method produces a much more sophisticated relationship between oxidant and 6:00 to 9:00 a.m. precursor concentrations, while the equivalent of linear rollback is used to relate the desired and present $NO_x$ levels to the required emission reductions.

The relationship between morning precursors and maximum 1-hr oxidant was first derived from the smog chamber data of Dimitriades

(57). These chamber runs were modeled numerically by Dodge (58). After reasonable fits to the chamber data were obtained, the model was altered to make the simulation conditions closer to those of an urban environment.

Initial $HNO_2$ was set to zero, chamber contamination effects were removed from the mechanism, initial $NO_2$ was set to 25 percent of initial $NO_x$, diurnal variation of photolytic rate constants was employed, and a period of from 7:00 a.m. to 4:00 p.m. was simulated with the assumption of 3 percent $hr^{-1}$ dilution during this time. The model computations were repeated over a range of NMHC from 0.2 to 5.0 ppmC and a range of $NO_x$ from 0.08 to 1.4 ppm. The results were used to plot oxidant isopleths as shown in Figure 6.

This diagram is now used to calculate the desired levels of 6:00 to 9:00 a.m. NMHC and $NO_x$ by the following steps:

(1) For a given geographical region, the maximum 1-hr oxidant concentration and the average 6:00 to 9:00 a.m. $NMHC/NO_x$ ratio and its 90 percent confidence interval during the smog season are determined for a base year. The average ratio and maximum oxidant define a "chamber counterpart" as shown by point e in Figure 6 at the intersection of the 0.4 ppm $O_3$ isopleth and the 8 $NMHC/NO_x$ ratio line.

(2) The percent reduction of annual mean $NO_2$ to achieve the $NO_2$ air quality standard is calculated. Assuming that the reduction of the 6:00 to 9:00 a.m. $NO_x$ will be proportional to the reduction in the annual mean, point e' is determined by applying that percentage reduction to point e.

(3) To achieve the oxidant air quality standard a reduction of NMHC along line e'f is required. It is assumed that the required percentage reduction of NMHC in the atmosphere is equal to the percentage reduction from Figure 6 even though the resulting NMHC and $NO_x$ in the atmosphere is not necessarily equal to the concentrations at point f in the diagram.

(4) Similar calculations are performed using the 90 percent confidence interval values of $NMHC/NO_x$ ratio, and the greatest percentage

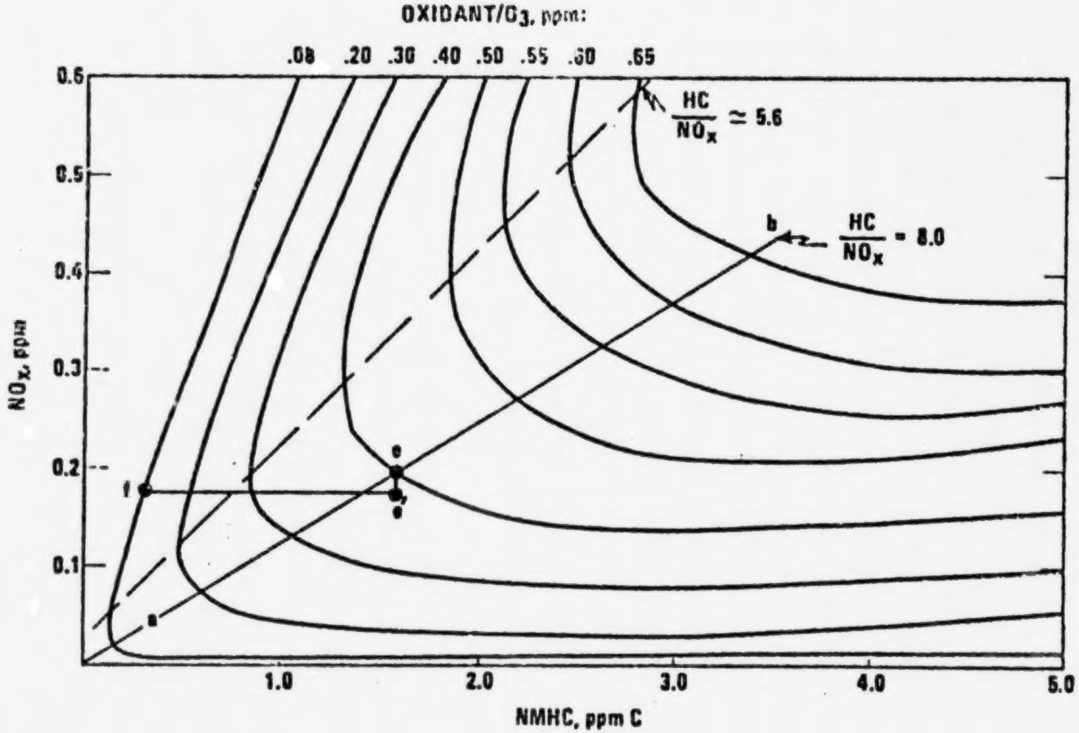

Figure 6. Oxidant/$O_3$ isopleths derived from combined use of smog chamber and photochemical modeling techniques (56).

reduction of NMHC from the three NMHC/$NO_x$ ratios considered is used as the control requirement.

In relating the worst case NMHC/$NO_x$ ratio with the maximum observed oxidant, assurance of adequate control is maintained even under conditions of the simultaneous occurrence of ratios favorable to oxidant production in the early morning and meteorological conditions favorable to oxidant formation later in the day. The advantages of this technique over the present EPA method are undeniable. Dimitriades (56) pointed out these advantages and several limitations in relation to the Appendix J approach. This approach rests primarily on a cause-and-effect relationship derived from smog chamber data. Also, the role of $NO_x$ in oxidant formation is considered. On the negative side, the chamber and chamber model do not exactly simulate the atmosphere. Also, the relationship obtained by Figure 6 does not contain information concerning frequency of occurrence of oxidant levels, while the air quality standard is specified in terms of frequency of occurrence.

One major assumption of this method should be pointed out. Although the actual oxidant level in Figure 6 at any NMHC-$NO_x$ point may not be the same as the atmospheric oxidant for the same NMHC and $NO_x$, it is assumed that a given oxidant reduction may be accomplished in Figure 6 and in the atmosphere by the same percentage reduction of NMHC. At this point in the computation the desired $NO_x$ level has been determined, thus this assumption is concerned with the relation of oxidant to NMHC at constant $NO_x$ both in the atmosphere and in the adjusted chamber data (Figure 6). For this assumption to be correct, a figure similar to Figure 6 plotted for atmospheric oxidant levels would be exactly the same shape as Figure 6. That is equivalent to saying that the oxidant in Figure 6 may be related to atmospheric oxidant by a multiplicative factor which is constant over the entire hydrocarbon-$NO_x$ plane. There is no atmospheric data available to support or refute such an assumption. Nevertheless, recent efforts to assess the validity of this technique have indicated that changes in the shape of Figure 6 which result from different light intensity, dilution rates, emission patterns, and hydrocarbon reactivity have little impact on the predicted control requirements (59). This also implies that small differences in shape between Figure 6 isopleths and atmospheric isopleths will have only small effects on the outcome of the implementation of controls based on this method. Comparison of predicted and observed maximum $O_3$ in Los Angeles from 1968 to 1975 showed excellent agreement, but some discrepancies were noted in the observed and predicted decrease in reactive hydrocarbon emissions (mobile sources) from the 1968-1971 period to the 1972-1975 period (59).

The criticisms of the rollback methods are also applicable to the manner in which $NO_x$ control requirements are calculated. Nevertheless, the method proposed by Dimitriades is a great improvement over the present EPA method of relating oxidant to precursor emissions.

## CONCLUSIONS

All the methods discussed above with the exception of the LAAPCD method and the Dimitriades method rely on ambient monitoring data to relate oxidants to precursors. Thus, the NMHC and $NO_x$ ranges explored by these relationships are mainly the result of meteorological variation, not emission variation. The LAAPCD approach, while it uses smog chamber data to relate oxidant to precursors, employs the highly suspect "Hamming transformation" equation to relate chamber results to the outdoor air.

Most of the methods discussed make use of stationary monitoring data. Such data cannot reflect transport of pollutants in the air basin, thus they cannot yield cause-and-effect relationships. A true cause-and-effect relationship can only be obtained by following ambient air, captive air experiments, or using some technique to determine precursors in the same air in which elevated oxidant is present. Data obtained by following ambient air are quite expensive, requiring instrumented aircraft and tracking equipment. Certainly an entire approach to relating oxidant to precursors cannot be based on such data because of the extreme cost. Smog chamber experiments, while much less expensive, have not been shown to simulate the behavior of ambient air. Methods for determining precursors in the same sample in which oxidants are measured have not been developed.

# SECTION 5

# THE LOS ANGELES REACTIVE POLLUTANT PROGRAM

## GENERAL DESCRIPTION

The Los Angeles Reactive Pollutant Program (LARPP) was a Lagrangian air monitoring study funded by the Coordinating Research Council and the Environmental Protection Agency. The purpose of the project was to assemble a data package for studying the processes of transport, diffusion, and chemical reaction associated with photochemically reactive air pollutants. The field work phase of LARPP was carried out from early September to mid-November, 1973.

On a day of an operation, three tetroons, ballasted to float below the inversion base, were released from a ground station in the early morning. Transponders were suspended beneath the tetroons so that they could be identified and their positions could be determined by the radar unit located on Flint Peak; a position determination could be made each minute taking each tetroon in turn. As soon as the tetroons reached a more or less stable altitude, the centroid of the triangle formed by projection of the tetroon positions onto the earth's surface was determined. A helicopter, flying a one-half mile square pattern around the centroid at an altitude approximately midway between the ground and the inversion base, released fluorescent tracer particles. After the tracer release, an instrumented Bell 212 helicopter provided by EPA-Las Vegas began flying square, constant altitude patterns around the centroid at constant air speed (60 knots). The helicopters used were also equipped with transponders as well as radar altimeters. A second radar unit was used to track the helicopters and to position them at the beginning of a pattern. Patterns were flown at four altitudes between the ground and the inversion base; the lowest level used was 200 feet above the ground.

Usually, a helicopter started at the upper level flying patterns at descending altitudes down to the lowest level, then completed another ascending and descending series of patterns before returning to base. Prior to completion of its last low pattern, it was often joined by the other helicopter flying an upper level pattern at the commencement of its own series of pattern levels. A typical pattern flown at constant air speed is shown in Figure 7. In addition to the helicopters, LARPP also utilized a mobile van which attempted to remain close to the tetroon centroid.

The helicopters and van were equipped to measure $O_3$, NO, $NO_x$, CO, $CH_4$, non-methane hydrocarbons, fluorescent tracer, air temperature, and dew point and to take samples in Mylar bags for later gas chromatographic analysis in the El Monte laboratory of the California Air Resources Board (ARB).

Other information collected during the operations included: total solar and UV radiation at five stations, lidar data, and monitoring data from the Battelle and GM vans. After the data were collected, they were brought together with stationary-site monitoring data, meteorological data and traffic data from state and nearby county agencies for the days on which LARPP operations were carried out. All the data, with the exception of the lidar measurements, were merged into a huge time series to produce archive tapes. Thus, data records of different types and lengths were intermingled in a fixed block format. Archive tapes are available in 7-track and 9-track versions from NTIS.

## ANALYSIS OF OPERATION 33

### General Description of Run

LARPP operation 33 was carried out on November 5, 1973. The tetroon triad was launched at 0715 PST. The data record from the helicopters begins at 0748 PST and runs through to 1427 PST. During this time the helicopters flew 49 complete patterns: more than any other LARPP operation. The tetroon trajectories are shown in Figure 8. During the early morning the tetroons were carried southward on very

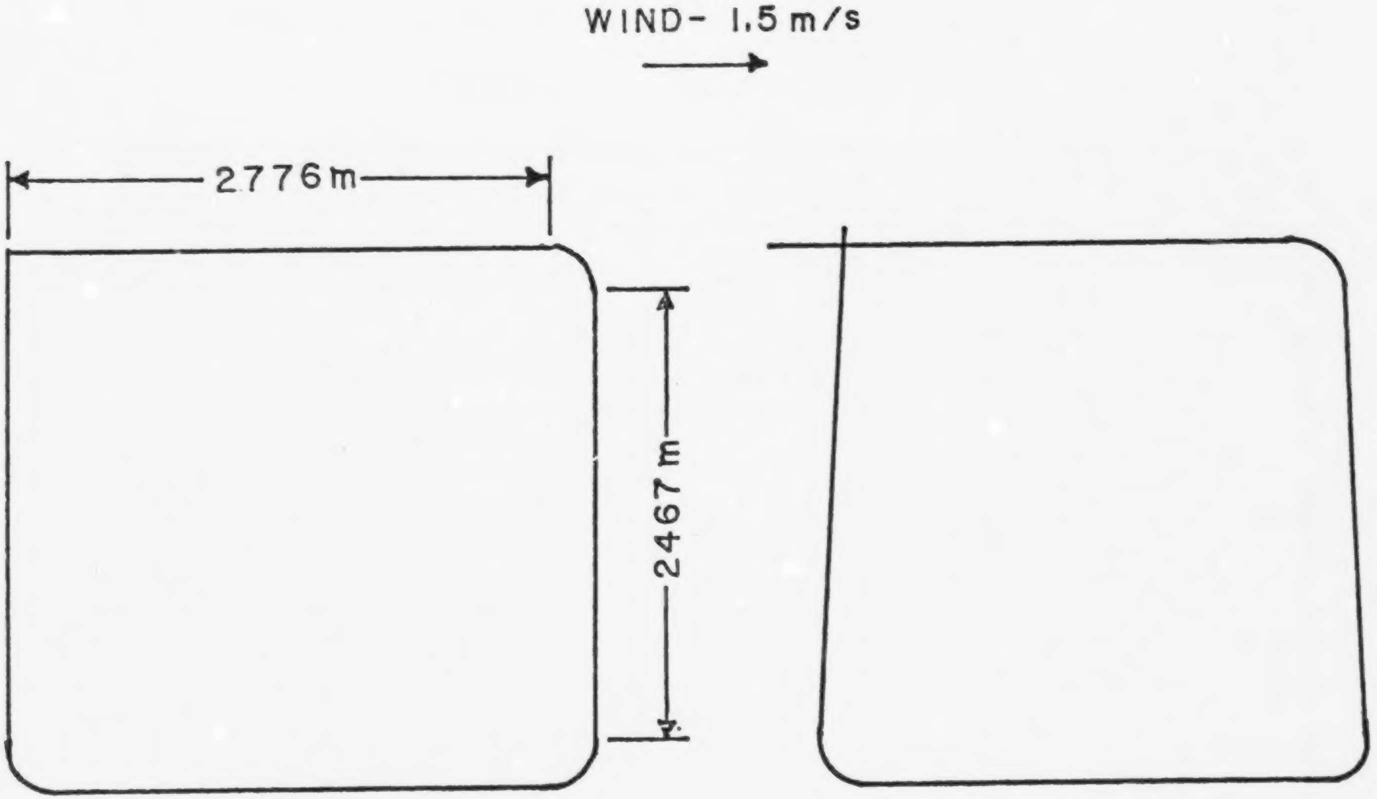

(a) Lagrangian

(b) Eulerian

Figure 7. Typical LARPP helicopter pattern from (a) Lagrangian (moving with mean wind) viewpoint, and from (b) Eulerian (fixed point and ground) viewpoint, in a 1.5 m. $sec^{-1}$ mean wind.

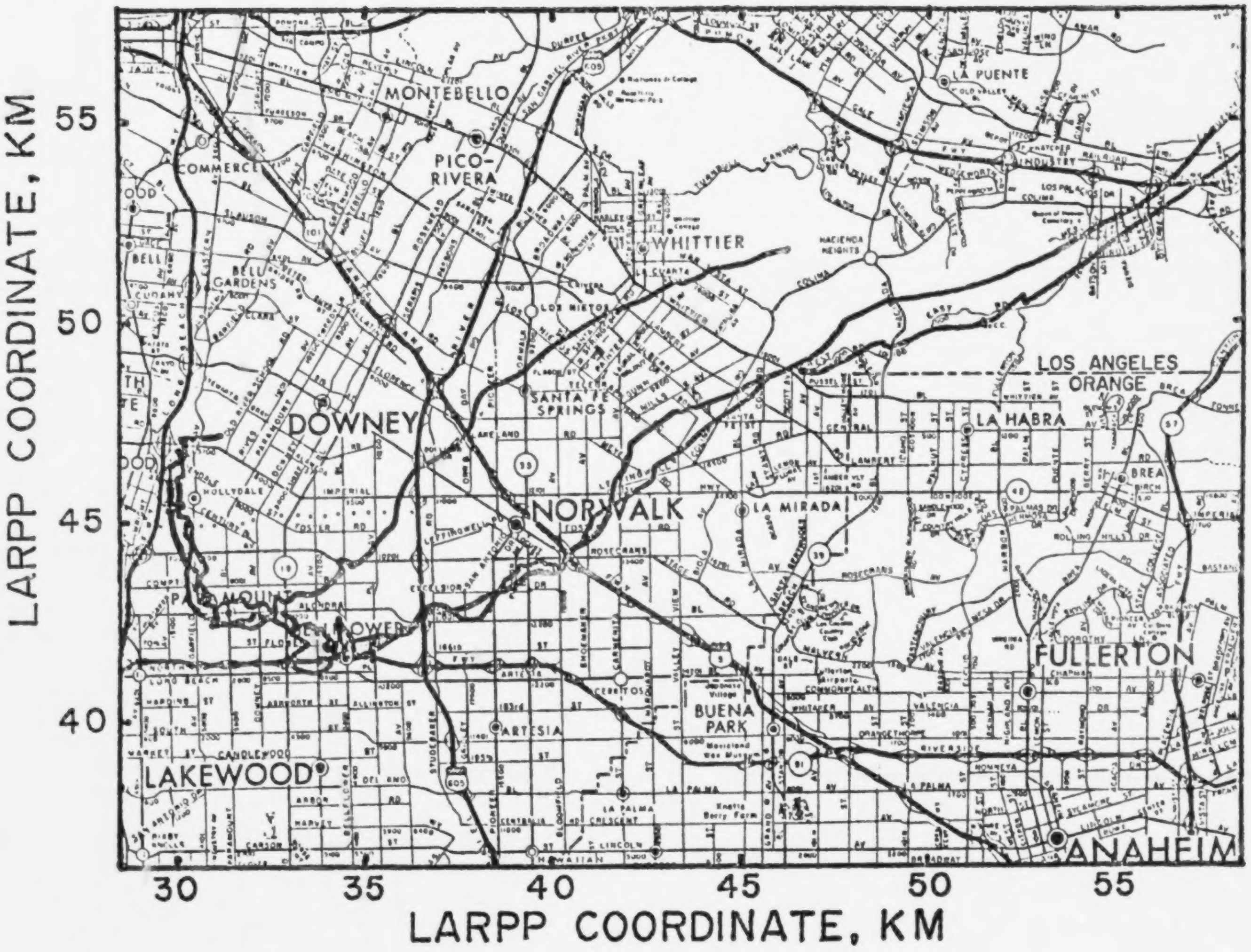

Figure 8. Tetroon trajectories for LARPP Operation 33.

light winds typical of the nocturnal mountain winds in Los Angeles. At 0920 PST, the sea breeze regime was established and the tetroons, now over Paramount, veered to an easterly heading at an increasing speed. At this time, tetroon number 3 was carried along a more northerly trajectory. While tetroons 1 and 2 remained relatively near each other for the entire run, the trajectory of number 3 continued to diverge, as would be expected after the initial separation. The location of the centroid was based on tetroons 1 and 2 only, after the separation of 3 became significant. At 1100 PST, tetroons 1 and 2 took a northeasterly route at an increasing speed. Just after 1300, they encountered the Puente Hills. Convection currents flowing up the warm hillsides carried the tetroons to much higher altitudes as may be seen in Figure 9. Only 4 of the 49 helicopter patterns did not enclose the centroid.

Because of the number of patterns flown and the length of the operation, 33 was chosen as the run to be studied by five consultants, whose task was to evaluate the data and to suggest ways in which the data might be used. Although much useful information and ideas for further analysis are contained in the consultant reports, only the material pertinent to simulation of the smog system of operation 33 will be referenced here.

### Initial Analysis

Prior to receiving the LARPP data, background material was collected. The coordinate locations of all stationary air monitoring and meteorological stations in the Los Angeles air basin were obtained from numerous sources. These stations are listed in the LARPP archive document (60) in Tables 32 through 35, 38, 41 through 43, 45 and 46 (of above document). The coordinates of these stations were estimated in universal transverse mercator (UTM) coordinates. Also, during this period, topographical, relief and road maps of the Los Angeles basin were procured. Stationary source information for Los Angeles and Orange Counties was obtained on tape from EPA's National Emission Data System on a magnetic tape.

The LARPP data archive was received in July 1975. The original data retrieval program developed by Parker and Martinez (60) could not

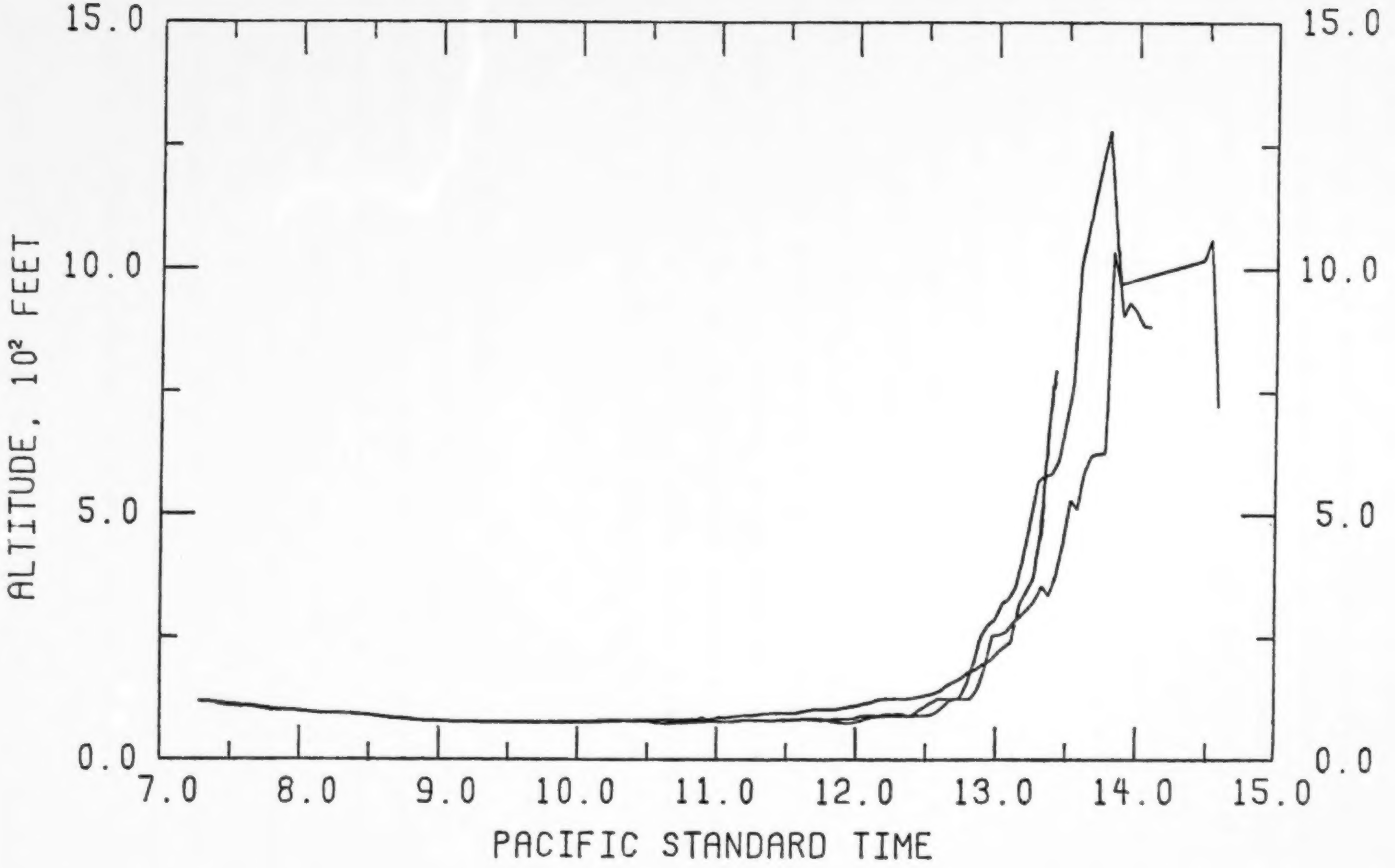

Figure 9. Tetroon altitude above ground level versus time.

be employed because it is machine-dependent and had some limitations for the work at hand; thus, the first stage of data anlaysis was to develop programs for the examination of the data. It was decided to sort the 25 different record types which were potentially present within the operation 33 data into separate data files on an off-line, 2314 disk. Program UNMERGE was written to perform this sorting operation. Table 4 shows the types of data files produced and indicates the number of records of each type which were present. After briefly examining the listings, more specific tasks were undertaken. The programs developed for the initial examination of LARPP data are listed and briefly described in Table 5.

## Helicopter Data

From a chemical point of view, the most important data in the archive is that from the two instrumented helicopters. The quantity of information in the helicopter data file exceeds that of all the other files combined. Each helicopter record contains values of the variables listed in Table 6; the sources of these values are also presented. In the archive obtained, corrections for the effects of temperature and altitude on the instrument readings had been made, but obviously incorrect data, such as negative concentrations and electronically produced glitches, still remained in the data. At the LARPP Symposium (35), it was mentioned that helicopter radio transmissions often caused erroneous spikes in the data, especially the ozone data.

The first look at the helicopter data was obtained from program HELIST which produced a formatted listing of the helicopter file. This listing is about 200 pages long. Since all the information would not fit across a computer page, the listing was divided into two portions: one concerning instrumental measurements and the other one concerning the auxiliary information such as position of the helicopter, bag sample number during the pattern, and others. The flag field in each helicopter record is a string of 640 bits. Many of these bits refer to a list of conditions, each of which relate to some aspect of how the data were collected. In preparing the tape obtained for this work, the archivists had ignored this bit field in translating the 7-track BCD

### TABLE 4. FILES PRODUCED BY PROGRAM UNMERGE AND THE NUMBER OF RECORDS TRANSFERRED FROM THE OPERATION 33 ARCHIVE TO EACH FILE TYPE

| Record Type No. | No. of Records | Description |
|---|---|---|
| 01 | 5610 | Helicopter data (automatic) |
| 02 | -- | ARB van data (automatic) |
| 03 | 300 | Helicopter radar data |
| 04 | 405 | Tetroon radar data |
| 05 | 432 | Aerometric data from Los Angeles Air Pollution Control District |
| 06 | 30 | Gas chromatographic data |
| 07 | -- | Aerometric data collected by Battelle Memorial Institute |
| 08 | 48 | Aerometric data collected at El Monte |
| 09 | -- | (Unused) |
| 10 | 24 | Meteorological data collected by California Dept. of Transportation |
| 11 | -- | Manual helicopter data |
| 12 | 330 | Manual ARB van data |
| 13 | 24 | Traffic counts |
| 14 | 161 | Airport weather data |
| 15 | 24 | Aerometric data from Community Health Air Monitoring Program |
| 16 | 14 | Temperature and relative humidity from Los Angeles APCD |
| 17 | 68 | Radiometer data |
| 18 | 2 | Soundings from EMSU |
| 19 | -- | $HNO_3$ and PAN data |

(Continued)

Table 4 (Continued) -- Files Produced by Program Unmerge and the Number of Records Transferred from the Operation 33 Archive to Each File Type

| Record Type No. | No. of Records | Description |
|---|---|---|
| 20 | 24 | Meteorological data from Los Angeles Air Pollution Control Dist. |
| 21 | 24 | Aerometric data collected by ARB for surrounding counties |
| 22 | 36 | CO bag samples collected by California Dept. of Transportation |
| 23 | -- | Aerometric data from California Department of Transportation van |
| 24 | 9 | Radiosonde data |
| 25 | -- | Winds aloft at specified height levels |
| 26 | 4 | Winds aloft at constant pressure levels |

## TABLE 5. SOME PROGRAMS DEVELOPED FOR EXAMINATION OF LARPP DATA

| Program | Description |
|---|---|
| CDCTRAN | Translates data from CDC internal display code to (IBM-compatible EBCDIC code (not needed) |
| EXAMINE | Prints data from a single LARPP operation in raw form |
| UNMERG | Sorts data from a single operation into 26 separate disk files |
| HELIST | Prints a formatted listing of helicopter data |
| DUMPxx | Prints raw listing of specific disk files |
| RADBOND | Prints radiosonde data and converts dew point to water concentration in ppm |
| BSDATA | Scans helicopter data file and computes the average altitudes at which hydrocarbon bag samples were collected |
| TETLOOK | Computes running averages and standard deviations of altitudes for each tetroon on a variable number of sequential data values |

### TABLE 6. CONTENTS OF HELICOPTER DATA RECORDS AND SOURCES OF DATA

| Items | Source |
|---|---|
| Record Type (01 or 11) | |
| Local Time (HHMMSS) | |
| Turn Number | Manual |
| Data Quality (1-bit per flag)* | Manual |
| Julian Date | |
| Bag Sample Time | Manual |
| Helicopter ID (20, 30) | Manual |
| Selected Channel Value | |
| Time (HHMMSS) | |
| Position N-S (XXX.X) | Manual |
| Position E-W (XXX.X) | Manual |
| Bag Sample No. | Manual |
| Fluor. Part Count | Mie 110 Flourescence Device |
| NO Concentration (ppm) | TECO 14B Chemiluminescent Instrument |
| $NO_x$ Concentration (ppm) | TECO 14B Chemiluminescent Instrument |
| BSCT (visibility) | MRI 1550 Nephelometer |
| CO Concentration (ppm) | Andros 7000 non-dispersive IR |
| Temp ($^oF$) | Cambridge CS137 |
| Dewpt ($^oF$) | Cambridge CS137 |
| NMHC Concentration (ppm) | MSA 11-2 Env. Chromatograph |
| CH4 Concentration (ppm) | MSA 11-2 Env. Chromatograph |
| O3 Concentration (ppm) | REM 612 Chemiluminescent Instrument |
| X-POS (radar) (XXXX.X) | Radar |
| Y-POS (radar) (XXXX.X) | Radar |
| Altitude MSL (XXXX.X feet) | Barometric Altimeter |
| Altitude AGL (XXXX.X feet) | Radar Altimeter |

tape to a 9-track EBCDIC tape. Since the translation took the field to be coded characters, not bits, the field became rearranged. Thus, a program was written to translate the field to the original BCD representation and to list the messages corresponding to the flags present in field. These messages are given in Appendix A.

A quick scan of the listings revealed that variation of concentrations from one data point to the next made direct interpretation of the listing very difficult. The records from the two helicopters were often interspersed since the helicopter file was still a strict time series. This added to the problem of visually scanning the data. Some general trends were noted however. It appeared that concentration variation was greater in the horizontal legs of the patterns than on the vertical portions of the flight. Also, it was seen that general trends were present in the concentrations, with both altitude and time, although the significance of these trends was difficult to assess. Thus, it was determined that other methods of displaying the data must be explored. Because the quantity of data was so great, computerized techniques were preferable.

SYMAP --

One method which seemed to promise a quick means of viewing all the data for a particular pollutant was the SYMAP program, a line printer mapping program distributed by the Harvard Laboratory for Computer Graphics and Spatial Analysis. The program has the ability to reduce three-dimensional data to a two-dimensional form. It is used most often for displaying data of a dependent variable (such as population density, mean income, number of buildings per square kilometer) as a function of position in geographical coordinates. After the program has read the input data, it proceeds to interpolate the values of the dependent variable at all points in a regularly-spaced, two-dimensional grid via a complex algorithm (61). These points correspond to print positions in the output map. Next, the numerical values at the grid points are reduced to a categorical representation according to the level groups supplied by the user. Thus, a particular print symbol is assigned to each print position in the output grid. In general, the higher the level of the dependent variable, the more dense (or darker) the symbol used. This is accomplished by the use of standard print train characters and overprinting for the denser symbols. SYMAP was to be used to display concentrations as a function of altitude and time.

There were many problems to be overcome before SYMAP could be applied to the LARPP data. Because SYMAP was designed to work with geographical coordinates, the scaling from independent variable units to map units (inches on the page) is fixed by the vertical axis. That is, scaling of the map ordinate and abscissa are not independent. Thus, it was necessary to prescale the time values for each reading so that the scaled values came out similar in the range and magnitude to the altitude values. The next problem encountered was that SYMAP, being written in FORTRAN, has fixed data storage limitations. It is limited to approximately 1000 points; however, the helicopter record contains over 5000 points. After contacting the programmer at Harvard responsible for SYMAP, it was decided that the needed alterations to SYMAP were possible. Lacking access to and familiarity with SYMAP source code, the UNC Computation Center's Contract Services group was employed to obtain a load module of the expanded version of SYMAP and the JCL (Job Control Language) procedures for executing the load module, and linking a user-supplied subroutine with the load module. Another major problem was that the interpolation algorithm produced "zero divide" errors because of the close spacing in the altitude-time plane of the data points. While the system action on zero divide was the proper action, the error messages were printed out in the middle of the map and eventually caused the job to terminate abnormally. Thus, the error messages and termination on zero divide error were suppressed.

Although great effort was expended in using SYMAP, the results were not entirely satisfactory. The interpolation algorithm produced some strange effects that seemed unwarranted based on the data. Also, no attempt had been made to screen out erroneous values except that negative concentrations were not used in interpolation. Dissatisfaction with SYMAP results led to an effort to develop other graphic techniques for examining the data.

It was decided to look at each horizontal helicopter pattern as a unit. Since there had been an effort to fly patterns at more or less fixed altitude levels, the data were stratified according to level. Program HELBRAK was written to segregate records from the large helicopter data file into five files for the following altitude ranges: 100-300 feet, 300-500 feet, 500-700 feet, 700-900 feet, and > 900 feet. All altitudes referred to are elevation with respect to ground level (altitude AGL). Very few patterns crossed these altitude range boundaries except quite late in the run. Formatted lists of each level file were produced with program LEVLIST. From these listings it was easier to see erroneous data since the data had been broken up into distinct patterns and the concurrent records from the two helicopters were no longer interspersed since the helicopters were generally at different levels. Then, the files were edited to remove all large strings of records with obviously erroneous data, or data for which the helicopter's location was in question. Program CORCT was written to remove specific records by selective copying of the files.

Concentration-Position Figures --

The next data display technique employed consisted of producing three-dimensional figures from the individual pattern data. Two dimensions of the figures were the helicopter position vectors in the LARPP coordinate system; and the height of the figures was the concentration value at that position. The three-dimensional figures were then projected onto a two-dimensional plane. The two dimensional matrix of points defining the projection was then processed by the Broomall X-Y plotter at the UNC Computation Center to produce figures like that shown in Figure 10. The line to the right of the figure is a scale line. The tic marks are at 1 pphm intervals, except for the ozone figures which have 5 pphm. Two versions of the plotting program PLOT 3D were written. The first version used a vector 3-D to 2-D projection algorithm; the second version used a more general transformation matrix approach in which the transformation matrix is constructed analytically prior to

OPERATION 33
ALTITUDE 400 FT.
TIME 091500 TO 092220

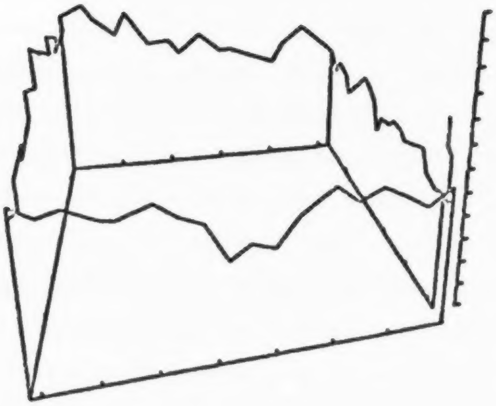

Figure 10. Example of concentration-position figure for carbon monoxide.

programming, and evaluated only once at the beginning of each execution. Both versions give identical pictures, but the matrix approach is slightly faster.

After the projections were completed for all patterns for CO, $NO_x$, NO, and $O_3$, the figures were trimmed and composited on pieces of poster board. The photographic reductions of the projections are presented in Figures 11 through 18. Each pattern is shown as if the viewer were at a point 10 km south of, 2 km west of and 7 km above the center of the figure's base. Touch-up was needed on some of the patterns since some noise spikes still remained in the data.

Examination of the CO concentration in the earlier patterns, shown in Figure 11, leads to an understanding of some of the meteorological processes occurring along the trajectory. As the helicopter flew the descending series of patterns beginning just before 0800 PST and ending at the 200-foot level at 0822 PST, the high CO concentration from morning traffic had not reached the 400-foot level. The next pattern, flown at the 400-foot level from 0822 to 0829, shows that the mixing depth had just reached this level at the northwest corner of the pattern and to a lesser extent at the southeast corner. It is tempting to assume that this pattern intersected warm, rising air parcels with high concentrations of mobile source pollutants. The NO and $NO_x$ bear out this interpretation; also, the $O_3$ was almost totally absent in the northwest pattern corner. Although they have not been plotted, the NMHC, $CH_4$, and b-scat also show a trend similar to CO for this pattern. There is no significant difference between the temperatures at the northwest corner and the temperature values in other parts of the pattern. This would indicate that the high concentration air parcels were not rapidly rising when intercepted by the helicopter, but they had, at this altitude, cooled to the temperature of the surrounding air.

Referring to the CO patterns, it may be seen that the turbulent entrainment has raised the mixing depth to the 600-foot level between 0836 and 0852 PST. And, similarly, the mixing depth reached the 800-foot level between 0923 and 1001 PST. The pattern between 0912 and 0915 PST, at the 600-foot level is incomplete. If it is compared with the

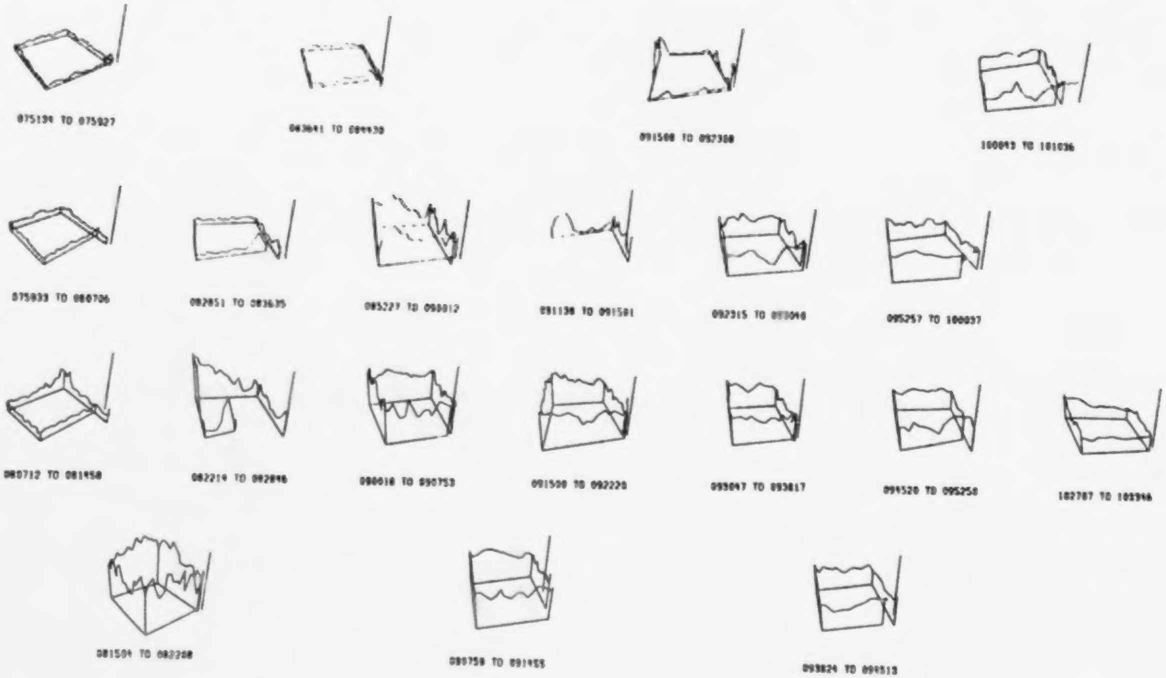

Figure 11. Concentration-position figures for Operation 33 carbon monoxide before 1030 PST.

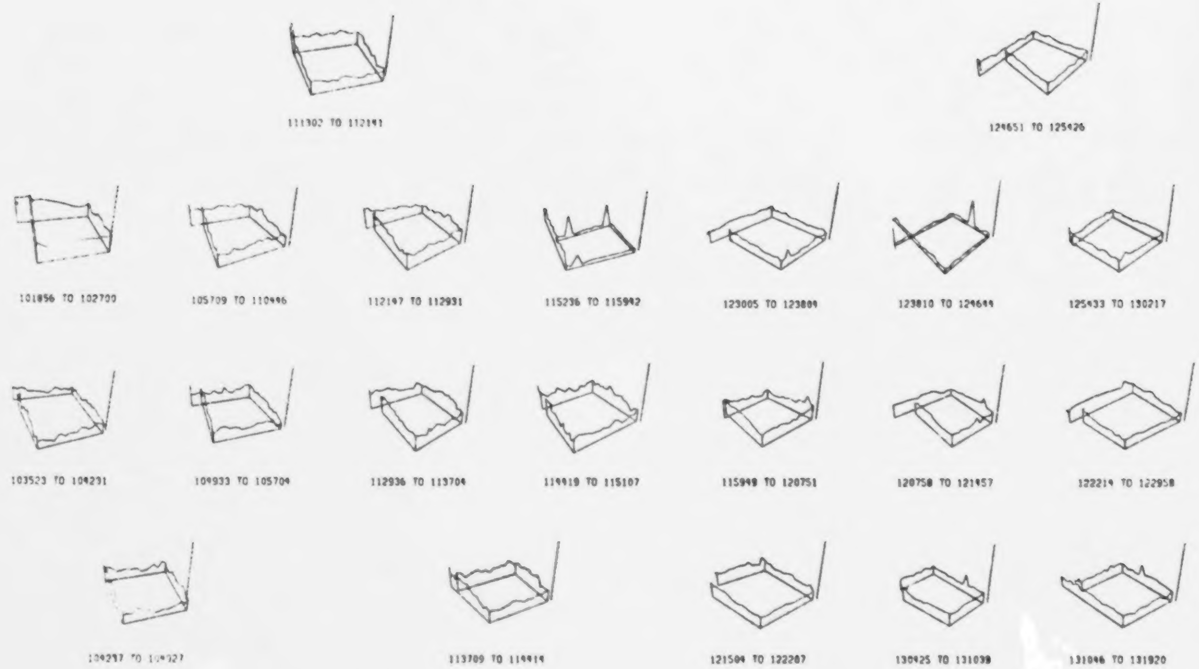

Figure 12. Concentration-position figures for Operation 33 carbon monoxide after 1030 PST.

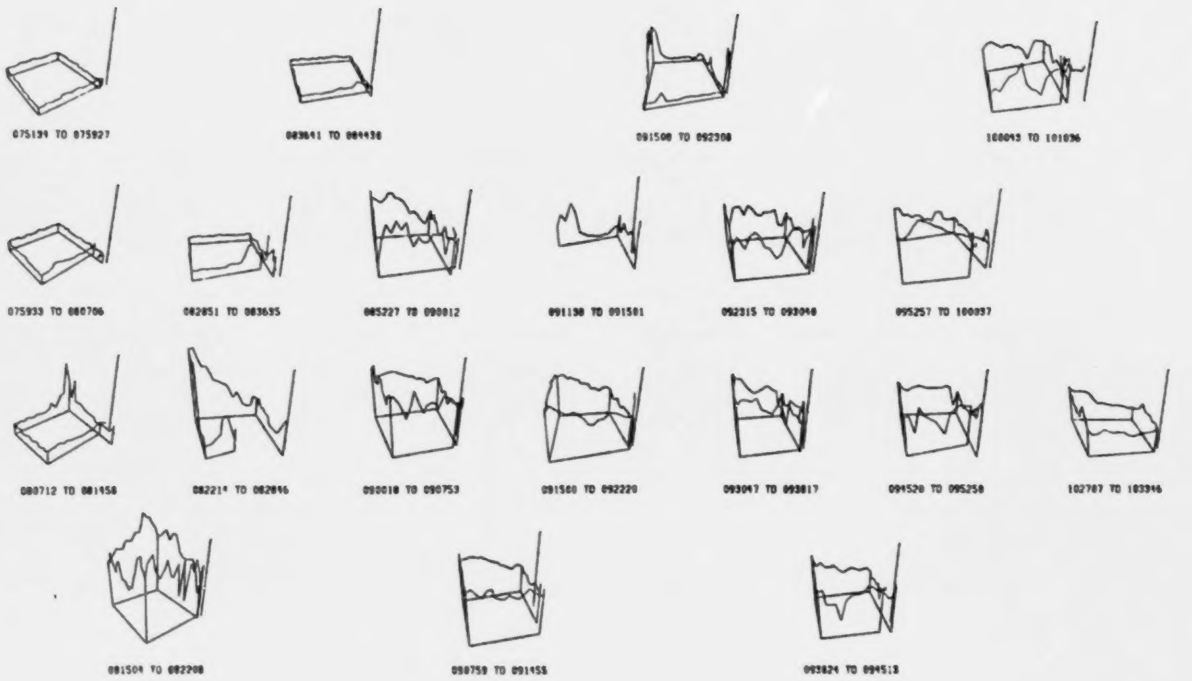

Figure 13. Concentration-position figures for Operation 33 nitrogen oxides before 1030 PST.

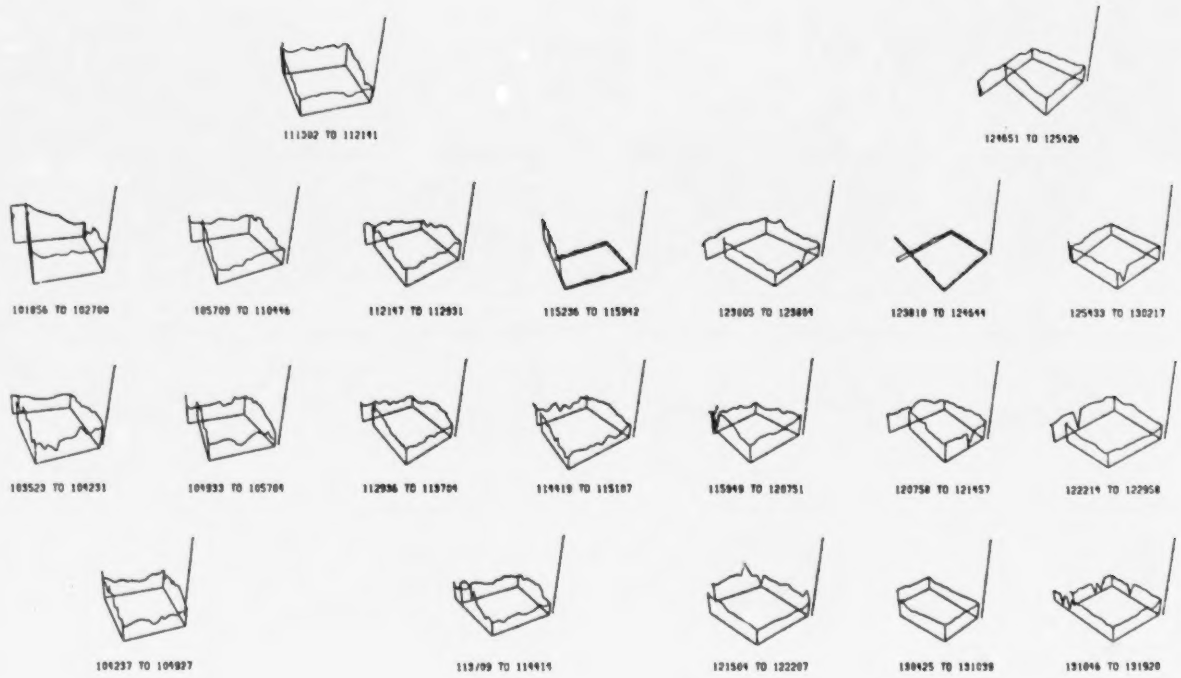

Figure 14. Concentration-position figures for Operation 33 nitrogen oxides after 1030 PST.

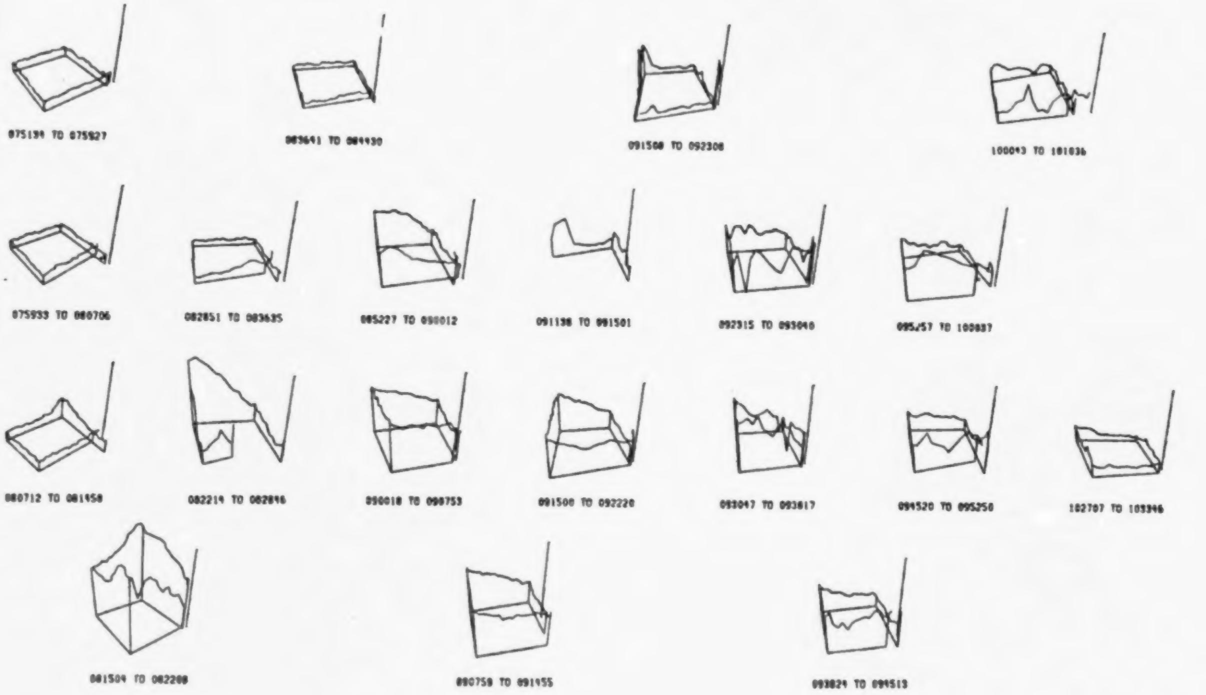

Figure 15. Concentration-position figures for Operation 33 nitric oxide before 1030 PST.

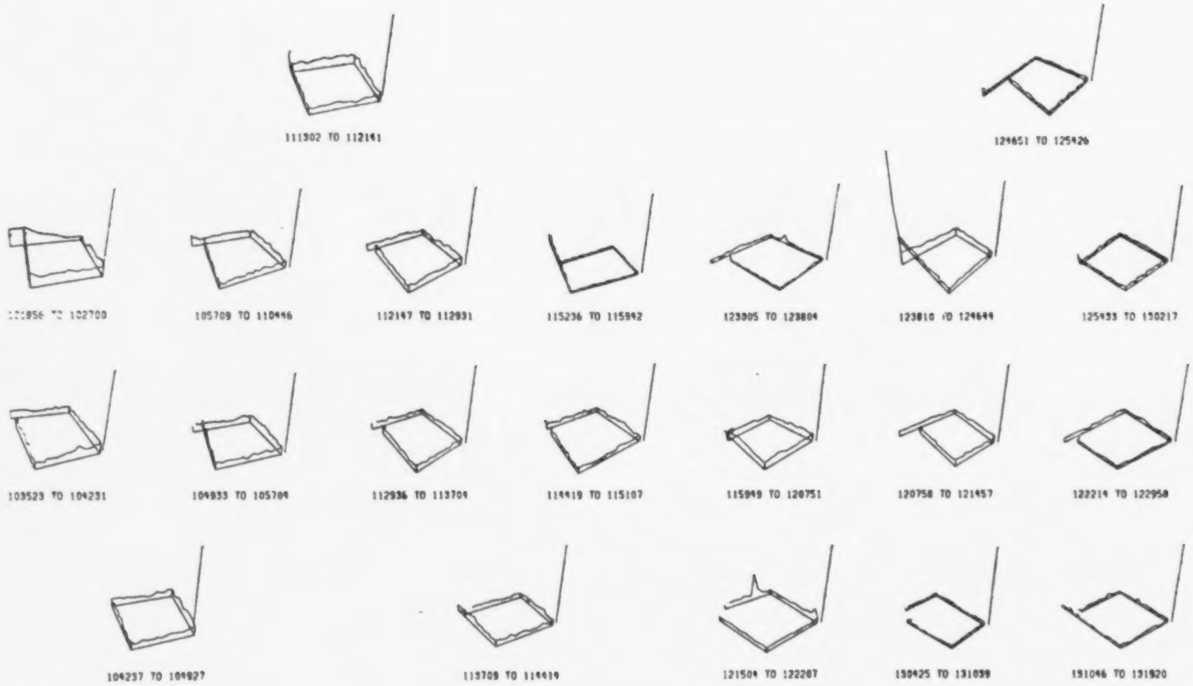

Figure 16. Concentration-position figures for Operation 33 nitric oxide after 1030 PST.

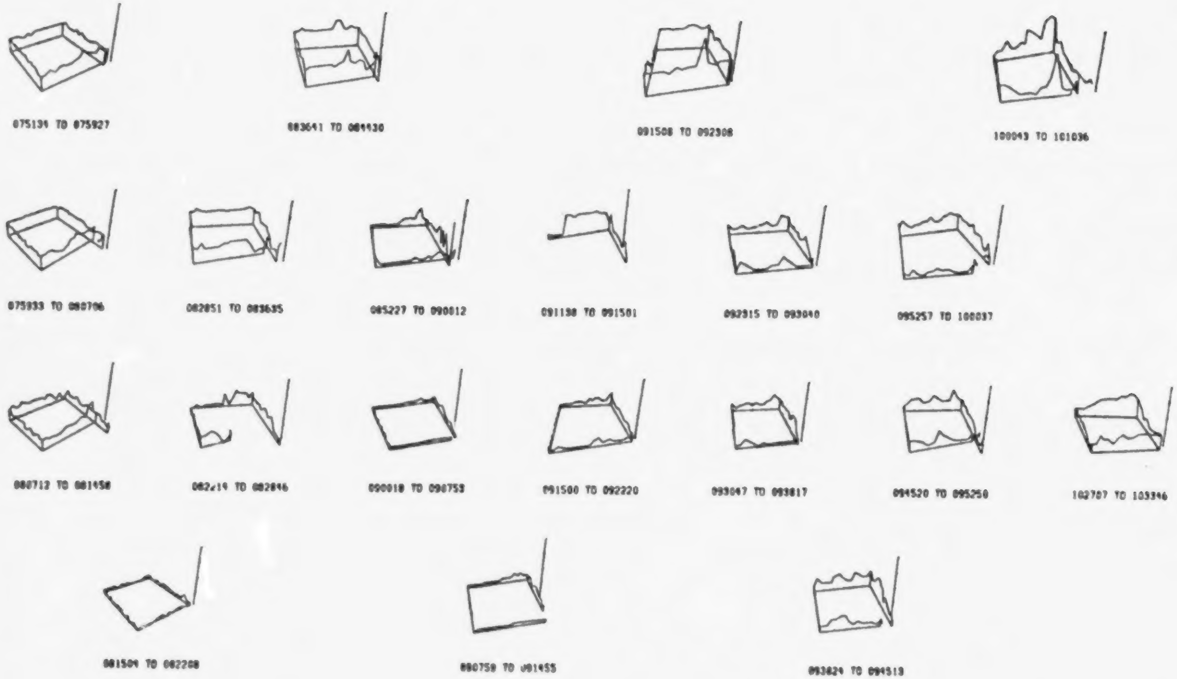

Figure 17. Concentration-position figures for Operation 33 ozone before 1030 PST.

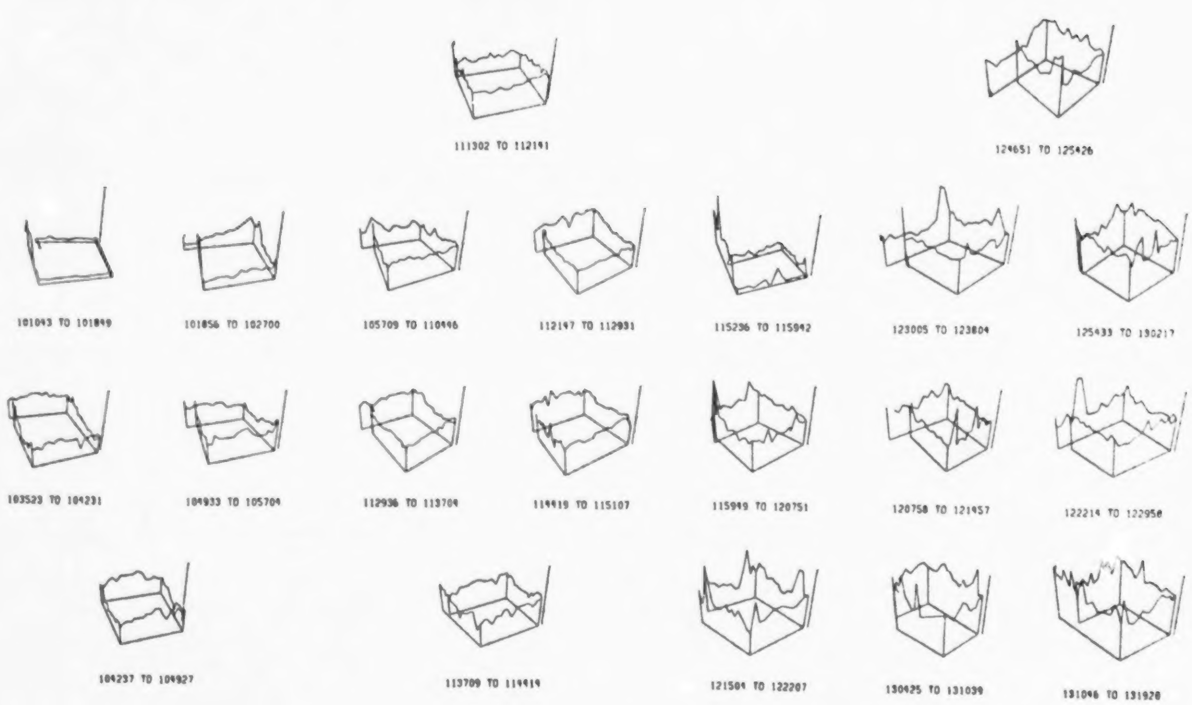

Figure 18. Concentration-position figures for Operation 33 ozone after 1030 PST.

previous pattern at this altitude, it appears that only the air on the low concentration side of the pattern was sampled. Thus, it probably does not reflect the average pollutant concentrations at this level and time.

The variability of concentrations with horizontal position is striking. The inhomogeneity regarding CO, $NO_x$, and NO is most noticeable in the morning. Later in the day, as the concentrations at all levels get lower, it becomes more difficult to see this inhomogeneity. Certainly the absolute variability around the patterns has decreased, but it is difficult to determine if there is any trend in the variability relative to the mean concentrations. Ozone shows the opposite trend. Its concentration is increasing during the day, and its inhomogeneity becomes more prominent during the later portion of the operation.

Ozone exhibits some other interesting trends. The first three patterns at the 800-foot level show a distinct increase in $O_3$ concentrations prior to the arrival at this altitude of fresh pollutants from surface sources. This indicates the presence of an active photochemical system above the inversion base. This is not an unusual situation in the Los Angeles air basin and has been described by Lea (62), Edinger et al. (41), Edinger (63) and more recently by Johnson and Singh (64). Edinger (65) in his analysis of operation 33 pointed out that the levels of ozone found above the inversion in the morning hours could be left from the previous day's reactions. Ozone could be trapped aloft as the nocturnal inversion propagates into the mixed layer, or it may have been injected into the inversion of the previous day along the heated slopes of the mountains which surround the Los Angeles basin. This second mechanism comes into effect when heating of air passing up the mountain slopes produces air parcels whose density is identical with that of the air within the inversion. Tracer experiments with liquids easily show that when a vertical density gradient exists in a fluid medium, a fluid of intermediate density injected into the medium tends to seek its level and then to spread rapidly in the horizontal. Thus, polluted air may be injected into the inversion as laminae of high concentration. Edinger, nevertheless, points out that these same processes affect CO as well as

$O_3$ and that the CO concentration above the inversion in operation 33 is much lower than that within the mixed layer. This indicated that air entering the inversion is greatly diluted in the process. Edinger felt the fact that ozone reached elevated levels in the inversion under these circumstances was evidence for photochemical formation above the inversion and ozone destructive processes in the mixed region.

It seems probable that the mountain injection mechanism is not responsible for the presence of $O_3$ or $O_3$ precursors at these low altitudes. It is more likely that this material was the result of the deepening nocturnal inversion capturing $O_3$ and precursors from the previous day. The increase of ozone at the 600-foot and 800-foot levels prior to the arrival of the fresh pollutant at these altitudes strongly suggests photochemical synthesis from second day materials. Smog chamber experiments at Research Triangle Institute and at the University of North Carolina indicate the ability of such dilute, second-day systems to produce ozone early in the day (88). Ozone destruction in the mixed layer is demonstrated by the strong negative correlation of $O_3$ and NO, as one would expect.

### Pattern Averages and Relative Standard Deviations --

After having examined Figures 11 through 18, which emphasize the inhomogeneity of the air, the question naturally arises: Is there anything here that can be modeled, either experimentally or mathematically, or are the processes which affect concentration simply too variable spatially for any sense to be made of the data? Also, are there any underlying trends which would suggest a model? To answer these questions it was decided to look at the averages and the standard deviations of data around each helicopter pattern. Program PATAVE was written to compute these statistics.

The pattern averages for all the concentrations, temperature and dew point are shown in Figures 19 through 27. Patterns were eliminated from consideration if they were not complete or if there were not a sufficient number of points within the altitude range for each level. These data are striking in that, for most of the variables plotted, the averages at all four levels are all nearly equal after about 0930 PST.

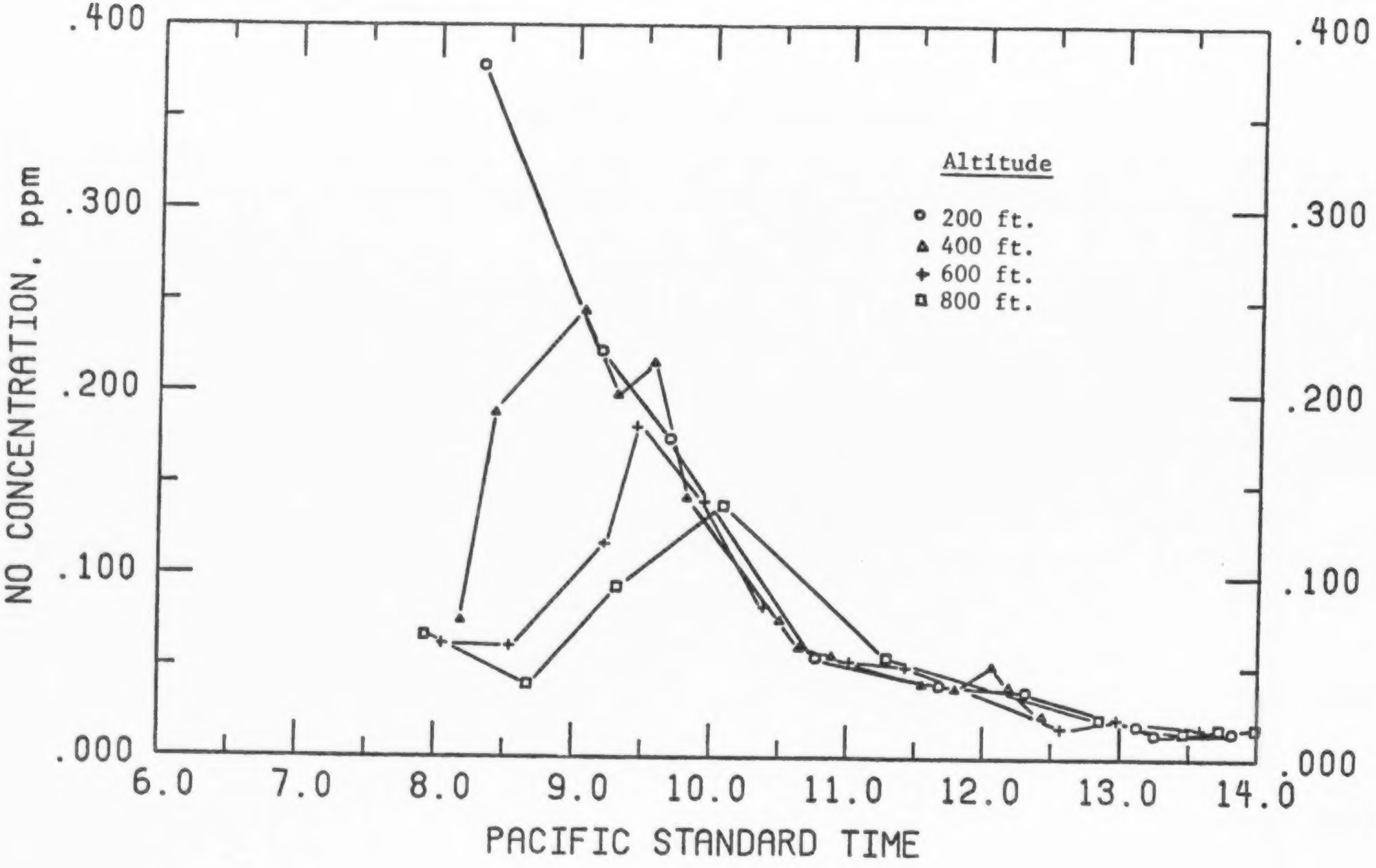

Figure 19. Helicopter pattern average nitric oxide concentrations for Operation 33.

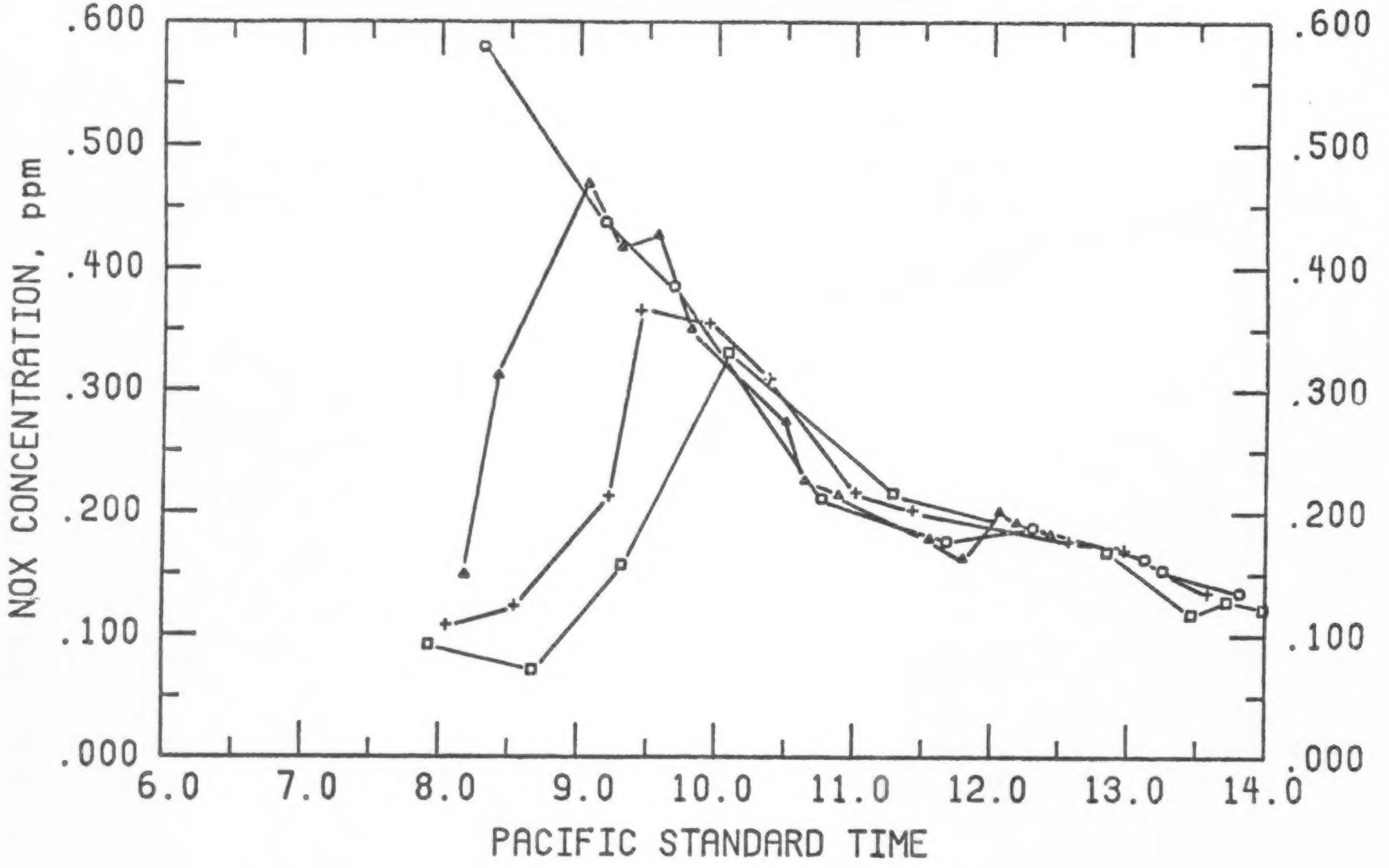

Figure 20. Helicopter pattern average nitrogen oxides concentrations for Operation 33.

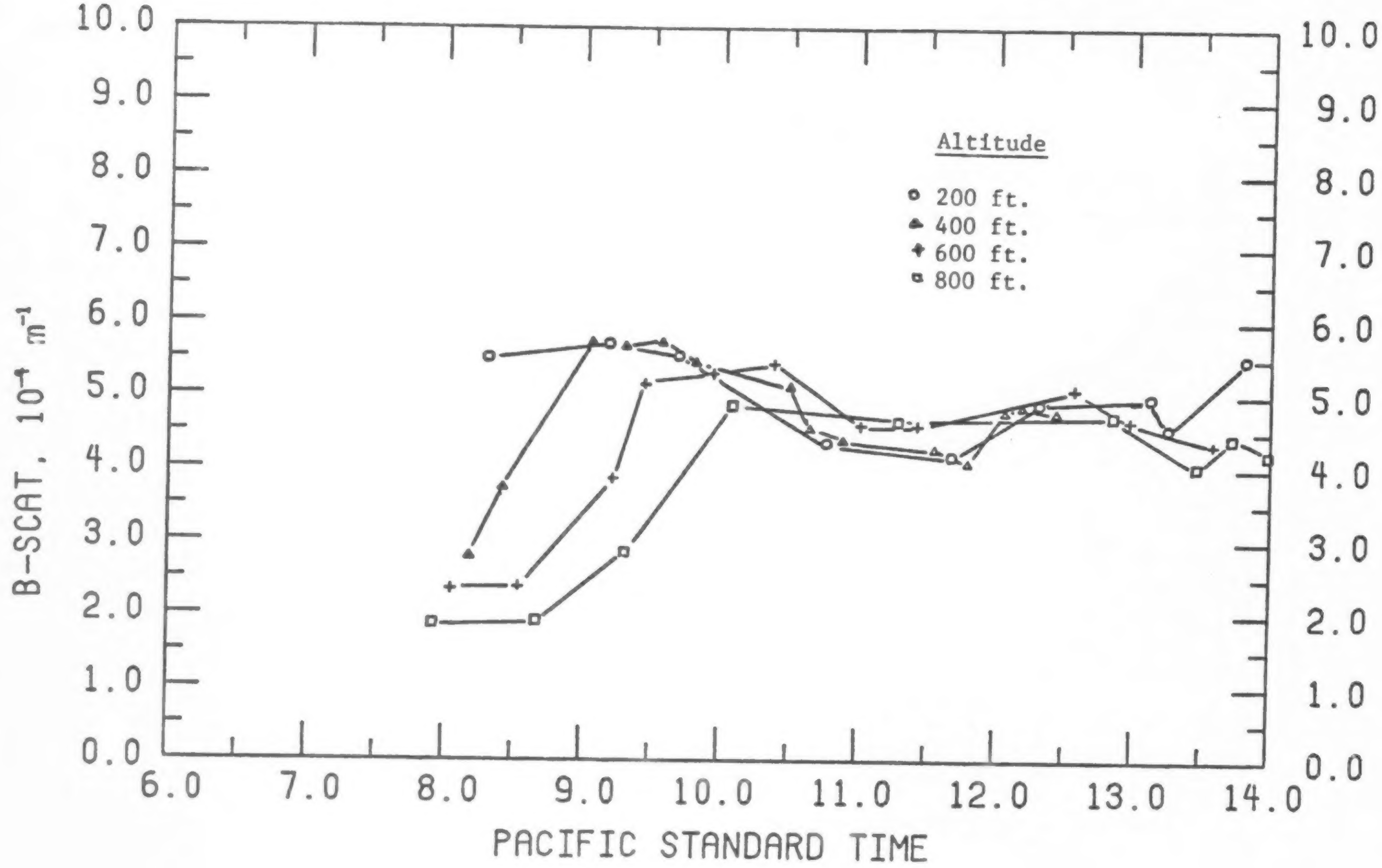

Figure 21. Helicopter pattern average scattering coefficients for Operation 33.

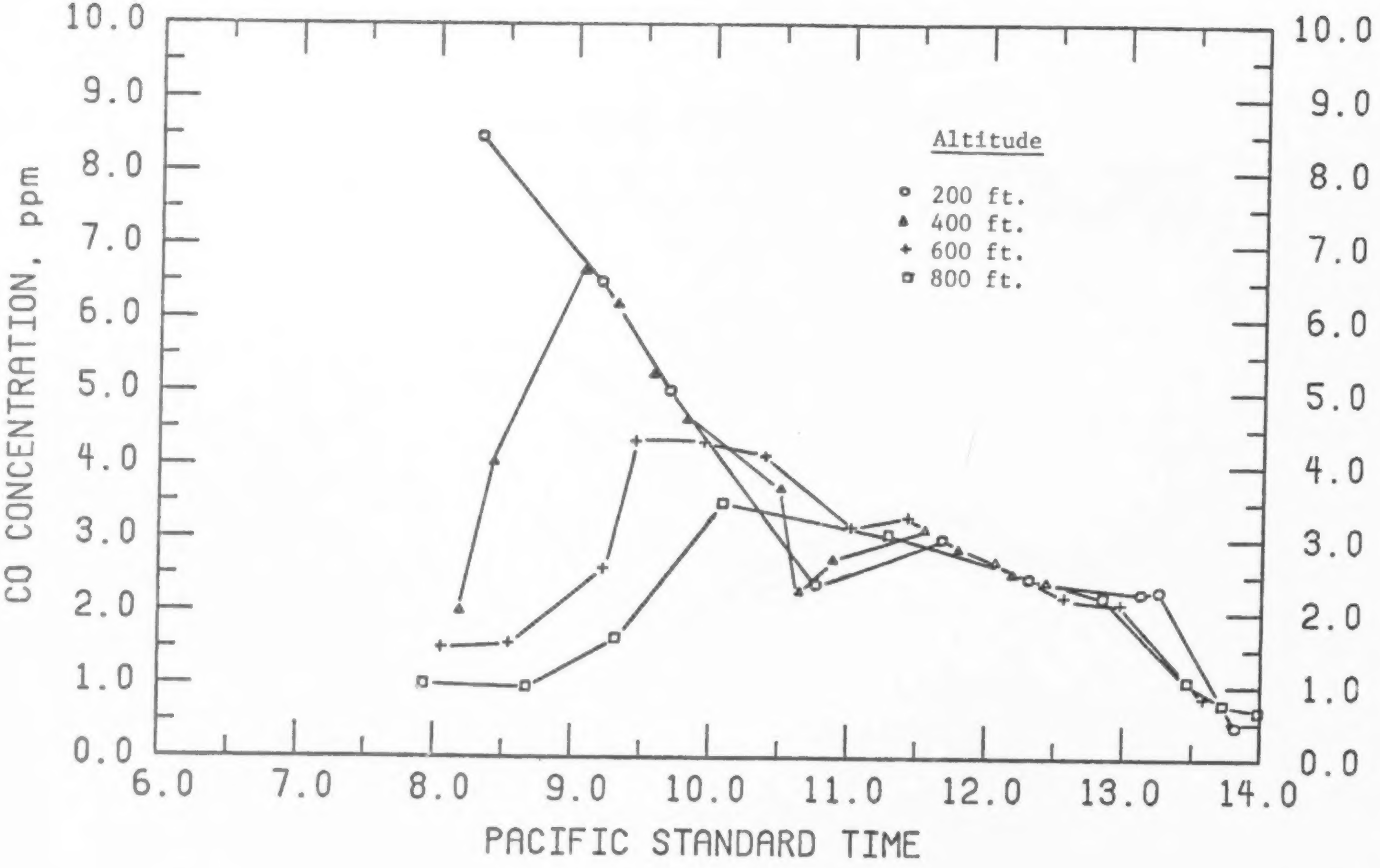

Figure 22. Helicopter pattern average carbon monoxide concentration for Operation 33.

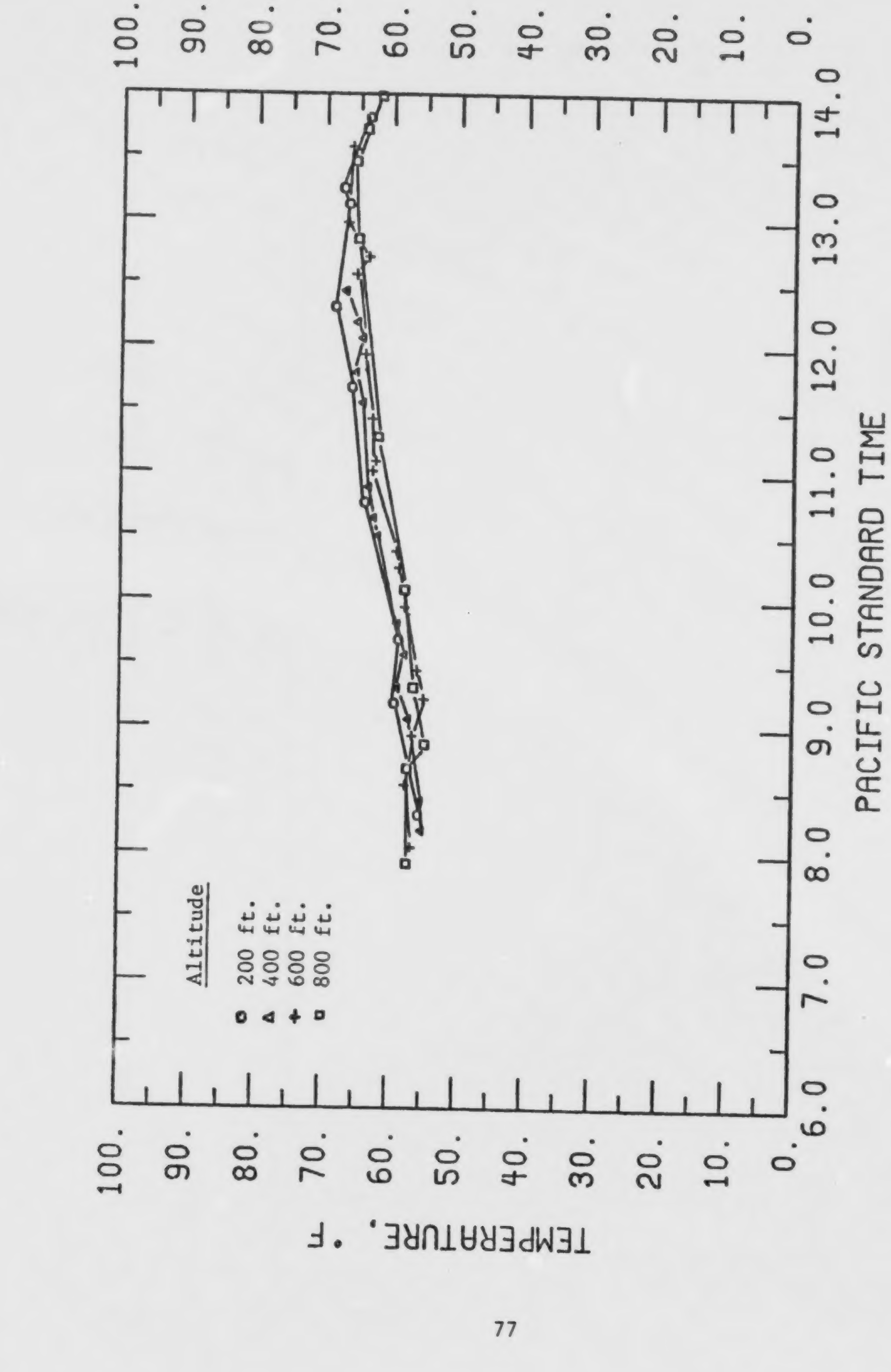

Figure 23. Helicopter pattern average temperatures for Operation 33.

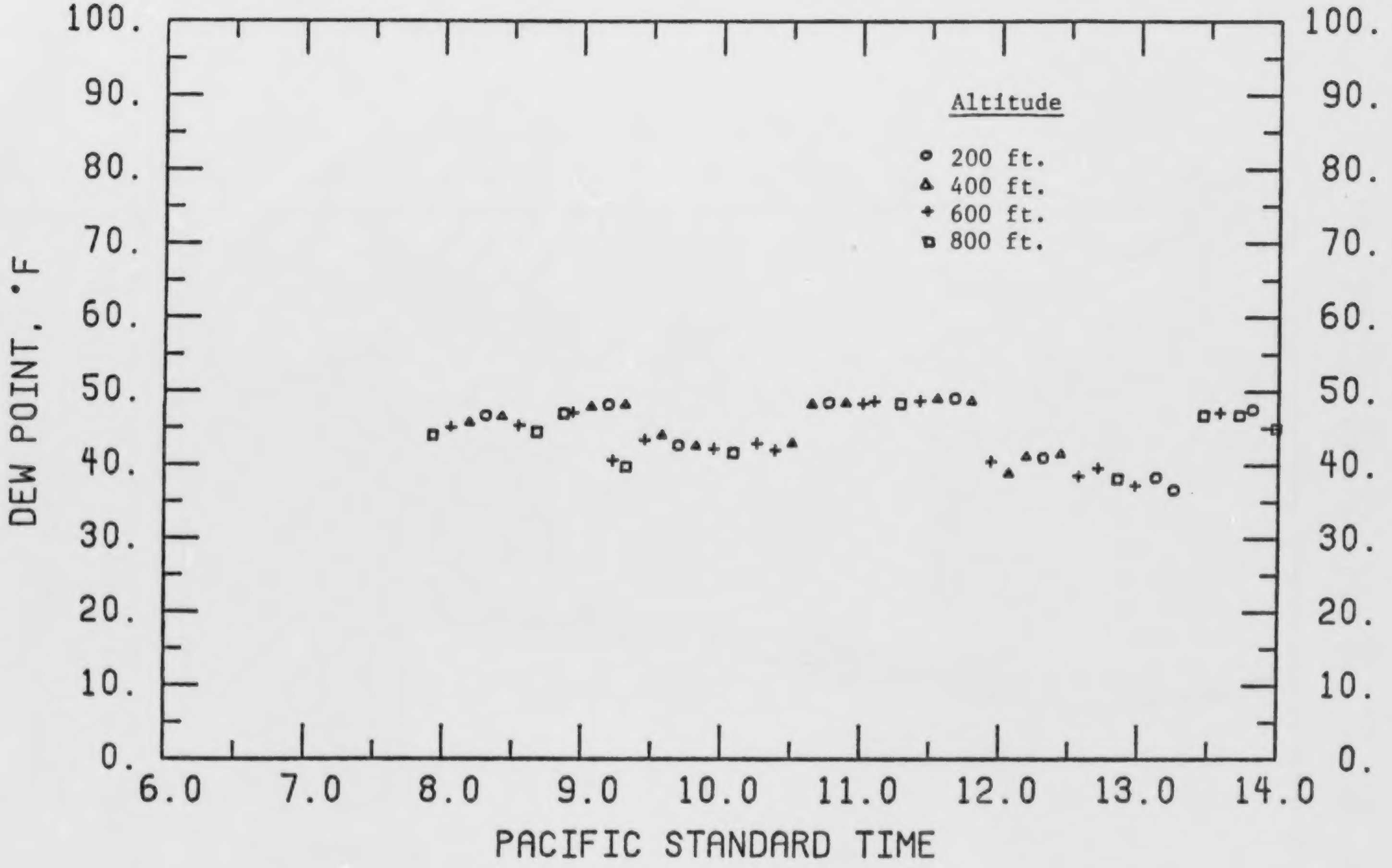

Figure 24. Helicopter pattern average dew points for Operation 33.

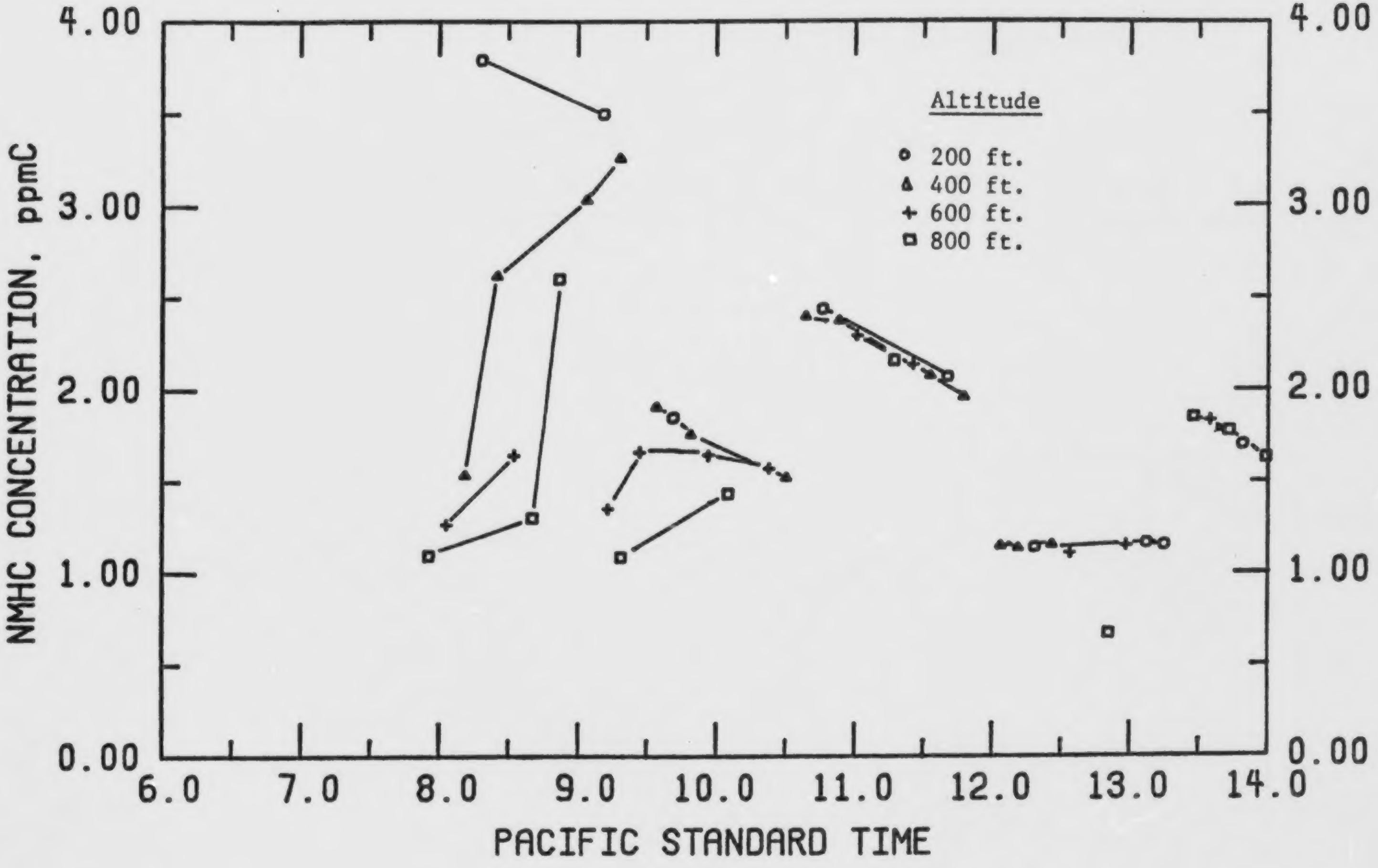

Figure 25. Helicopter pattern average nonmethane hydrocarbon concentrations for Operation 33.

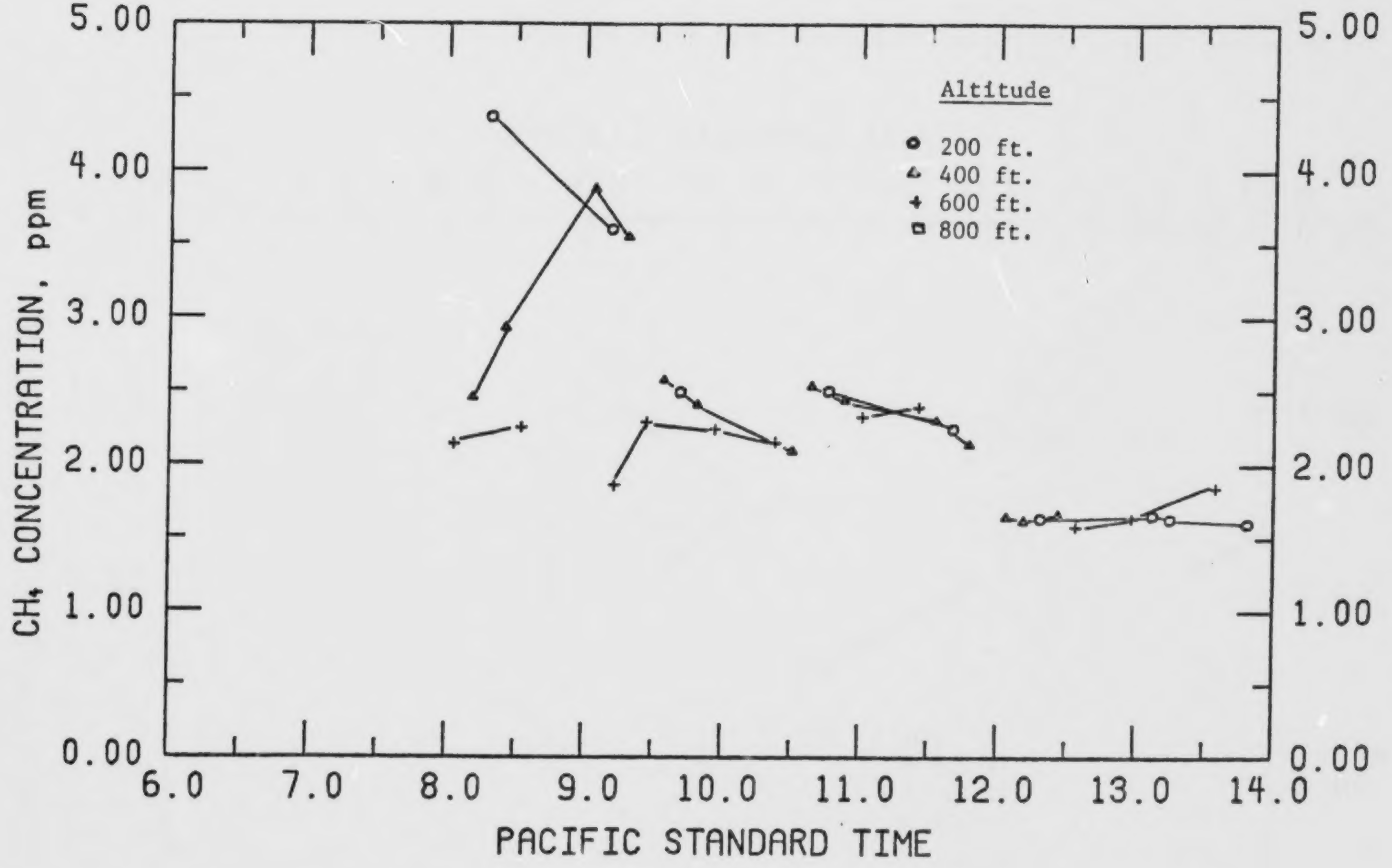

Figure 26. Helicopter pattern average methane concentrations for Operation 33.

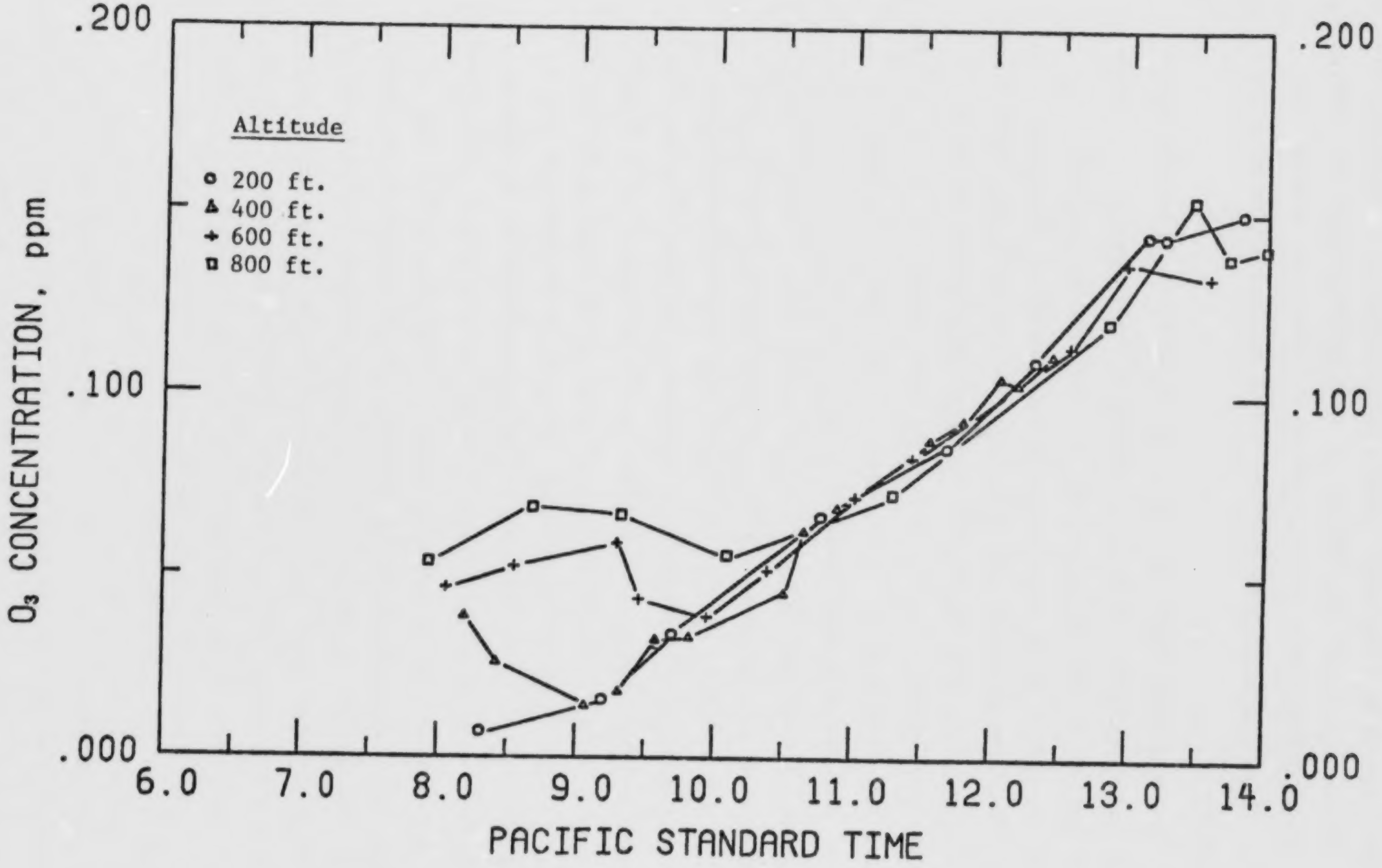

Figure 27. Helicopter pattern average ozone concentrations for Operation 33.

This implies, although individual measurements display a definite variability, that after a certain amount of spatial averaging the concentrations appear homogeneous with height during the late morning and afternoon. Thus, there is an overlying order to what seems chaotic on a smaller scale.

This is consistent with the basic characteristics of atmospheric turbulence and transport. Lumley and Panofsky (67) state: "The time and length scales of the turbulent motion that serves to transport properties are quite large, often of the same order as the time and length scales characterizing the distribution of properties being transported, and never greatly smaller." The turbulent regime present during LARPP operation 33 may be classified as "free convection" because of the very low wind speeds. Under these conditions, the vertical transfer of energy, momentum, and pollutants by mechanical turbulence can be neglected compared to that by heat convection, except in some small portions of the boundary layer. Mechanical eddies have smaller wavelengths and are more nearly isotropic than eddies from heating so that they are much less important in vertical transport than are the larger, convectional eddies. (An eddy may be thought of as a "glob" of fluid within a larger fluid mass which has a certain integrity and life history of its own, the activities and properties of the bulk fluid being the net result of the activities and properties of the eddies.) Thus, one would expect to find large eddies, with vertical scale lengths on the order of hundreds of meters, carrying high concentrations of pollutants aloft and cleaner air back down. Because the driving force for convective motion is the unstable vertical temperature structure created by heat input at the ground, the principle direction of motion is that which will most rapidly diminish the driving force, i.e., the vertical direction. Thus, convective turbulence is expected to be anisotropic, displaying a greater intensity in the vertical than the horizontal.

The helicopters, flying at an air speed of 60 knots (69.1 mph, or 30.9 m/s) and producing a new measurement every six seconds, have individual concentration values spaced approximately 185 m apart (608 feet). The values clearly do not represent point concentrations because the instruments have some characteristic averaging time. Since the helicopters are in constant motion, these averaging times represent spatial averaging as well as temporal. The variability of individual measurements about the pattern mean represents the variation of concentration from eddy to eddy, but this variation is underestimated because of spatial averaging.

Figures 28 through 36 show the standard deviation of measured variables for individual patterns relative to the pattern means. Ozone and nitric oxide concentrations exhibit relative standard deviations greater than the other measurements, and, like the other concentration measurements, show the greatest relative deviations in the morning. This is to be expected since the air just below the inversion base is a collection of air parcels from above the inversion with elevated ozone concentrations and parcels originating near the earth's surface with high concentrations of CO, $NO_x$, and hydrocarbons. The temperature measurements show the least relative deviations about the pattern means and dew point, the next lowest. The low deviation of temperature is predictable since it is self-equalizing; that is, air parcels rise until their density equals the density of the surrounding air and ambient air density is principally a function of temperature. Deviations of temperature from the mean for a given pattern level result partially from interception of air parcels just passing through that level. The relative standard deviations of precursors in the zero gradient region is rather low. The deviations are less than 0.3 for $NO_x$ and less than 0.2 for nonmethane hydrocarbons.

The primary concept to be drawn from the foregoing discussion is that there was a deep layer in the atmosphere which may be characterized at a particular time, for many purposes, by the mean concentrations of pollutants and that these means were constant with height within the layer. This is a consequence of vertical mixing within the layer which was rapid with respect to advection, and horizontal mixing in the free convection regime of operation 33. Individual measurements within this

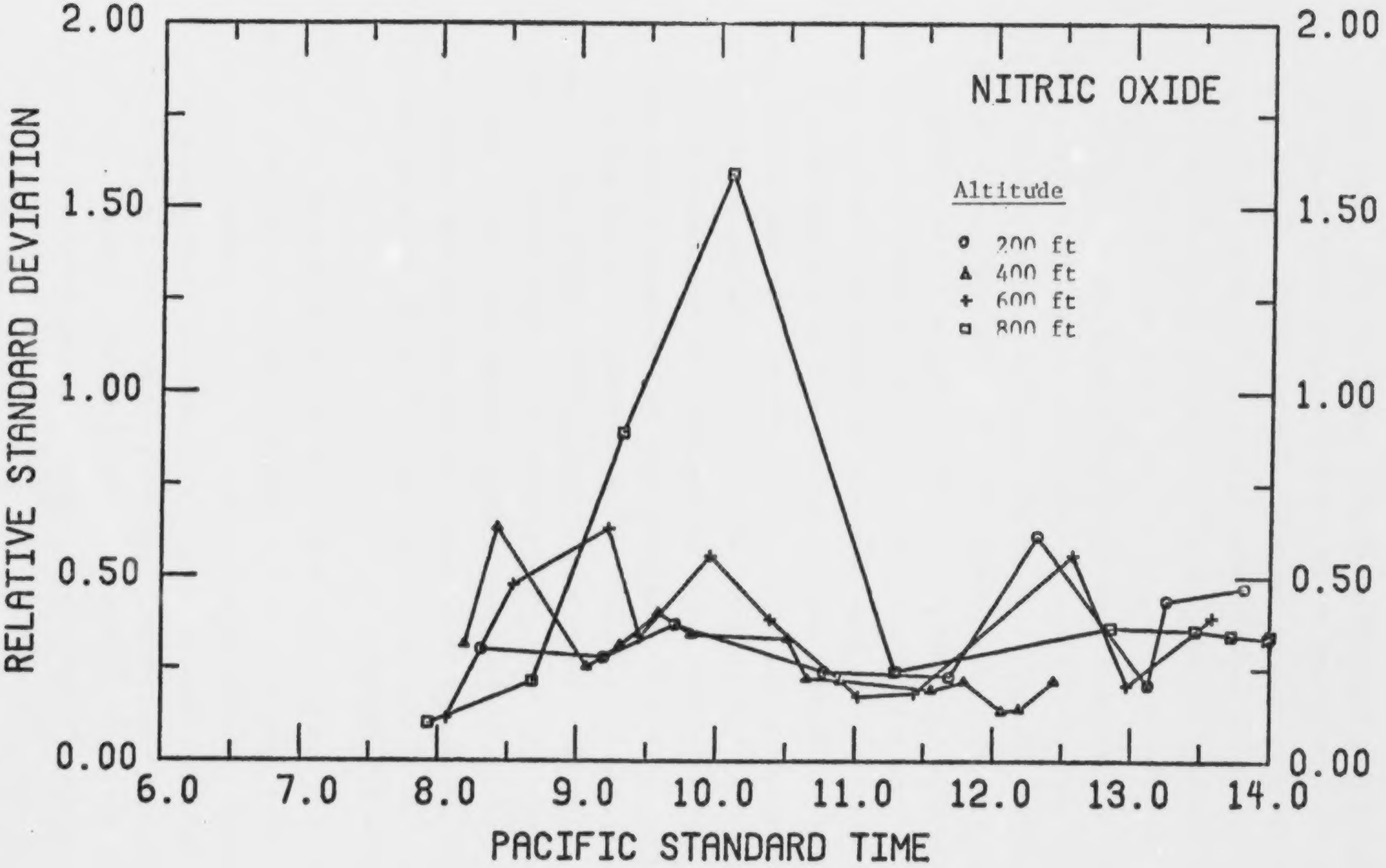

Figure 28. Helicopter pattern standard deviation of nitric oxide concentrations.

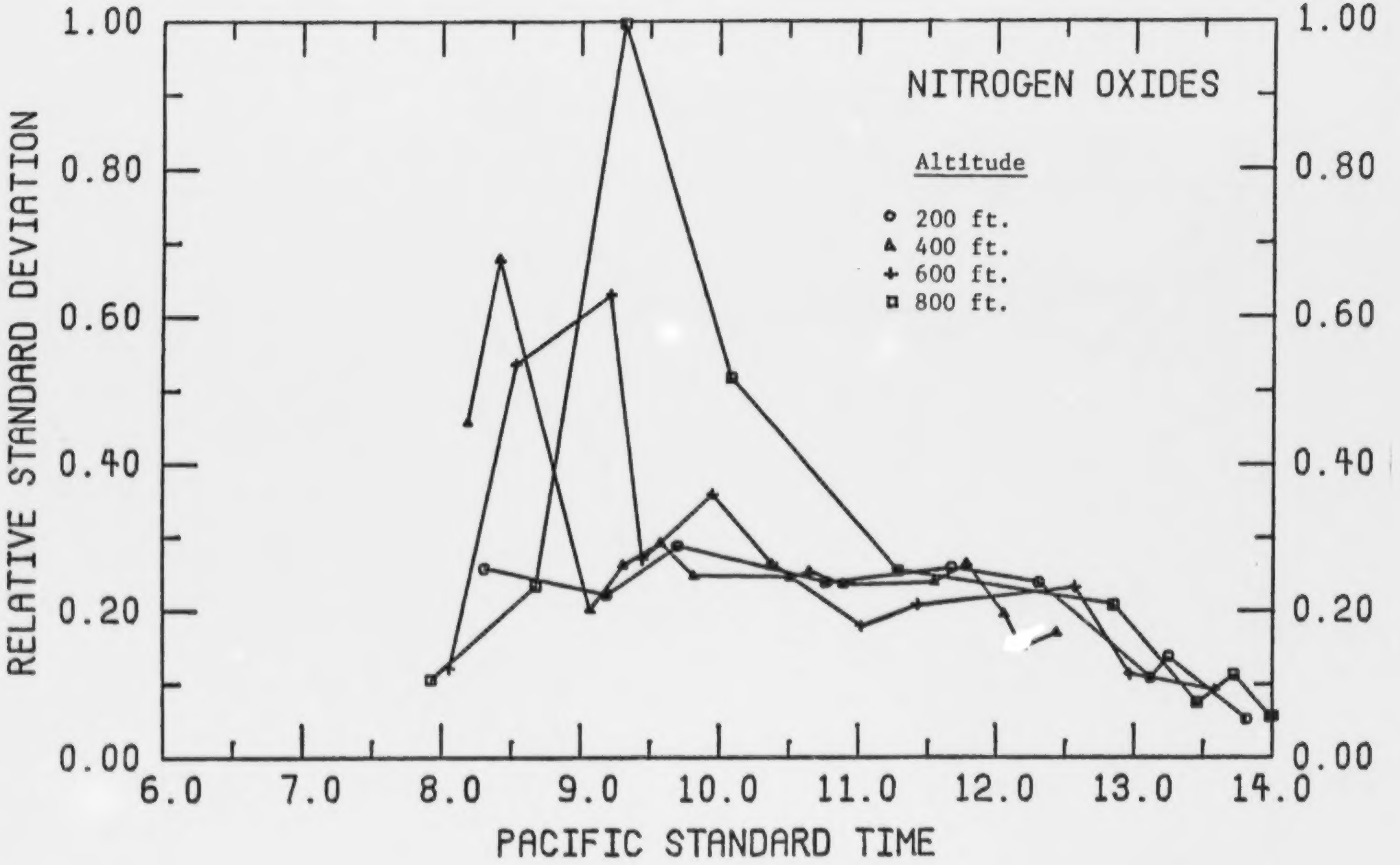

Figure 29. Helicopter pattern relative standard deviation of nitrogen oxides concentrations.

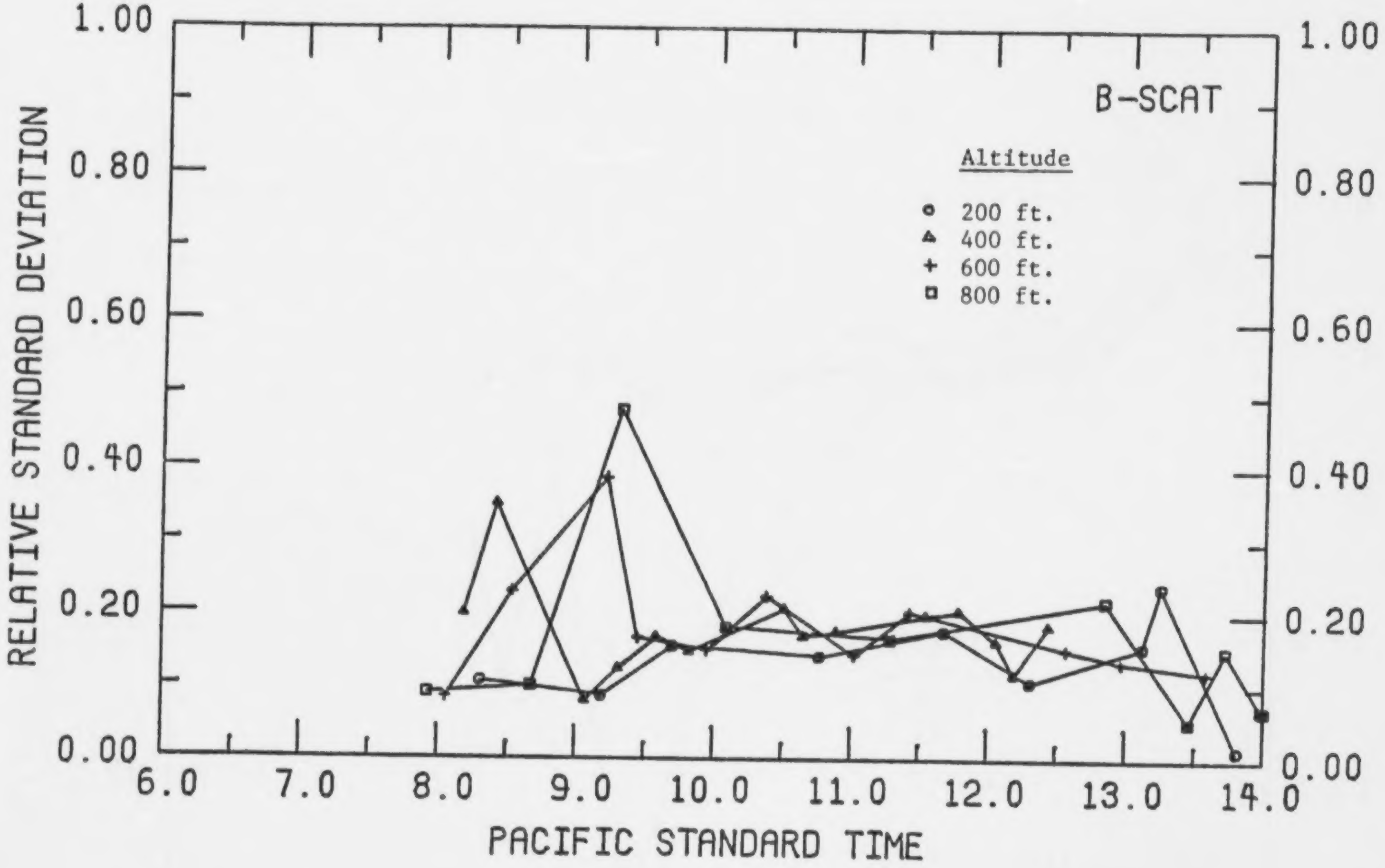

Figure 30. Helicopter pattern relative standard deviations of scattering coefficients.

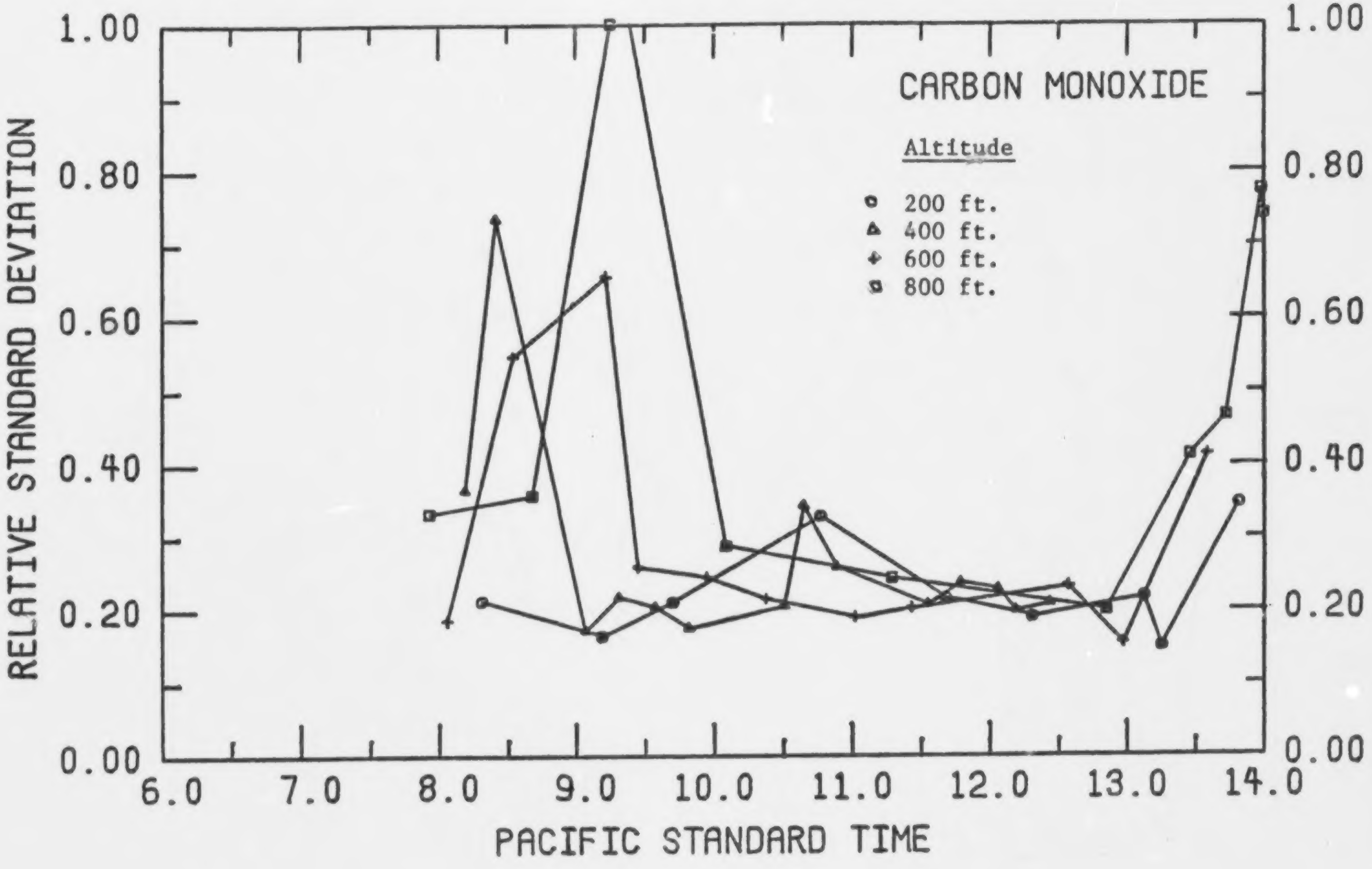

Figure 31. Helicopter pattern relative standard deviations of carbon monoxide concentrations.

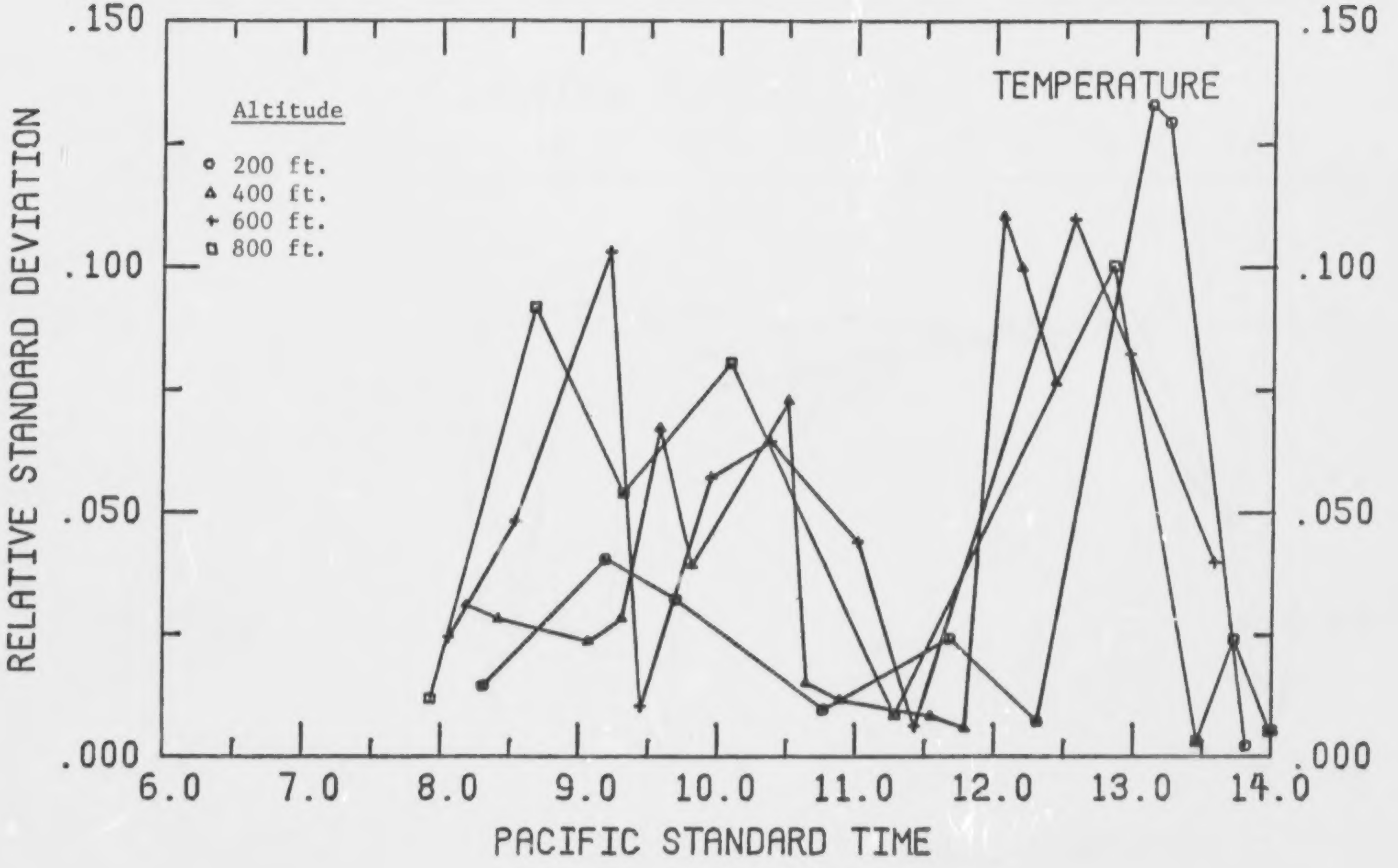

Figure 32. Helicopter pattern relative standard deviations of temperatures.

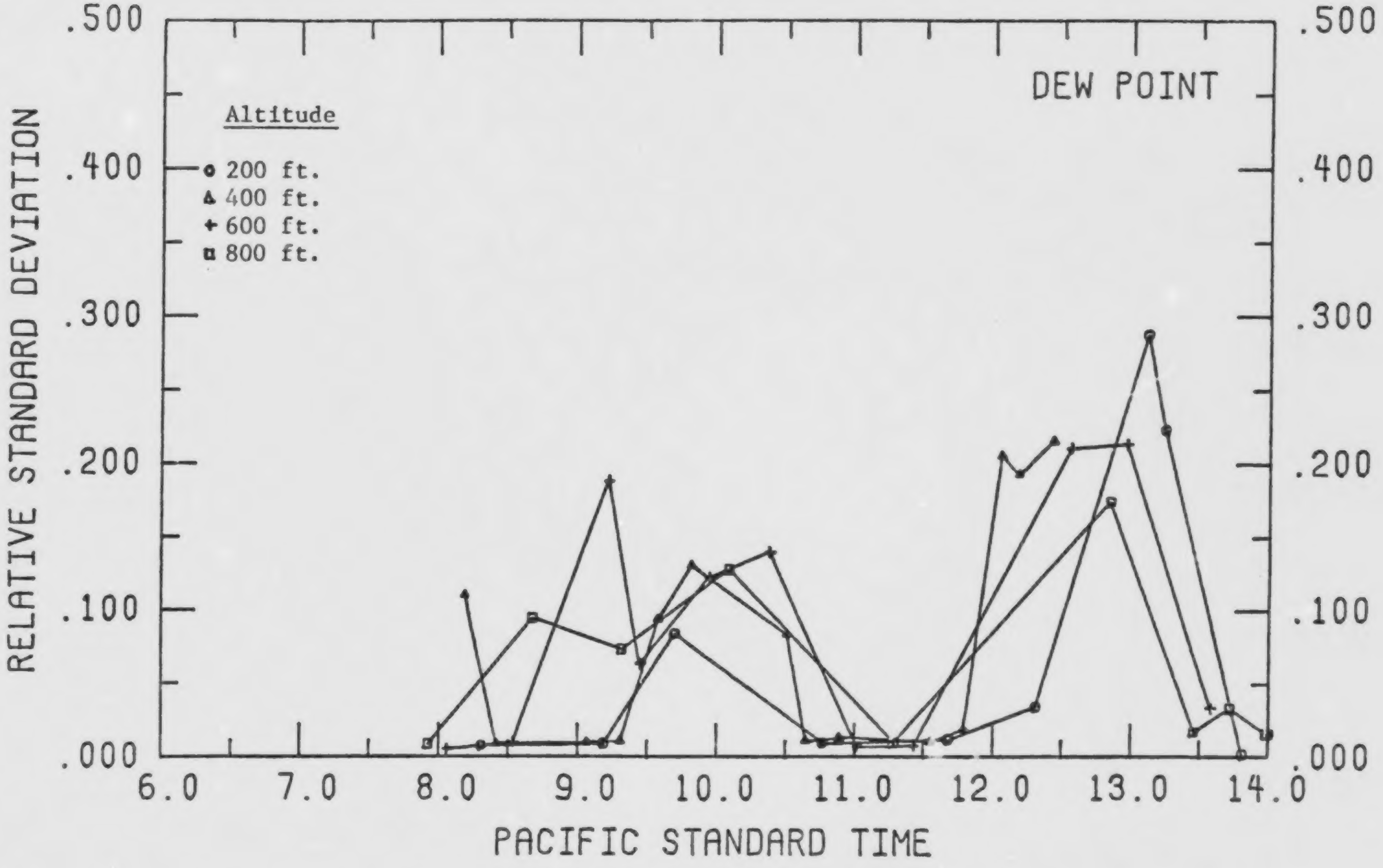

Figure 33. Helicopter pattern relative standard deviations of dew points.

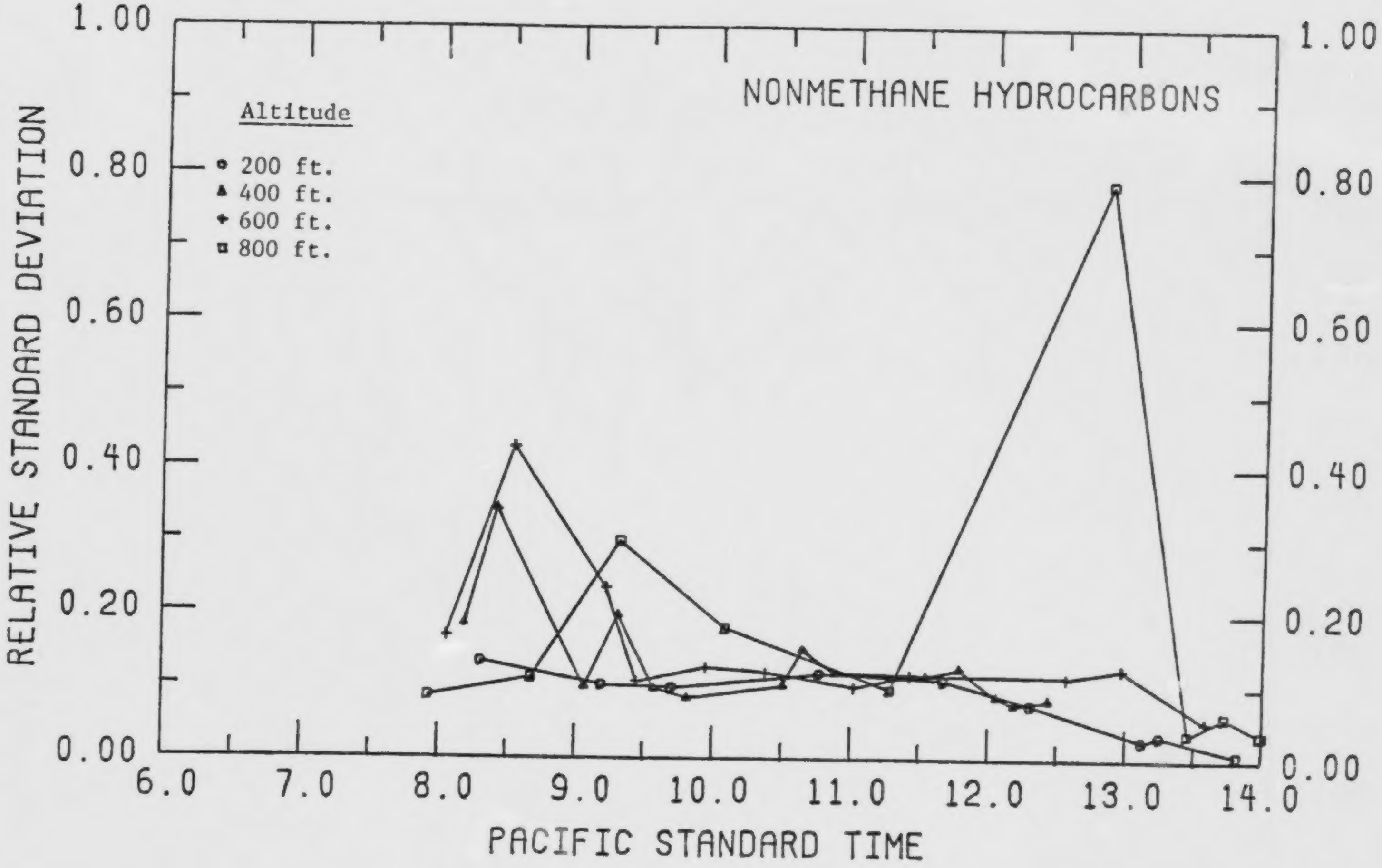

Figure 34. Helicopter pattern relative standard deviations of nonmethane hydrocarbon concentrations.

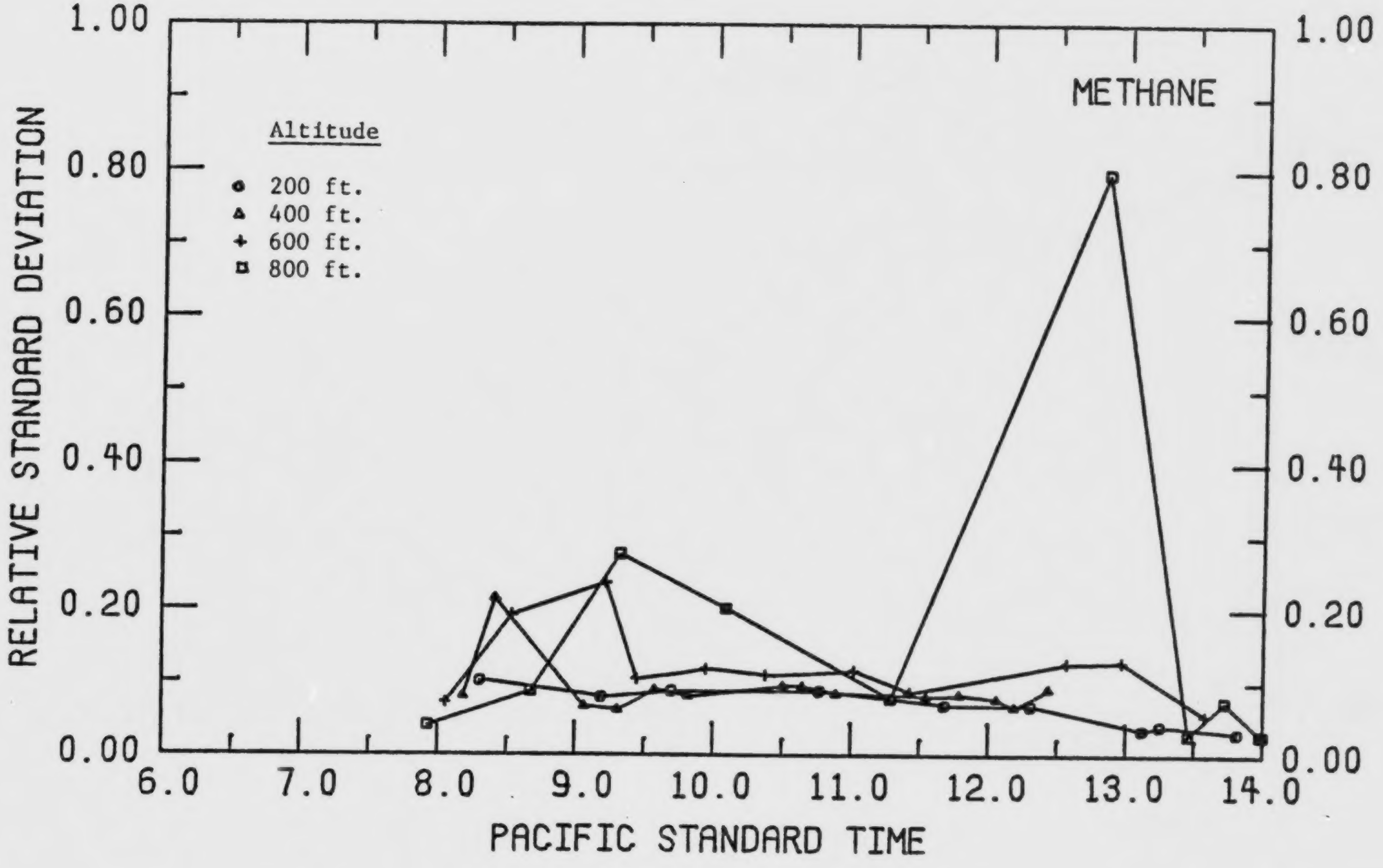

Figure 35. Helicopter pattern relative standard deviations of methane concentrations.

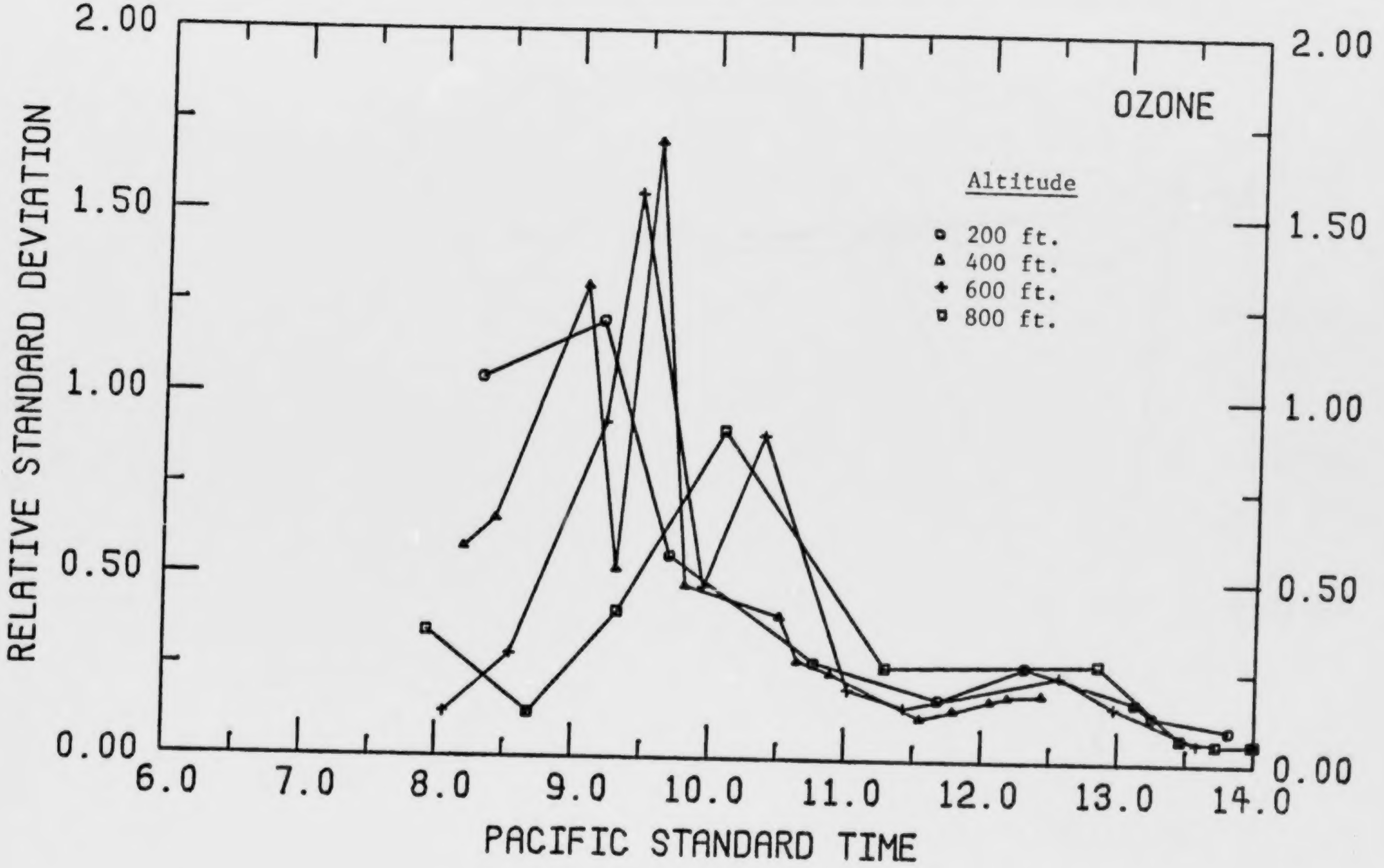

Figure 36. Helicopter pattern relative standard deviations of ozone concentrations.

region of zero vertical gradient varied about the mean concentrations. Thus, the region is not homogeneous on a molecular level.

## METHOD OF COMPARISON OF SMOG CHAMBER RESULTS WITH LARPP DATA

Before a smog chamber can be validated, one must first decide what constitutes a legitimate validation experiment; more specifically, what injection and dilution rates should be used to simulate the emission and dilution occurring along a LARPP trajectory so that an honest comparison may be made. Since it is actually the chemical characteristics of the chamber which are to be validated, a basic assertion of this work is that if the emission and dilution profiles in the air parcel are faithfully reproduced, then differences in the time profiles of the participating chemical species result only from differences in the way chemical reactions are affected by the chamber and differences in inhomogeneity, light, and temperature. The effects of differences between chamber and atmospheric inhomogeneity, light, and temperature may be estimated; the remaining discrepancies are, then, the chamber effects. Errors in estimating dilution and emissions may also be significant. The means of relating the dilution and emission in the atmosphere to the dilution and injection in the chamber may be examined by analyzing both causes as chemical reactors.

### Variable-Volume Reactor Model

A simplified model of air moving along a LARPP trajectory is a reactor with a fixed base area and a height, corresponding to the depth of the mixed portion of the atmosphere, which is variable. For a conservative substance, the reactor mass balance equation is the following:

$$V_2C_2 - V_1C_1 = F_bA(t_2 - t_1) - F_tA(t_2 - t_1) \qquad (6)$$

where V is the volume of the reactor, C is the average concentration of the species in mass/volume units and their subscripts indicate different times at which the variables are evaluated. $F_b$ is the flux of pollutant (averaged from $t_1$ to $t_2$) into the bottom of reactor, $F_t$ is the flux of pollutant (averaged from $t_1$ to $t_2$) out the top of the reactor, A is the base area, and t is time. In general, it will be assumed that horizontal diffusion may be neglected since most of the emissions are from area sources. Roth et al. (22) stated that 99 percent of the CO, 71 percent of the reactive hydrocarbons and 58 percent of the $NO_x$ emissions in the Los Angeles area are from mobile sources. Trijonis and Arledge (68) found that three-fourths of the reactive hydrocarbon emissions in the Metropolitan Los Angeles Air Quality Region are accounted for by mobile sources; the remaining quarter is equally divided between stationary source organic fuel processes and organic chemical processes. The major fixed sources for hydrocarbons and $NO_x$ combined are airports and refineries, while power plants are the major fixed sources for $NO_x$ alone. The trajectory studied in operation 33 is close to several oil refineries, but no power plants or airports.

Dividing through both sides of Equation 6 by $t_2 - t_1$ and then taking the limit as $t_2$ approaches $t_1$ yields the differential form:

$$\frac{d(VC)}{dt} = F_b A - F_t A$$

or

$$\frac{d(HC)}{dt} = F_b - F_t$$

where H is the variable reactor height, equal to V/A. Solving for dC/dt:

$$\frac{dC}{dt} = \frac{F_b}{H} - \frac{F_t}{H} - \frac{C}{H}\frac{dH}{dt} \tag{1}$$

Panofsky (69) observed that for LARPP operation 33 the vertical concentration gradients vanish within the region between about 50 m and an altitude approximately equal to one half the mixing depth. While direct evidence of the height of the zero gradient region with respect to mixing depth is only available until 0915 PST, recent theories concerning the parameterization of the boundary layer suggest that the vertical eddy diffusivity should be a function of the ratio of altitude, z, to mixing depth, h (112). Thus, the vertical extent of the zero gradient region is likely to remain at the same z/h value later in the day (25, 69). Also, data from Edinger (21, 63) show vertical concentration isopleths for much of the atmosphere below the inversion base.

Thus, there is a region of the atmosphere observed in operation 33 with zero pollutant gradient after a certain amount of horizontal averaging. While this region is not completely mixed on a molecular level as may be seen from the relative standard deviations of pollutant concentrations around helicopter patterns, the inhomogeneity decreases considerably between 0900 and 1200 PST. These inhomogeneities may cause the photochemical smog system to behave somewhat differently than would be expected based on average precursor concentrations. Several different approaches have been applied to this problem (71-74, 72). While it has been concluded that it may be necessary to account for this effect in numerical models under certain circumstances, the atmospheric smog models generally have not been able to treat this problem. The most promising approach seems to be the recent work of Lamb (74). The effects of inhomogeneities will be considered in greater detail in SECTION 7, but for the purposes of simulation, mean values of precursors were used.

Traditionally, modeling of photochemical processes along a trajectory has been concerned with matching ground level concentrations. Indeed, the only data available for model validation has been surface data. Receptors are exposed to ground level concentrations. These concentrations, however, may be greatly affected by local sources. On the other hand, the zero-gradient region represents a much greater mass of air laying above the surface layer. Surface concentrations may be thought of as mere deviations from the mean zero-gradient region concentrations, deviations produced by local emissions before they are completely diffused into the boundary layer. Also, the grid scales of current emission inventories are too coarse to fully represent the importance of sources very close to monitoring stations. Thus, it may be that simulation of the processes in the zero-gradient region is of greater general interest than simulation of the concentration profiles at a single, ground-level monitoring station.

## Hydrocarbon Emission Estimates Using Source Reconciliation

To quantitate the processes affecting pollutant concentrations in the region of zero gradient, the terms on the right of Equation 1 must be evaluated. This is easily done for a conservative substance whose vertical concentration profile is known from the bottom of the zero-gradient region to the inversion base at many points along the trajectory. Hydrocarbons, however, are: (1) not, as a class, conservative; (2) nor are their concentrations known up to the inversion base after 0920 PST. The first of these difficulties was averted by use of the data from bag samples which were obtained on many of the helicopter patterns. Hydrocarbons with low reactivity toward oxidative species were used as tracers to estimate the total hydrocarbon which would have been present in the air in the absence of consuming chemical reactions. These estimates were obtained using a source reconciliation approach similar to that of Mayrsohn and Crabtree (75). Such concentration estimates behave as conservative substances to the extent that the assumption of no reaction of the selected tracer species is upheld; reaction of tracer species may lead to underestimation of hydrocarbon emissions.

The relative amounts of selected tracer species in both atmospheric samples and in major hydrocarbon source emissions must be known for source reconciliation. The reconciliation algorithm, then, estimates a weighting coefficient for each source by least-squares regression of sample concentration on source concentrations. The major hydrocarbon source categories for the Los Angeles area are auto exhaust, gasoline vapor, gasoline, commercial natural gas, geogenic natural gas and liquefied petroleum gas. Gasoline is distinct from gasoline vapor in that all the liquid gasoline components were converted to a gas, while for gasoline vapor, gasoline components are partitioned according to their vapor pressures. Gasoline vapor is rich in the lighter gasoline components. Carburetor "hot soak" emissions would be classed as gasoline, while emissions produced by filling cars at a service station would be gasoline vapor.

Mayrsohn and Crabtree (75) employed ethane, acetylene, propane, isobutane, butane, isopentane, and pentane as tracers, leaving only one degree of freedom in the solution of the regression equations (degrees of freedom = number of tracer species - number of coefficients to be estimated), if all sources are deemed significant and included in the regressions. The present study used an additional two tracers, hexane and methane (minus background). Table 7 shows the source weight fractions of tracers used in source reconciliation. These values were taken from Mayrsohn and Crabtree (76) except where indicated. Once the best fitting coefficients were determined, it was possible to calculate the total nonmethane hydrocarbons which would have been emitted to produce the observed tracer concentrations by using average source compositions. The compositions used were taken from Mayrsohn (77). These are shown in Table 8. The calculations performed by the source reconciliation program are discussed in Appendix B. The following items were calculated for each bag sample: source weighting coefficients; $R^2$ for the regression fit; estimated micrograms/$m^3$, ppm by volume, and ppm as carbon for each substance from each source category and total for all sources; estimated weight fraction of carbon for each compound in the sample; residuals for all tracer species. Due to the large amount of data, only selected portions will be included here.

Table 9 contains the estimated weight fraction of NMHC from each source and the $R^2$ values.

Mayrsohn and Crabtree (75) performed source reconciliation calculations on hydrocarbon samples from downtown Los Angeles, Azusa, and a rural site in Redlands, California during June and July, 1973. They analyzed samples for three time periods during the day: early morning, morning traffic peak, and early afternoon. All samples were taken relatively close to the earth's surface. They found that only about 50 percent of the non-methane hydrocarbons (weight basis) in the air came from auto exhaust. About 25 percent resulted from emissions of gasoline and gasoline vapor, and about 25 percent from commercial and geogenic natural gas. Further works in 1974 by Mayrsohn et al. (79) confirmed these findings at other sites.

### TABLE 7. WEIGHT FRACTIONS OF TRACER SPECIES IN MAJOR HYDROCARBON SOURCES IN THE LOS ANGELES AREA[*]

| Tracer | Auto Exhaust | Gasoline Evap. | Gasoline Vapo. | Comm. Nat. Gas | Geogenic Nat. Gas | Liq. Pet. Gas |
|---|---|---|---|---|---|---|
| Ethane | 0.57 | 0 | 0.1 | 11.30 | 3.38 | 4.04 |
| Acetylene | 5.13 | 0 | 0 | 0 | 0 | 0 |
| Propane | 0 | 0.1 | 1.6 | 3.47 | 5.40 | 88.50 |
| Isobutane | 0.85 | 0.5 | 6.1 | 0.34 | 1.26 | 2.38 |
| N-butane | 2.56 | 2.2 | 18.8 | 0.50 | 3.13 | 0.03 |
| Isopentane | 5.50 | 8.0 | 29.3 | 0.11 | 1.33 | 0 |
| Pentane | 2.85 | 4.2 | 10.6 | 0.11 | 1.33 | 0 |
| Hexane | 1.61 | 3.6 | 2.5 | 0.07 | 0.39 | 0 |
| Methane | 5.09[†] | 0[#] | 0[#] | 83.72[**] | 78.58[††] | 0.04 |

[*] Data directly from Mayrsohn and Crabtree (76) unless noted otherwise.

[†] R. W. Hurn (78) presented a table with some compounds in auto exhaust. The ratio of methane to ethane was 0.726 and methane to propane was 1.516. Based on these ratios and the ethene and propene measurements of Mayrsohn and Crabtree (76), methane weight percentage is 5.23 and 4.90. Also, Stephens and Burleson (1969) state that "methane, ethene and acetylene are present in auto exhaust in roughly equal amounts."

[#] Mayrsohn and Crabtree (76) found no ethane, ethylene or propylene in liquid gasolines, thus, no methane would be present since gasoline is produced by distillation.

[**] Mayrsohn and Crabtree (76) give data indicating that the ratio of methane to ethane in commercial natural gas as 7.41.

[††] Mayrsohn and Crabtree (76) give data indicating that the methane to ethane and methane to propane ratios are 24.6 and 13.7 which indicates methane weight fractions of 79.5 and 77.5.

### TABLE 8. NONMETHANE HYDROCARBON DISTRIBUTIONS FOR AUTOMOTIVE EXHAUST, GASOLINE, GASOLINE VAPOR, COMMERCIAL NATURAL GAS, AND GEOGENIC NATURAL GAS (77)

| Compound | Weight Percent | | | | | |
|---|---|---|---|---|---|---|
| | A.EX | GAS | VAP | CNG | GNG | LPG |
| Ethane | 0.6 | --* | 0.1 | 69.4 | 15.8 | 4.1 |
| Ethylene | 7.6 | -- | -- | -- | -- | -- |
| Acetylene | 5.4 | -- | -- | -- | -- | -- |
| Propane | -- | 0.1 | 1.6 | 21.3 | 25.2 | 90.4 |
| Propylene | 3.4 | -- | -- | -- | -- | 5.1 |
| Methylacetylene | 1.0 | -- | -- | -- | -- | -- |
| Isobutane | 0.9 | 0.5 | 6.1 | 2.1 | 5.9 | 0.2 |
| Butane | 2.7 | 2.2 | 18.8 | 3.1 | 14.6 | -- |
| Butenes | 4.1 | 0.4 | 1.8 | -- | -- | -- |
| Isopentane | 5.8 | 8.0 | 29.3 | 0.7 | 6.2 | -- |
| Pentane | 3.0 | 4.2 | 10.6 | 0.7 | 6.2 | -- |
| Pentenes | 2.3 | 2.5 | 6.2 | -- | -- | -- |
| Isoprene | 1.3 | -- | 0.1 | -- | -- | -- |
| 2-methylpentane | 3.0 | 5.8 | 6.1 | 0.3 | 2.9 | -- |
| 3-methylpentane | 1.5 | 2.9 | 2.5 | 0.1 | 1.5 | -- |
| Hexane | 1.7 | 3.6 | 2.5 | 0.4 | 1.8 | -- |
| Hexenes | 1.5 | 1.7 | 1.4 | -- | -- | -- |
| Methylcyclopentane | 1.7 | 3.5 | 2.0 | 0.1 | 2.6 | -- |
| Benzene | 2.8 | 2.4 | 1.1 | -- | -- | -- |
| 2,3-dimethylpentane | 1.7 | 3.3 | 1.1 | 0.3 | 0.8 | -- |
| 3-methylhexane | 1.2 | 2.4 | 0.8 | 0.2 | 4.5 | -- |
| 2,2,4-trimethylpentane | 2.0 | 3.5 | 1.0 | 0.3 | 0.9 | -- |
| Heptane | 1.3 | 2.5 | 0.6 | 0.2 | 1.2 | -- |
| Methylcyclohexane | 0.8 | 1.2 | 0.3 | 0.1 | 2.2 | -- |
| Dimethylhexane | 0.9 | 1.6 | 0.3 | 0.2 | 1.8 | -- |
| Toluene | 7.8 | 9.5 | 2.0 | -- | -- | -- |
| Iso-octane | 1.3 | 3.5 | 0.6 | 0.4 | 3.3 | -- |
| Octane | 1.6 | 1.2 | 0.1 | -- | 1.0 | -- |
| Isononane | 1.1 | 1.2 | 0.2 | -- | 1.8 | -- |
| m & p-Xylene | 8.1 | 10.1 | 1.3 | -- | -- | -- |
| o-Xylene | 3.5 | 3.5 | 0.5 | -- | -- | -- |

(continued)

Table 8 (Continued) -- Nonmethane Hydrocarbon Distributions for Automotive Exhaust, Gasoline, Gasoline Vapor, Commercial Natural Gas, and Geogenic Natural Gas (77)

| Compound | Weight Percent | | | | | |
|---|---|---|---|---|---|---|
| | A.EX | GAS | VAP | CNG | GNG | LPG |
| Nonane | 0.9 | 0.6 | 0.1 | -- | -- | -- |
| Propylbenzene | 0.6 | 0.4 | -- | -- | -- | -- |
| 2,2,3,3-tetramethylhexane | 0.3 | -- | -- | -- | -- | -- |
| 3-ethyltoluene | 5.9 | 6.3 | 0.6 | -- | -- | -- |
| 1,2,4-trimethylbenzene | 4.4 | 3.7 | 0.3 | -- | -- | -- |
| 1,2,3-trimethylbenzene | 1.3 | 1.3 | 0.1 | -- | -- | -- |
| Dimethylbenzene | 0.9 | 2.6 | -- | -- | -- | -- |
| Butylbenzene | 2.1 | 1.7 | -- | -- | -- | -- |
| C4-benzenes | 2.1 | 2.1 | -- | -- | -- | -- |

*Less than 0.1%.

## TABLE 9. BAG SAMPLE TIME AND ALTITUDE ESTIMATED WEIGHT FRACTION OF NMHC FROM EACH SOURCE CATEGORY AND $R^2$ FROM SOURCE RECONCILIATION

| Time, PST | Altitude, ft | Weight Fraction | | | | | | $R^2$ |
|---|---|---|---|---|---|---|---|---|
| | | AEX | GAS | VAP | CNG | GNG | LPG | |
| 0745 | 0 | 0.510 | 0.470 | 0.000 | 0.021 | 0.000 | 0.000 | 0.863 |
| 0752 | 845 | 0.390 | 0.564 | 0.000 | 0.019 | 0.000 | 0.027 | 0.875 |
| 0759 | 666 | 0.410 | 0.518 | 0.000 | 0.044 | 0.000 | 0.029 | 0.972 |
| 0807 | 493 | 0.457 | 0.475 | 0.000 | 0.374 | 0.000 | 0.031 | 0.950 |
| 0815 | 337 | 0.000 | 0.964 | 0.000 | 0.357 | 0.000 | 0.000 | 0.820 |
| 0823 | 500 | 0.000 | 0.950 | 0.000 | 0.000 | 0.051 | 0.000 | 0.831 |
| 0923 | 682 | 0.412 | 0.528 | 0.000 | 0.307 | 0.000 | 0.029 | 0.896 |
| 0931 | 499 | 0.000 | 0.928 | 0.000 | 0.050 | 0.000 | 0.022 | 0.951 |
| 0939 | 337 | 0.350 | 0.582 | 0.000 | 0.043 | 0.000 | 0.026 | 0.951 |
| 0945 | 0 | 0.523 | 0.413 | 0.000 | 0.034 | 0.000 | 0.030 | 0.982 |
| 0946 | 558 | 0.724 | 0.000 | 0.171 | 0.057 | 0.000 | 0.047 | 0.983 |
| 0954 | 600 | 0.420 | 0.497 | 0.000 | 0.058 | 0.000 | 0.027 | 0.974 |
| 1012 | 900 | 0.460 | 0.477 | 0.000 | 0.035 | 0.000 | 0.028 | 0.945 |
| 1020 | 881 | 0.712 | 0.000 | 0.203 | 0.038 | 0.000 | 0.048 | 0.894 |
| 1027 | 700 | 0.493 | 0.439 | 0.000 | 0.040 | 0.000 | 0.028 | 0.962 |
| 1035 | 516 | 0.413 | 0.532 | 0.000 | 0.031 | 0.000 | 0.025 | 0.950 |
| 1043 | 320 | 0.716 | 0.000 | 0.186 | 0.052 | 0.000 | 0.046 | 0.951 |
| 1045 | 0 | 0.474 | 0.472 | 0.000 | 0.030 | 0.000 | 0.024 | 0.980 |
| 1145 | 0 | 0.464 | 0.469 | 0.000 | 0.034 | 0.000 | 0.033 | 0.944 |
| 1200 | 516 | 0.476 | 0.454 | 0.000 | 0.037 | 0.000 | 0.034 | 0.960 |
| 1208 | 517 | 0.695 | 0.000 | 0.207 | 0.052 | 0.000 | 0.046 | 0.950 |
| 1215 | 342 | 0.652 | 0.000 | 0.258 | 0.040 | 0.000 | 0.050 | 0.882 |
| 1223 | 552 | 0.000 | 0.905 | 0.000 | 0.050 | 0.000 | 0.046 | 0.930 |
| 1231 | 700 | 0.641 | 0.000 | 0.268 | 0.041 | 0.000 | 0.050 | 0.900 |
| 1245 | 0 | 0.000 | 0.901 | 0.000 | 0.060 | 0.000 | 0.041 | 0.960 |
| 1320 | 833 | 0.000 | 0.960 | 0.000 | 0.045 | 0.000 | 0.000 | 0.885 |
| 1327 | 1052 | 0.000 | 0.930 | 0.000 | 0.046 | 0.000 | 0.031 | 0.898 |
| 1335 | 1267 | 0.497 | 0.440 | 0.000 | 0.035 | 0.000 | 0.030 | 0.941 |
| 1345 | 1655 | 0.462 | 0.473 | 0.000 | 0.036 | 0.000 | 0.029 | 0.930 |
| 1354 | 1900 | 0.464 | 0.474 | 0.000 | 0.033 | 0.000 | 0.029 | 0.922 |

Source reconciliation results from LARPP bag sample data showed that a somewhat greater weight fraction of NMHC were believed to have resulted from the emission of auto exhaust plus liquid gasoline plus gasoline vapor. These combined sources were estimated to contribute an average of 93 percent of the total NMHC. The sample standard deviation of this combined contribution was only 2 percent. The variability of the estimated AEX, GAS, and VAP weight fractions individually is somewhat greater than that of the sum of these three sources. For a majority of samples, the best fits were obtained for source configurations excluding gasoline vapor; for these cases, the estimated weight fractions of AEX and GAS were often nearly equal. For six samples, GAS was the only auto-related source to be included in best fitting model, accounting for 90 percent or more of the total NMHC. Commercial natural gas was estimated to account for an average of 4 percent and liquified petroleum gas, another 3 percent of the total NMHC observed, for a combined average of 7 percent. This was much less than the 25 percent from CNG and GNG estimated by Mayrsohn and Crabtree.

To explain the differences between the results of this work and those of Mayrsohn and Crabtree (75), source reconciliation was performed on the LARPP data employing the same source compositions and tracer species as Mayrsohn and Crabtree. The results of this yielded estimated NMHC weight fractions quite a bit like those of Mayrsohn and Crabtree. Auto exhaust contributed an average of 54 percent, gasoline plus gasoline vapor averaged 21 percent and CNG plus GNG averaged 25 percent. Thus, it must be concluded that the differences between the findings of this study and those of Mayrsohn and Crabtree were caused by the use of the additional tracer species, methane above background and hexane. The use of more tracer species is believed to improve the weight fraction estimates, just as an increasing number of cases improves the estimation of coefficients in other regression applications, by increasing the number of degrees of freedom.

### Estimates of Flux in the Boundary Layer

The lack of data between 1000 feet and the inversion base after 0920 PST represents a severe limitation in that the flux of pollutants as a function of altitude cannot be determined directly from the data. For the period up to 0915 PST, Panofsky (69) calculated the vertical flux of CO by the expression:

$$F_z = \int_z^h \rho \frac{dc}{dt} dz \tag{7}$$

where $\rho$ is air density, $F_z$ is the vertical flux at altitude z, h is the height of the inversion base and c is the mixing ratio of CO. He then was able to calculate vertical exchange coefficient, $K_z$:

$$K_z = -F_z / \frac{\partial c}{\partial z} \tag{8}$$

During the morning period, $K_z$ between the top of the zero-gradient region of the inversion base approximately follows the relationship

$$K_z = -A \log_{10} (\frac{\partial z}{h} - 1) \tag{9}$$

where z is altitude, h is the altitude of the inversion base and A is an empirical constant. Panofsky calculated an A value of about 5 $m^2 sec^1$ for operation 33. Based on the LARPP data it is not possible to determine whether this relationship holds all day long; however, work by Deardorff and Willis (70) suggests that $K_z$ should scale as some function of z/h (Panofsky, 25). It was assumed for this work that the relationship holds for the remainder of operation 33.

To determine flux as a function of altitude, a computer program was written to solve numerically the equation

$$\frac{dc}{dt} = \frac{\partial}{\partial z} (K(z,t) \frac{\partial c}{\partial z}) \tag{10}$$

where K(z,t) is the vertical eddy diffusivity which is a function of altitude and time. The details of this solution are given in Appendix C. Input to the program consists of initial conditions of concentration at all altitudes, the average concentrations in the zero-gradient region throughout the operation, and the mixing depth throughout the day.

The mixing depth used for flux calculations is shown in Figure 37. The mixing depth prior to 0924 PST was taken from Panofsky (69). The mixing depth at 1130 PST was estimated by Edinger (65), and at 1400 PST, by Keith (80). Earlier estimates based on ground temperature and radiosonde data yielded afternoon mixing depths approximately twice as large. This is probably due to the extreme sensitivity of this graphical method to errors in the vertical temperature profile.

The initial conditions of CO concentration were determined from helicopter data up to 800 feet. As an initial guess, the CO concentration above 1000 feet was assumed to be equal to that above the inversion base early in the day, i.e., about 1 ppm. This is probably a good upper limit value; concentrations have been measured in non-urban air masses over continental California from 0.05 to 1.0 ppm and 1 ppm seems to represent an upper limit for other background measurements (29). The lower boundary condition for the solution of Equation 10 is the concentration in the zero-gradient region; the values used for the CO calculation are shown in Figure 38 as well as the calculated CO profiles at one hour intervals. The estimated CO fluxes for 150 feet and for h/2 are given in Figure 39.

Panofsky (69) estimated the flux of CO at six altitudes for the early morning when concentration data is available up to the inversion base. Panofsky's computational approach, while not described in any detail, seems to have been to first establish concentration profiles at various altitude levels, and then evaluate dc/dt graphically between 0 and 250 m at steps of 50 m. The integration in Equation 7 was performed numerically to estimate the fluxes. Table 10 compares these flux estimates with the estimates obtained from the numerical solution of Equation 10. The greatest discrepancies occur at 0815 PST; the numerical solution estimated a much greater vertical flux. The principal differences in the two methods are the data utilized. While Panofsky's direct calculations use concentration data at all levels, the numerical approach uses only the data in the zero-gradient region except on the initial step. Also, the numerical solution depends on the validity of Equation 9. This equation generally fits the data used but the fit is not

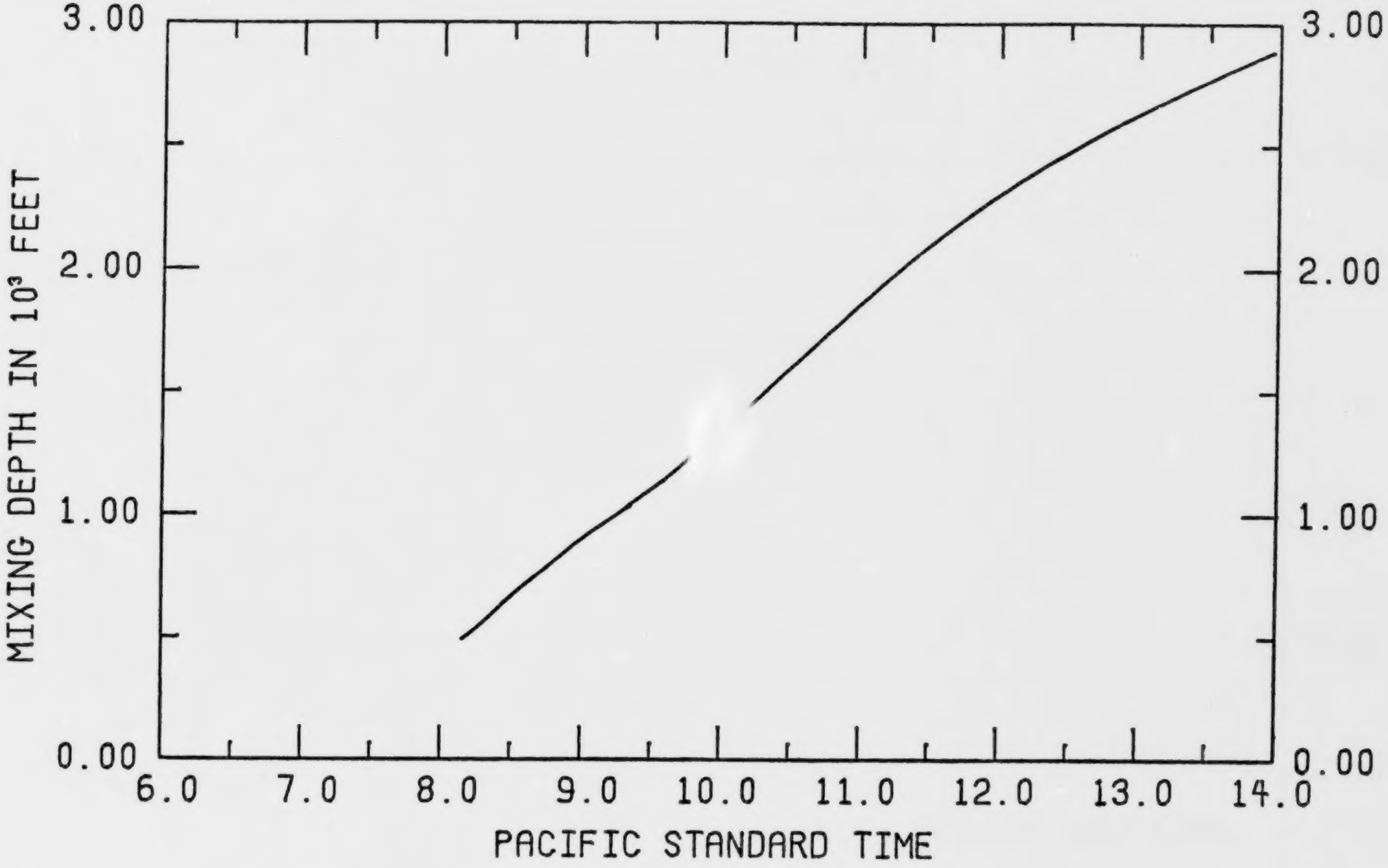

Figure 37. Mixing depth estimated for the LARPP Operation 33 trajectory.

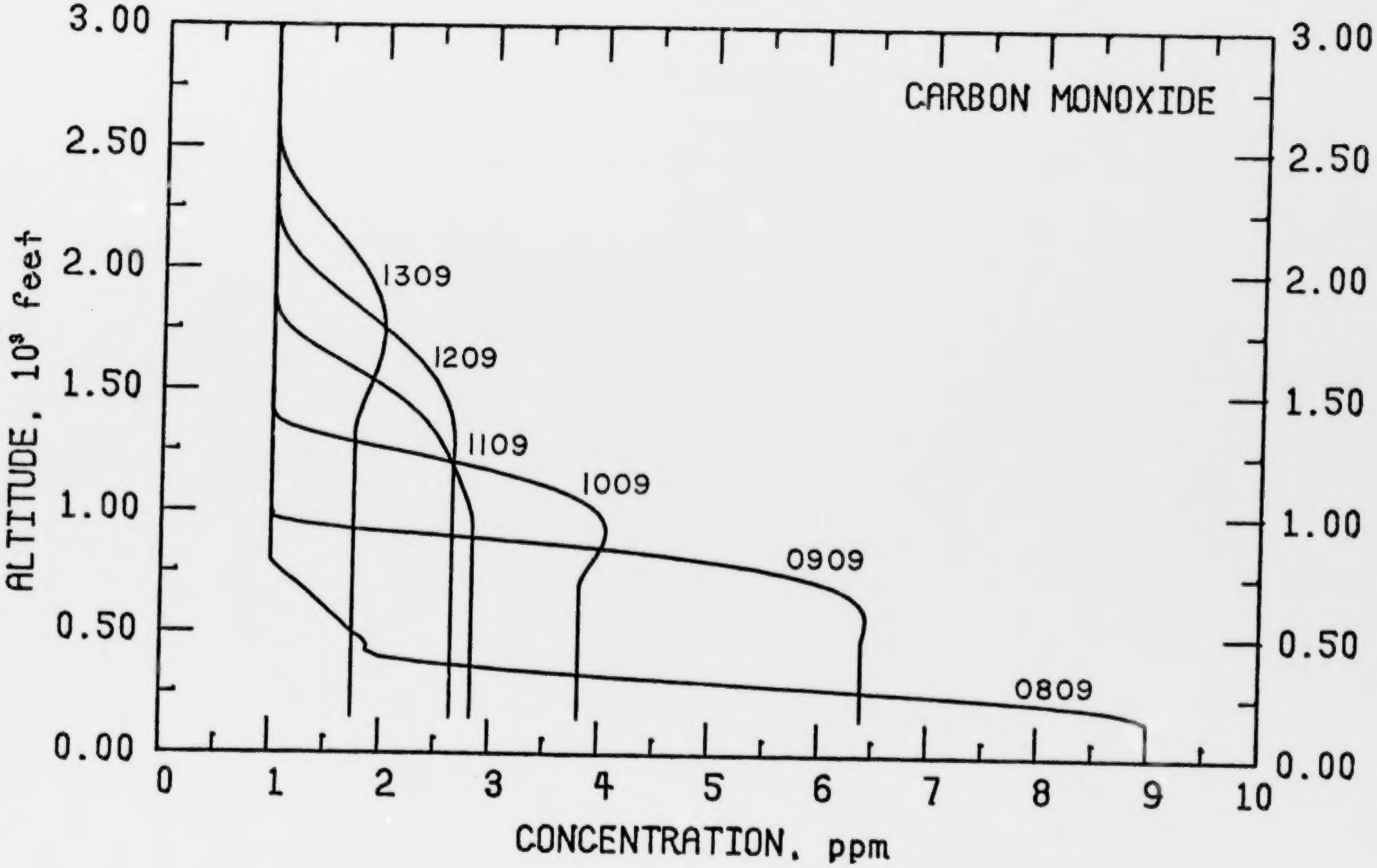

Figure 38. Carbon monoxide vertical concentration profiles for Operation 33 at one-hour intervals estimated by numerical solution.

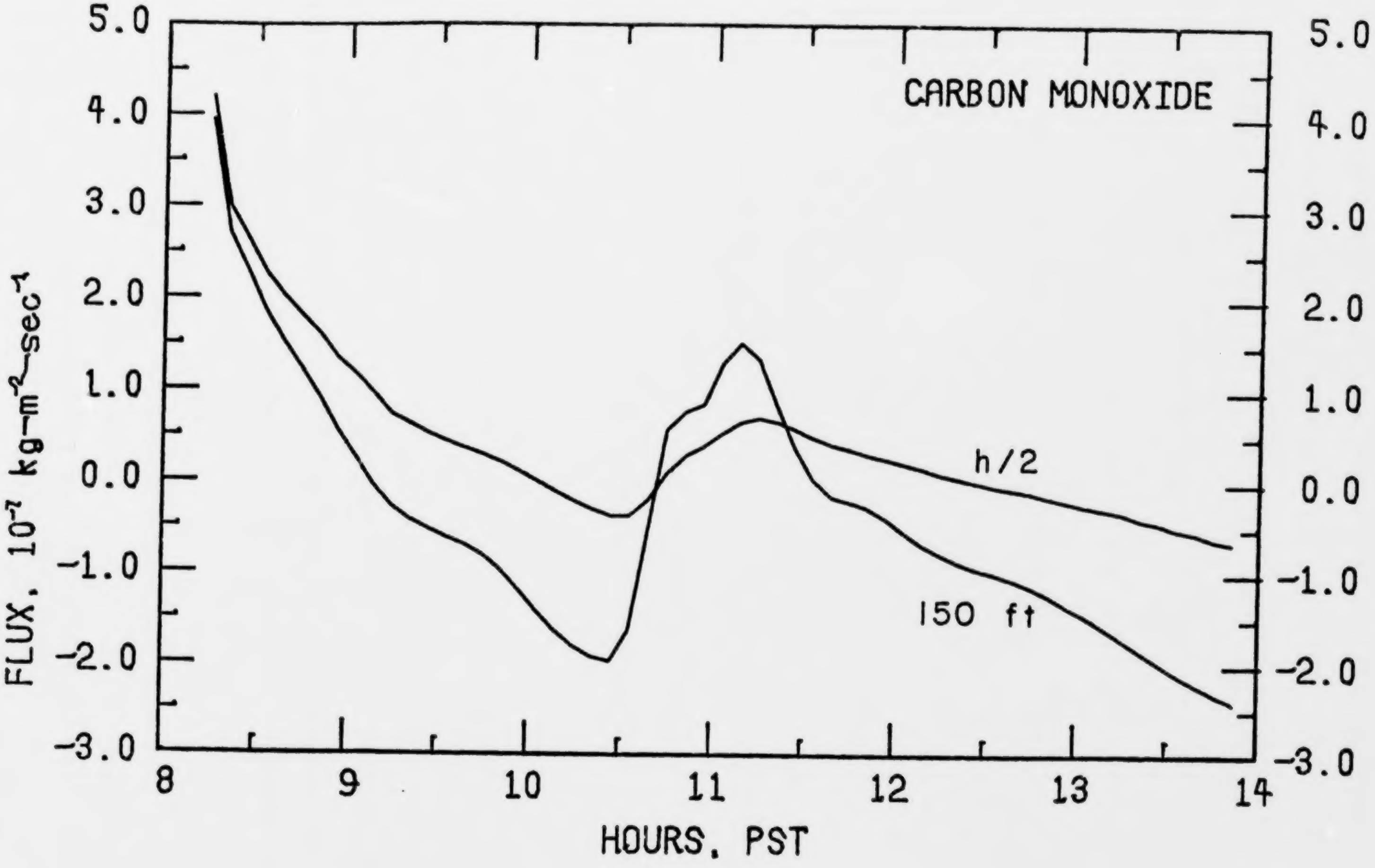

Figure 39. Estimated carbon monoxide flux at altitudes of 150 feet and half the mixing depths from numerical solution.

TABLE 10. COMPARISON OF CO FLUX ESTIMATES FROM PANOFSKY (69) AND FROM NUMERICAL FLUX COMPUTATION

| Altitude | Time, PST | | | | | | | | | |
|---|---|---|---|---|---|---|---|---|---|---|
| | 0815 | | 0830 | | 0845 | | 0900 | | 0915 | |
| | P[*] | N[†] | P | N | P | N | P | N | P | N |
| 50 m (167 ft) | 79 | 400 | 154 | 232 | 139 | 141 | 97 | 59 | 59 | -10 |
| 100 (333 ft) | 64 | 446 | 179 | 264 | 176 | 178 | 135 | 105 | 102 | 35 |
| 150 (500 ft) | 12 | 132 | 66 | 257 | 121 | 211 | 141 | 147 | 127 | 84 |
| 200 (667 ft) | 0 | 0 | 2 | 10 | 41 | 168 | 70 | 174 | 71 | 127 |
| 250 (833 ft) | 0 | 0 | 0 | 0 | 2 | 2 | 4 | 70 | 18 | 126 |

[*] P - estimates by Panofsky (69).

[†] N - numerical solution of Equation 4.

perfect. Examination of estimated concentration profiles at 0815 and 0830 PST revealed that the transport to the upper altitude levels was overpredicted, thus so was the flux at all lower levels. This is the result of the inexact fit of the equation for the eddy diffusivity.

The estimates of flux at 0845 and 0900 agree quite well. There are some differences at the upper levels, however. These disagreements are probably due to the combined effects of Panofsky's large vertical spacing and his use of trapezoid rule integration. The use of trapezoid rule assumes that dc/dt may be approximated by a straight line between the altitudes for which dc/dt was evaluated. The calculations of dc/dt on the finer grid spacing used in the numerical solution indicates that such an assumption could result in considerable error. Thus, it may be concluded that reasonable agreement was obtained when Equation 9 gives good estimates of the eddy diffusivities. In addition, the numerical solution offers the advantage of finer grid spacing so that errors in integration are greatly reduced. The assumption that Equation 9 accurately estimates the diffusivities later in the day may not be checked against the LARPP data, but must be accepted on theoretical justification.

After the computation of the CO fluxes, total nonmethane hydrocarbon concentrations from source reconciliation were considered. The concentrations, based on bag samples from the zero-gradient region, were plotted versus time as shown in Figure 40. Since one would expect this measure to behave similarly to conservative pollutants emitted from the ground such as CO, the considerable scatter of these data must be assumed to be the result of: (1) the simplicity of the source reconciliation concept, and (2) the errors in measuring tracer concentrations. The first source of error mentioned above is that which results from assuming that all ambient air hydrocarbons emanate from just six sources of fixed composition. In reality, nearly each automobile has its own emission characteristics which vary with time; each source of natural and geogenic gas has composition slightly different from other sources. The second source of error above encompasses all the factors which could cause errors in measurement. Loss of material during collection, or during storage as suggested by Calvert (81), and errors in gas chromatographic analysis are included.

Since it was believed that the scatter was the result of error rather than a genuine characteristic of the data, these concentrations were smoothed by fitting with a least-squares, straight line. This line was then compared with nonmethane hydrocarbon data from the helicopters. During the morning, the agreement between the concentration measured aboard helicopter Smog 2 and the concentration estimated by source reconciliation is excellent, as can be seen from Figure 41. Helicopter Smog 3 is measuring considerably lower concentrations; it may be that this instrument was not calibrated correctly, or that the calibration changed for some reason. This would not be surprising since many environmental chromatographs are so noisy that calibration can be greatly

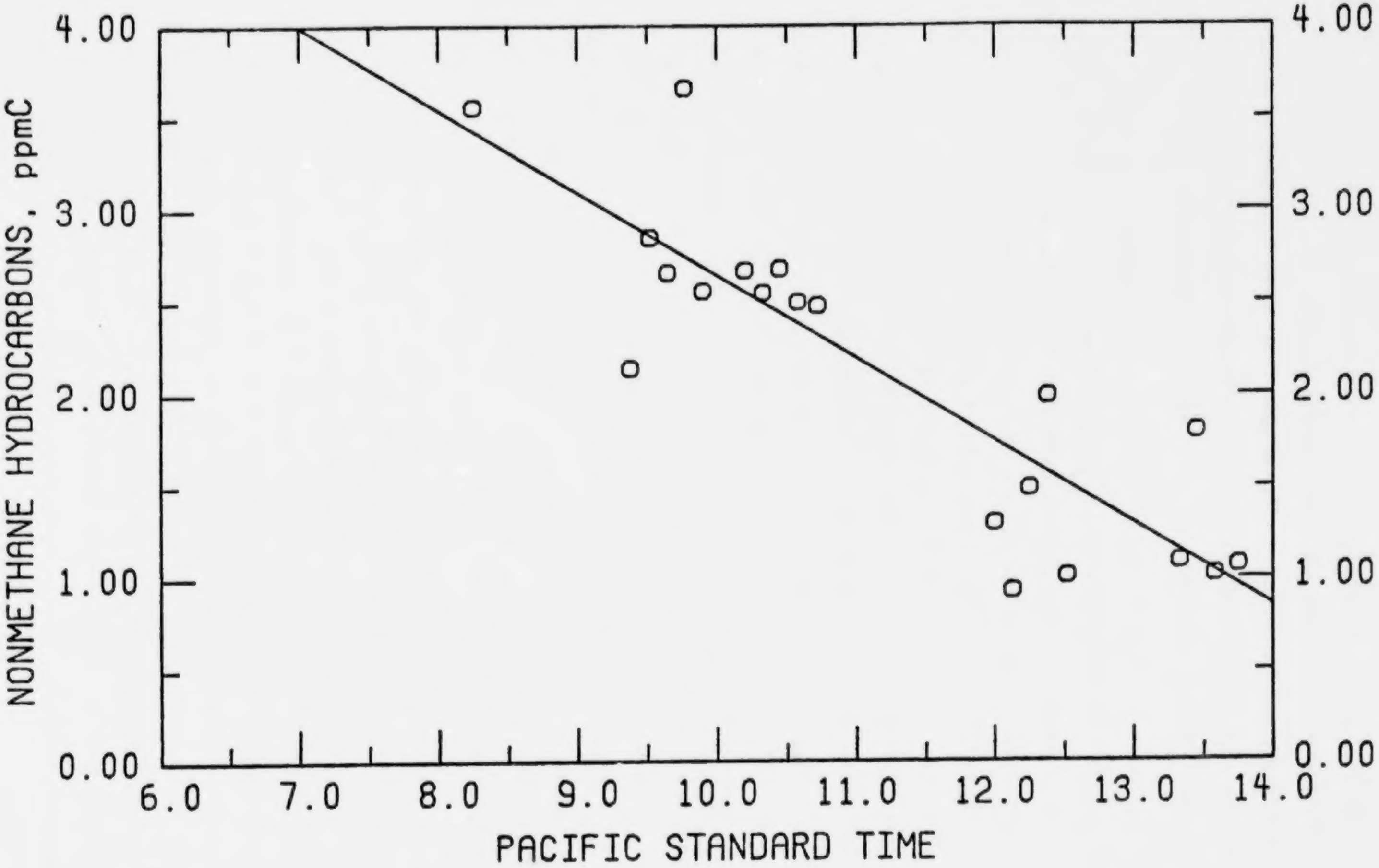

Figure 40. Zero gradient nonmethane hydrocarbon concentrations in the absence of reactions as estimated from source reconciliation results and regression line.

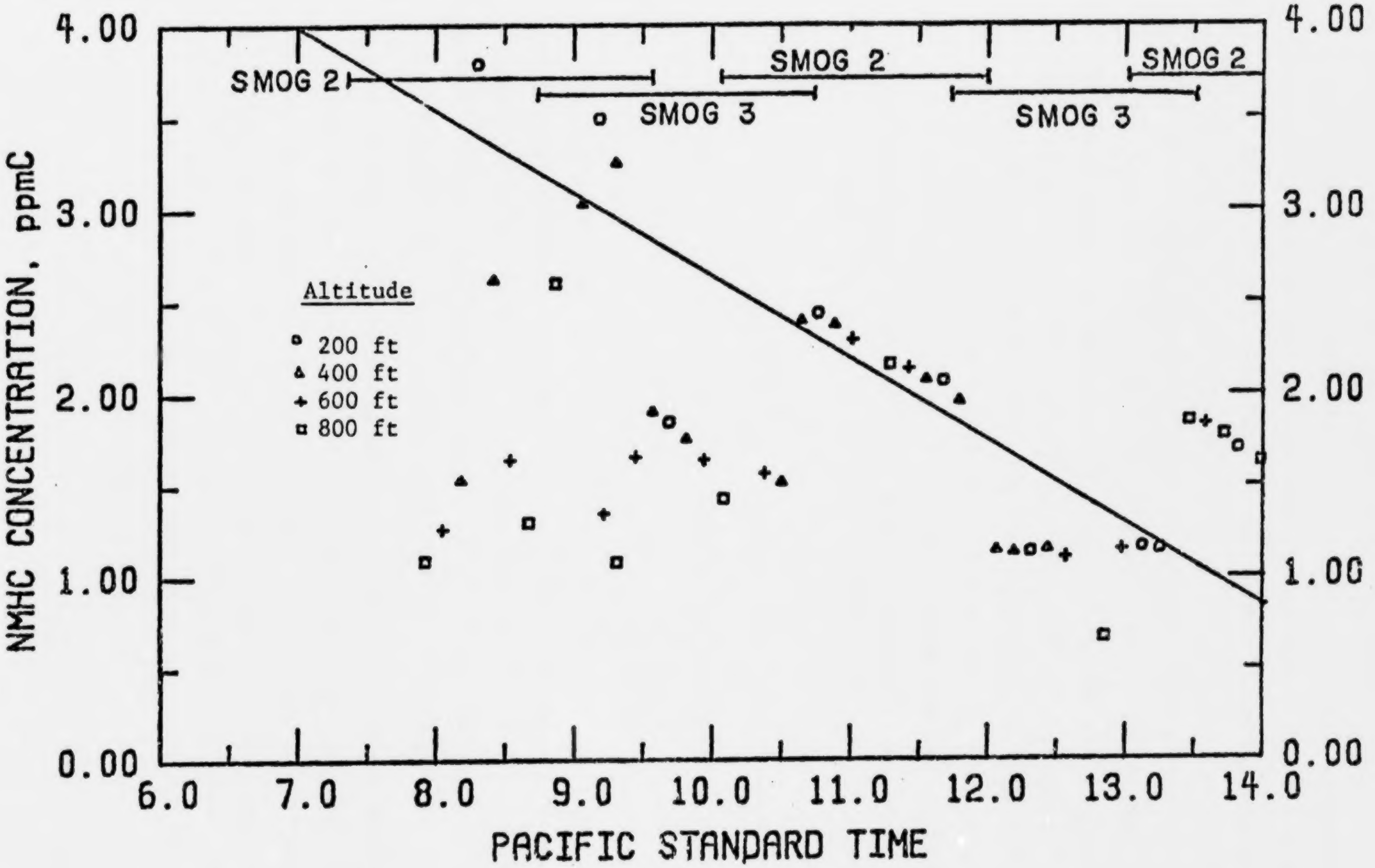

Figure 41. Comparison of nonmethane hydrocarbon. Concentration line from source reconciliation and nonmethane hydrocarbon concentration as measured by environmental chromatograph.

affected, even under laboratory conditions. In the early afternoon, NMHC measurements drop below the source reconciliation values. This is quite understandable since the hydrocarbons in the air are, at this time, undergoing chemical conversion to compounds such as acids, aldehydes, and nitrates which give a lower response per carbon atom in a flame ionization detector. Given the excellent agreement of the two sources of hydrocarbon data, it was decided to use the straight-line approximation of the source reconciliation data as the lower boundary condition in the solution for the NMHC fluxes. The initial conditions were taken from early morning source reconciliation results and the concentration above an altitude of 1000 feet was assumed to be the same as that just below 1000 feet. The initial conditions are shown in Figure 42 with the calculated vertical NMHC concentration profiles for later times. The estimated NMHC fluxes at 150 feet and h/2 are given in Figure 43.

## Specifying Injection and Dilution Rates for Simulation

Now that estimates of nonmethane hydrocarbon fluxes in Equation 1 are available, it is necessary to consider their use in specifying conditions of the simulation. The flux through the bottom and top of the variable-volume reactor does not take into account the extent to which the hydrocarbons have reacted. For instance, material emitted at the ground is in the air for some amount of time before reaching the bottom of the reactor at 150 feet. It is, nevertheless, reacting during this time. Thus, the time available for reaction must be estimated.

The lower limit of the zero-gradient region was specified as 50 m (167 feet) by Panofsky because this is the upper extent of the "surface boundary layer" estimated for the conditions of wind and irradiation on that day. The "surface boundary layer" or simply the "surface layer" is defined as the height through which the wind stress magnitude varies by less than 20 percent. Thus, h', the height of the surface layer is:

$$h' = 2000\ \tau \qquad (11)$$

where $\tau$ is the magnitude of the surface stress in dynes $cm^{-1}$ and h' is in cm. The range of $\tau$ is typically from 1 to 10 dynes $cm^{-2}$, thus h'

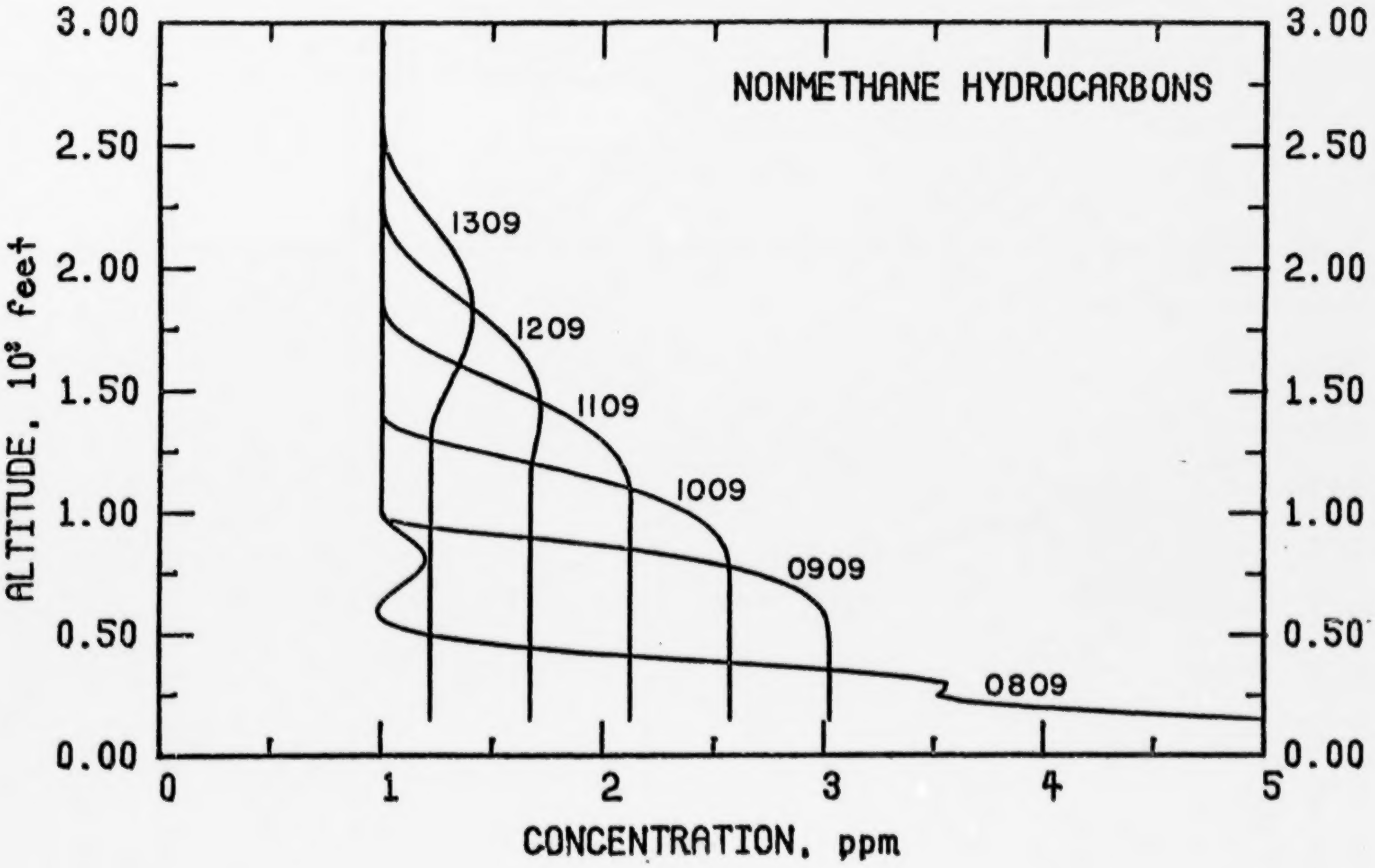

Figure 42. Nonmethane hydrocarbon vertical concentration profiles for Operation 33 at one-hour intervals estimated by numerical solution.

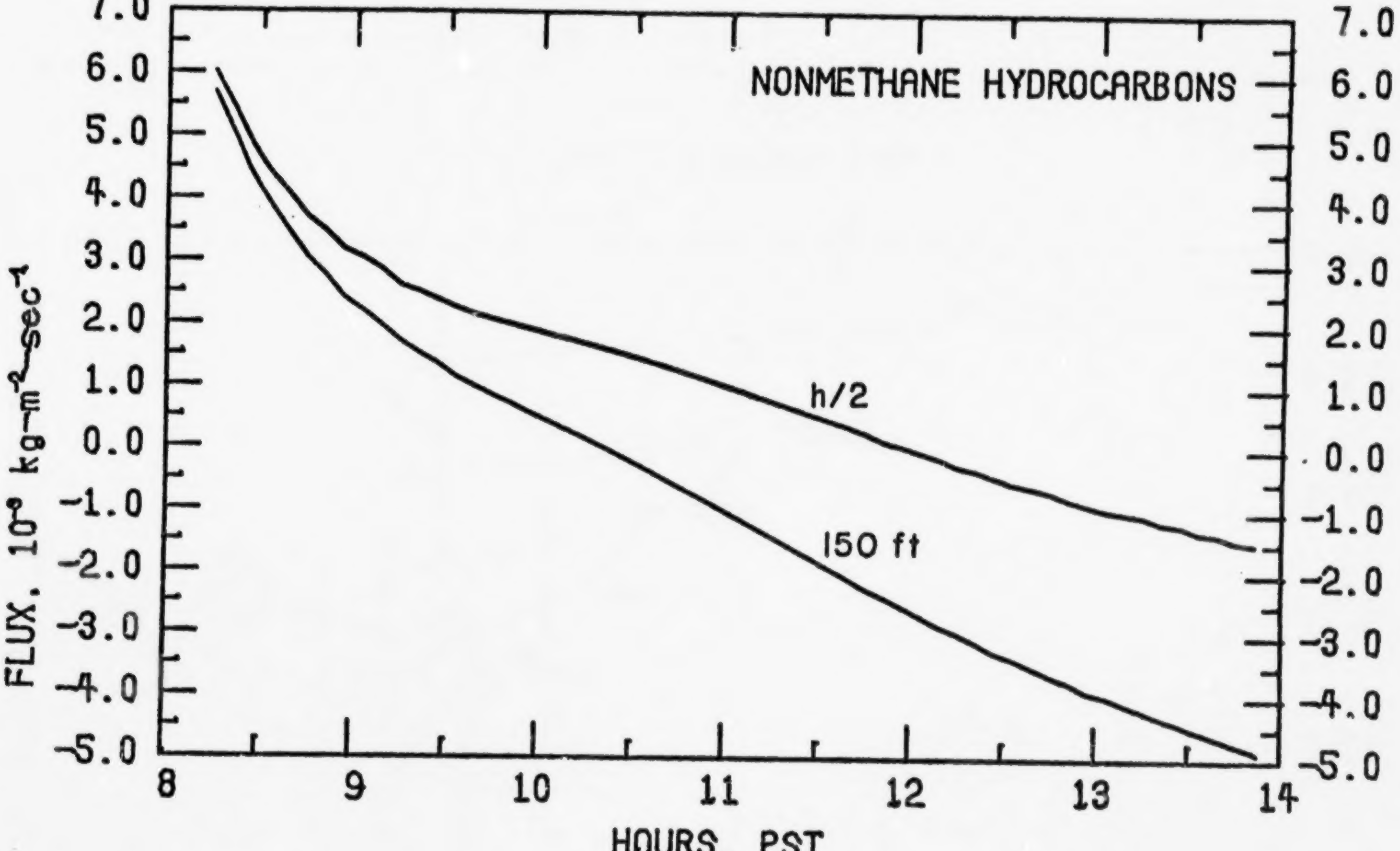

Figure 43. Estimated nonmethane hydrocarbon flux at altitudes of 150 feet and half the mixing depth from numerical solution.

ranges from 20 to 200 m. On a typical clear day, h' calculated from heat flux is about 50 m (Lumley and Panofsky, 1964). A typical value of the exchange coefficient in this region is 100 gm $cm^{-1}sec^{-1}$ for a clear afternoon at 15 m (82). This is equivalent to an eddy diffusivity of about 10 $m^2sec^{-1}$. The average time of transport is then calculated by dividing the eddy diffusivity into the distance squared. Thus, the mean time of transport of hydrocarbon species from the ground to 50 m is 4 to 5 minutes. Thus, the extent of reaction would be quite small even at rates characteristic of the most reactive hydrocarbon species. Earlier in the day, of course, transport to 50 m is not as rapid. Based on Panofsky's (69) calculation of CO flux and the gradient of CO in the lowest portion of the atmosphere, the average time of transport in the early morning (0815-0830 PST) was on the order of 20 minutes. At this time, the concentrations of $O_3$ and OH are probably lower and, thus, the rate of reaction of hydrocarbons are slower as is the rate of transport. Thus, it was concluded that little difficulty would be encountered by assuming that the NMHC flux at 150 feet represents fresh pollutant input.

The vertical hydrocarbon flux at h/2 is assumed to represent removal of material from the control volume with an extent of reaction which is equal to the mean extent of reaction within the zero-gradient region. This may be justified simply by pointing to the absence of pollutant gradients up to this altitude.

The simulation experiment was to be carried out in the UNC outdoor smog chamber which, when operated with continuous injection and dilution, has the characteristics of a nearly ideal continuous-flow, stirred tank reactor (CFSTR). A pollutant mass balance for such a system is the following:

$$\frac{dc}{dt} = I - \frac{cF}{V} \qquad (12)$$

where I is the injection rate in ppm $min^{-1}$, c is the concentration in ppm, f is the flowrate of clean dilution air in $ft^3min^{-1}$ and V is the chamber volume in $ft^3$.

The logic used in equating flux and mixing height terms in Equation 1 to the injection and flowrate terms is outlined in Figure 44. When the flux into the bottom of the control is positive, then the injection rate is based on this value. If the remaining terms in Equation 1 are then less than zero, their combined effect represents loss of material from the control volume. This must be simulated by selecting the proper flowrate of dilution air. Equation 12 may be solved for the concentration at time t, to yield:

$$c_t = \frac{IV}{f} + (c_o - \frac{IV}{f})\, e^{-\frac{f}{V}t} \tag{13}$$

where $c_o$ is the concentration at some initial time and $c_t$ is the concentration at time t. Since I and f are to be evaluated for separate 6 min intervals corresponding to the intervals for which the flux was estimated, the initial time and concentration correspond to the time and zero-gradient region concentration at the beginning of the interval, t equals 6 min, and $c_t$ is the zero-gradient region concentration at the end of the interval. The term I is already known, having been set equal to $F_b/H$. Equation 13 may not be solved algebraically for f, thus an iterative method was employed (Newton-Raphson method).

If $(-F_t/H - \frac{c}{H}\frac{dH}{dt})$ is positive or equal to zero, then it represents a condition in which the negative vertical flux at h/2 is increasing the control volume concentration more rapidly than it is being diminished by the increasing size of the control volume. Under these conditions, f is set to zero, and I is equated to the total rate of change of the zero-gradient region concentration. This situation is never encountered for NMHC calculations since dc/dt is always negative.

If the vertical flux at the bottom of the control volume is negative but dc/dt is positive, I is set equal to dc/dt and f is zero. Again, for NMHC dc/dt is never positive. If $F_b$ and dc/dt are negative, this would seem to represent situations in which ground-based sinks of NMHC exceed ground-based sources. This is probably never the case, but negative estimates of $F_b$ coupled with negative dc/dt could arise when the assumption of no horizontal dispersion is violated. Horizontal

$$\left(\frac{dC}{dt}\right)_{atm} = \frac{F_b}{H} - \frac{F_t}{H} - \frac{C}{H}\frac{dH}{dt}$$

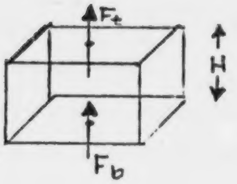

$$\left(\frac{dC}{dt}\right)_{chamber} = I - \frac{Cf}{V}$$

```
IF  $F_b \geq 0$
```

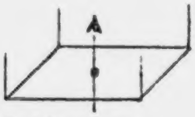

```
    THEN do the following:
            $I = F_b/H$
            IF  $\left(- \frac{F_t}{H} - \frac{C}{H}\frac{dH}{dt}\right) < 0$
```

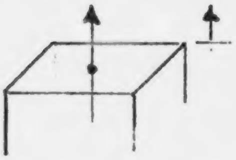

```
                THEN  Solve for f in non-linear expression
                ELSE  do the following:
                        $f = 0$
                        $I = \left(\frac{dC}{dt}\right)_{atm}$
    ELSE  IF  $\left(\frac{dC}{dt}\right)_{atm} \geq 0$
```

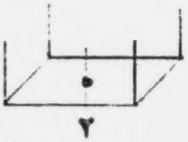

```
                THEN  do the following:
                        $I = \left(\frac{dC}{dt}\right)_{atm}$
                        $f = 0$
```

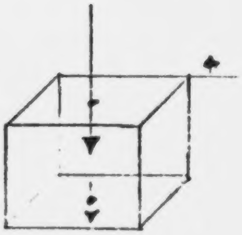

```
                ELSE  do the following:
                        $I = 0$
                        $f = \frac{V \cdot \ln(C_i/C_{i+1})}{\Delta t}$
```

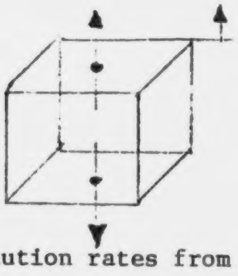

Figure 44. Logic for calculating injection and dilution rates from flux and mixing height estimates.

removal of material from the imaginary reactor volume could lead to negative estimates of $F_b$. This is not a serious concern with respect to simulation since either case is simply treated as removal of material. The value of I is zero and f may be determined directly from the simplified form of Equation 13.

The calculated NMHC injection rates and dilution rates are shown in Figures 45 and 46, and the cumulative injection and cumulative volume are shown in Figures 47 and 48. Having completed the calculations of the required injection and dilution rates, it was then possible to commence the experimental phase of this project.

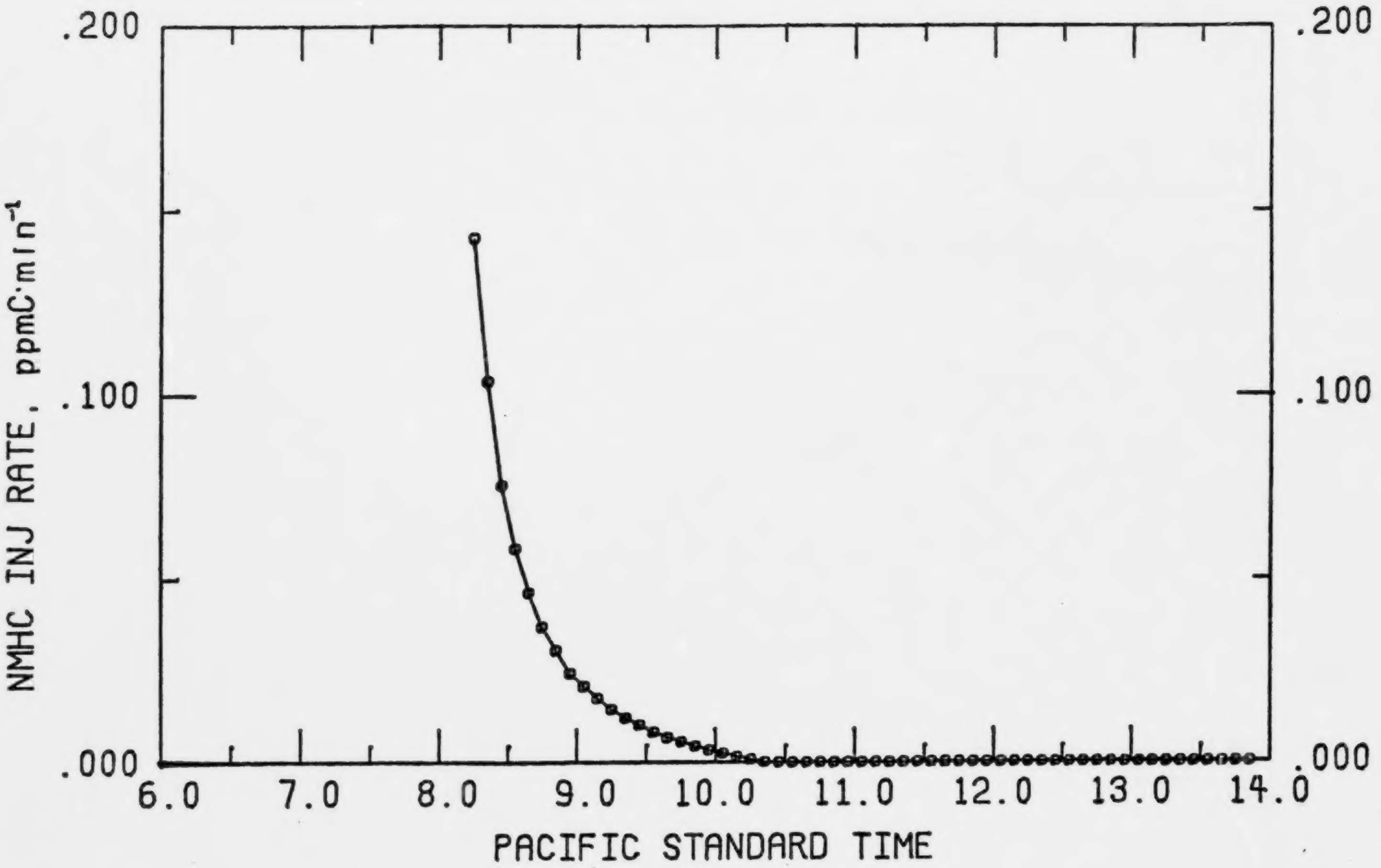

Figure 45. Nonmethane hydrocarbon injection rates for simulation of LARPP Operation 33.

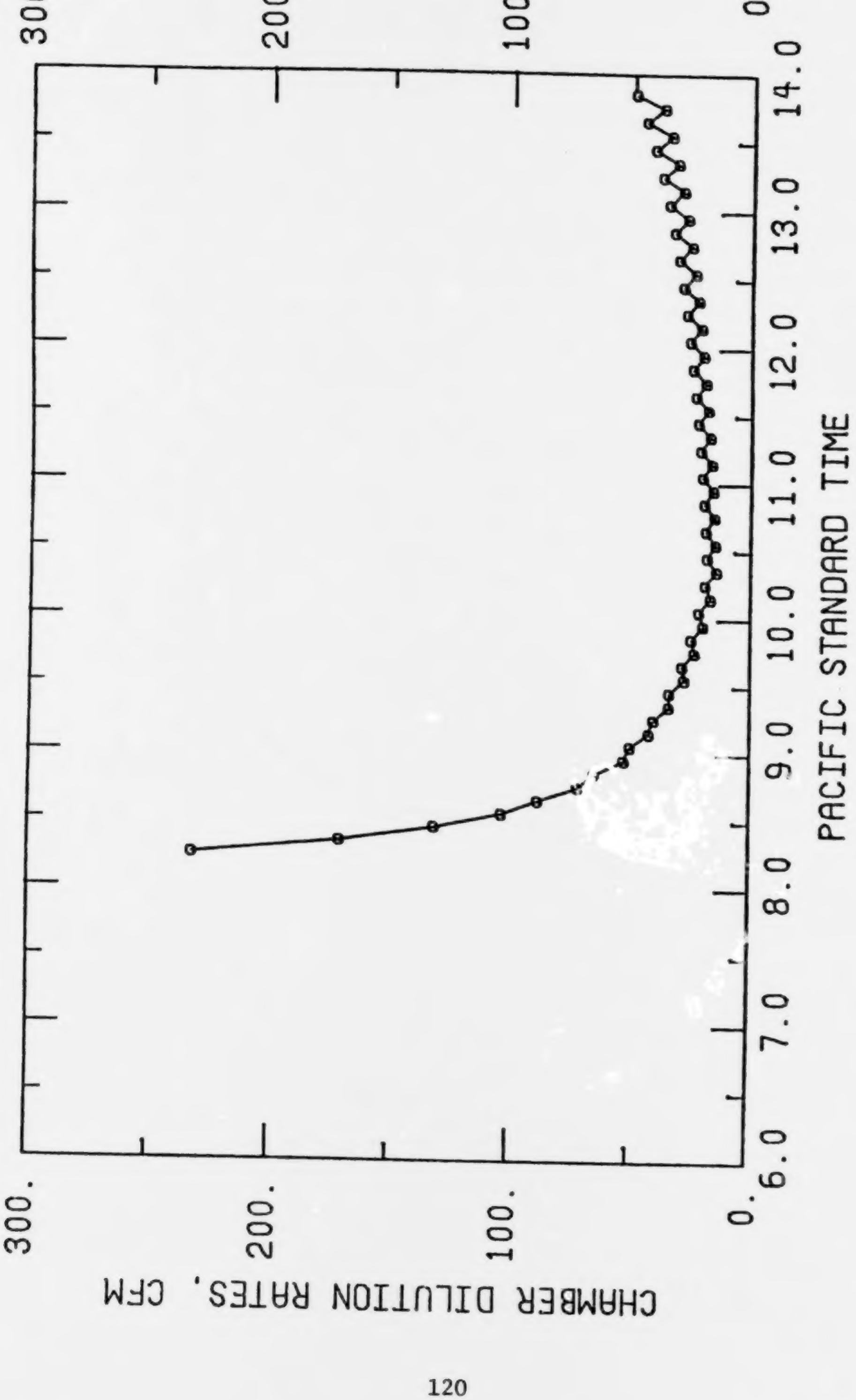

Figure 46. Chamber dilution rates for simulation of LARPP Operation 33.

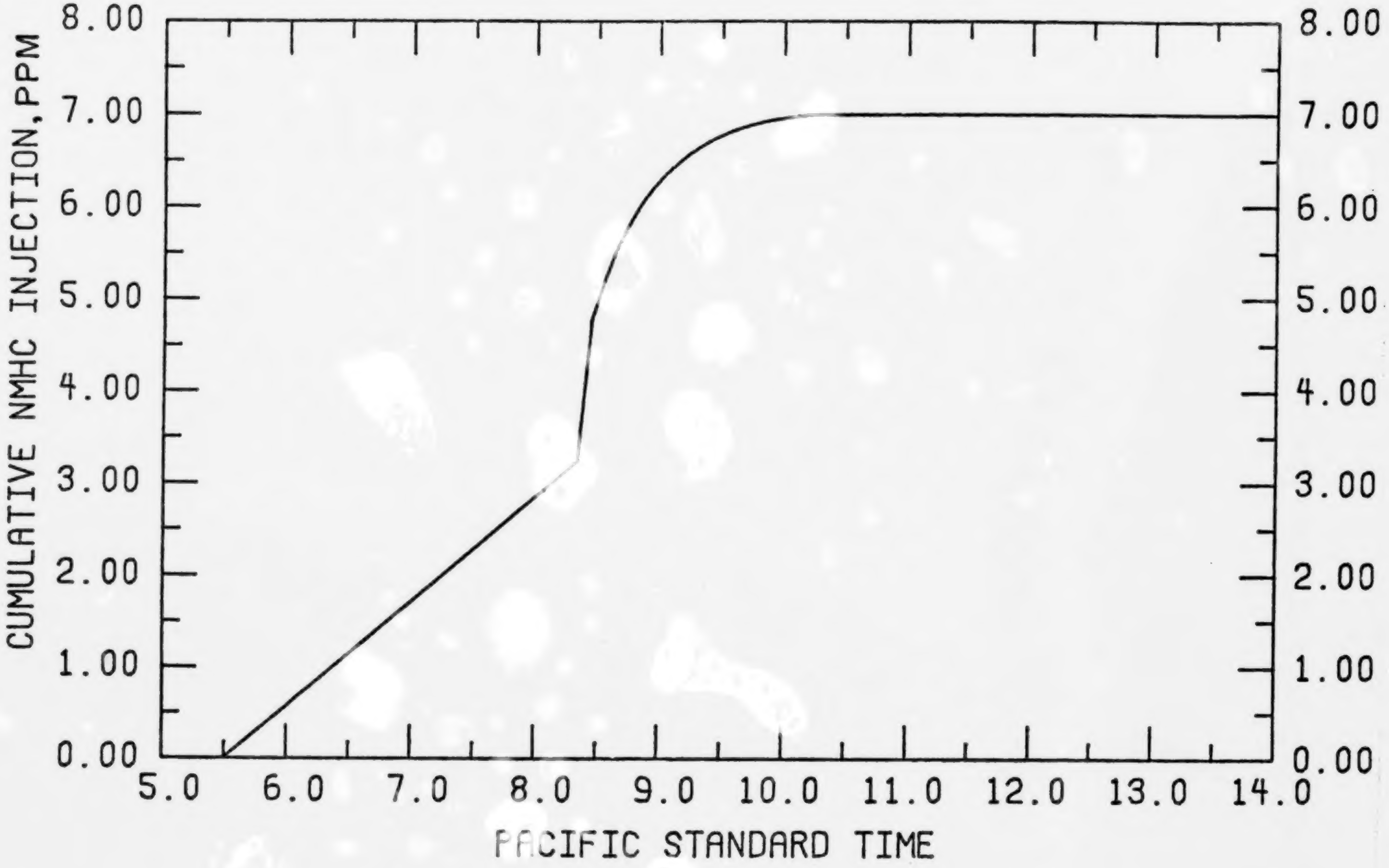

Figure 47. Cumulative nonmethane hydrocarbon injection rates for simulation of LARPP Operation 33.

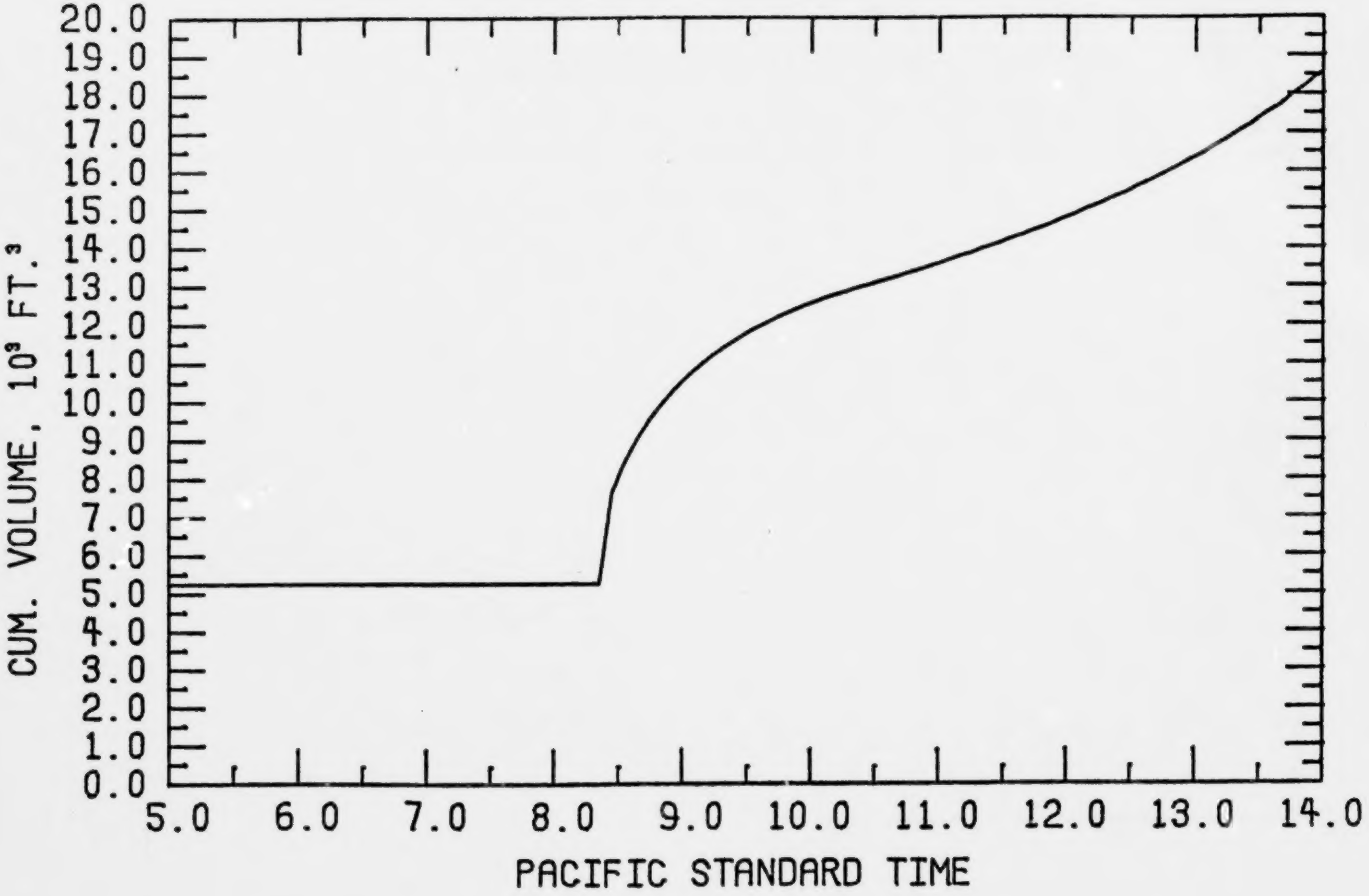

Figure 48. Cumulative dilution volume for simulation of LARPP Operation 33.

# SECTION 6

# EXPERIMENTAL METHODS AND RESULTS

## METHODS

The simulation of LARPP operation 33 was performed in the UNC outdoor smog chamber which has been described by Jeffries, Fox and Kamens (83 and 84). Only a brief discussion of the facility is presented here. The chamber is located in a rural area, 17 miles southwest of Chapel Hill, North Carolina. The background $NO_x$ concentration is less than 0.015 ppm and the nonmethane concentration is less than 0.20 ppmC, thus ambient air is used for chamber experiments. The chamber consists of an external wooden A-frame which supports a covering of 5-mil (FEP) Teflon film. A center panel divides the chamber into two "sides" or "halves;" each side has a volume of 148 $m^3$ (5230 $ft^3$).

### Measurement

The instrumentation used for the simulation experiments include the following:

1. Carle automated gas chromatograph (FID);
2. Bendix NO - $NO_x$;
3. Bendix ozone;
4. Cambridge dew point hygrometer;
5. Eppley total solar pyranometer;
6. Eppley UV radiation pyranometer;
7. Continuous chemical actinometric measurement of the photolysis rate of $NO_3$ (85).

Data from these instruments, except the gas chromatograph, are collected by a computer-based data acquisition system. This computer also performs much of the experimental control functions required for complex simulations.

The NO and $NO_x$ channels of the NO-$NO_x$ analyzer were calibrated against a known concentration of NO and the $NO_2$ channel was calibrated by gas phase titration. The high concentration NO stream was diluted down to 0.7 to 0.8 ppm in air dynamically. Laboratory air was drawn through an $O_3$ generator at a moderate setting so that traces of NO in the air would be converted to $NO_2$. The air was then passed through a Purafil bed to remove $NO_2$ and $O_3$. The instrument was then zeroed. The flowrate at the outlet of the Purafil was measured with a 448 cc soap bubble flowmeter and the flow delivered from the NO bottle through a stainless steel needle valve was measured with a 50 cc soap bubble flowmeter. Both these streams were then blended in a Pyrex mixing bulb. The $NO_x$ concentration was monitored on the outlet of the bulb. The NO concentration in the tank used agreed with those measured in two other tanks from different manufacturers within 3 percent.

After the NO and $NO_x$ channel outputs on the digital voltmeter were adjusted to match the calculated value, the $O_3$ production was cut off, the Purafil trap removed, and the flow through the $O_3$ generator measured again (since it is greater with the Purafil removed). The $NO_2$ and NO were then measured at a new, slightly lower value. The $O_3$ generator was set to deliver roughly 0.4 to 0.5 ppm of $O_3$. After allowing several minutes for the system to reach steady-state, the $NO_2$ channel output was adjusted to equal the NO decrease.

The $O_3$ was then measured at the outlet of the mixing bulb. With the NO flow turned off the increase in ozone was used to check the span of the $O_3$ instrument. While the $NO_x$ instrument required calibration about once each week during the experimental period, the $O_3$ instrument was extremely stable and required no adjustment other than occasionally setting the ethylene flow.

## Hydrocarbon Measurements

Hydrocarbons were measured with an automated Carle gas chromatograph with a flame ionization detector (85). The column switching and bypassing valves are controlled by an electromechanical valve minder. Using a 15 min cycle time, it was possible to separate the $C_1$ through $C_8$ alkanes, and the $C_2$ through $C_5$ alkenes in the mix. The instrument uses three columns: (1) 6' x 1/8" 5% Carbowax 1540 and 5% Apeizon L on Supelcoport 80/100 mesh; (2) 6' x 1/8" N-octane/Poracil C 100/120 mesh and 2' x 1/8" 20% Apeizon L on Supelcoport 80/100 mesh; (3) 2' x 1/8" FL alumina treated with 5% NaCl. Column 1 separates $C_6$-$C_8$ paraffins, olefins and aromatics; column 2 separates $C_4$ and $C_5$ olefins and some $C_6$ paraffins; and column 3 separates $C_1$-$C_3$.

During the experimental period, total mix concentrations were measured based on two complete calibrations performed on August 24, 1976. Two samples of diluted hydrocarbon mix were introduced into the chromatograph and the instrument response was recorded on a stripchart recorder at a chart speed of 2 in. per min. A sample from a tank containing 3.00 ppmC of propylene was also sampled. The recorded peaks were Xeroxed, cut out, and weighed. The areas were then calculated correcting for paper density. Using the ratio between the propylene concentration and peak area, it was possible to determine the total concentration in the dilute mix sample and the relative concentrations of all species resolved in the chromatogram. For rapid calculation during an experiment, the height of the n-pentane peak, the largest peak in the hydrocarbon mix chromatogram, was used as a measure of the amount of mix injected in the morning. On August 24, the ratio of mix concentration to n-pentane peak height was 0.311 ppmC/inch. To use this relationship on other days, it is necessary to correct for variation in instrument response per molecule of carbon input due to changing carrier gas flow, electronic drift, etc. This was done by measuring a known concentration of propylene early in each run. The mix concentration, x, was then calculated as the height of the n-pentane peak, P, times 0.622 ppmC/inch times the ratio of the height of the propylene cal gas peak on August 24 to the height of the propylene cal gas peak on the day of the experiment, H. Thus,

$$X,\ \text{ppmC} = (P,\ \text{in})\ (0.622\ \frac{\text{ppmC}}{\text{in}})\ (\frac{4.18\ \text{in}}{H,\ \text{in}}) \tag{14}$$

given that the propylene calibration peak was measured on the X8 scale and the n-pentane peak was measured on the X2 scale. Combining the constants:

$$X = P\ (\frac{2.60}{H})\ . \tag{15}$$

This relationship was used for all the LARPP experiments. Similar relationships derived for the isopentane and ethylene from August 24 data were used to check the calculations. Agreement between the n-pentane, isopentane, and ethylene calculations was excellent indicating that the mix composition did not change during the experimental period (at least with respect to these three compounds).

Data collected on October 4 and 6, 1976 were analyzed after the experimental work was completed. These data agree well with one another and yield the relationship

$$X = P\ (\frac{2.72}{H})\ . \tag{16}$$

This latter value yields closer agreement in predicting the height of peaks of individual mix constituents. Thus, it was used to recalculate the quantities of mix injected during the simulations.

## Injections

Pollutants were injected into the chamber sides via the return side of the glass sampling manifolds. These manifolds remove air from points near the center of the chamber halves and return the unused portion to the chambers just under a mixing fan. The flow is in excess of 60 lpm. The return manifolds passing through the injection house are fitted with SVL connectors through which the injections are made.

Pollutants are kept in gas cylinders at high concentration and delivered to the injection system through two-stage, stainless steel regulators. The injection system consists of on-off solenoid valves, followed by either capillary flow restrictors or precision needle valves with vernier handles. In the hydrocarbon and NO injection systems, either of two needle valves may be selected by a manual three way valve. By setting these two valves at greatly different flow rates, and making use of the computer to turn the solenoid on and off, it was possible to produce a wide range of injection rates. The tank concentrations, flowrates, and maximum injection rates are shown in Table 11.

TABLE 11. POLLUTANT INJECTION DATA

| Pollutant | Tank Concentration (ppm) | Flow Setting, lpm | Chamber Injection Rate, ppm/min |
|---|---|---|---|
| HC mix | 5920 ppmC | 10 | 0.4 ppmC/min |
| | | 1 | 0.04 ppmC/min |
| NO | 9127 | 6 | 0.37 |
| | | 0.3 | 0.018 |
| $NO_2$ | 2664 | 10 | 0.18 |
| acetaldehyde | 2200 ppmC | 2.96 | 0.044 ppmC/min |
| | | 0.30 | 0.0044 ppmC/min |

The hydrocarbon mixture used in these simulations is nearly the same as the mixtures employed in the UNC chamber for other experiments (83). The exact composition is given in Table 12.

The injection flowrates greater than 1 liter per minute (lpm) were set and routinely checked with a Matheson 10-lpm mass flowmeter. The mass flowmeter was calibrated against a 2-liter soap bubble flowmeter. The soap bubble flowmeter had been carefully compared against a spirometer, and its volume measured using a volumetric flask and a burette. Occasionally the soap bubble flowmeter was also used directly. The flowrates from 0.1 lpm to 1 lpm were measured with both a 1-lpm mass flowmeter and a 48-ml soap bubble flowmeter. An initial comparison of these two meters (considering barometric pressure, gas temperature, and

TABLE 12. HYDROCARBON MIX COMPOSITION
CONCENTRATION OF COMPOUND, ppmC

| Compound | Manufacturer's Analysis | Aug. 24, 1976* | Oct. 8, 1976 |
|---|---|---|---|
| 2-methyl pentane | 690 | 494 | 491 |
| 2,4-dimethyl pentane | 504 | 481 | 623 |
| 2,2,4-trimethyl pentane | 712 | 636 | 663 |
| ethylene | 736 | 738 | 568 |
| 1-butene | 164 | 147 | 180 |
| Cis-2-butene | 168 | 193 | 241 |
| isopentane | 725 | 807 | 805 |
| n-pentane | 1230 | 1428 | 1405 |
| 2-methyl-1-butene | 285 | 128 | 147 |
| 2-methyl-2-butene | 185 | 134 | 122 |
| propylene | 303 | 731 | 701 |
| acetylene | 492 | | |
| total | 6194 | | 4920 |

*Based on total tank concentration of October 8, 1976, and relative component concentrations of August 24, 1976.

pressure at critical points in the system, and evaporation of water from the soap bubble solution) revealed that the factory calibration of the mass flowmeter was 10 percent low and the appropriate adjustment was made. The lower acetaldehyde flowrate was set using a 50-ml soap bubble flowmeter. Once set, these flowrates varied very little. Temperature fluctuations of the injection house were reduced by a small, thermostatically controlled, electric heater. This was necessary for some of the experiments in October because of the large diurnal temperature ranges at this time of year.

### Dilution

The dilution and exhaust systems are shown schematically in Figure 49. Prior to most experiments both sides of chamber were exhausted for six to eight hours. Ambient air was drawn down the intake stacks from an altitude of about 25 feet above the ground. It entered the

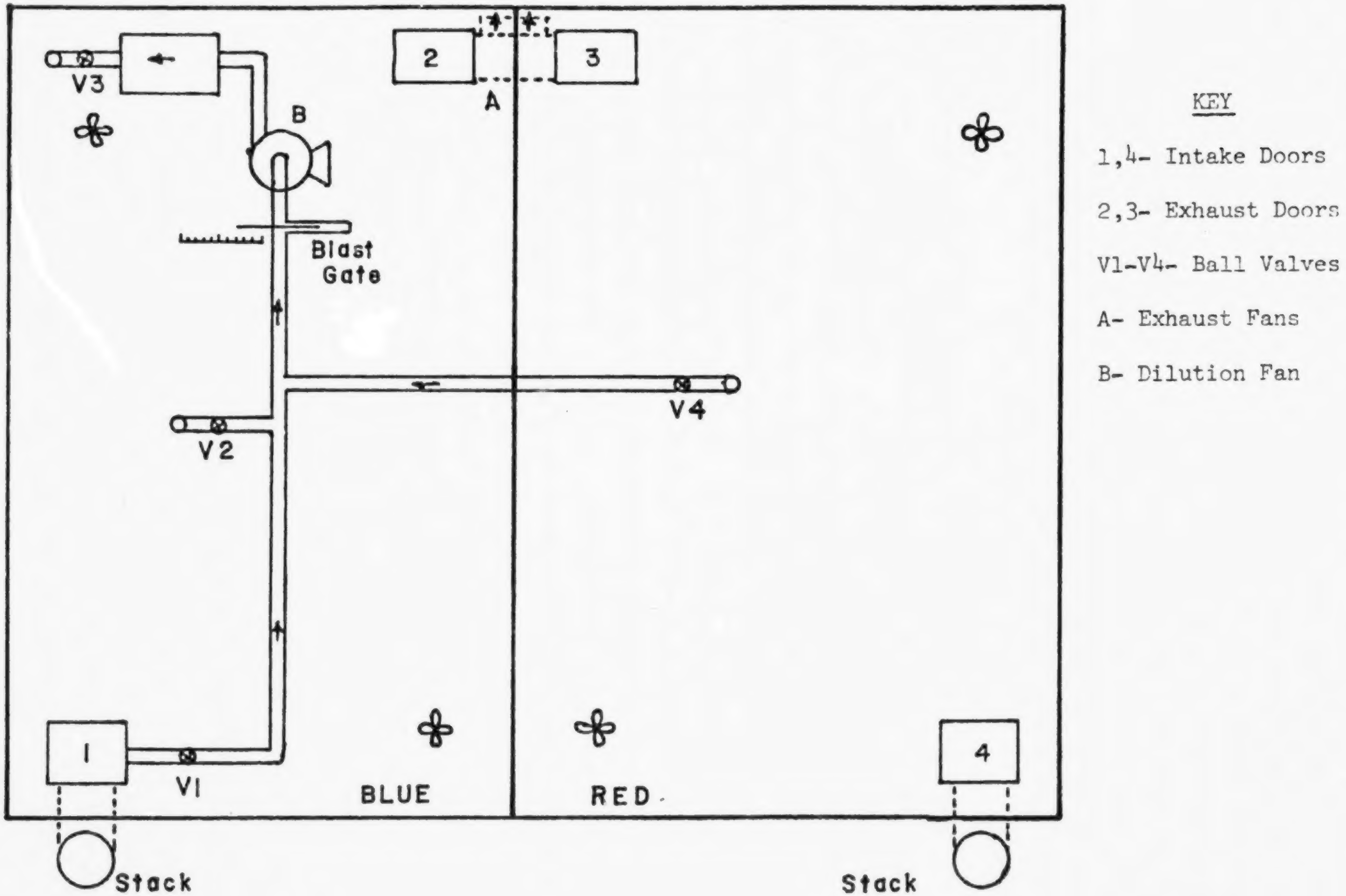

Figure 49. Schematic diagram of UNC outdoor smog chamber dilution and exhaust system.

chamber halves via intake doors 1 and 4 and was drawn out by exhaust blower A through exhaust doors 2 and 3. The chamber halves are mixed by Teflon-coated impellers mounted on Teflon-coated, vertical shafts. When dilution was required in the blue side for the simulations, door 1 and valves 2 and 4 were closed; door 2 and valves 1 and 3 were open. Fab B pulled air from the intake stack and blew it into the chamber, forcing an equal quantity of air out the exhaust door. The dilution flowrate was controlled by a blastgate upstream of the fan which was manually adjusted every 6 min during the portion of the experiments requiring dilution.

The blast gate was calibrated by measuring duct velocities in four-point horizontal and vertical traverses of the 5-in. diameter duct at various blast gate settings. Points in the traverse were selected as representative of two concentric, equal-area zones (87). Measurements were performed with a hot-wire aenomometer, at a point in the duct about 4 duct diameters upstream of the blast gate and over 10 duct diameters downstream of the branch coming from valve 4. The range of flows investigated ran from 23 CFM, when the blast gate was completely closed, to 210 CFM, corresponding to the highest velocity measurable with the hot-wire aenomometer. Above 30 CFM, the blast gate flow control is not very sensitive, i.e., small changes in the blast gate setting result in large changes in flowrate. Thus, a great deal of care was exercised in positioning the blast gate. It was found that even at flows near 200 CFM the suction just upstream of the blast gate was 0.2 to 0.3 in of water, regardless of upstream valve configuration so long as some flow pathway remained open from outside the chamber. Thus, the blast gate calibration is valid whether simply drawing in outside air or diluting with material from the red chamber (as in the final simulation experiment).

## Experimental Procedures for Simulations

Because it was possible to estimate dilution and emission along the LARPP trajectory for the period from 0815 PST to 1400 PST only, it was necessary to bring the concentrations of precursors in the chamber at 0815 up to those observed in the zero-gradient region in operation 33 at 0815. Two techniques were employed for this purpose. In the earlier experiments, "slug" injections were made before sunrise so that concentrations of precursors were immediately brought up to their 0815 levels. In the latter runs, precursors were "ramped" into the chamber, that is, injected at a constant, slower rate so that the proper concentrations will be reached by 0815. This last technique is a more realistic, although quite simplified, representation of emissions in Los Angeles (23). Prior to 0815, the chamber contents were not diluted.

After 0815 PST, both injection and dilution proceeded at the rates determined from the LARPP data for the zero-gradient region. After 1400 PST, the reactions were allowed to proceed without additional injection or dilution.

Preparation for a typical simulation experiment began the night before the experiment was to take place. At this time, the computer was set up for the data collection and control functions which were to be performed, and the facility check out procedure was followed. The computer is set up by running the data collection program and reading in command files. Command files contain information about all the automatic control functions to be performed. Some commands specify action that is to occur once each time the command is given, while others specify a repeating sequence of actions which are to occur until the command is cancelled by another command, or until repeated the specified number of times, Thus, the command files contain a list of commands, each command specifies some of the following items: the action to be taken, the priority of the command relative to other commands, the specific computer channel on which the command is to be performed, cycle time, "on" time during cycle, and computer time at which command should be performed or initiated. In addition to action commands, there are commands for saving a text string entered from the keyboard in a comment file, altering the value of constants used in converting voltage to physical units terminating the program and altering the computer software clock.

The following functions were under computer control during a typical simulation run:

1. Purge of chamber;
2. Shut off exhaust blower and close doors;
3. Commencement of scanning data channels, digitizing and storing data on the disk;
4. Start up of automated GC and strip charts;
5. Slug or ramp injection of pollutants prior to 0815 in the morning to establish initial concentrations;
6. After 0815, control variable rate, profile injection;
7. At the end of the experiment, open doors, exhaust chamber;
8. Turn off GC and strip charts;
9. Terminate program.

The following functions were controlled manually:

1. Unplugging red exhaust door and opening blue exhaust door;
2. Blast gate setting and turning dilution blower on and off;
3. Switching from large flowrate injection needle valve to small flowrate valve at the proper time;
4. Calibrating GC;
5. Resynchronizing exhaust doors after the dilution was no longer required;
6. Entering command files into computer at the proper time.

Two people were required to perform a simulation principally because changing dilution settings consumed most of one person's time. The sixth manual task above was eliminated in the later experiments because the addition of more core enabled storage of all command files at once.

## RESULTS

During the period September 1, 1976 through October 16, 1976, 10 simulation experiments were performed. Conditions of these runs are given on pages 134-169. In all but one of the experiments, the blue side was operated in a dynamic mode to reproduce the processes of emission and dilution along the trajectory, while the red side was operated in the static mode (as a batch reactor). In run number 9, both sides were static in an attempt to determine what initial hydrocarbon concentration would produce $O_3$ equal to that observed on the LARPP trajectory at the same initial $HC/NO_x$ ratio as LARPP. In the first eight static runs, attempts were made to produce initial concentrations of precursors equivalent to the total moles injected in the dynamic chamber during the day divided by the total volume into which these injections were made (chamber volume plus total dilution volume). The results of these experiments are shown in Figures 50 through 75. The results from each day are preceded by a summary of experimental conditions.

### $NO_2$ Injection

In the earlier experiments, hydrocarbon mix, NO, and $NO_2$ were injected early in the day and later in the simulation, the injection consisted of hydrocarbons and NO only. In order to match the LARPP NO and $NO_2$ profiles, it was necessary to modify this approach. The desired initial $NO_2$ was raised from 20 percent to 40 percent of the total $NO_x$ injected after the second run. Beginning with run number 7 it was decided to add 35 percent $NO_2$ during the profile portion of the run as well as the 40 percent initial $NO_2$ injection. There are two justifications for this increased proportion of $NO_2$: (1) the uncertainty of the extent of oxidation of NO that occurs in auto exhaust just after emission, and (2) the conversion of NO to $NO_2$ by the $O_3$ above the inversion base in the LARPP operation.

Nitrogen oxides have presented considerable problems in the modeling of photochemical smog in the atmosphere. Eschenroeder and Martinez (23) observed that the ratios of acetylene and carbon monoxide to $NO_x$ were nearly always higher than the ratios based on these components in auto

Run #1 -- September 1, 1976

Time: EDT

Blue Chamber: slug injections 0530 - 0600 EDT

initial concentrations:

HC - 2.89 ppmC

$NO_x$ - 0.56 ppm

$NO_2$ - 20%

Simulation profile injection and dilution began at 0815 EDT.

All $NO_x$ was NO.

Manual switch from high to low value for NO injection was not made soon enough. NO shot up to 1.44 ppm. Thus, simulation was cancelled.

Red Chamber: slug injections 0530 - 0600 EDT

Static all day

initial concentrations:

HC - 2.96 ppmC

$NO_x$ - 0.56 ppm

$NO_2$ - 20%

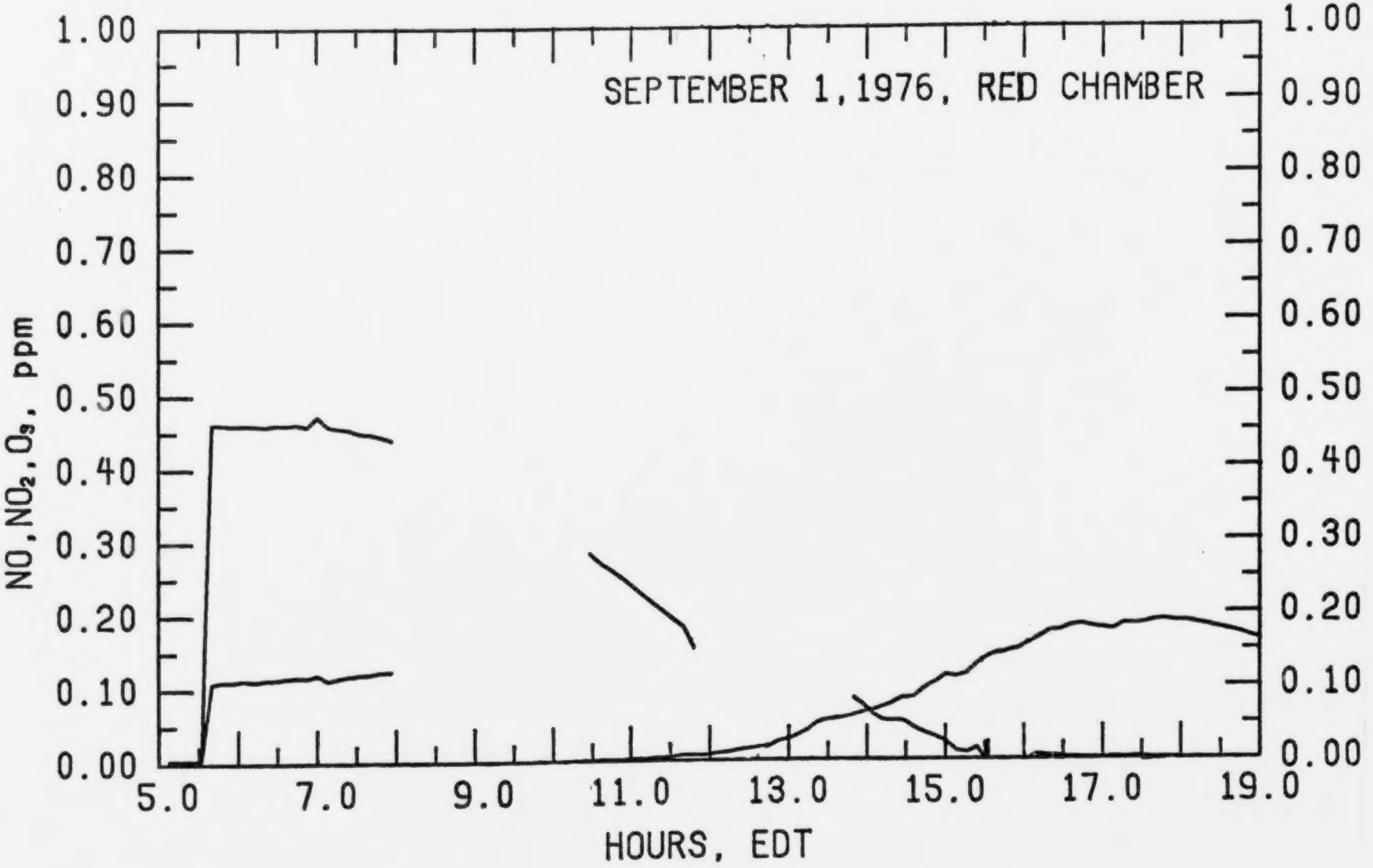

Figure 50. NO, $NO_2$, and $O_3$ profiles from static experiment of September 1, 1976.

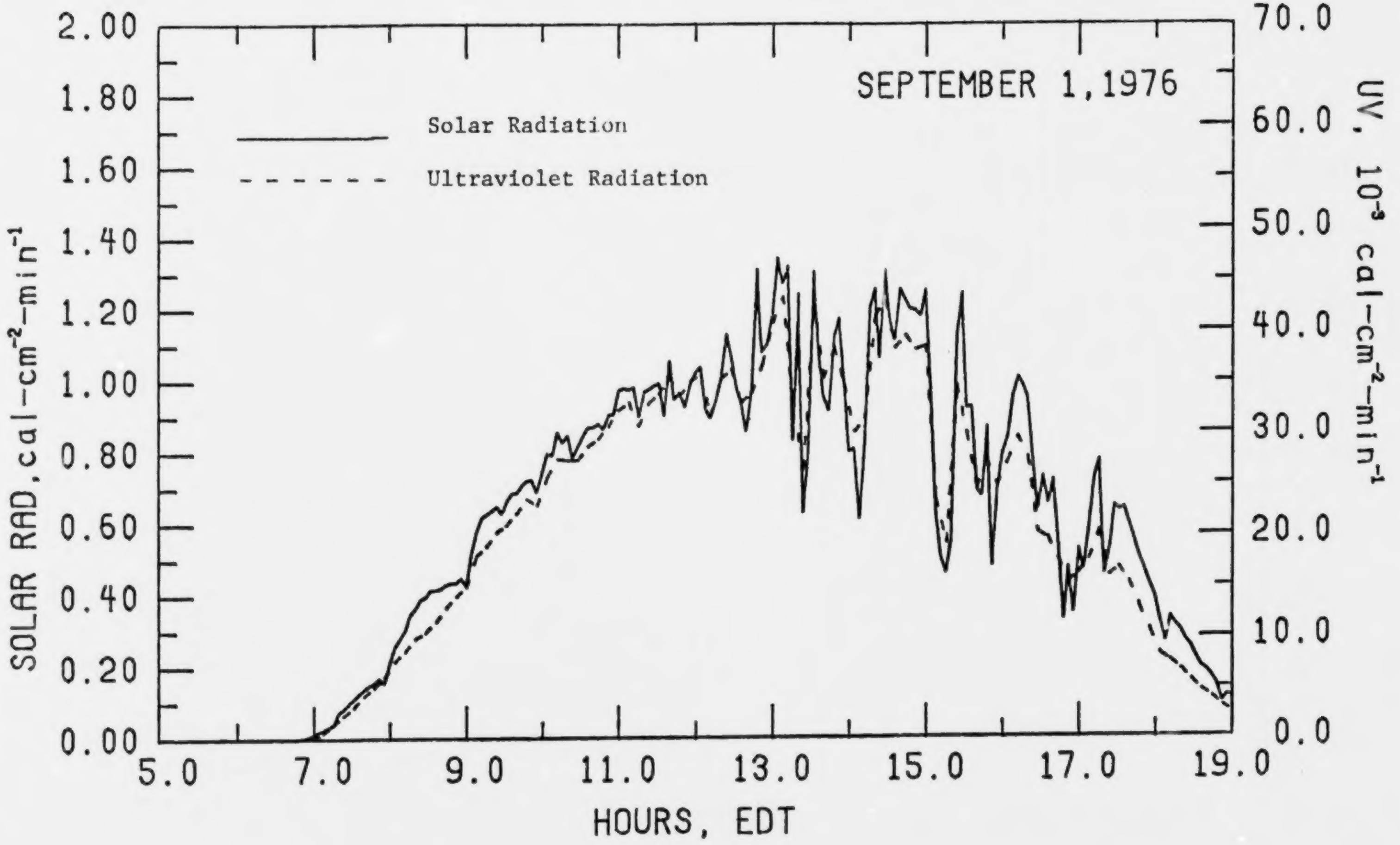

Figure 51. Solar radiation and ultraviolet radiation for September 1, 1976.

Run #2 -- September 6, 1976

Time: EDT

Weather: Sky had been clear in the east very early in morning. By 0930 EDT, it was almost totally overcast and remained mostly cloudy until noon.

Blue Chamber: slug injections 0530 - 0600 EDT

initial conditions:

HC - 3.55 ppmC

$NO_x$ - 0.598 ppm

$NO_2$ - 29%

Simulation profile injection and dilution began at 0815 EDT. All $NO_x$ input as NO during dynamic portion of run.

Ozone max of only 0.045 ppm occurred rather late (1538 EDT) and was light limited. This was partially the result of morning cloudiness.

Red Chamber: slug injections 0530 - 0600 EDT

initial conditions:

HC - 3.90 ppmC

$NO_x$ - 0.531 ppm

$NO_2$ - 28%

The static side, while initial NO oxidation was slow, eventually got going. Reached $O_3$ max of 0.327 at 1458 EDT -- about twice the $O_3$ produced in the LARPP run.

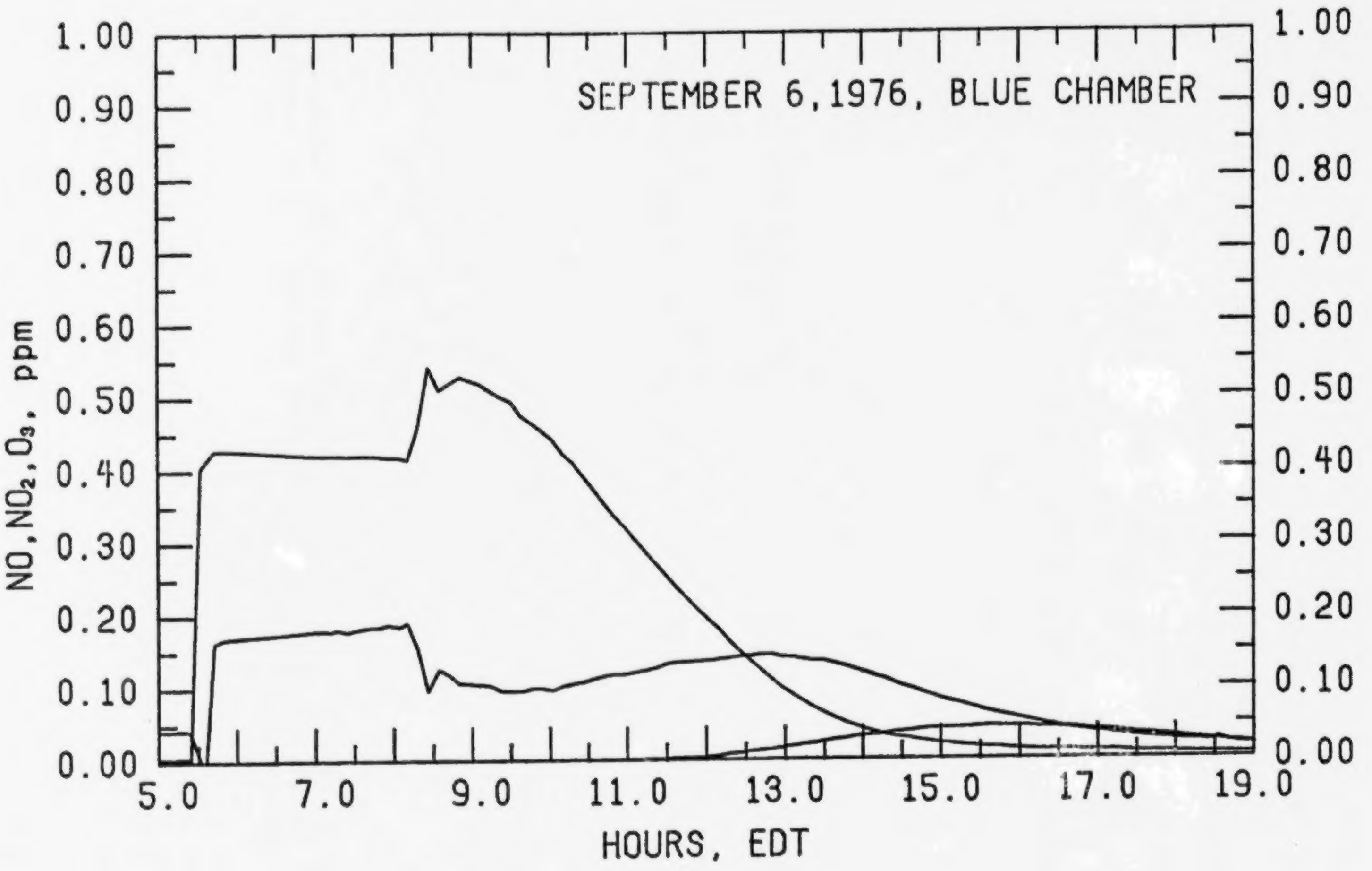

Figure 52. NO, $NO_2$, and $O_3$ profiles from simulation experiment of September 6, 1976.

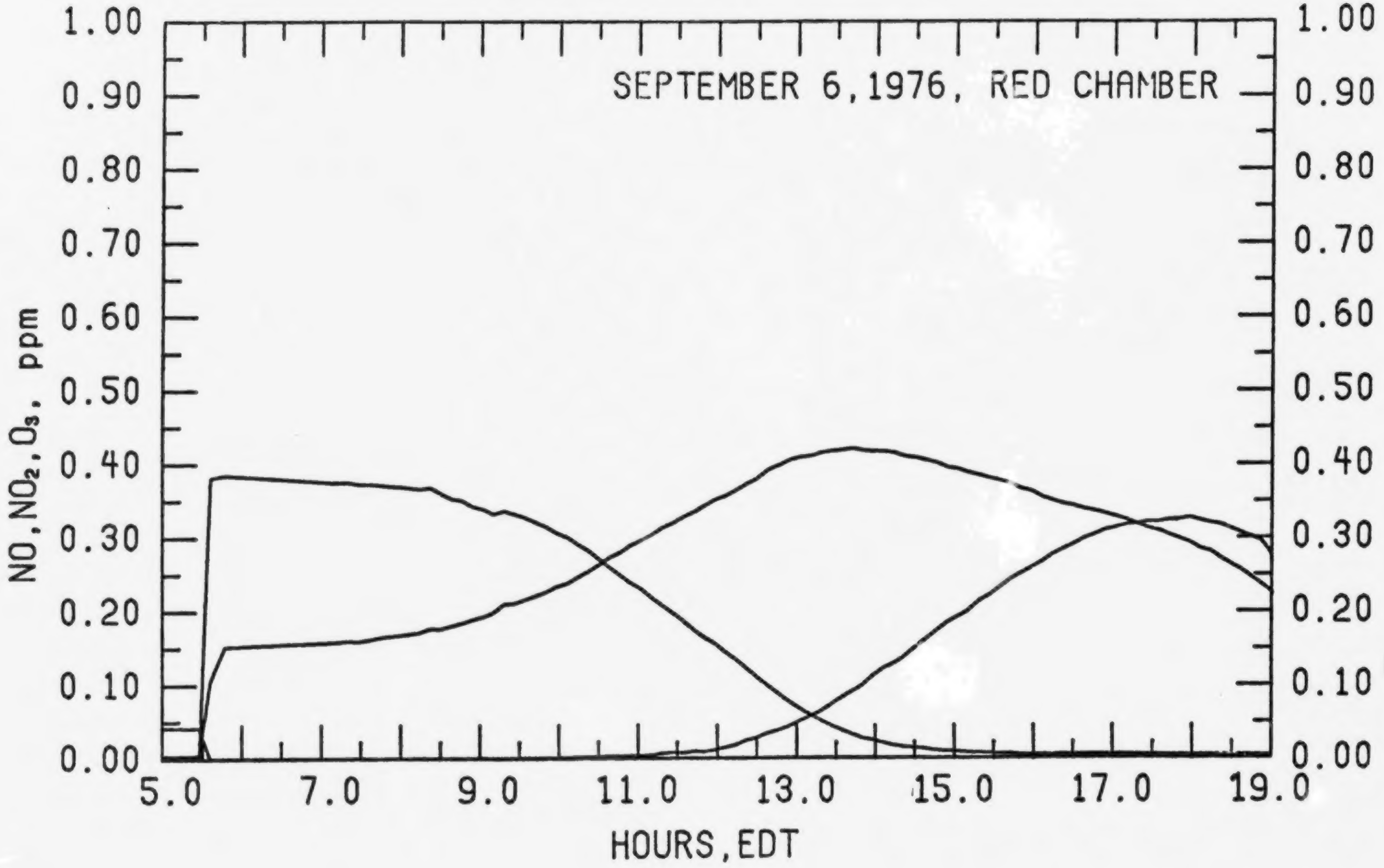

Figure 53. NO, $NO_2$, and $O_3$ profiles from static experiment of September 6, 1976.

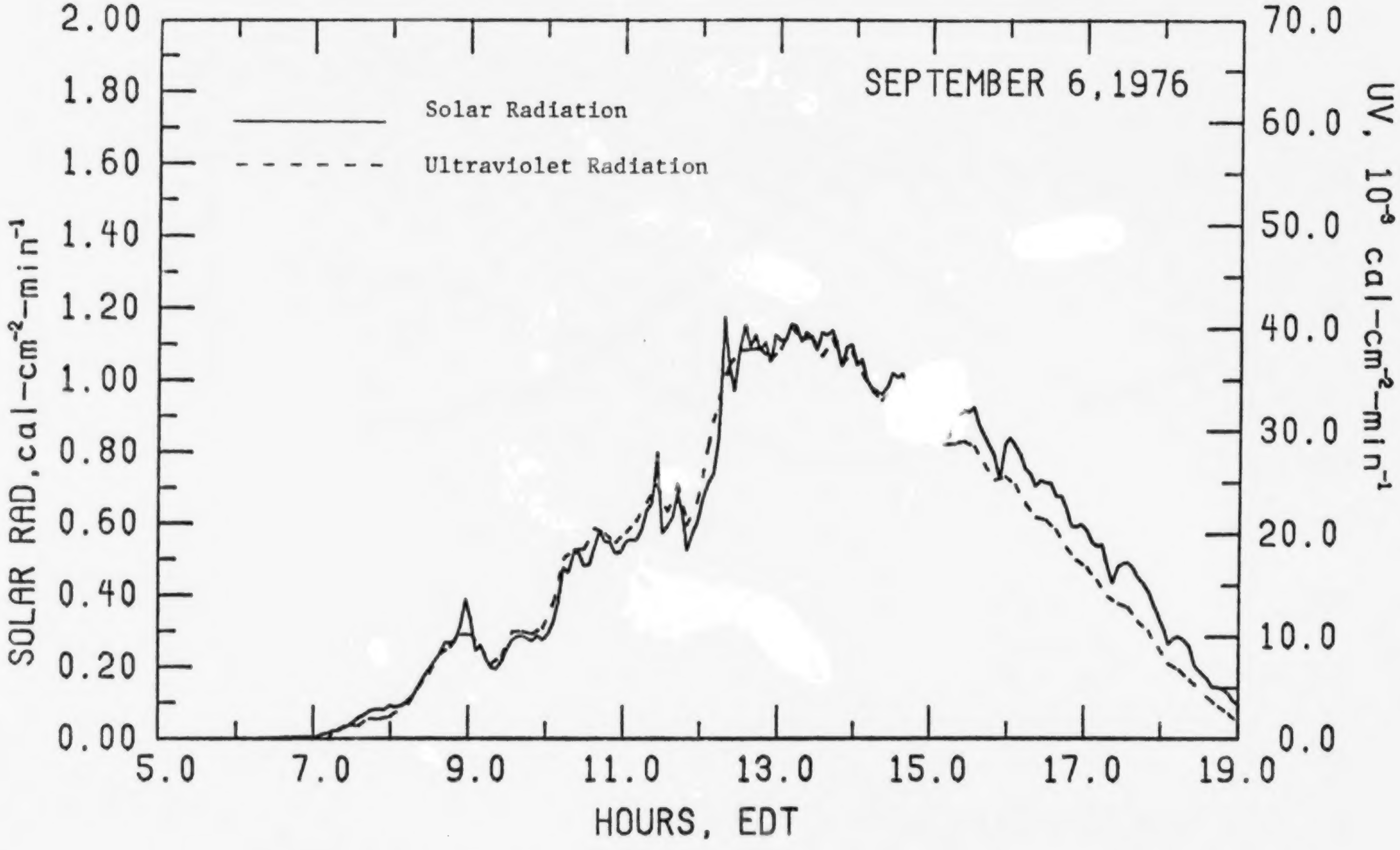

Figure 54. Solar radiation and ultraviolet radiation from September 6, 1976.

Run #3 -- September 25, 1976

Time: EDT

Weather: Sky was totally obscured by fog in the early morning. By 0818, a light mist was falling. The fog started to break up around 1000 and was clear by 1030 EDT.

Blue Chamber: slug injections 0530 - 0600 EDT

initial conditions:

HC - 4.85 ppmC

$NO_x$ - 0.527 ppm

$NO_2$ - 45%

Simulation profile injection and dilution began at 0815 EDT. Decided to abort at 0907 EDT because of weather and buildup of NO. Chamber run in static mode for remainder of day.

At 1400 EDT, $O_3$ was about half that observed in LARPP. Eventually made 0.20 ppm at 1630 EDT.

Red Chamber: slug injections 0530 - 0600 EDT

initial conditions:

HC - 4.85 ppmC

$NO_x$ - 0.549 ppm

$NO_2$ - 40%

Static side mode 0.60 ppm of $O_3$ peaking at 1630 EDT also.

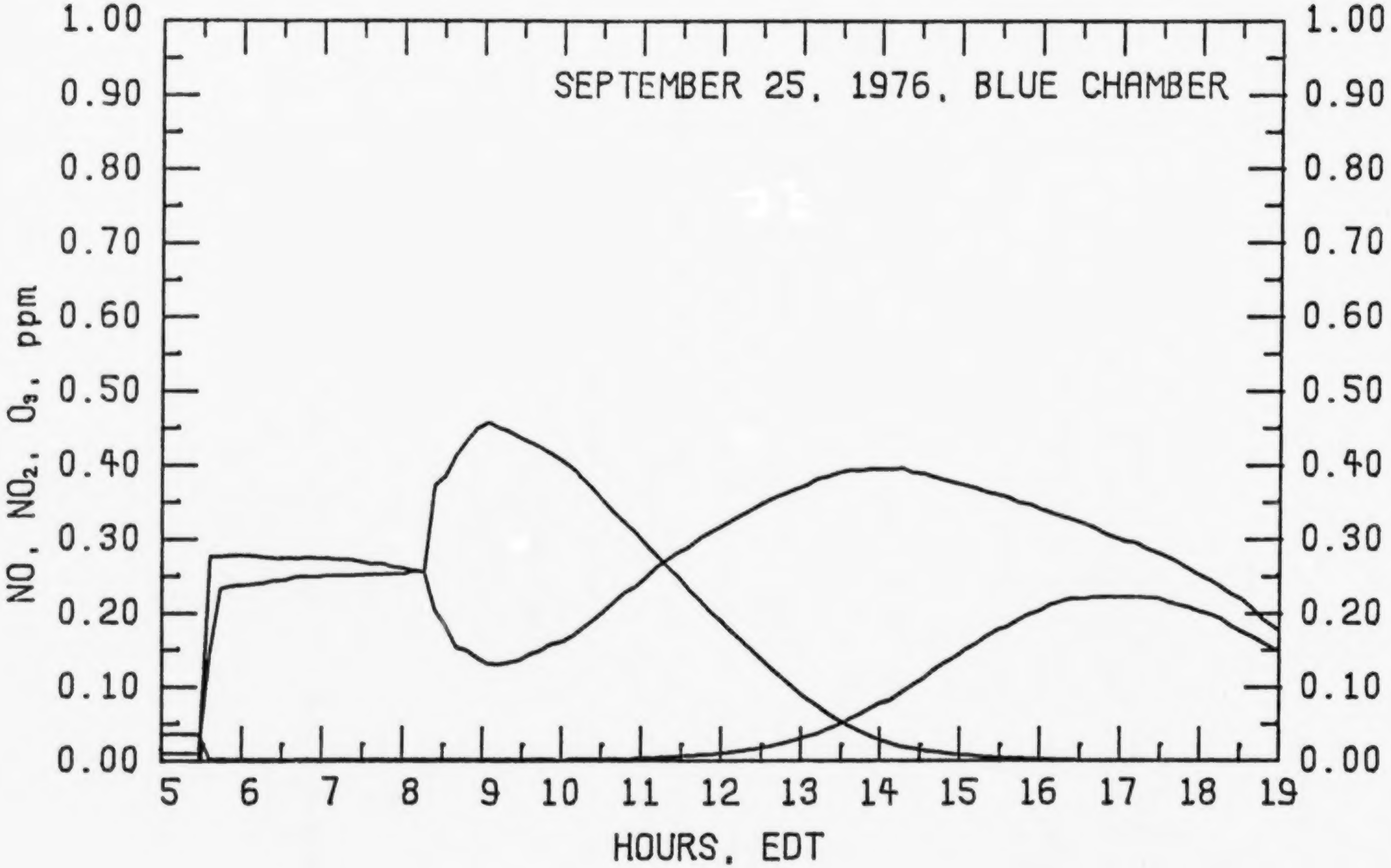

Figure 55. NO, $NO_2$, and $O_3$ profiles from simulation experiment of September 25, 1976.

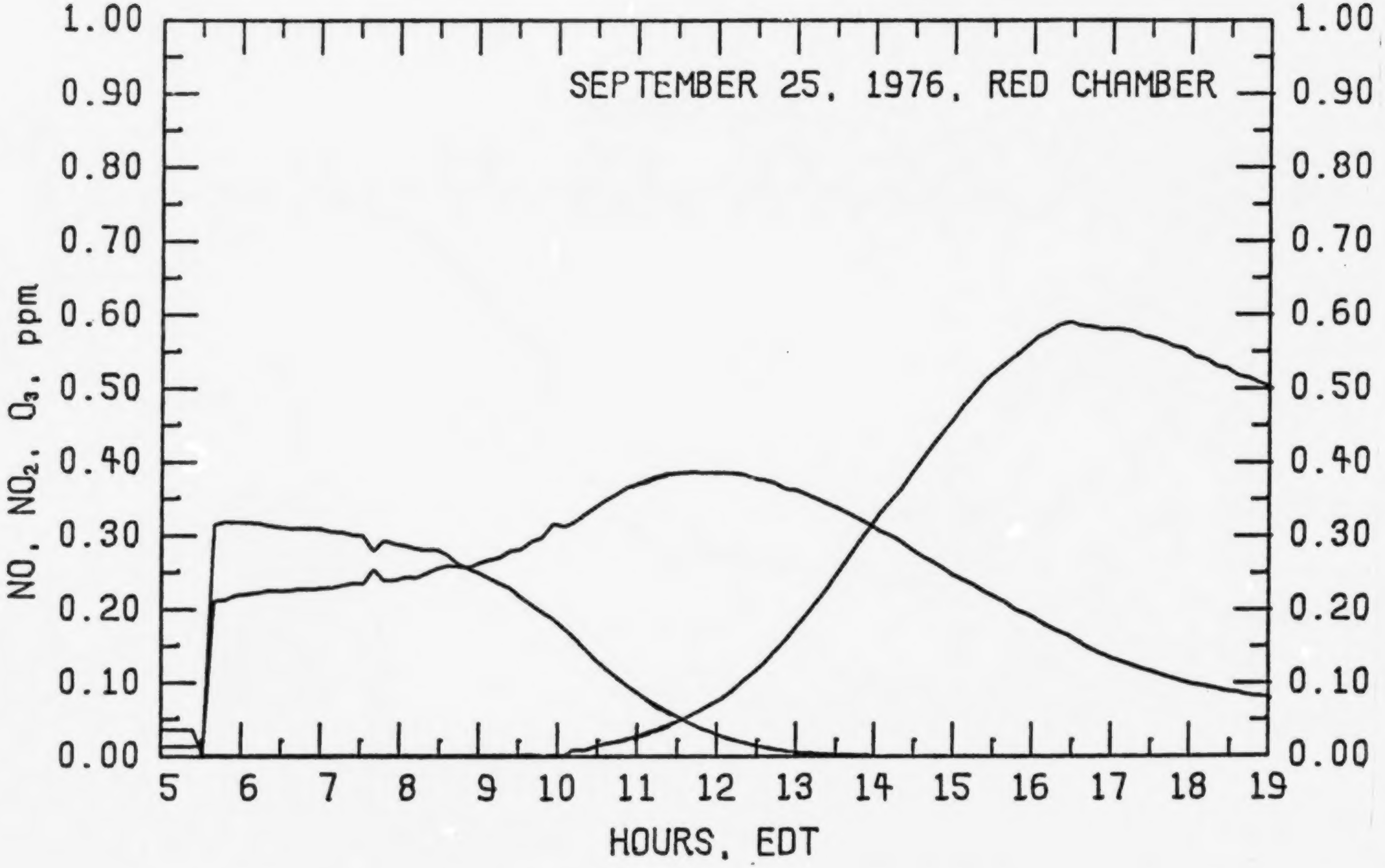

Figure 56. NO, $NO_2$, and $O_3$ profiles from static experiment of September 25, 1976.

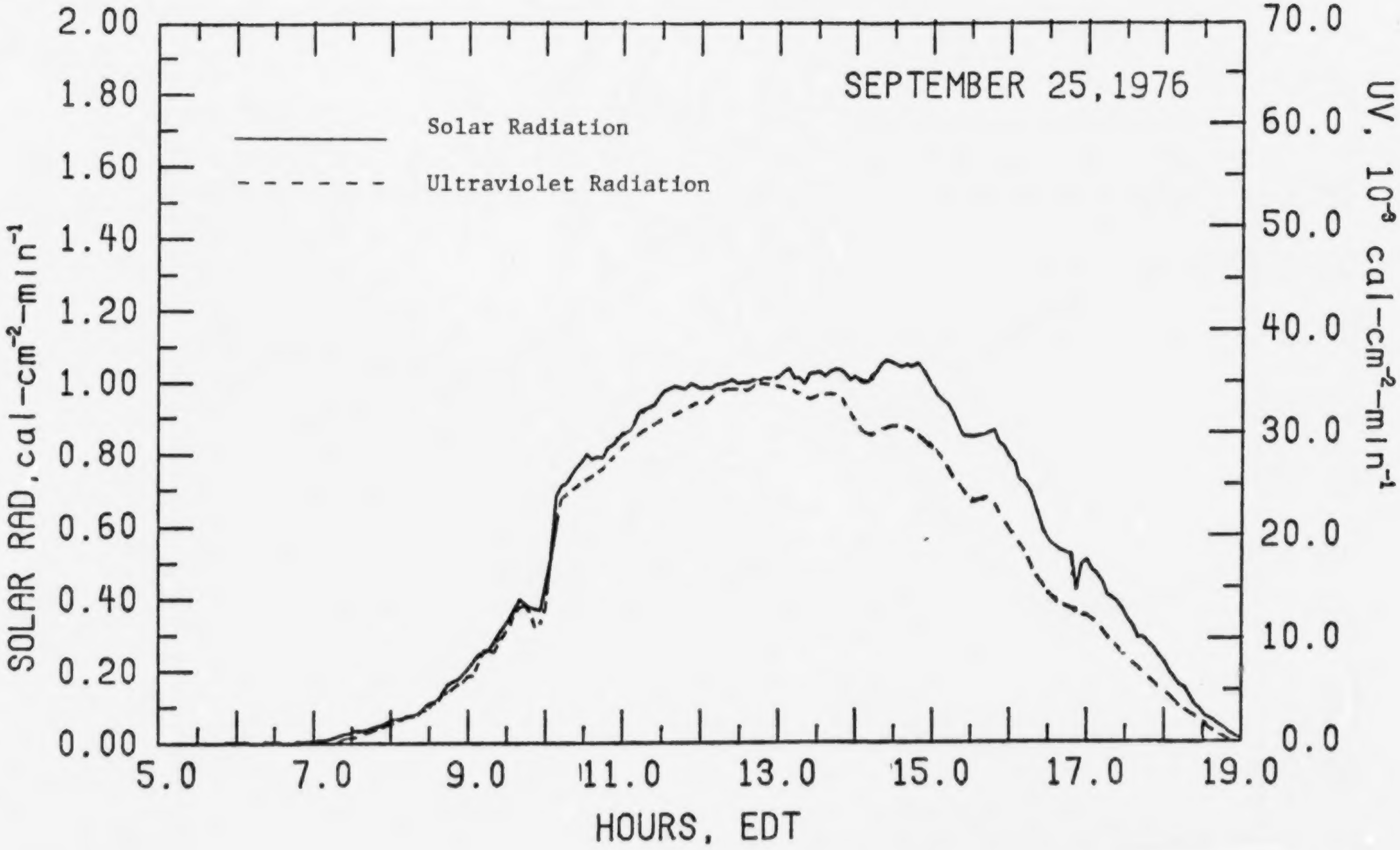

Figure 57. Solar radiation and ultraviolet radiation from September 25, 1976.

Run #4 -- October 4, 1976

Time: EDT

Weather: At 0826 EDT, sky was partially cloudy but bright. By 0932, sky was totally clear but at 0945 became very cloudy again, and remained so for the rest of the day.

Blue Chamber: ramp injection 0530 - 0815 EDT

concentrations at 0815:

HC - 3.24 ppmC

$NO_x$ - 0.503 ppm

$NO_2$ - 40%

acetaldehyde - 0.36 ppmC

Simulation profile injection and dilution began 0815 EDT.

All $NO_x$ injected as NO.

System was slow and produced little $O_3$ due to cloudy conditions.

Red Chamber: slug injection 0515 - 0530 EDT

initial conditions:

HC - 3.44 ppmC

$NO_x$ - .495 ppm

$NO_2$ - 20%

acetaldehyde - 0.38 ppmC

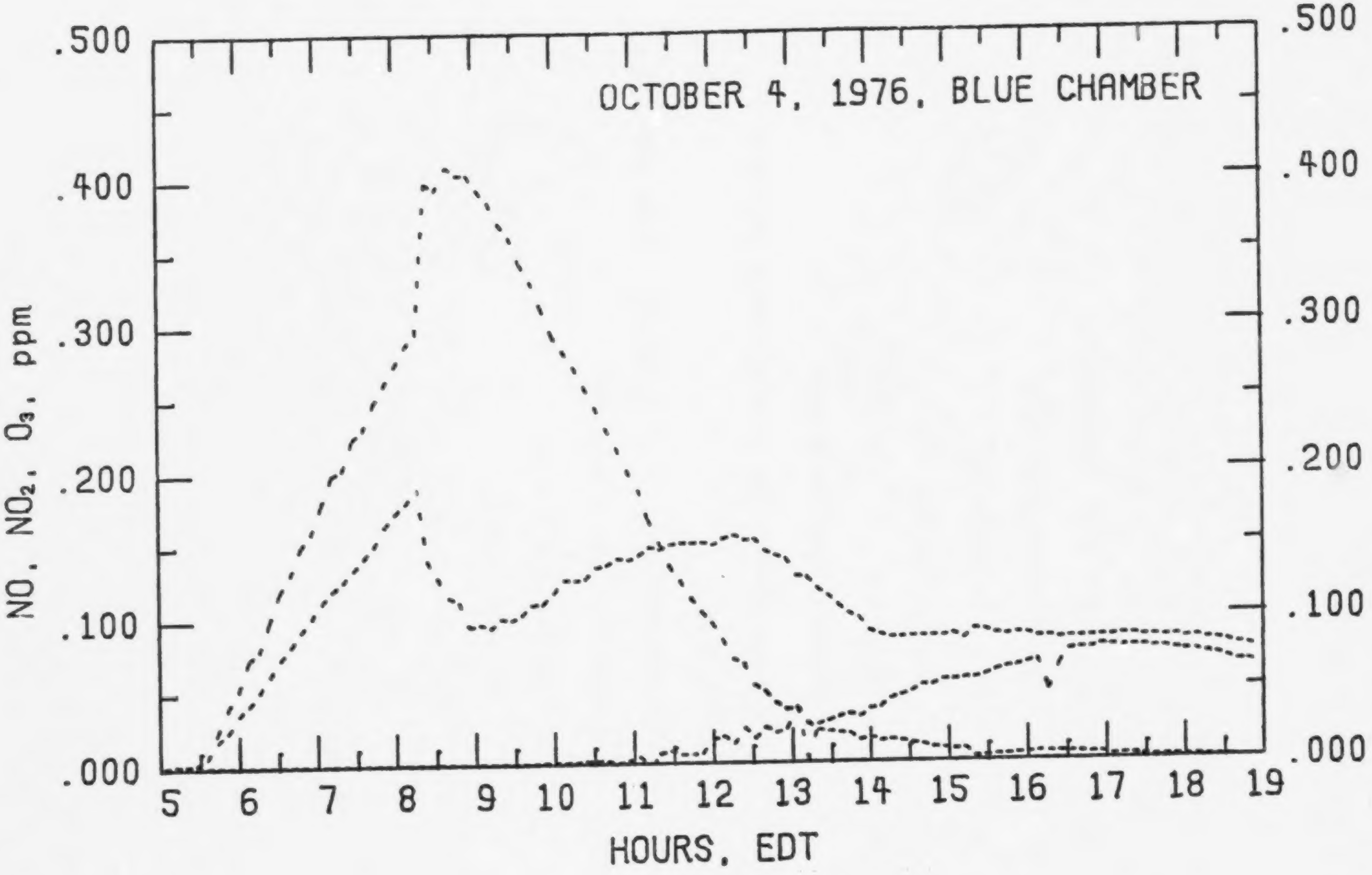

Figure 58. NO, $NO_2$, and $O_3$ profiles from simulation experiment of October 4, 1976.

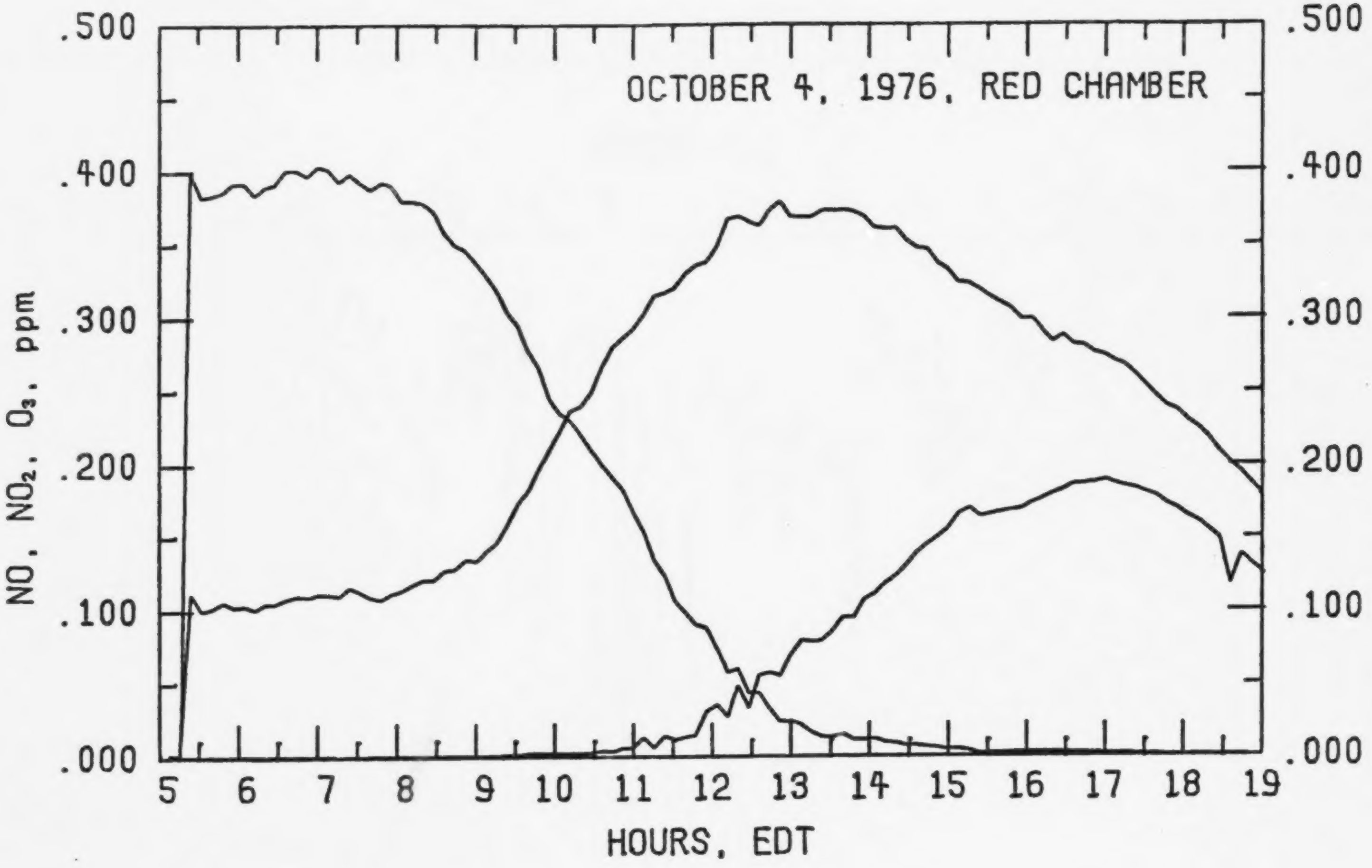

Figure 59. NO, $NO_2$, and $O_3$ profiles from static experiment of October 4, 1976.

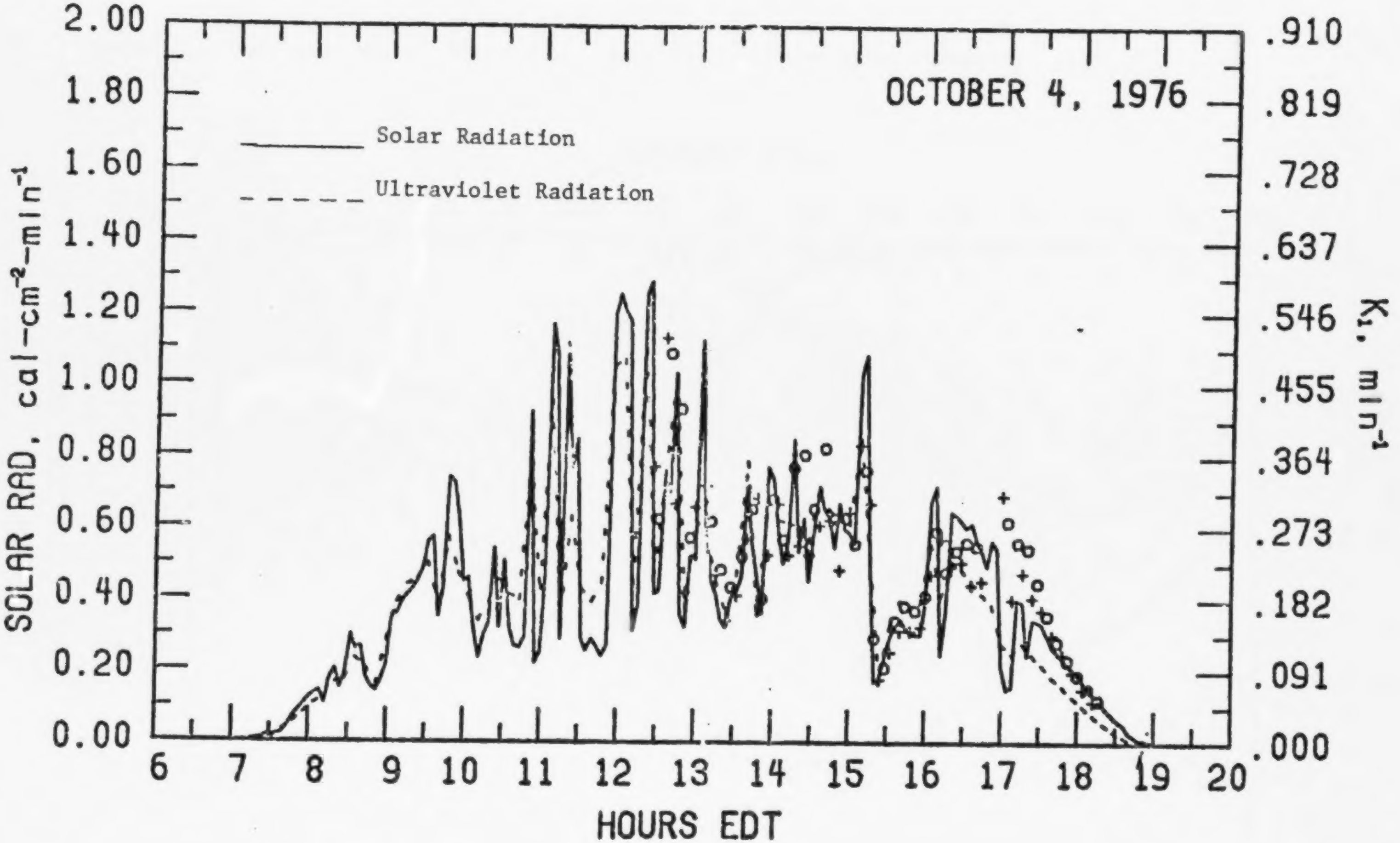

Figure 60. Solar radiation, ultraviolet radiation, and $NO_2$ photolysis rate constant from October 4, 1976. (UV scale is 74.57 mLy/min. maximum).

Run #5 -- October 6, 1976

Time: EDT

Weather: Clear until noon; partly cloudy afternoon

Blue Chamber: initial injection command file failed to execute, thus pollutants were slug injected manually at 0630 - 0700 EDT

initial conditions:

HC - 3.31 ppmC

$NO_x$ - 0.500 ppm

$NO_2$ - 40%

acetaldehyde - 0.37 ppmC

Simulation profile injections started at 0815 EDT.

Results here bear a much closer resemblance to the LARPP data. The main difference is that events occurred later in the day. The $O_3$ produced was equal to that of the LARPP run, but it reached this level 1 1/2 to 2 hours later in the day. This difference was seen to be mainly due to the differences in solar time. The solar time at any time during the morning in EDT in early October is equivalent to the solar time on the LARPP run 90 min later in PST. The subsequent simulations were performed by matching solar times at which events occurred.

Red Chamber: slug injections 0630 - 0645 EDT

initial conditions:

HC - 3.27 ppmC

$NO_x$ - 0.496 ppm

$NO_2$ - 19%

acetaldehyde - 0.36

Static side produced a 0.28 ppm $O_3$ max at 1556 EDT.

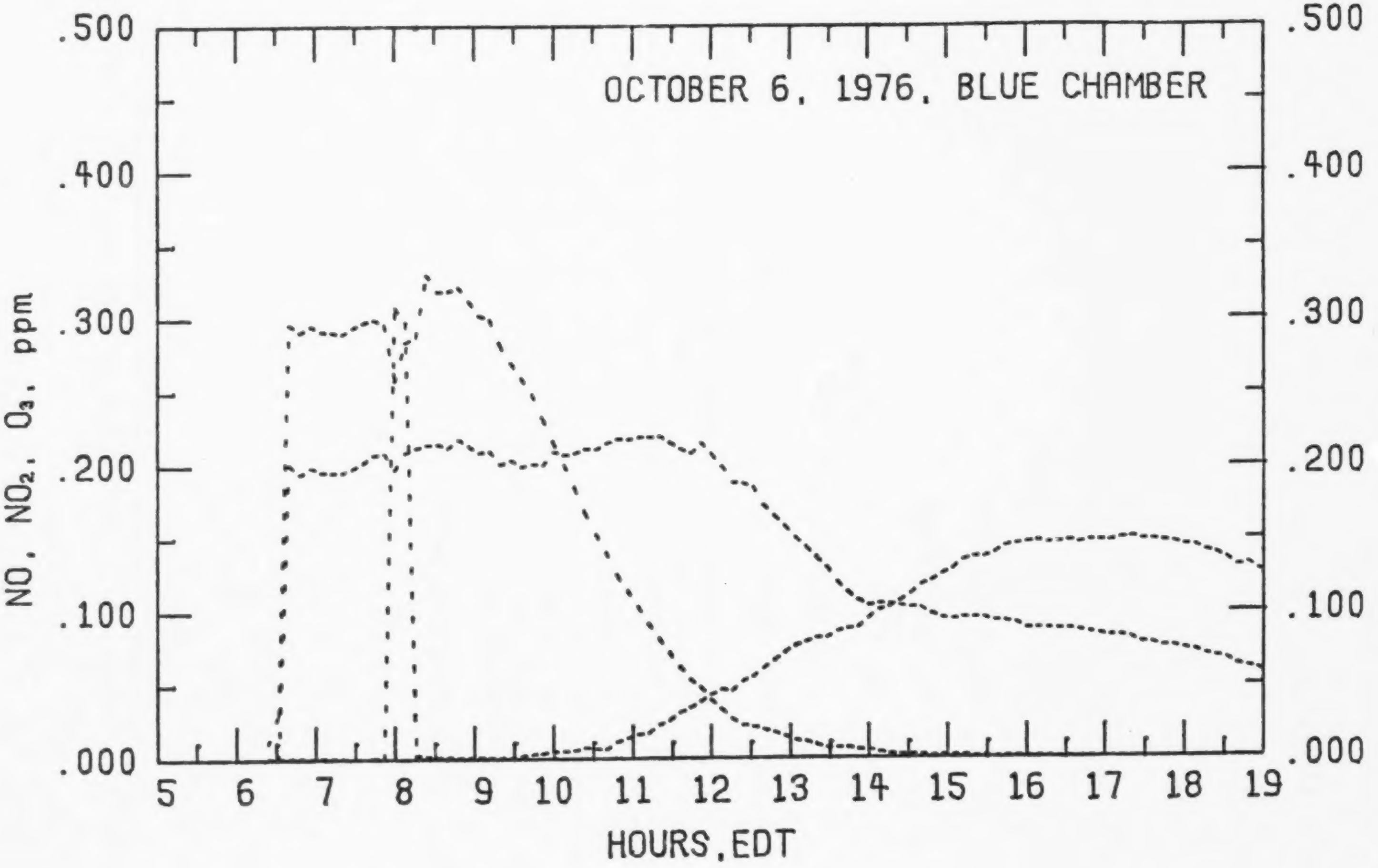

Figure 61. NO, $NO_2$, and $O_3$ profiles from simulation experiment of October 6, 1976.

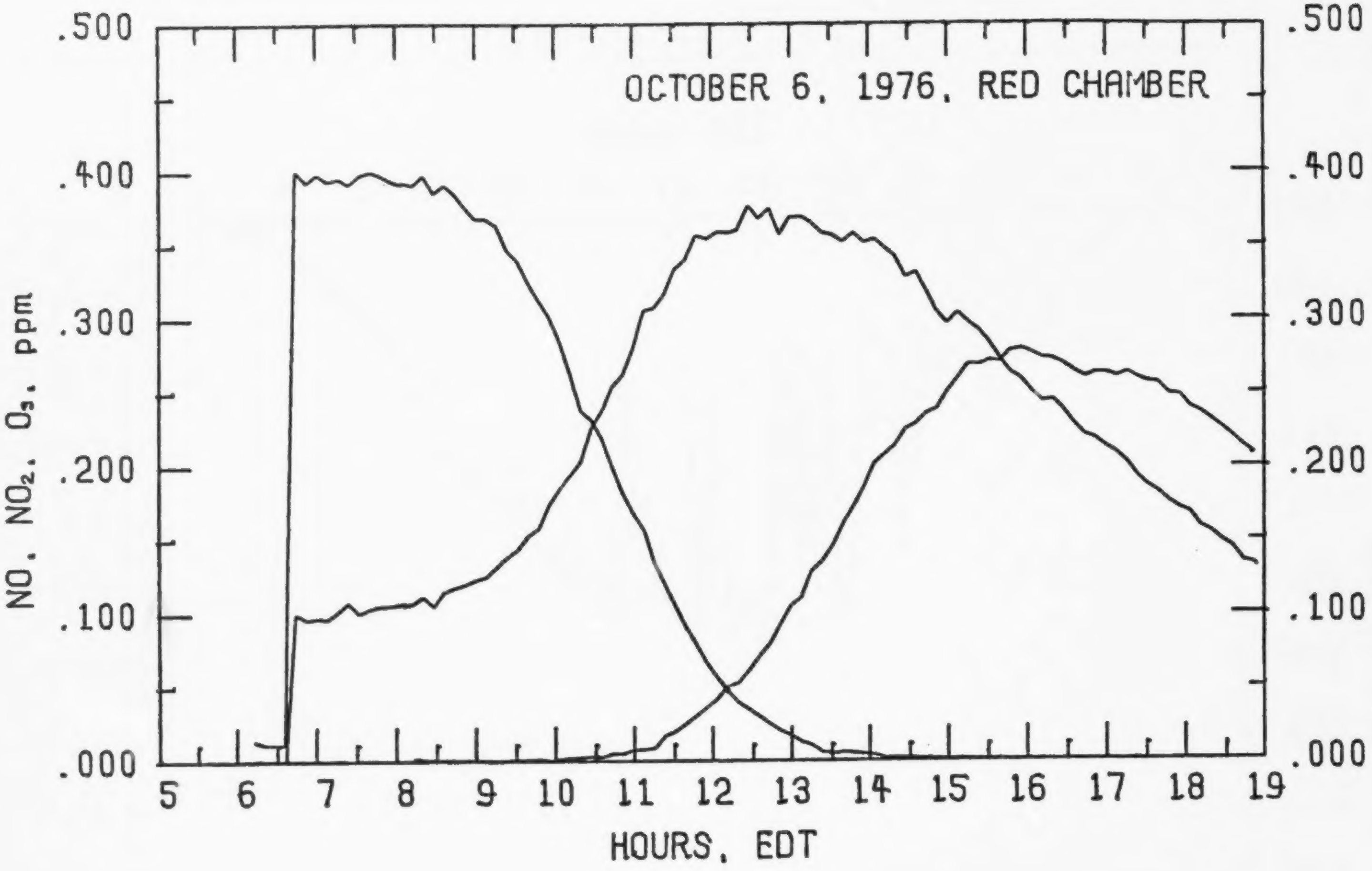

Figure 62. NO, $NO_2$, and $O_3$ profiles from static experiment of October 6, 1976.

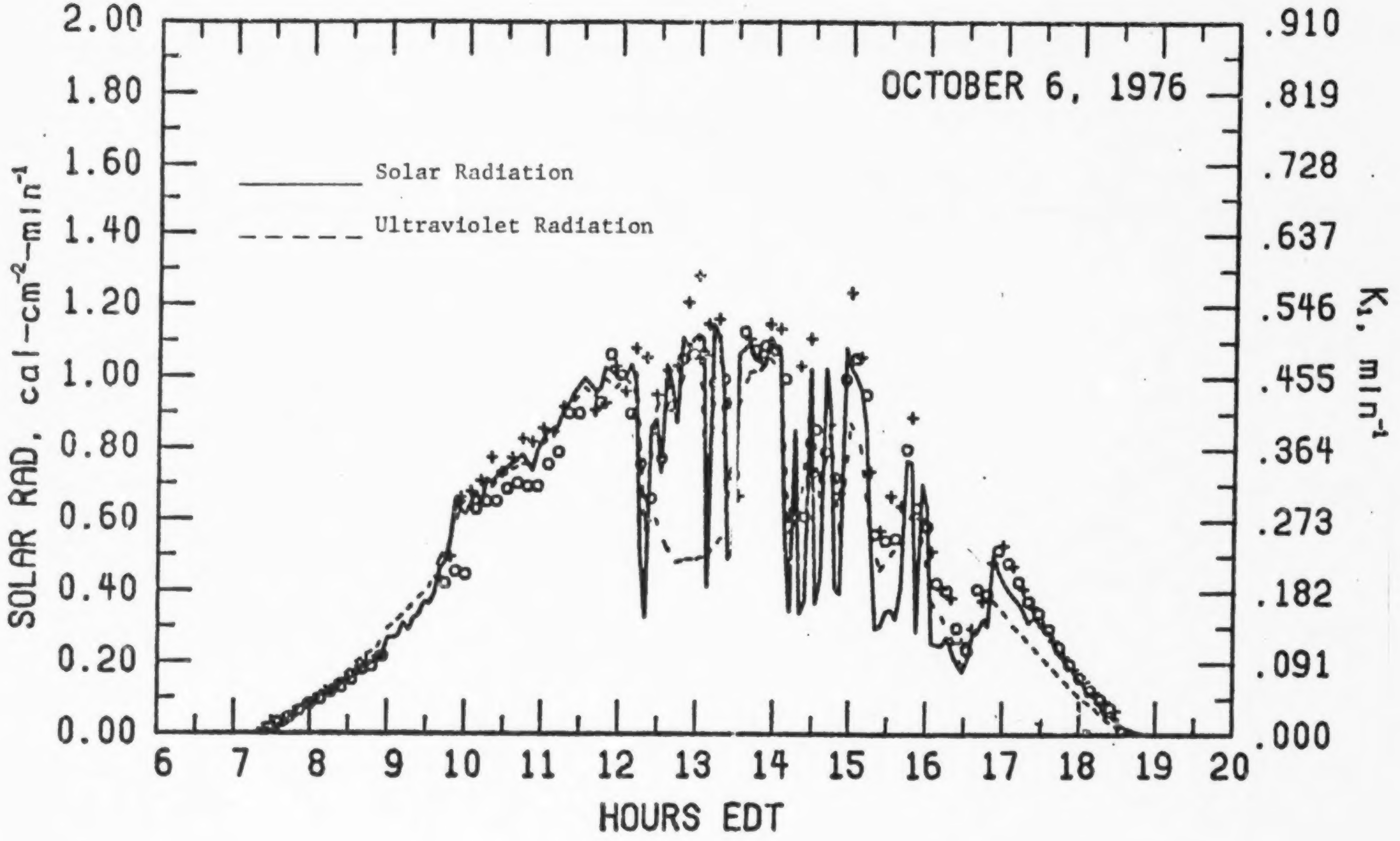

Figure 63. Solar radiation, ultraviolet radiation, and $NO_2$ photolysis rate constant from October 6, 1976. (UV scale is 67.13 mLy/min. maximum.)

Run #6 -- October 11, 1976

Time: Corrected to PST

Weather: Clear until 1130 PST, then partially cloudy

Blue Chamber: ramp injection began at 0530 PST, but computer failure caused this simulation to be aborted at 0602 PST

Red Chamber: slug injection 0500 - 0530 PST

initial conditions:

HC - 4.33 ppmC (based on injections)

$NO_x$ - 0.506 ppm

$NO_2$ - 29%

acetaldehyde - 10% of total hydrocarbons as carbon

Static side had $O_3$ max of 0.257 ppm at 1506 PST.

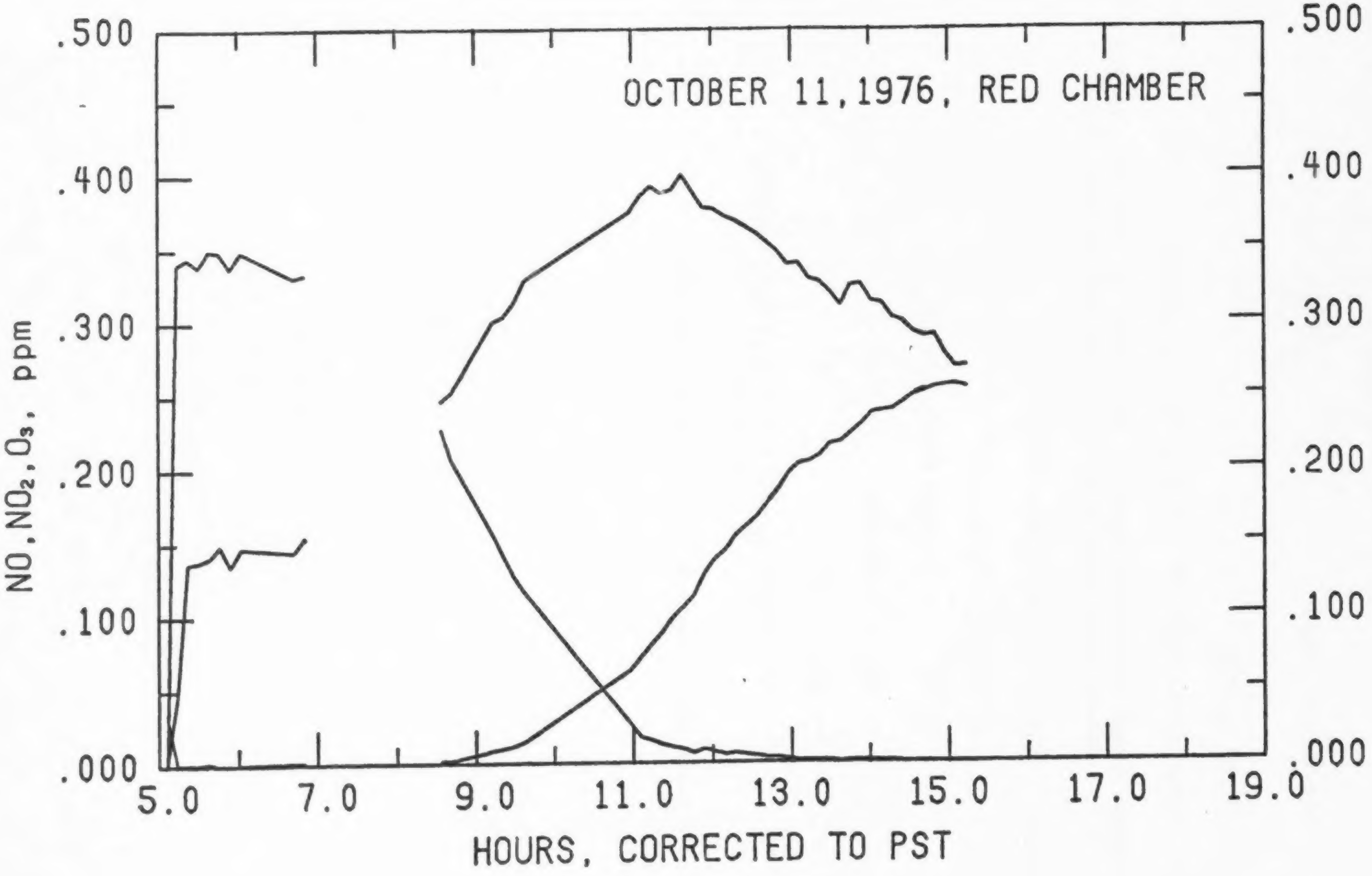

Figure 64. NO, $NO_2$, and $O_3$ profiles from static experiment of October 11, 1976.

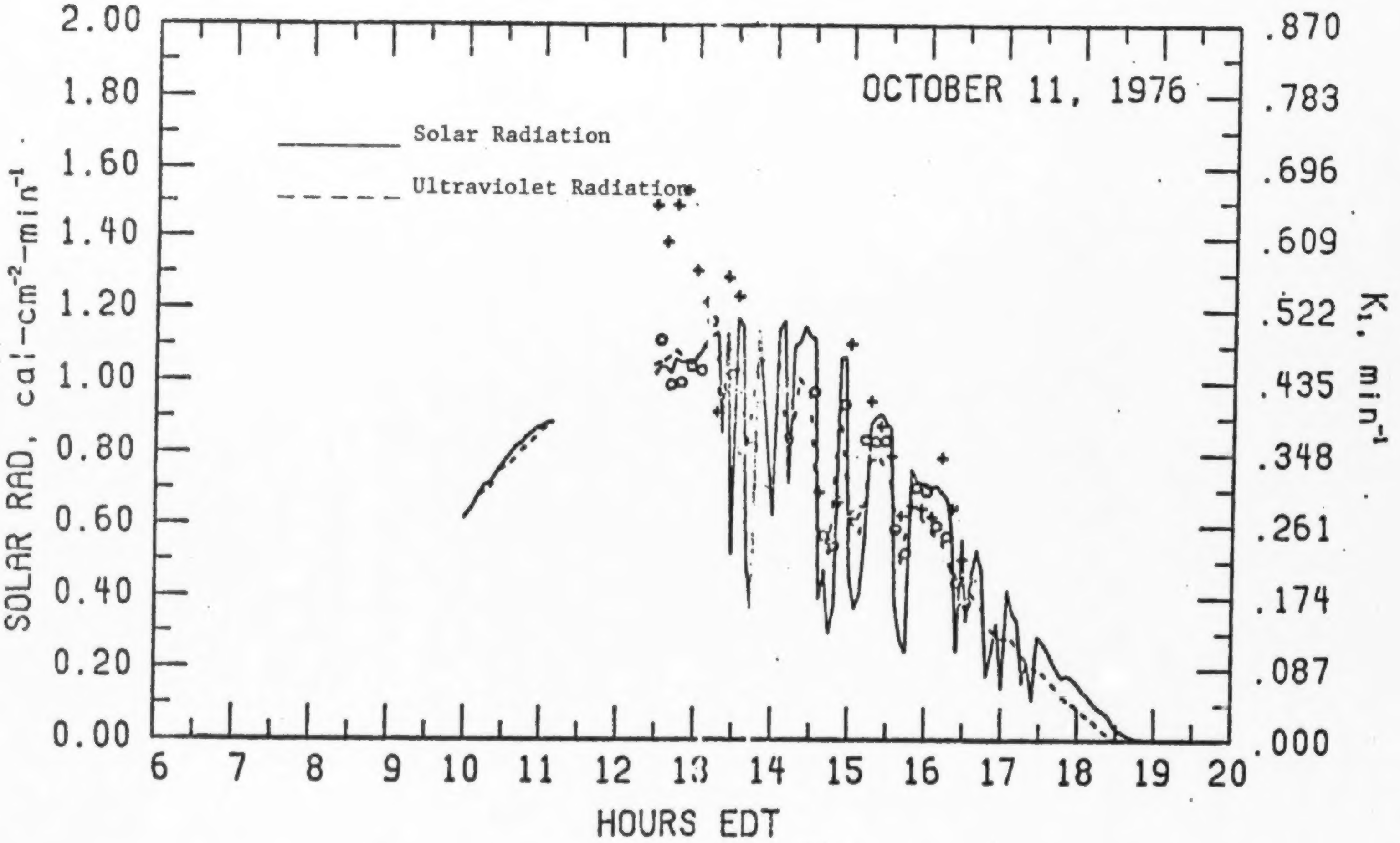

Figure 65. Solar radiation, ultraviolet radiation, and $NO_2$ photolysis rate constant from October 11, 1976. (UV scale is 64.90 mLy/min. maximum.)

Run #7 -- October 12, 1976

Time: Corrected to PST

Weather: Clear all day

Blue Chamber: Ramp injection began at 0530 PST, but was stopped by computer failure at 0534. Computer was not operable until 0702 PST. At this time, slug injections were made.

initial conditions:

HC - 3.76 ppmC

$NO_x$ - 0.517 ppm

$NO_2$ - 39%

acetaldehyde - 0.42 ppmC

Acetaldehyde added with profiled HC injection so that it made up 10% of total HC as carbon.

35% $NO_x$ in profile injection was $NO_2$.

Simulation profile injection and dilution started at 0815.

This simulation produced morning NO and $NO_2$ profiles which match the LARPP profiles quite well. In the early afternoon however, the $NO_2$ is somewhat lower than the LARPP values. This run produced about half the ozone observed in the LARPP run at 1400 PST but the general shape of the ozone curve is the same.

Red Chamber: slug injection 0500 - 0530 PST

initial conditions:

HC - 4.38 ppmC

$NO_x$ - 0.499 ppm

$NO_2$ - 21%

acetaldehyde - 0.49 ppmC

Static run made about 0.33 ppm of $O_3$ at 1500 PST.

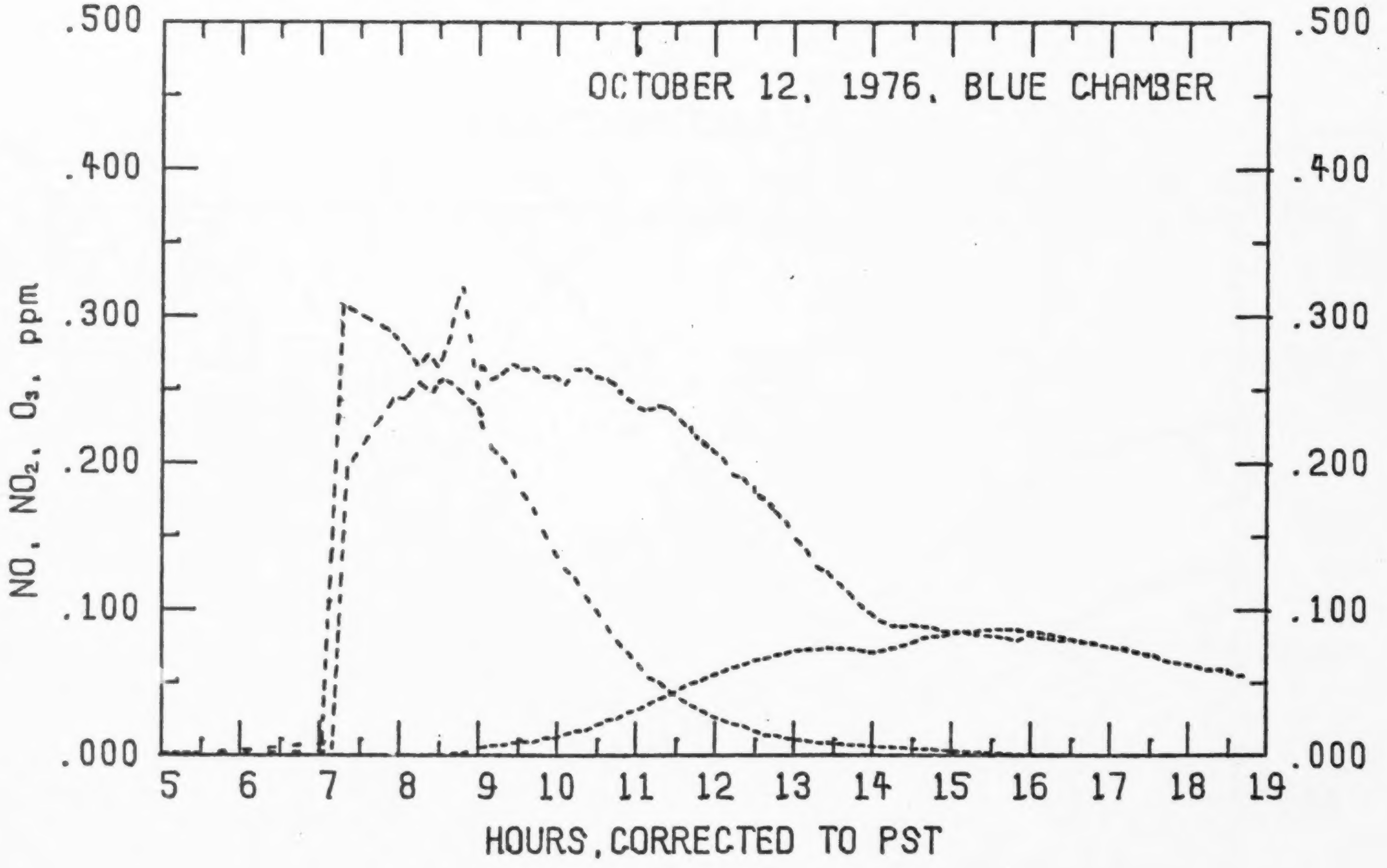

Figure 66. NO, $NO_2$, and $O_3$ profiles from simulation experiment of October 12, 1976.

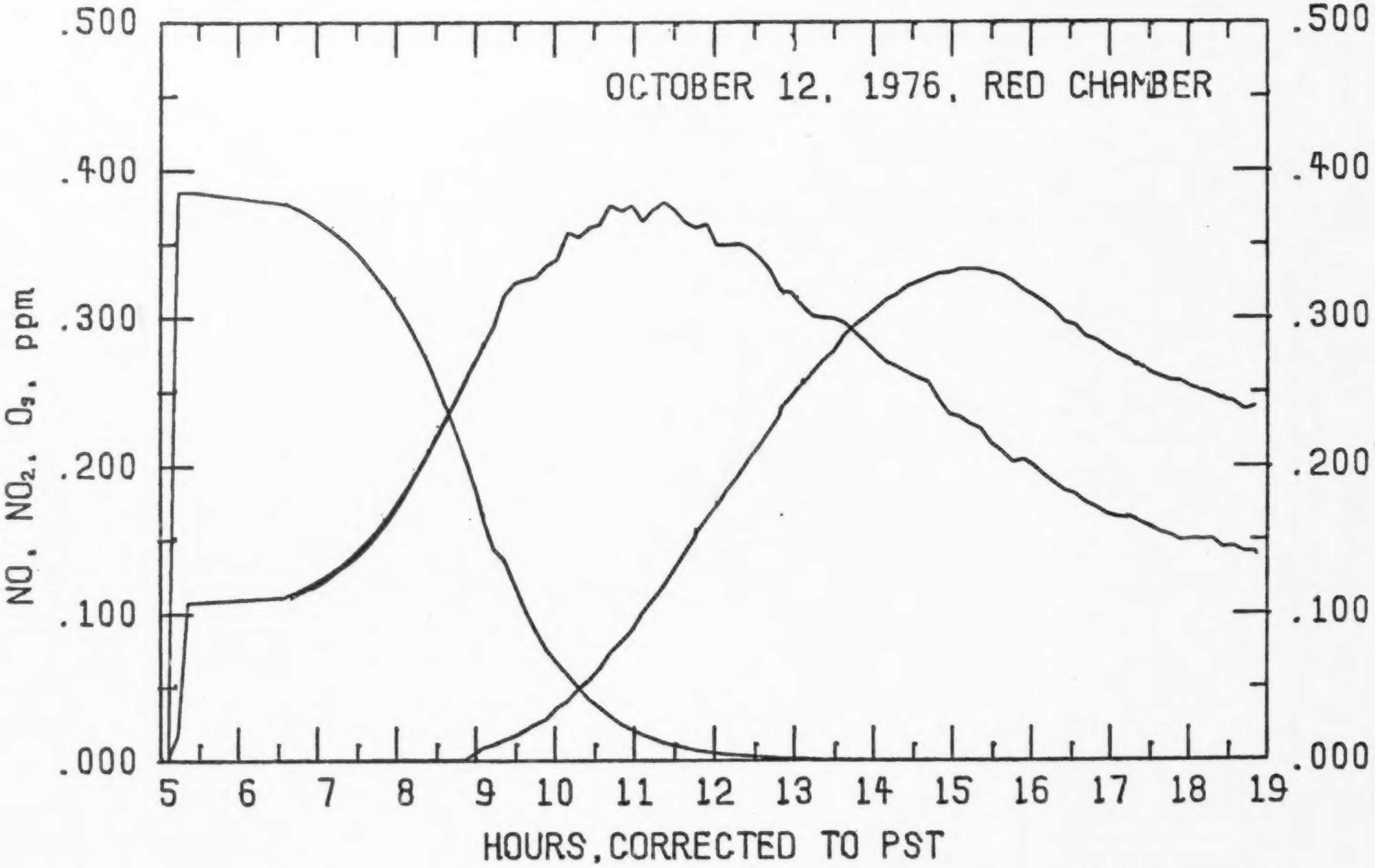

Figure 67. NO, $NO_2$, and $O_3$ profiles from static experiment of October 12, 1976.

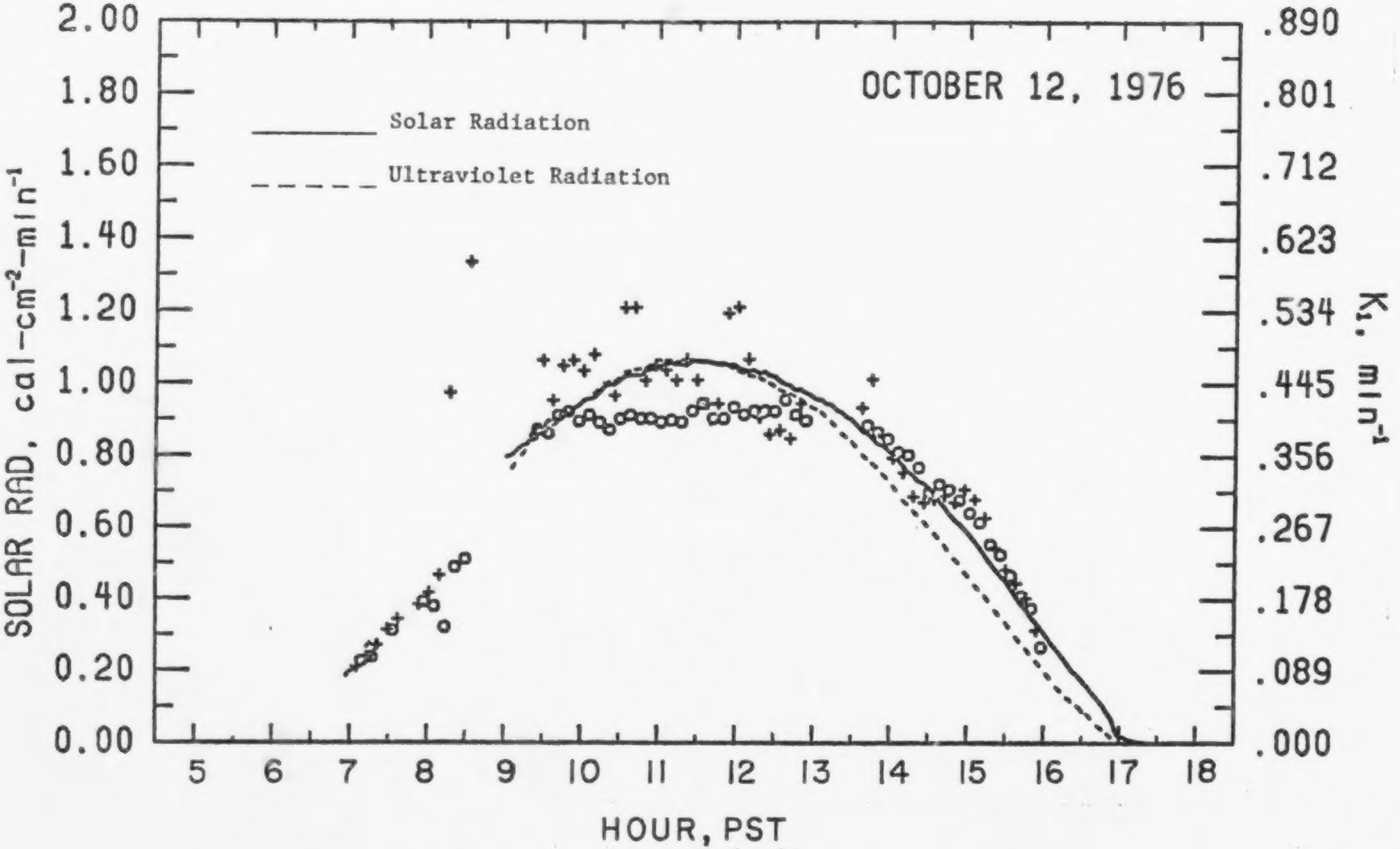

Figure 68. Solar radiation, ultraviolet radiation, and $NO_2$ photolysis rate constant from October 12, 1976. (UV scale is 66.00 mLy/min maximum.)

Run #8 -- October 13, 1976

Time: Corrected to PST

Weather: The sky was clear with a few scattered clouds in mid-morning. The day was warmer than the two previous simulations, with chamber temperatures in the lower 80s by early afternoon. This is about $10^{o}$ warmer than the two previous runs.

Blue Chamber: ramp injections 0530 - 0815 PST

initial conditions at 0815 PST:

HC - 4.01 ppmC

$NO_x$ - 0.472 ppm

$NO_2$ - 47%

acetaldehyde - 0.45 ppmC

Simulation profile injection and dilution began at 0815 PST. Dilution profile terminated at 1200 PST.

35% of $NO_2$ was as $NO_2$.

Acetaldehyde was injected such that it equalled 10% (as carbon) of the total hydrocarbon injected.

This simulation came closest to the pollutant profiles observed in the LARPP operation. $NO_2$ is slightly higher in the afternoon than the $NO_2$ in LARPP. NO and $O_3$ agree quite well with the LARPP profiles.

Red Chamber: slug injections were made 0500 - 0530 PST

initial conditions:

HC - 3.84 ppmC

$NO_x$ - 0.50 ppm

$NO_2$ - 22%

acetaldehyde - 0.43 ppmC

Static side reached an $O_3$ max of 0.45 at 1500 PST.

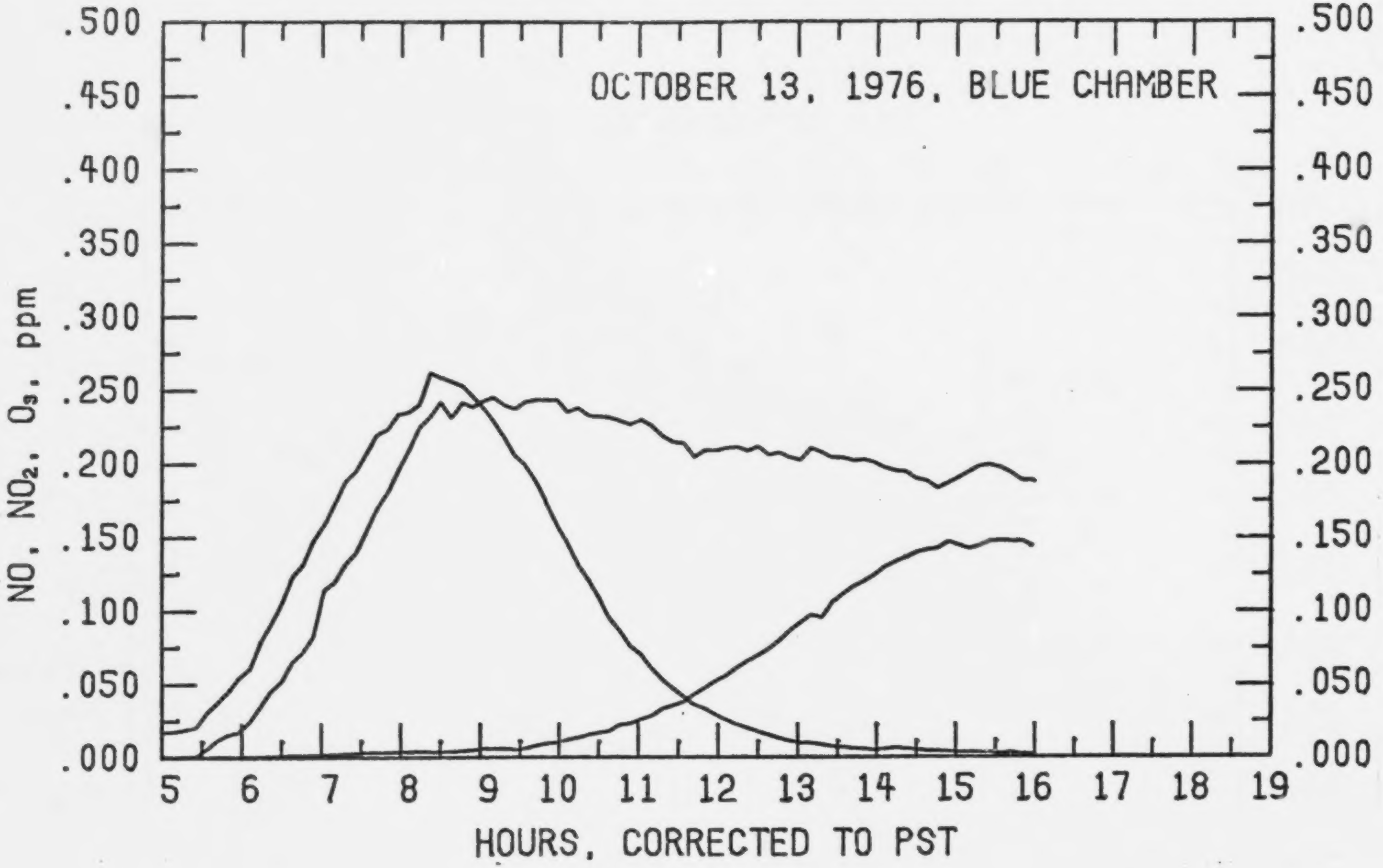

Figure 69. NO, $NO_2$, and $O_3$ profiles from simulation experiment of October 13, 1976.

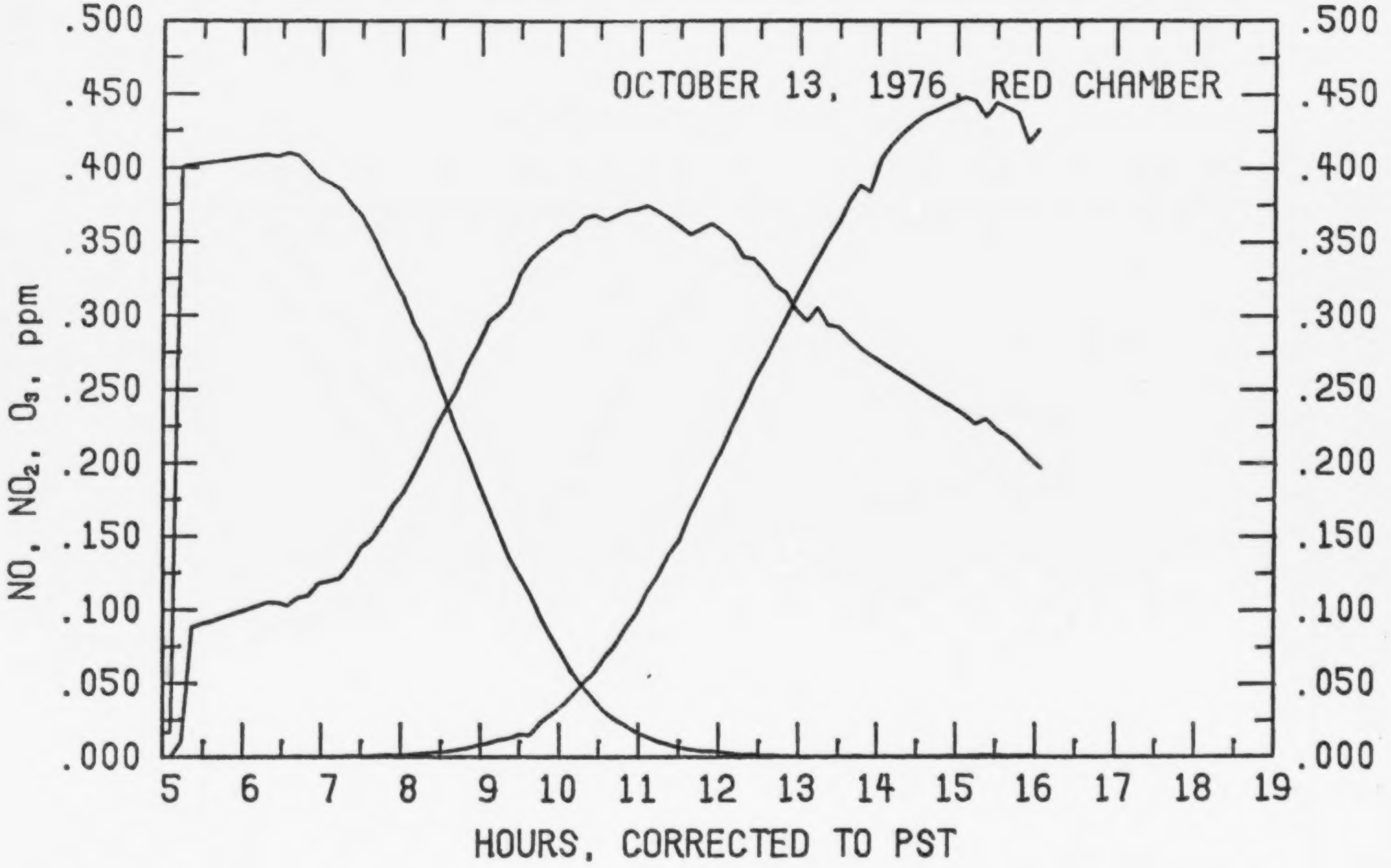

Figure 70. NO, $NO_2$, and $O_3$ profiles from static experiment of October 13, 1976.

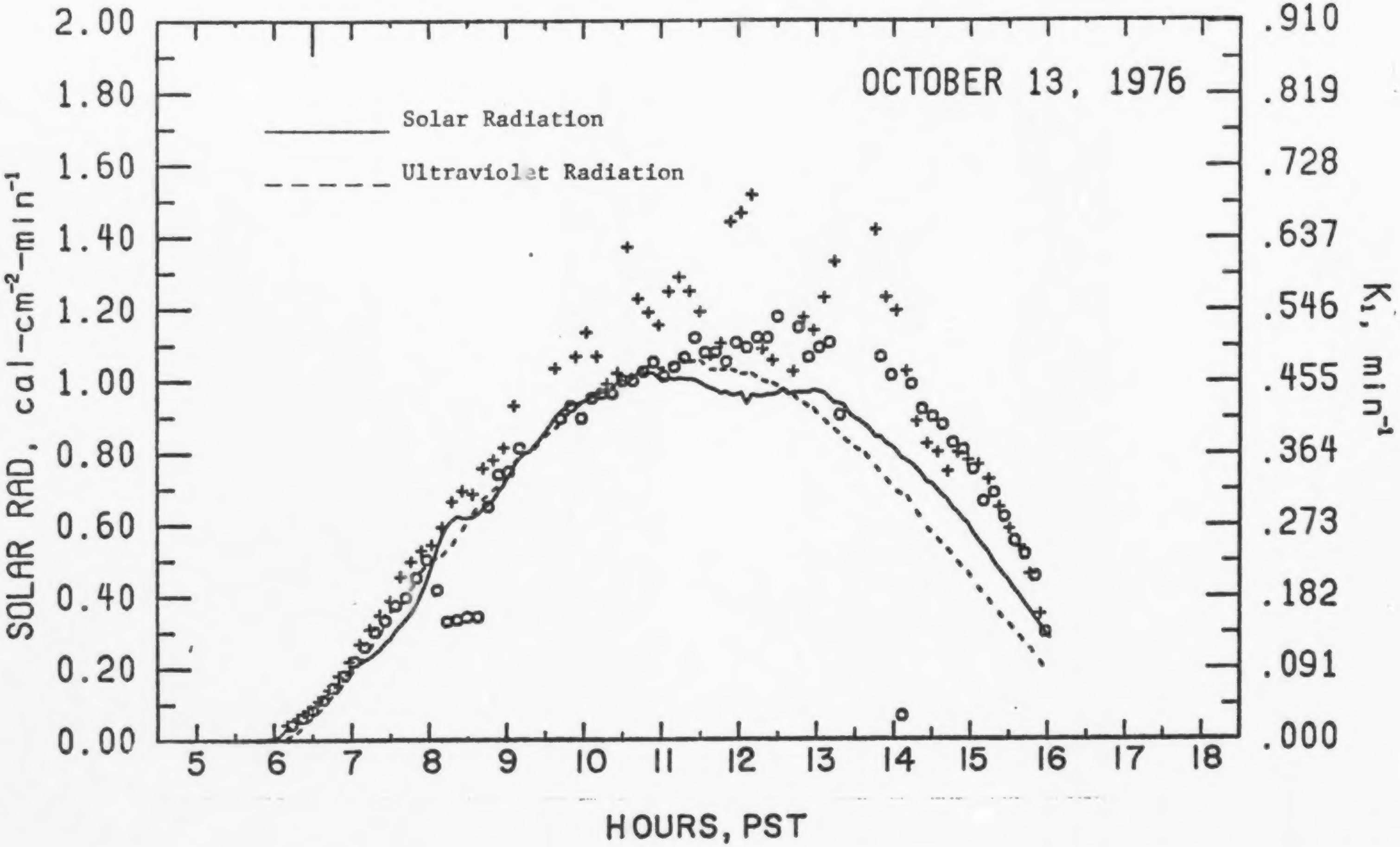

Figure 71. Solar radiation, ultraviolet radiation, and $NO_2$ photolysis rate constant from October 13, 1976. (UV scale is 64.24 mLy/min maximum.)

Run #9 -- October 15, 1976

Time: EDT

Weather: Clear

The intent of this run was to explore static run conditions which would produce ozone equivalent to that of the LARPP run, and to build up a second-day photochemical system for use in next day's simulation. Slug injections were made at 0530 EDT.

initial conditions:

| | Blue | Red |
|---|---|---|
| HC | 1 ppmC | 1.5 ppmC |
| $NO_x$ | 0.16 ppm | 0.24 ppm |
| $NO_2$ | 20% | 20% |
| $HC/NO_x$ | 6.22 | 6.22 |

The $NO_x$ meter was measuring blue chamber only, thus red NO and $NO_2$ profiles are not known. The blue chamber conditions produced an ozone concentration about 1 pphm higher than the LARPP day at 1530 EDT (equivalent to 1400 PST). The red side overshot, producing 0.26 ppm at 1530 EDT.

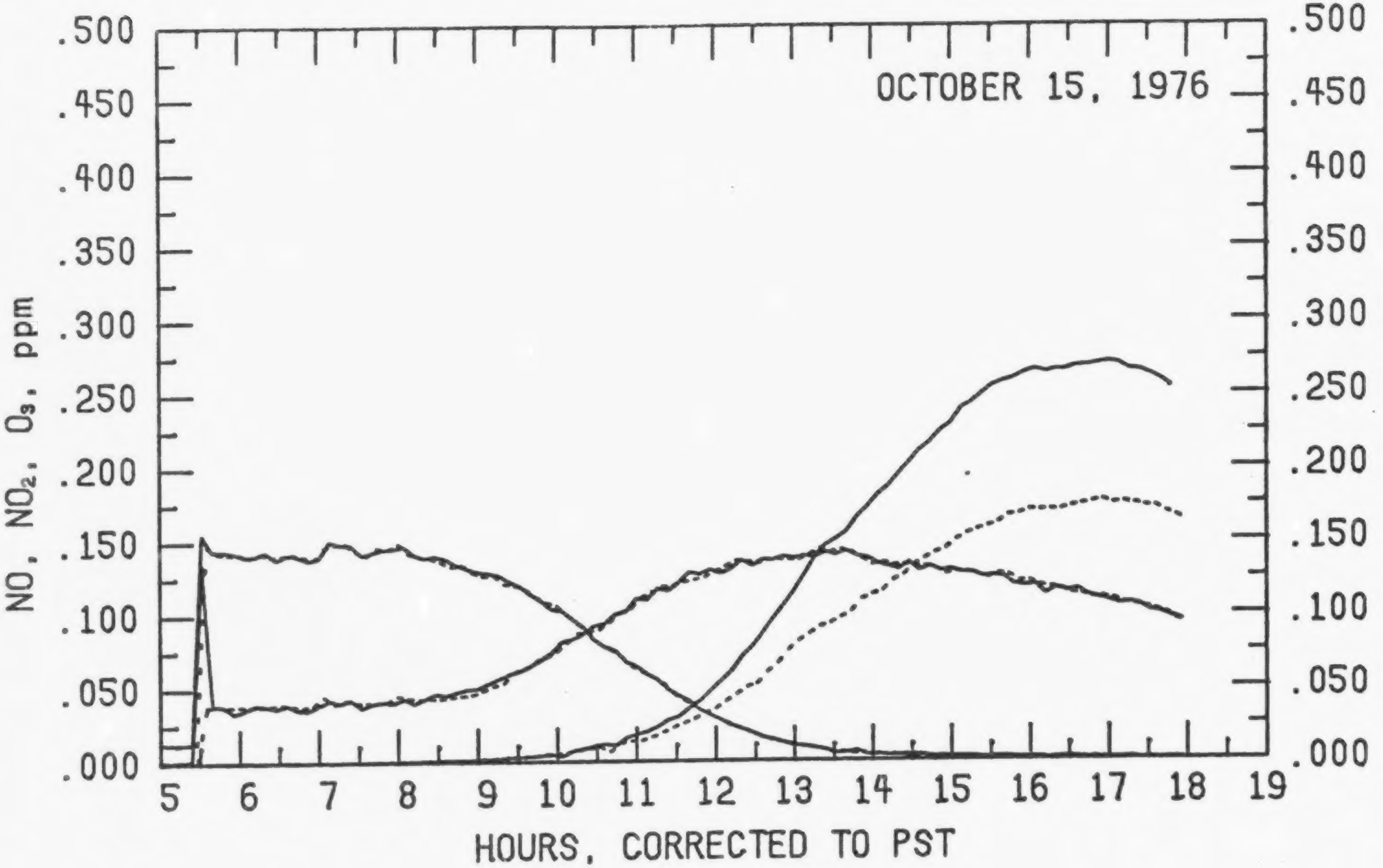

Figure 72. NO, $NO_2$, and $O_3$ profiles from static experiments of October 15, 1976. Blue side: 1 ppmC HC mix (dashed line); Red side: 1.5 ppmC HC mix (solid line); NO and $NO_2$ for blue side only.

Run #10 -- October 16, 1976

Time: Corrected to PST

Weather: Clear

In this run, the contents of the blue chamber from the previous day had been diluted so as to obtain a residual ozone concentration of about 0.07 ppm. The same ramp and profiles injections employed in Run #8 were made on top of the old material in the blue chamber. Provisions were also made for dilution of the blue chamber using material from the red chamber. The red chamber contained material from the previous day also, but no new precursors were introduced.

This system was very fast. Ozone production was quite rapid compared with previous runs. The $O_3$ max of 0.21 ppm occurred at 1300 PST.

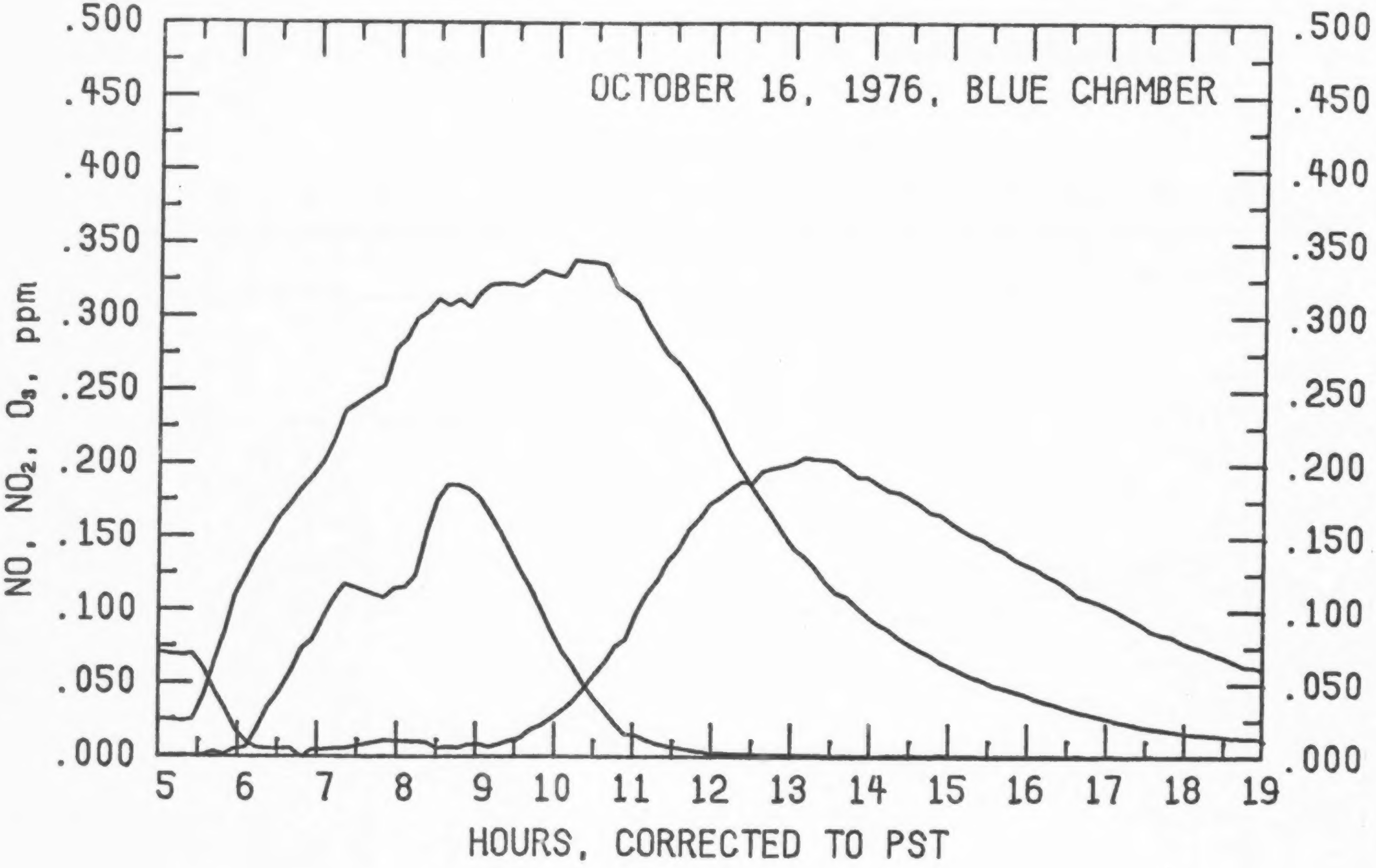

Figure 73. NO, $NO_2$, and $O_3$ profiles for simulation experiment of October 16, 1976. Performed with same material from previous day in chamber and same dilution with air from red side of chamber.

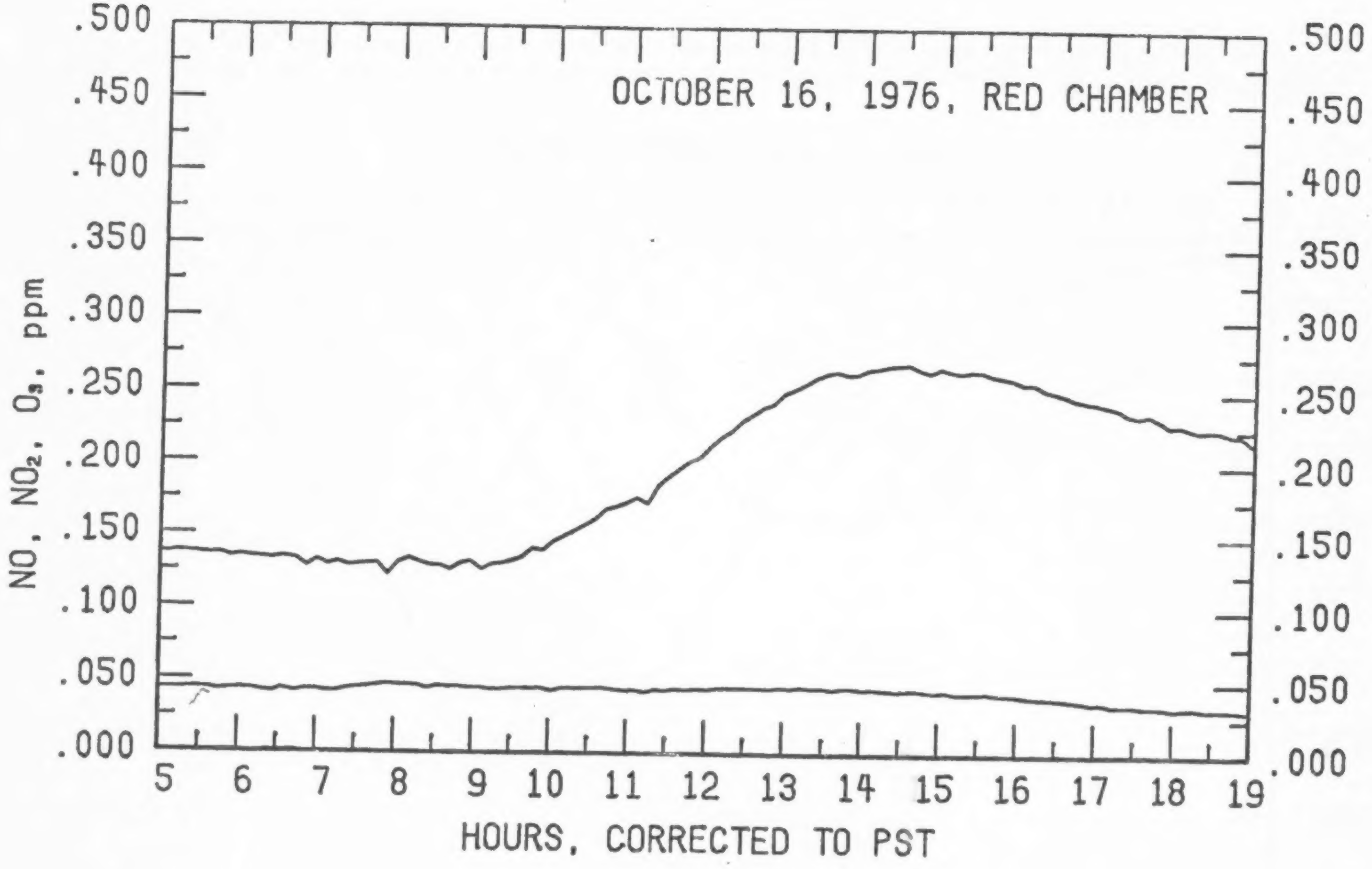

Figure 74. NO, $NO_2$, and $O_3$ profiles for October 16, 1976, red side. Materials left from the previous day only.

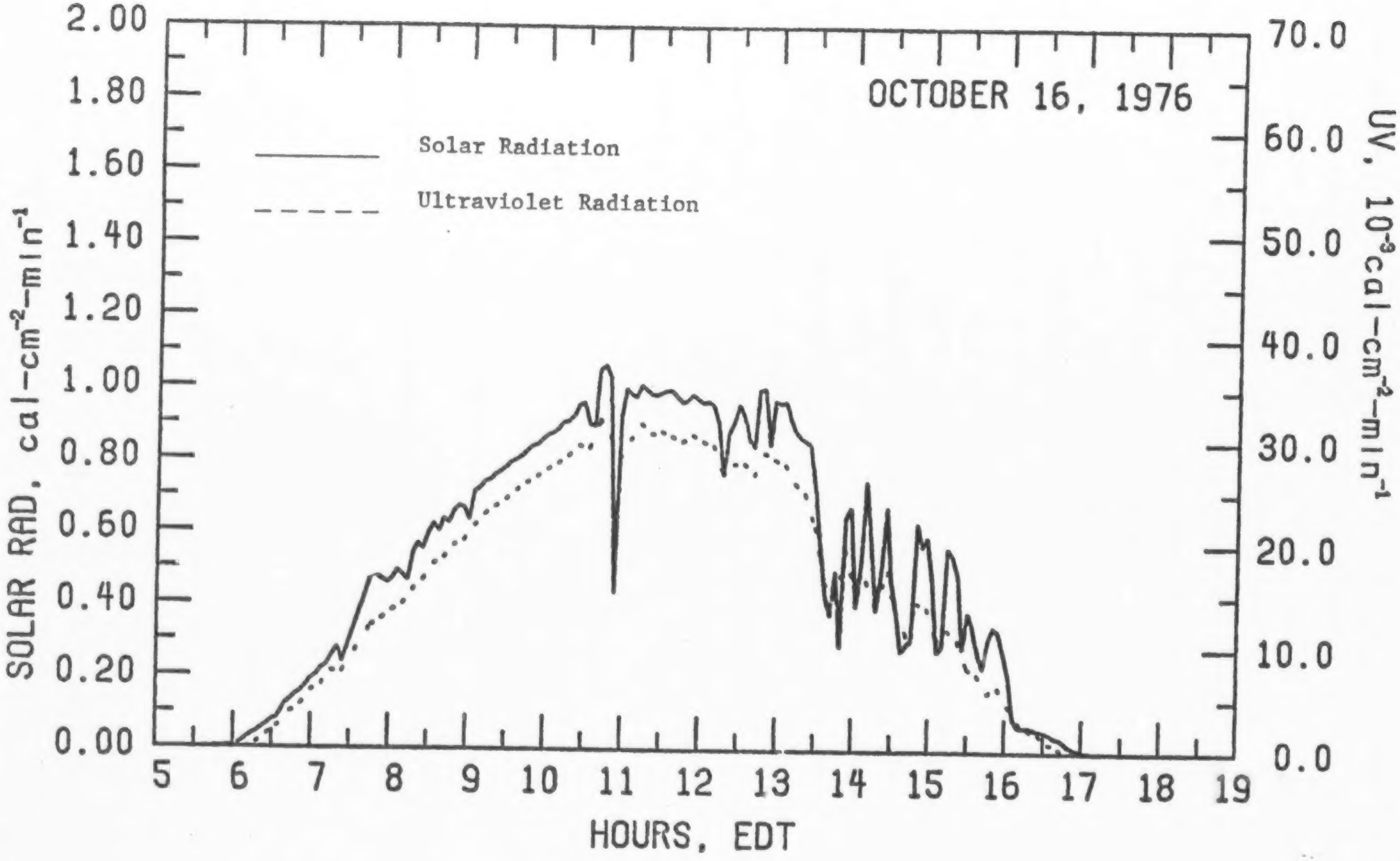

Figure 75. Solar radiation and ultraviolet radiation for October 16, 1976.

exhaust (California driving cycle). Since acetylene and CO are emitted almost exclusively from automobiles, they concluded that some as yet unknown process was removing $NO_x$ from the air, or at least from the gas phase. They were faced, when validating their model, to reduce the emission inventory $NO_x$ source strengths by a factor of 4 to obtain reasonable $O_3$ predictions. Reynolds et al. (87) refer to the substantial loss of $NO_x$ observed in chamber irradiations using auto exhaust as opposed to that observed for pure hydrocarbon-$NO_x$ systems. Both groups speculated that the loss was probably a conversion to the aerosol phase. Lee et al. (89), found that the nitrate content of exhaust particulates was increased by a factor of 175 if the gases were first irradiated until the oxidation of NO to $NO_2$ was well under way. Crittenden's (90) data on nitrogen aerosol difunctionals show double diurnal maxima which roughly correspond to the hours of heaviest traffic. Difunctionals not containing nitrogen displayed diurnal behavior similar to secondary species such as PAN or $O_3$ with a single maximum in the afternoon. Thus, the chemistry of recently emitted auto exhaust probably involves conversion of NO to nitrate. The first step in this process may be the rapid oxidation of some NO to $NO_2$ before the exhaust can be substantially diluted.

Chan et al. (91) hypothesize that Reaction 38 may result in the oxidation of 25% of the NO in auto exhaust

$$NO + NO + O_2 \rightleftarrows 2\ NO_2 \tag{38}$$

to $NO_2$ during this dilution process. In addition to this, Reactions 39 and 40

$$NO + NO_2 + H_2O \rightleftarrows 2HONO \tag{39}$$

$$HONO + h\nu \rightarrow HO + NO \tag{40}$$

may provide a source of hydroxyl radicals to rapidly initiate the typical free radical NO oxidation pathway described in Chapter I. The estimates of the effectiveness of these processes in oxidizing NO to $NO_2$ depends upon assumptions concerning the dilution experienced by auto exhaust puffs on a molecular scale. Very little information is available concerning this phenomenon; however, it is reasonable to speculate that wind speed is an important factor in dilution of auto exhaust. The interaction of the wind with roughness elements on the ground is the major source of small-scale turbulence necessary for mixing of the exhaust puffs with surrounding air. Thus, the higher the wind speed, the less important the above reactions should become. The very low wind speed during operation 33 would tend to emphasize their effects.

The second factor which could result in conversion of NO to $NO_2$ in the morning was the turbulent entrainment of ozone-bearing air from above the inversion base. The $O_3$ concentration below 1000 feet and above the inversion base was 6 to 7 pphm by 0920 PST. From 0815 to 0915 PST, the mixing depth rose from 500 to 1000 feet. Thus, the $O_3$ in this time period could account for the oxidation of 3500 pphm-feet of NO. At 0915, the total $NO_x$ below the inversion was about 40,000 pphm-feet. Thus, during this time period, about 8-9 percent of the total nitrogen oxides could have been oxidized by direct reaction with ozone.

Thus, the injection of $NO_x$ as 35% $NO_2$ is a reasonable estimate of the effects of various localized processes which affect the $NO_2/NO_x$ ratio.

## Acetaldehyde Injection

Another modification of the experimental procedure was the addition of acetaldehydes to the hydrocarbon mixture for all the runs during October. Dimitriades and Wesson (92) stated that the total aldehyde levels in auto exhaust from automobiles at that time was about 5 percent of the total hydrocarbon on a carbon atom basis. They reported the typical composition of exhaust aldehydes in mole percent as follows:

| | |
|---|---|
| formaldehyde | 60 |
| aliphatic with more than 1 carbon | 32 |
| benzaldehyde | 5 |
| aromatic with more than 7 carbons | 3 |

The contributions of exhaust aldehydes to the reactivity of a mixture containing the typical constituents of auto exhaust is a function of aldehyde type. Aldehydes react primarily in three ways: (1) photolysis to give radicals; (2) photolysis to give stable species; and (3) reaction with hydroxyl radicals.

Formaldehyde, when photolyzed to radicals, produces two hydroperoxy radicals, since $k_{4.6}$ is

$$CH_2O + h\nu\ (\lambda < 3700\ \mathring{A}) \rightarrow H + HCO \tag{41}$$

$$H + O_2 \rightarrow HO_2 \tag{42}$$

$$HCO + O_2 \rightarrow CO + HO_2 \tag{33}$$

$$HCO + O_2 + M \rightarrow HCOO_2 + M \tag{43}$$

expected to be greater than $k_{4.7}$ (8). On HO attack, formaldehyde yields one $HO_2$ radical (by way of HCO).

$$HO + CH_2O \rightarrow H_2O + HCO \tag{44}$$

On photolysis to radicals, acetaldehyde yields one $HO_2$ (by way of HCO) and the $CH_3$ radical. $CH_3$ may participate in further chain oxidation, to convert one NO to $NO_2$ or to generate another $HO_2$. On hydrogen abstraction by an oxidizing agent such as HO, acetaldehyde may produce PAN when NO concentration is low, or may oxidize two NO molecules to $NO_2$ and regenerate an $HO_2$ by chain degradation. Thus, the principal difference between the effects of formaldehyde and acetaldehyde from a mechanistic point of view is that formaldehyde is expected to have a greater effect on NO to $NO_2$ conversion at the beginning of a run, while higher aliphatic aldehydes have the potential for slightly greater direct contributions to the conversion of NO to $NO_2$ per carbon atom over a longer time. In the outdoor chamber, it may be expected that the effects of an early initial production of $HO_2$ would be more important than the longer term effects since timing of events is quite important under diurnal light variation. Also, it was thought from the September simulations that conversion of NO to $NO_2$ was slower than the LARPP runs in the early morning. Thus, it was decided to add aldehydes in amounts to simulate the effects of aldehydes in the early portion of the runs.

Because formaldehyde is difficult to inject (adsorbs to walls of manifold and chamber), it was decided to simulate the effects of all aldehydes by addition of acetaldehyde. The photolysis rate constant, considering only radical producing photolysis, for formaldehyde is almost twice that for acetaldehyde in simulated sunlight (93).

Formaldehyde is 60 mole percent of exhaust aldehydes, and it would require the addition of twice that many moles of acetaldehyde on the basis of photolysis rate and roughly two times that again on the basis of $HO_2$ yield just after photolysis. Thus, it was believed that about four times as many moles of acetaldehyde would be required to simulate the initial effects of formaldehyde on the photochemical system. Since aldehydes are about 10 mole percent of the total hydrocarbons, it would require about 22 mole percent acetaldehyde to simulate the initial effects of the mixed aldehydes present in auto exhaust. This is roughly 10 percent of the total hydrocarbons on a carbon atom basis. Since the hydrocarbon injection rates based on source reconciliation estimates did not include an estimate of aldehydes in the air, it was decided to add acetaldehyde such that they would represent 10 percent of the total hydrocarbon on a carbon atom basis after addition, with no change in the amount of hydrocarbon mix added.

### Solar Time Correction

The run of October 6 was the first run for which the weather and experimental technique were both reasonably good, although the afternoon was partially cloudy. It was noted that the $NO$-$NO_2$ crossover and the onset of $O_3$ production were occurring at later times than during LARPP operation 33. It was thought that this may be due to differences between the solar time on November 5 in Los Angeles and the solar time on October 6 in Chapel Hill. The UV radiation measured during the LARPP operation at the downtown LAAPCD headquarters plotted against pacific standard time was compared to the UV measured on October 6 versus eastern daylight time. When the time scales were initially matched hour for hour, it was necessary to translate the October 6 UV curve 90 minutes to the left to make it match the LARPP curve. Thus, the simulation injection and dilution profiles had been applied to the chamber 1 1/2 hours too early in the solar day to match the events of LARPP. In subsequent runs, a correction was made for this by setting the internal computer clock back 90 min from eastern daylight time. The time for these runs is reported as "corrected to PST." Thus, injection and dilution events were made to occur at approximately the same solar time as the atmospheric events they simulate.

## Summary

The best simulations of LARPP operation 33 are runs 7 and 8 (October 12 and 13). The NO, $NO_2$, and $O_3$ profiles for these two experiments are shown with the LARPP zero-gradient region concentration profiles in Figures 76 and 77. It may be seen from Figure 76 that the $NO_2$ concentration in the simulation was above the observed $NO_2$ until about 1300 PST. The match between the observed and simulated NO was excellent. The $O_3$ concentration observed along the trajectory was a little less than twice that observed in the simulation.

On October 13, the experimental $NO_2$ values remained higher than the LARPP values for the entire experiment. The $O_3$ values, as in run 7, were below the observed ozone concentration during the morning, but ozone production after noon was more rapid. Thus, by 1400 PST the ozone had climbed to within 2 pphm of the observed value.

The hydrocarbon mix concentrations for both October 14 and 15 are compared with the NMHC regression line from source reconciliation in Figure 78. The mix concentrations represent the mix concentration in the chamber if none were removed by reaction since it was calculated from the concentrations of relatively unreactive n-pentane. The rate of removal of n-pentane is probably quite low, as may be seen from the nearly flat mix profiles at the end of these two experiments, after dilution and injection had terminated. The hydrocarbon concentrations were slightly below the source reconciliation line.

The differences between the profiles of secondary species in the simulation and along the LARPP trajectory will be considered in detail in Section 7.

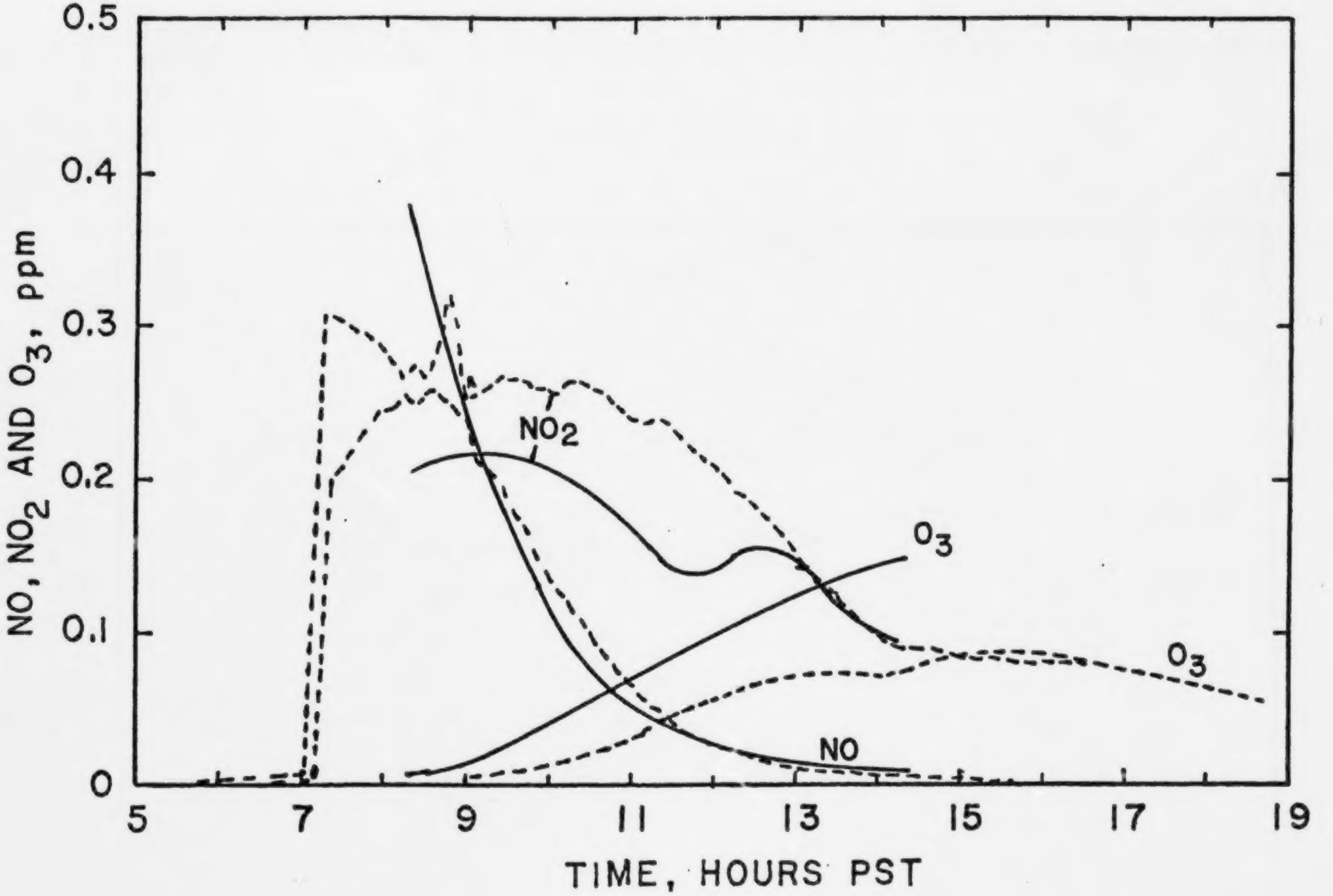

Figure 76. Comparison of NO, $NO_2$, and $O_3$ profiles for October 12 simulation (dashed line) and LARPP zero-gradient region (solid line).

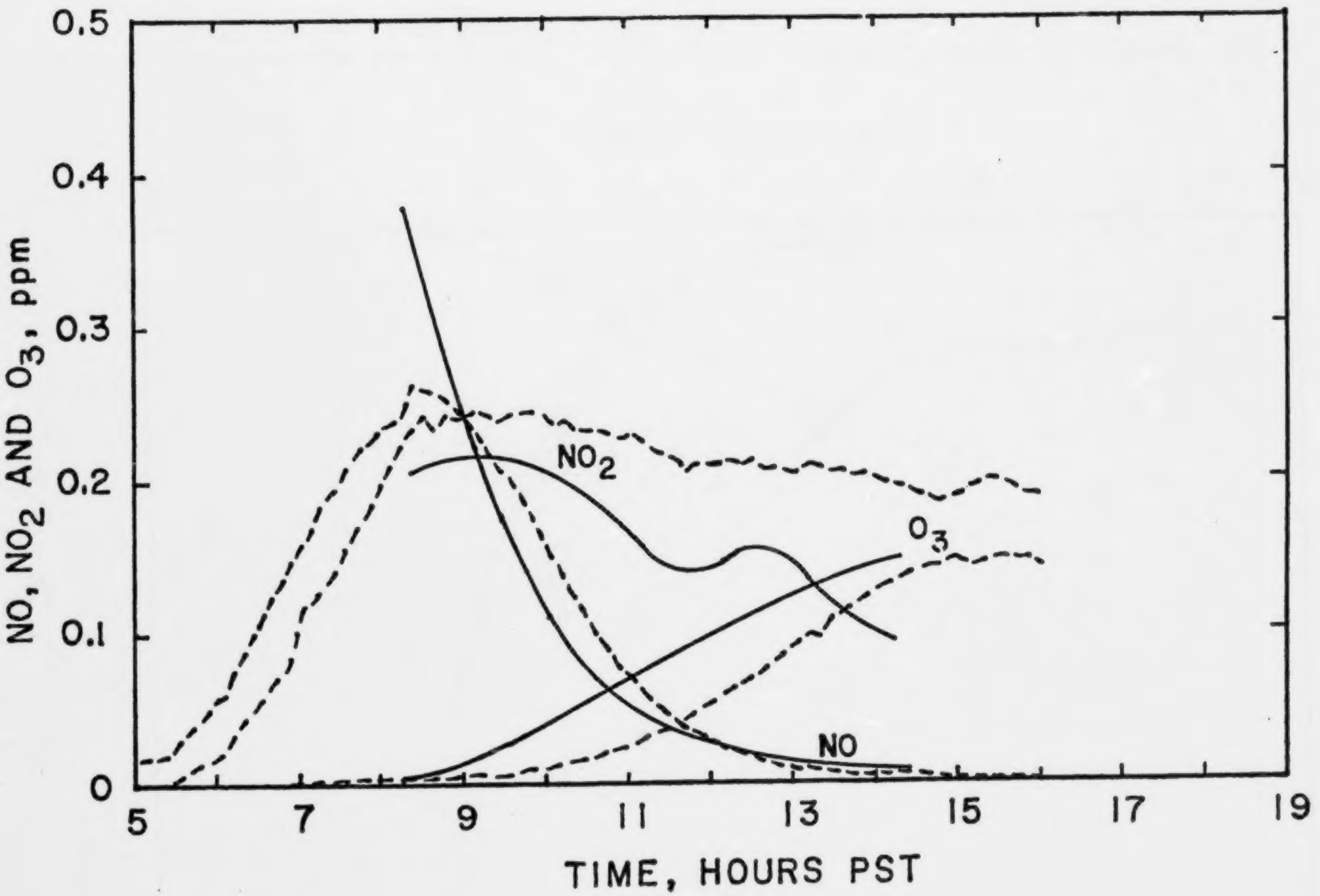

Figure 77. Comparison of NO, $NO_2$, and $O_3$ profiles for October 13 simulation (dashed line) and LARPP zero-gradient region (solid line).

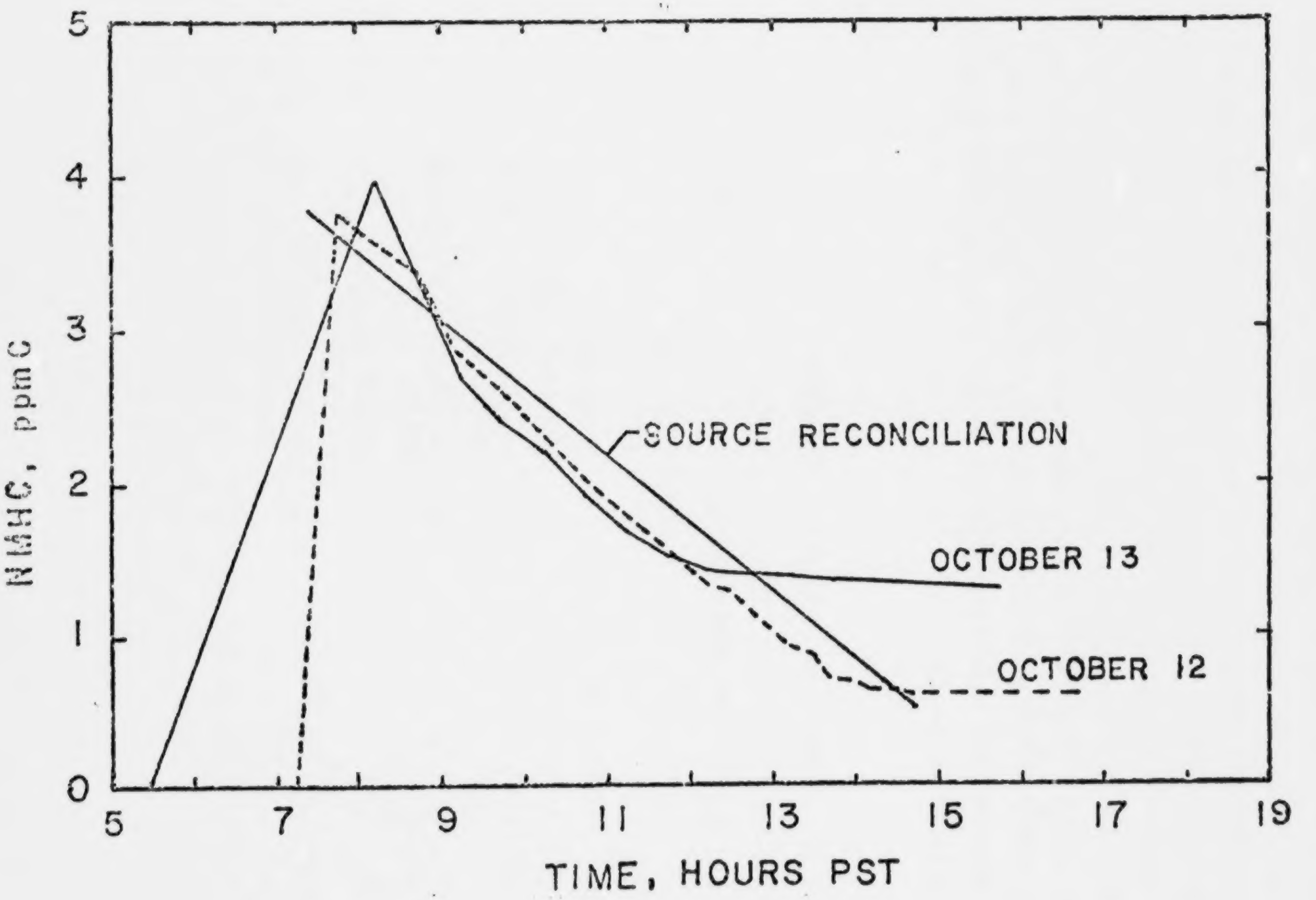

Figure 78. Comparison of NMHC source reconciliation regression line with NMHC mix concentrations estimated from n-pentane peak for simulations of October 12 and 13.

The static experiments performed during the experimental period were not carefully watched and checked to be sure the proper injections had been made; the simulation experiments consumed nearly all the time of those involved in the experimental work. Also, the concentrations employed were calculated from an earlier version of the INJECT program which did not take the mixing height into account. These concentrations are higher than would be used from the total injection over the total volume employed in the simulation experiments. The hydrocarbon concentration should have been 2 ppmC with an $NO_x$ concentration of 0.32 ppm. The experimental conditions and the ozone concentrations obtained are summarized in Table 13.

TABLE 13. SUMMARY OF CONDITIONS AND RESULTS OF STATIC RUNS

| Run No. | Date | Initial Conditions |  |  |  | Weather | Ozone, ppm |  |
|---|---|---|---|---|---|---|---|---|
|  |  | HC, ppmC | $NO_x$, ppm | $NO_2$, % | $HC/NO_x$ |  | @1400 PST | Maxi. |
| 1 | Sept. 1 | 2.96 | 0.56 | 20 | 5.29 | overcast | 0.03 | 0.19 |
| 2 | Sept. 6 | 3.90 | 0.53 | 28 | 7.36 | overcast morn. | 0.03 | 0.33 |
| 3 | Sept. 25 | 4.85 | 0.55 | 40 | 8.82 | foggy until 10:30 | 0.10 | 0.59 |
| 4 | Oct. 4 | 3.44 | 0.50 | 20 | 6.88 | cloudy after 09:45 | 0.09 | 0.18 |
| 5 | Oct. 6 | 3.27 | 0.50 | 19 | 6.54 | partly cloudy after noon | 0.06 | 0.28 |
| 6 | Oct. 11 | 4.33 | 0.50 | 29 | 8.66 | partly cloudy after 11:30 | 0.23 | 0.26 |
| 7 | Oct. 12 | 4.38 | 0.50 | 21 | 8.76 | clear | 0.30 | 0.33 |
| 8 | Oct. 13 | 3.84 | 0.50 | 22 | 7.68 | clear, warm | 0.40 | 0.45 |
| 9 blue | Oct. 15 | 1 | 0.16 | 20 | 6.25 | clear | 0.12 | 0.17 |
| 9 red | Oct. 15 | 1.5 | 0.24 | 20 | 6.25 | clear | 0.17 | 0.27 |

Based on the results from the three clear days, as shown in Figure 79, the increase of $O_3$ produced with initial hydrocarbon is noted for experiments with a small range of $HC/NO_x$ ratios. It may be concluded that a static experiment with 2 ppmC hydrocarbon mix and a $HC/NO_x$ ratio similar to these runs would produce more ozone than was observed along the LARPP trajectory (0.15 ppm at 1400 PST) or in the simulation experiments.

In experiment number 10, October 16, the effect of the presence of material remaining from the previous day was tested. The chamber contents from the 1 ppmC static run the day before had been diluted until the ozone reached about 8 pphm. This was to allow for dark reactions of ozone during the night, and was estimated to leave 5 to 6 pphm by morning. In addition, some of the diluent air was drawn from the red side of the chamber which contained an active second-day photochemical system. While this experiment was not a direct simulation of LARPP conditions, it may in an exaggerated way, demonstrate the effect of convective entrainment of the photochemical system above the inversion base observed in the morning of operation 33. The reactions were greatly accelerated and the experiment produced more $O_3$ than was observed along the LARPP trajectory.

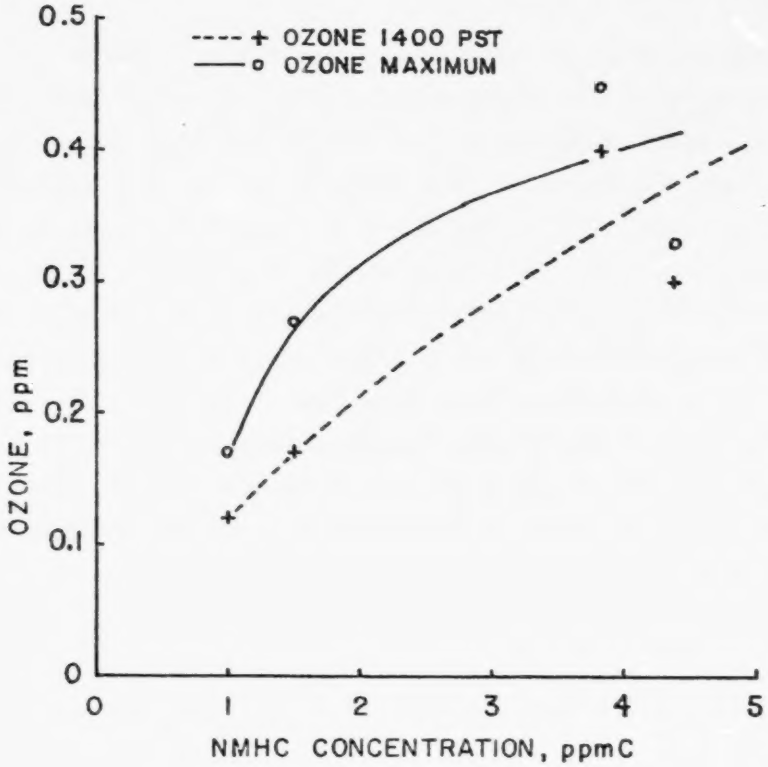

Figure 79. $O_3$ concentrations at 1400 hours and maximum produced versus initial NMHC concentration during static experiments on clear days.

# SECTION 7

# DISCUSSION

The results of experimental simulations were presented in the previous chapter. The simulations of October 12 and 13, 1976, most closely simulate the precursor emissions and dilution which occurred along the trajectory in LARPP operation 33. Several important variables, however, were not under the control of the experimenter, namely, solar radiation, temperature and reactant inhomogeneity. The effects of these factors on the simulation must be evaluated in order to explain differences between the simulation results and the LARPP data. Only the experiments of October 12 and 13 (runs 7 and 8) will be considered in detail.

## SOLAR RADIATION

Solar radiation influences the formation of photochemical smog in many ways. The most direct effect is that the photolysis rate of $NO_2$ and other species which photolyze is dependent upon the intensity and spectral distribution of solar radiation. Solar radiation also influences air temperature, mixing depth, and wind field characteristics. For the purpose of comparing the simulation to the LARPP operation, only the effects on photolysis rate need be considered in this section. The effects of temperature will be considered elsewhere, and the other effects were accounted for in specifying the conditions for simulation.

The photolysis of $NO_2$ is the most important photochemical reaction in the smog system. As discussed in Chapter I, only photons with wavelengths less than about 410 nm are likely to cause photodissociation of $NO_2$ after absorption. The intensity of actinic radiation in the zero-gradient region at any time of day is a function of zenith angle of the sun, the concentration of absorbing species and scattering particles (particularly along the path of the direct solar beam), and the albedo of the earth's surface.

Calvert (26) computed $k_1$ for LARPP operation 33 based on solar constant data of Johnson (94) and Ackerman (95) which is roughly 10 percent higher than the values of some other investigators. For estimating the attenuation due to $O_3$ absorption, aerosol, and molecular scattering, Calvert used the "standard relations adjusted to the conditions that approximate Operation #33" from Leighton (3). An $O_3$ column of 2.8 mm was employed but no reference was made to the estimates of the water and dust factors used to calculate the transmissity for particulates. Calvert's estimates of the ultraviolet (UV) (290-390 nm) flux on a horizontal surface above the boundary layer agrees incredibly well with actual UV radiometer measurements from Mt. Disappointment. When an attempt was made to duplicate these calculations using Johnson's solar constant data, the same $O_3$ column and Leighton's tabulated attenuation coefficients for molecular scattering, it was found that some adjustment of the water and dust coefficients was necessary to obtain agreement with Mt. Disappointment radiometer values from operation 33. Figure 80 shows radiometer readings and the estimated UV flux from theory for a water vapor factor of 2 and a dustiness factor of 2. These water and dust values seem to be somewhat high compared with those cited by Leighton; however, it was more important to obtain a good fit with the radiometer. It may be that the solar constant data employed is too high, thus forcing the use of higher water and dust attenuation to fit the observations.

Calvert (26) calculated $k_1/k_3$ taking into account absorption within the boundary later by $NO_2$, reflection at the earth's surface and attenuation of the reflected beam by $NO_2$. He compared the $k_1/k_3$ values for albedoes of 0, 0.25 and 0.5 with $[O_3][NO]/[NO]$ from the LARPP data. Under homogeneous conditions, $k_1/k_3$ should be approximately equal to the concentration ratio. The best estimate of albedo for wavelengths important in $NO_2$ photolysis is about 0.05 according to Peterson (96). Interpolating to this albedo in Calvert's figure, it was noted that the

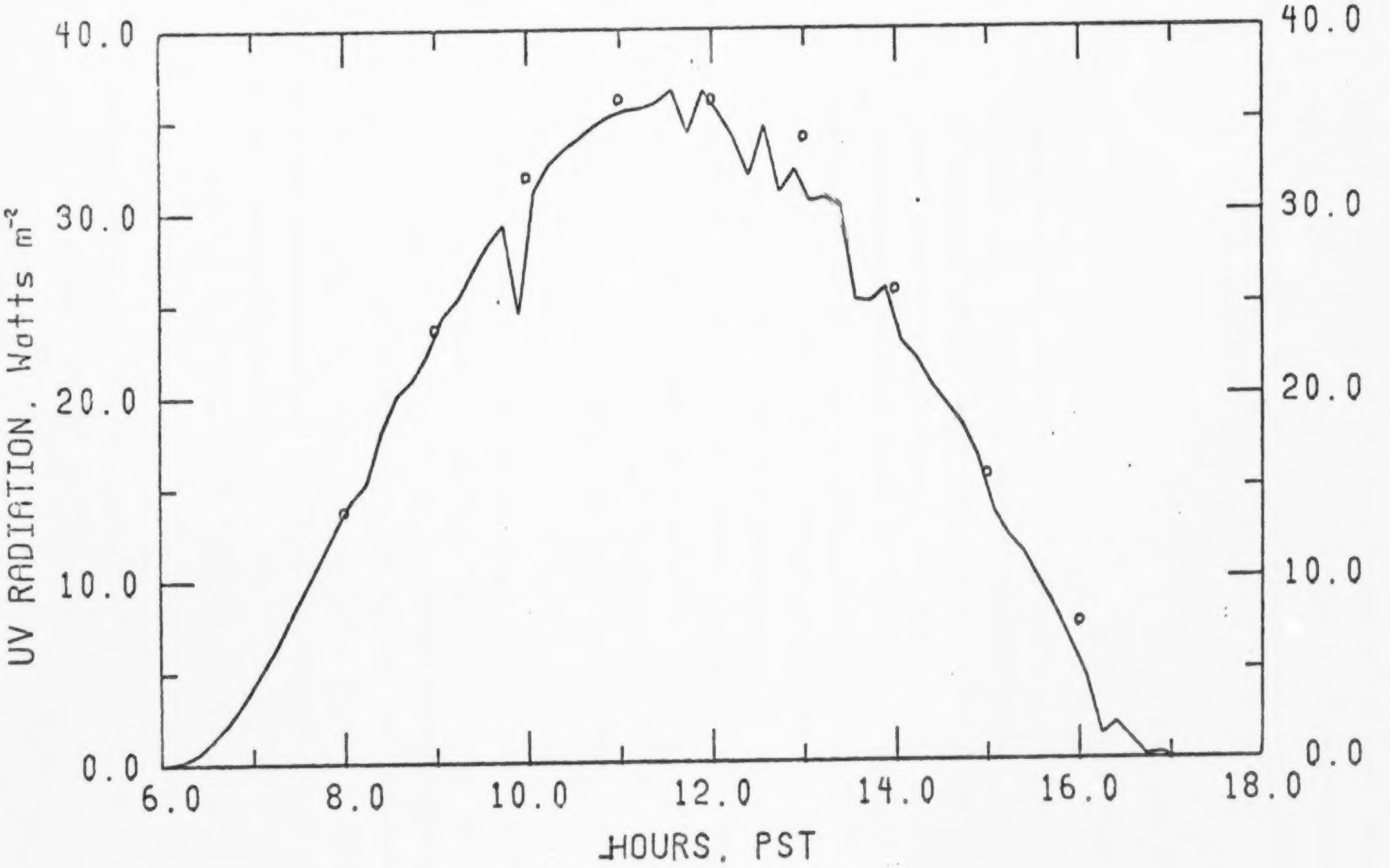

Figure 80. Comparison of Mt. Disappointment UV radiometer measurements with theoretical calculation of UV radiation from 290 to 390 nm above the boundary layer in Los Angeles on November 5, 1973.

vast majority of ratio points fall well above the $k_1/k_3$ line. Calvert noted that this may be due to inhomogeneity.

Computations were performed to estimate $k_1$ and $k_1/k_3$ as described in Appendix D. The resulting values are shown in Figures 81 and 82.

## ATMOSPHERIC INHOMOGENEITY

### General Characterization

Before the effects of atmospheric inhomogeneity can be estimated, the general nature of inhomogeneity must be considered. The mixing of one fluid into another takes place by two distinct processes when the fluids are miscible (97). First, the fluid is broken up into clumps, or packets. The shape of the clumps will depend upon the mechanism of mixing. For instance, the shape of clumps of auto exhaust of a moving auto will probably be somewhat elongated in the direction of motion. The mean size of these clumps decreases with continued mixing so long as the size of some of the clumps is greater than the smallest scale size of turbulent eddies. It should also be noted that if the clump sizes are much greater than the scale size of eddies, then breakup of the clumps occurs only around the edges of the clumps, and thus is rather slow.

Concurrently, molecular diffusion occurs across the boundaries of the clumps. This has the effect of diluting the material within the clumps and the boundary between clumps and diluent fluid becomes progressively blurred. This process, given sufficient time, will reduce a mixture of miscible fluids to uniformity even in the absence of turbulence although it is rather slow unless turbulence has reduced the size of the clumps. If diffusion does not occur (as with immiscible fluids), then the fluids cannot be made homogeneous regardless of turbulence.

### The Scales of Inhomogeneity

In considering the effects of inhomogeneity on the interpretation of the LARPP simulation, it is useful to distinguish between two distinctly different effects.

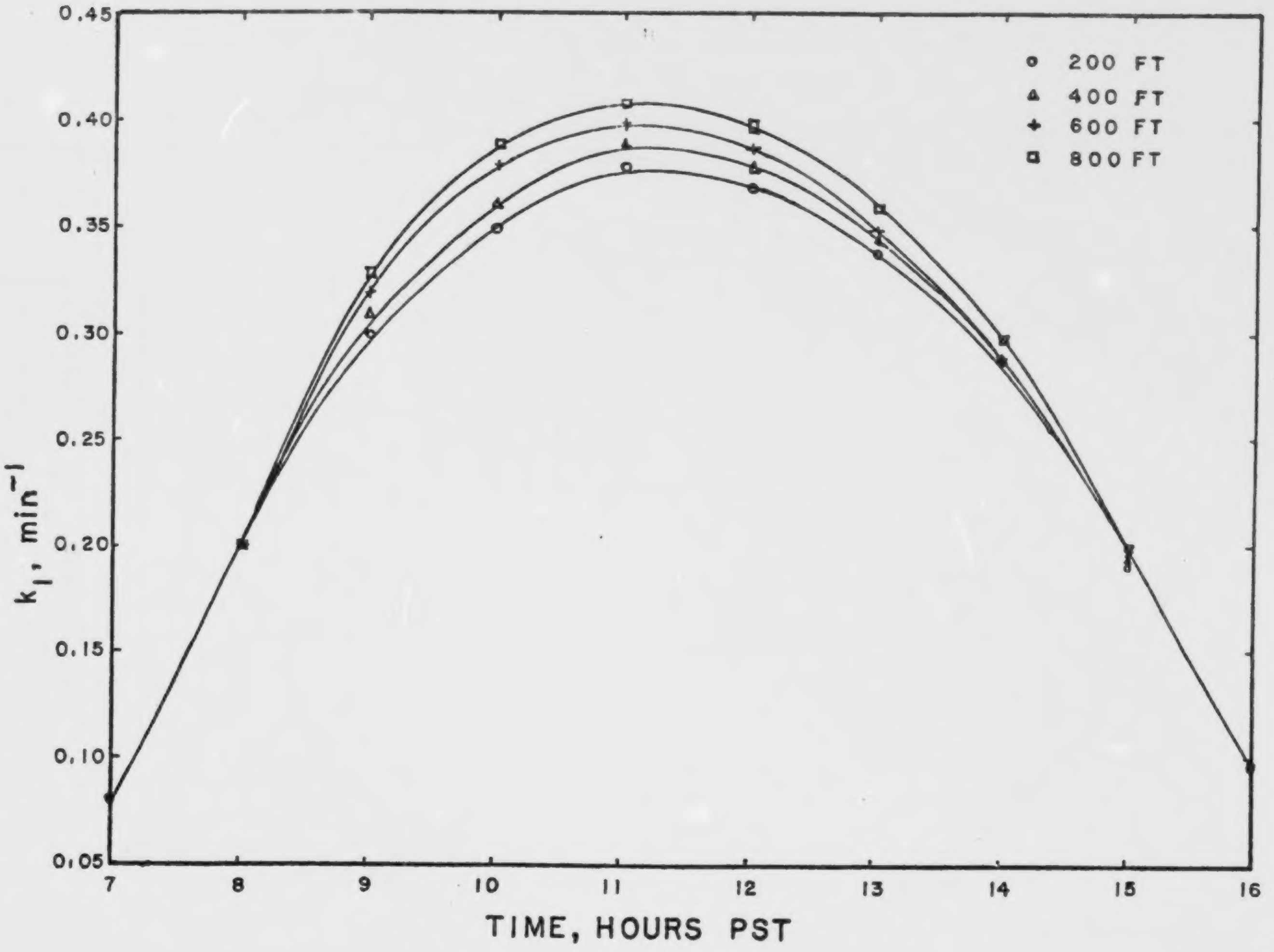

Figure 81. Theoretical estimates of $k_1$, the rate constant of $NO_2$ photolysis at four altitudes above ground level in Los Angeles on November 5, 1973.

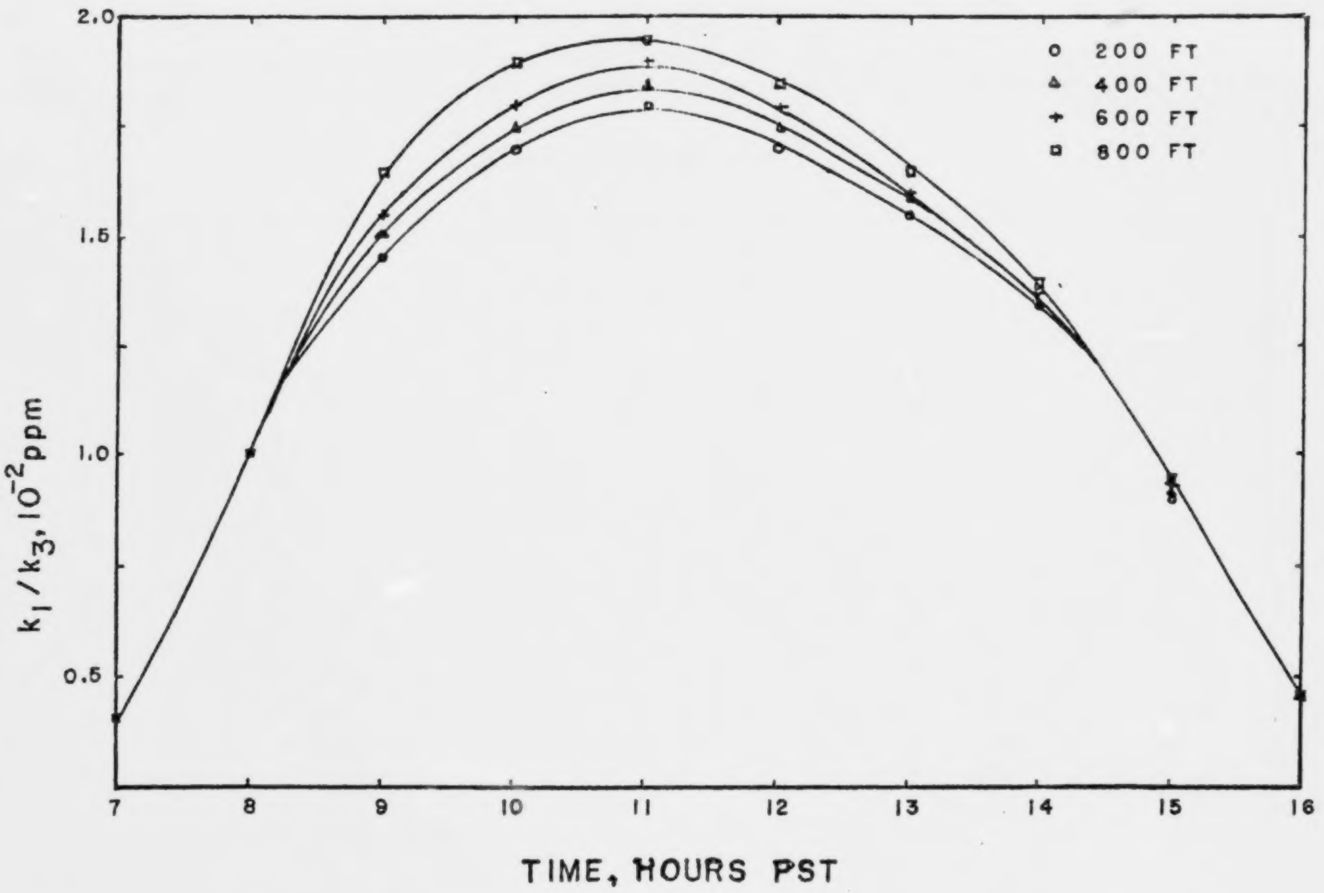

Figure 82. Theoretical estimates of $k_1/k_3$, the ratio of the $NO_2$ photolysis rate constant to the rate constant of the NO-$O_3$ reaction at four altitudes above ground level in Los Angeles on November 5, 1973.

### Small Scale Inhomogeneity --

Small scale inhomogeneity affects individual measurements. Since each instrument has a finite averaging time and the helicopters were in motion, each measurement is a spatial composite, a weighted average concentration over some distance. Because many of the species are reactive, their spatial average concentrations may not be identical to their concentrations under well-mixed conditions. To demonstrate this effect, consider two parcels of air which have arrived at a given altitude level. Parcel 1 has just arrived from ground level and contains 0.005 ppm of $O_3$, 0.09525 ppm of $NO_2$, and 0.30476 ppm of NO. Parcel 2, just entrained from above the inversion, contains 0.05 ppm of $O_3$, 0.03788 ppm of $NO_2$, and 0.01212 ppm of NO, as shown in Figure 83. Both parcels are in photostationary state at a $k_1/k_3$ of 0.016 ppm. If measurements of the NO, $NO_2$, and $O_3$ are taken within either air parcel, the photostationary state equation for ozone,

$$\frac{k_1}{k_3} = \frac{[NO]\ [O_3]}{[NO_2]} \tag{17}$$

should be very nearly correct. The only processes causing deviations from this equality are a few reactions which may compete for $O_3$ with the NO reaction (for example, reaction with $NO_2$ or alkenes). On the other hand, consider an instrumented aircraft measuring NO, $NO_2$, and $O_3$ concentrations which crosses the air parcel boundary in such a way that the instrument readings represent the average of the concentrations within the two air parcels: 0.02750 ppm of $O_3$, 0.06657 ppm of $NO_2$, and 0.15844 ppm of NO. If the $k_1/k_3$ is calculated from Equation 17 using measured concentrations, a value of 0.065 ppm is founded: about 4 times greater than the true $k_1/k_3$. This is quite similar to Calvert's (26) results. Inhomogeneity on a sub-measurement scale was probably responsible for a large portion of the disagreement of the theoretical $k_1/k_3$ and the estimates from Equation 17 in Calvert's results.

When such small scale inhomogeneity exists, the average rate of reactions of order greater than one is not necessarily equal to the rate based on mean concentrations. In the example given above, the reason

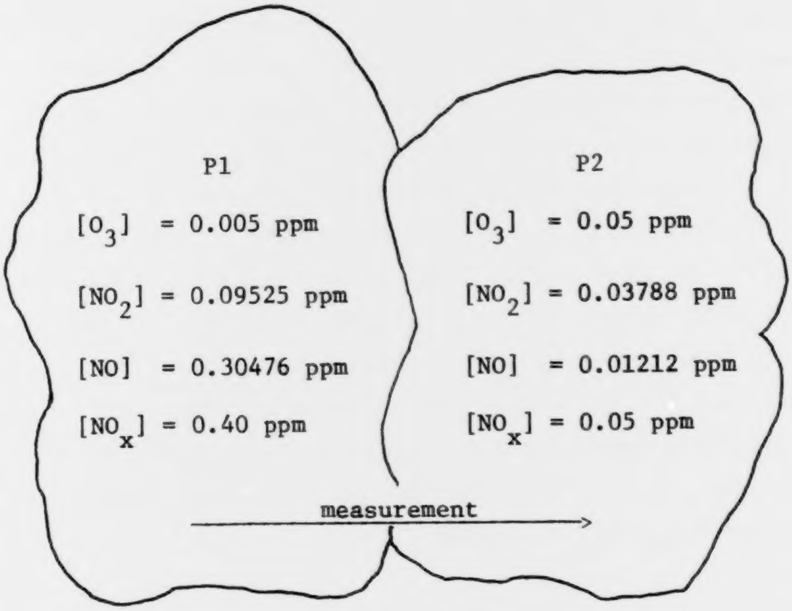

Figure 83. Two hypothetical parcels of air at photostationary state at $k_1/k_3 = 0.016$ ppm.

for the large difference between the true $k_1/k_3$ and $[NO][O_3]/[NO_2]$ is that the rate of the NO-$O_3$ reaction is much slower than would be calculated from the average NO and $O_3$ concentrations. Let the instrument readings for NO and $O_3$ be represented by $[\hat{NO}]$ and $[\hat{O}_3]$ (spatial averages from a single measurement) and the deviations of the true concentration from the instrument reading at any point in space be represented by $[NO]'$ and $[O_3]'$. Then the actual concentrations at a point are given by

$$[NO] = [\hat{NO}] + [NO]' \qquad (18)$$

$$[O_3] = [\hat{O}_3] + [O_3]' \qquad (19)$$

Substituting these concentrations into the rate equation for the NO-$O_3$ reactions yields:

$$-\frac{d[O_3]}{dt} = k_3(([\hat{NO}] + [NO]')\ ([\hat{O}_3] + [O_3]')) \qquad (20)$$

the rate of reaction at any point. The average rate of reaction over the spatial region from which the $[\hat{NO}]$ and $[\hat{O}_3]$ were measured requires averaging both sides of the above equation.

$$-\frac{d[\hat{O}_3]}{dt} = k_3(\widehat{[\hat{NO}][\hat{O}_3]} + \widehat{[\hat{NO}][O_3]'} + \widehat{[\hat{O}_3][NO]'} + \widehat{[NO]'[O_3]'}) \qquad (21)$$

$$\widehat{[\hat{NO}][\hat{O}_3]} = [\hat{NO}][\hat{O}_3] \qquad (22)$$

$$\widehat{[\hat{NO}][O_3]'} = [\hat{NO}]\widehat{[O_3]'} = 0$$

$$\widehat{[NO]'[\hat{O}_3]} = \widehat{[NO]'}[\hat{O}_3] = 0$$

Thus,

$$-\frac{d[\hat{O}_3]}{dt} = k_3([\hat{NO}][\hat{O}_3] + \widehat{[NO]'[O_3]'}) \qquad (23)$$

The fluctuation term on the right of Equation 23, $\widehat{[NO]'[O_3]'}$, is equal to the covariance of the actual NO and $O_3$ concentrations (71). Thus, the equation may be written

$$-\frac{d[\hat{O}_3]}{dt} = k_3([\hat{NO}][\hat{O}_3] + \text{cov}(NO,O_3)) \tag{24}$$

Under photostationary state conditions the rate of ozone destruction by NO is approximately equal to the rate of $NO_2$ photolysis. Thus, the ratio of $k_1$ to $k_3$ under inhomogeneous conditions is:

$$\frac{k_1}{k_3} = \frac{[\hat{NO}][\hat{O}_3] + \text{cov}(NO,O_3)}{[\hat{NO}_2]} \tag{25}$$

where the hat concentrations represent single instrument readings from composite sampling such as those obtained by aircraft cutting across many air parcels during a single measurement.

In the above example concerning the two air parcels, the covariance of NO and $O_3$ is -0.00329 $ppm^2$; this yields the correct value of $k_1/k_3$ in Equation 25.

Equation 25 is very useful. If $k_1/k_3$ may be estimated by some method and if the NO, $NO_2$, and $O_3$ concentrations are measured, the covariance of NO and $O_3$ may be estimated in the atmosphere for each measurement. It should be repeated that in Equation 25, the hat concentrations represent single measurement values. In a well-mixed smog chamber the covariance is zero; thus, Equation 25 reduces to the more familiar form under homogeneous conditions.

### Large Scale Inhomogeneity --

Large scale inhomogeneity results in variation of helicopter measurements about the pattern means, rather than a variation of the composition of the material comprising a single sample. Based on the helicopter speed, the scale of such inhomogeneity is on the order of $5x10^2$ feet, the distance between 6-second measurements. This scale of inhomogeneity is best shown by the projection plots in Figures 11 through 17. This variability results in an alteration of the photostationary state equation for the pattern average ozone concentration.

Solving for the photostationary state ozone in Equation 25 yields:

$$[\hat{O}_3] = \frac{k_1}{k_3}\left(\frac{[\hat{NO}_2]}{[\hat{NO}]}\right) - \left(\frac{\mathrm{cov}(NO,O_3)}{[\hat{NO}]}\right) \qquad (26)$$

Thus, the mean photostationary state $O_3$ concentration around a helicopter pattern is

$$\overline{[\hat{O}_3]} = \frac{k_1}{k_3}\,\overline{\frac{[\hat{NO}_2]}{[\hat{NO}]}} - \overline{\frac{\mathrm{cov}(NO,O_3)}{[\hat{NO}]}} \qquad (27)$$

Since the covariance term is, for most measurements, negative, the atmosphere is capable of maintaining a greater mean photostationary state $O_3$ concentration than is the smog chamber *at the same mean $NO_2$ to NO ratio and the same $k_1/k_3$*.

In the above discussion, it was not the intention to imply that the NO-$O_3$ reaction is the only one affected by inhomogeneity in the atmosphere. Because the NO-$O_3$ reaction is the most rapid second order reaction in the atmosphere (in ppm/min), it is the best candidate for diffusion limitation. Other reactions whose rates approach those of NO-$O_3$ may be diffusion limited, for instance some of the reactions of HO or organic radicals (71). In general, the criterion for judging the importance of inhomogeneity for a particular reaction is that the rate of chemical reaction (in concentration/time units) must be at least as rapid as the rate at which turbulent mixing tends to bring the reactants together. Donaldson and Hilst (72) state this principle and characterize the potential for inhomogeneous effects by the ratio

$$N = \frac{2D}{\lambda^2 K_\alpha \overline{C}_\alpha} \qquad (28)$$

where D is the molecular diffusivity of the reactants (assumed to be equal for two different reactants, $\lambda$ is the dissipative scale length of turbulence in the atmosphere (taken to be 10 cm), $K_\alpha$ is the reaction rate constant and $\overline{C}_\alpha$ is the reactant concentration. In evaluating N, Donaldson and Hilst let $\overline{C}_\alpha$ equal one ppm for all reactions, which leads to exceedingly high values for the rates of some reactions involving species which have concentrations much lower than one ppm in the atmosphere. Thus, their conclusions concerning the importance of inhomogeneity for particular reactions must be looked on with skepticism.

The influence of inhomogeneities, while seeming to have a strong influence on the $O_3$ along the trajectory did not seem to greatly effect the NO or $NO_2$ profiles except as pointed out in Section 6 (rapid oxidation of NO in relatively undiluted, irradiated auto exhaust). Thus, in this work the primary concern is with the increased photostationary state $O_3$ concentration relative to the average $NO_2$ and NO.

In exploring the theoretical aspects of the effects of inhomogeneity, an effect of light on the ozone concentration was also shown, as in Equations 26 and 27.

The average $NO_2/NO$ ratio was also computed for each helicopter pattern so that the pattern mean $\mathrm{cov}(NO,O_3)/[\widehat{\mathrm{NO}}]$ could be estimated. This is the portion of the photostationary state $O_3$ concentration which resulted from atmospheric inhomogeneity. The average product of the NO and $O_3$ concentrations was also determined so that the pattern average covariance could be calculated as follows:

$$\overline{\mathrm{cov}(NO,O_3)} = \frac{k_1}{k_3}\,\overline{[NO_2]} - \overline{([NO][O_3])} \tag{29}$$

Figure 84 shows the pattern average covariances of NO and $O_3$. It is shown here that the covariance reached large negative values above the inversion base in the early morning. Within the zero-gradient region, there is no temporal trend evident; values fluctuated about a mean of about $-1 \times 10^{-3}$ ppm$^2$.

It should be pointed out that these are simply estimates of the true atmospheric covariances. There are several possible sources of error in these estimates. (1) Errors in estimating $k_1$ are possible but are not likely to be large since excellent agreement was obtained between theory and the radiometer on Mt. Disappoint. (2) The instrumental error, including interference, is another possibility. The values for $NO_2$ probably include PAN and possibly nitric acid. This would tend to

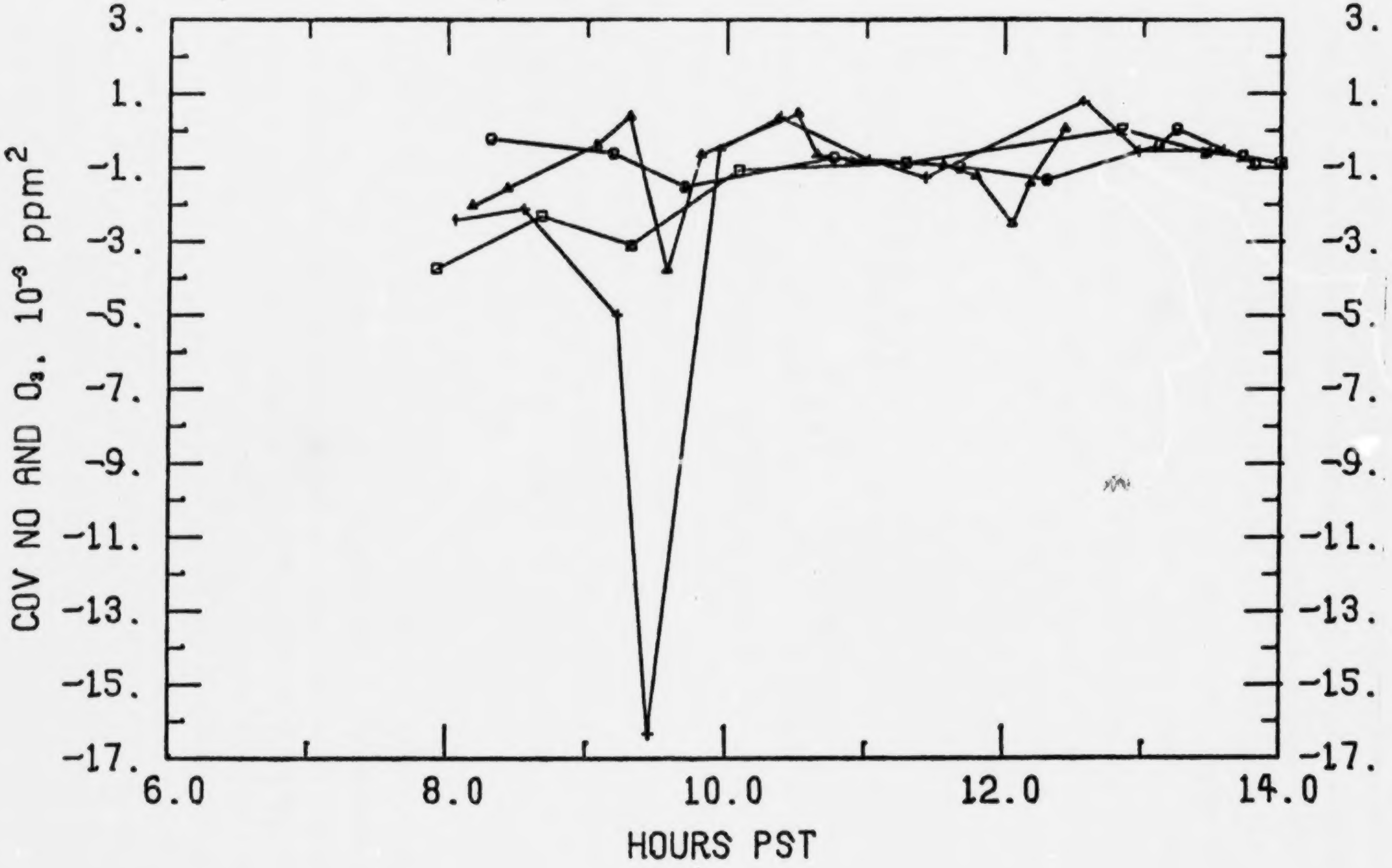

Figure 84. Estimated helicopter pattern average covariance of NO and $O_3$ from Operation 33.

lead to some overestimation. (3) In general, the instrument responses are weighted averages of concentrations in air from more than one air parcel. The accuracy of estimation of the average concentration is affected by the shape of instruments' weighting functions, the helicopter air speed, the size of the air parcels and the true variability of pollutant concentrations from one parcel to the next.

The pattern average ratios of the covariance to the NO concentration are shown in Figure 85. It is interesting to note that the most negative values of this ratio occurred in the morning above the inversion base. Inhomogeneity seems to account for 3 to 5 pphm of $O_3$ in this region. Thus, the absence of vigorous turbulent mixing in this region allowed segregation of $O_3$ and NO. The high value of $\mathrm{cov}/[\widehat{\mathrm{NO}}]$ at 1257 PST resulted from a small increase in the average $NO_2$ concentration. The trajectory seems to have passed over a source of $NO_2$ at this time. Emission of $NO_2$ would tend to produce air parcels with higher co-existent concentrations of both NO and $O_3$. For the purpose of comparing smog chamber results with the LARPP trajectory, the $\mathrm{cov}/[\widehat{\mathrm{NO}}]$ values from outside the zero-gradient region need not be considered. Also, the high positive value at 1257 PST seems to have affected boundary-layer $O_3$ for a very short time and the brief emission of $NO_2$ was not simulated since it seemed to have little affect on atmospheric $O_3$. Thus, excluding these points, the mean $\mathrm{cov}/[\widehat{\mathrm{NO}}]$ was found to be -1.90 pphm with a standard deviation of 2.24 pphm.

An interesting feature of the data is that the variability of $\mathrm{cov}/[\widehat{\mathrm{NO}}]$ exceeds the variability of the pattern mean ozone. A hand-fitted smooth curve was passed through the pattern mean $O_3$ points in Figure 27 and the deviations of pattern means from this line were measured. The root mean square deviation from the line was 0.58 pphm; this is only one-fourth the deviation exhibited by $\mathrm{cov}/[\widehat{\mathrm{NO}}]$. Thus, it must be concluded that, while Equation 27 is applicable at any time, it does not fully describe the dynamic behavior of the relationships among $O_3$, $NO_2$, NO, and the covariance of NO and $O_3$. This topic is discussed in Appendix E. The covariance of NO and $O_3$ is the result of processes which tend to reduce inhomogeneity (such as fresh emission and

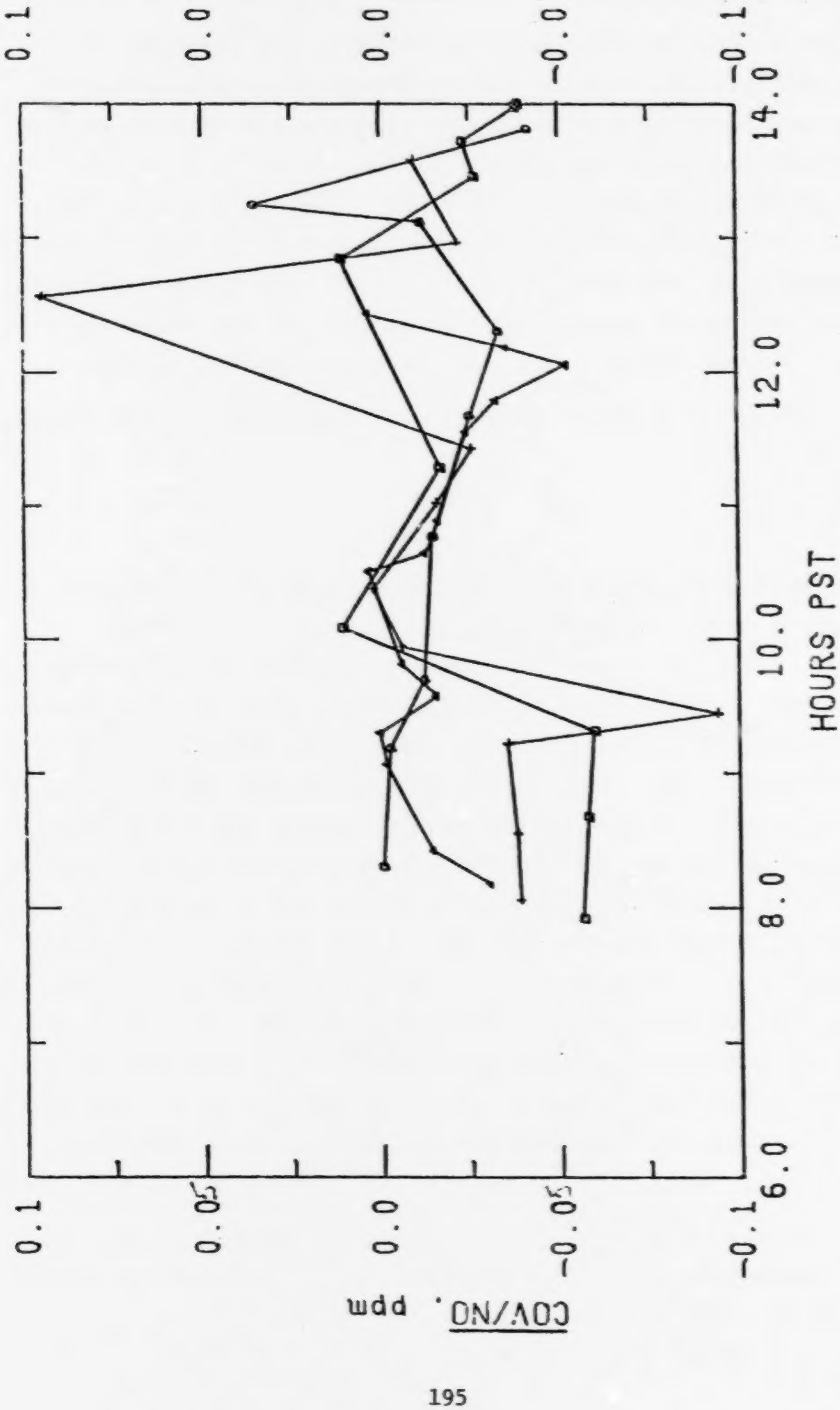

Figure 85. Estimated helicopter pattern average ratio of covariance of NO and $O_3$ to the NO concentration.

photochemical oxidation of NO). The average $O_3$ concentration is, in general, not as greatly affected as is $\overline{\mathrm{cov}/[\widehat{\mathrm{NO}}]}$. For instance, if turbulent mixing brings a portion of the atmosphere to homogeneity in which the covariance had originally been negative, the increase in the $NO_2$ to NO ratio partially compensates for the loss of $O_3$ due to the mixing of parcels containing low $O_3$-high NO. (See Appendix E.) Thus, the use of the $\overline{\mathrm{cov}/[\widehat{\mathrm{NO}}]}$ estimated from the atmosphere to show the effects of inhomogeneity in comparing the LARPP data with the chamber simulation is correct; however, it must not be assumed that, if the atmosphere were well-mixed, it would maintain an $O_3$ concentration equal to the mean observed ozone minus $\overline{\mathrm{cov}/[\widehat{\mathrm{NO}}]}$. Clearly such mixing would change the $NO_2$ to NO ratio.

## TEMPERATURE

The effect of temperature on the photochemical reaction complex is just beginning to be understood from a mechanistic point of view. Experiments in the UNC outdoor smog chamber have shown possible temperature effects. Figure 86 shows three propylene experiments at nearly the same initial NMHC, NO, and $NO_2$ concentrations. There was very little difference in the solar radiation on these days; however, the temperature profiles did differ. October 15 was the coolest of these days for most of the day. At 0800 EDT, the temperature was about $47^{\circ}$ F rising to $77^{\circ}$ F by 1300 EDT. October 12 showed nearly the same temperature profile between 0800 and 1040 EDT. After 1100 EDT, the temperature remained 3 to $4^{\circ}$ F above the temperature on October 15. October 16 was hotter than the other two days for the entire run. From 0800 to 1115 EDT, the temperature profile was about 5 to $6^{\circ}$ F above the profile of October 12; this difference decreased to about $3^{\circ}$ F by 1300 EDT. In this series of runs, the maximum ozone produced increased with the temperature.

Jeffries et al. (52) developed a mechanistic explanation for the effect of temperature. A typical treatment of PAN formation and decomposition is the following:

$$CH_3C(O)O_2\cdot + NO \rightarrow NO_2 + CH_3C(O)O\cdot \quad (45)$$

$$k_{45} = 800\ ppm^{-1}\ min^{-1}$$

$$CH_3C(O)O_2\cdot + NO_2 \rightarrow PAN \quad (46)$$

$$k_{46} = 100\ ppm^{-1}\ min^{-1}$$

$$PAN \rightarrow NO_3 + CH_3\cdot + CO_2 \quad (47)$$

$$k_{47} = 3x10^{-3}\ min^{-1}$$

Recent work by Hendry et al. (98), indicates that reaction 47 is not significant. Instead PAN decomposition is the reverse of reaction 46:

$$PAN \rightarrow NO_2 + CH_3C(O)O_2 \quad (48)$$

$$k_{48} = 1.507x10^{17}\ exp(-12931/T)min^{-1}$$

$$k_{45} = 2.45x10^{3}\ ppm^{-1}\ min^{-1}$$

$$k_{46} = 7.36x10^{2}\ ppm^{-1}\ min^{-1}$$

The sequence of reactions 45, 46, and 48 is then analogous to the reactions of $NO_3$ and $N_2O_5$, reactions 6, 9, and 10.

Another similar reaction sequence is:

$$HO_2 + NO \rightarrow NO_2 + OH \quad (49)$$

$$HO_2 + NO_2 \rightarrow HONO + O_2 \quad (50)$$

$$HONO \xrightarrow{h\nu} NO + OH \quad (51)$$

Hendry (1976) suggested that reaction 50 is not an elementary reaction but goes by way of an intermediate.

$$HO_2 + NO_2 \rightarrow HOONO_2 \quad (52)$$

$$HOONO_2 \rightarrow HO_2 + NO_2 \quad (53)$$

$$HOONO_2 \rightarrow HONO + O_2 \quad (54)$$

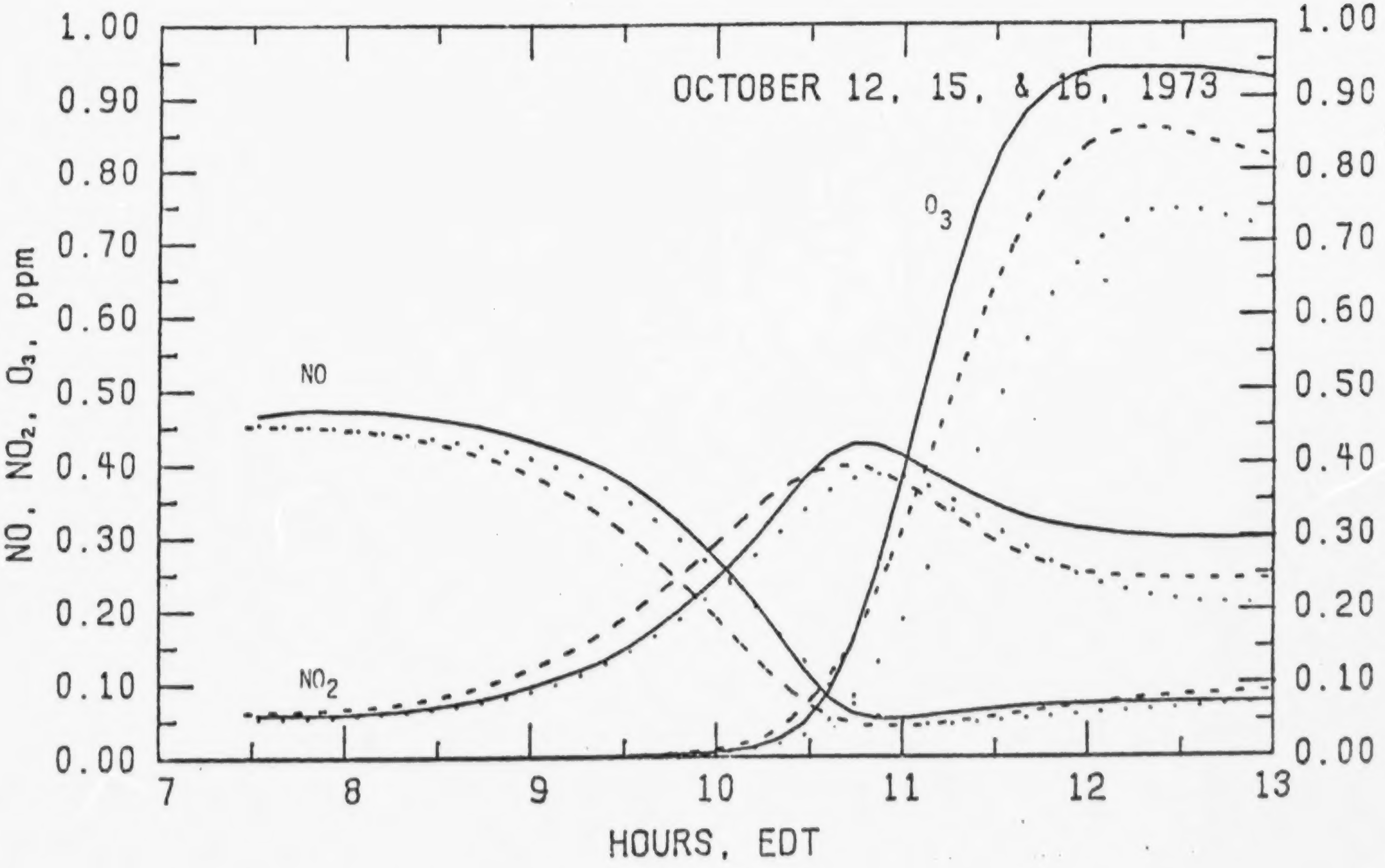

Figure 86. Comparison of NO, $NO_2$, and $O_3$ profiles from static propylene experiments in UNC outdoor chamber. Oct. 16 (______). NMHC = 3.88 ppmC; Oct. 12 (---), NMHC = 3.91 ppmC; Oct. 15 (....), NMHC = 3.88 ppmC.

The similarity of reactions 45, 46, and 48 with 49, 52, and 53 suggest that reaction 53 may have a large temperature dependence as does 48.

Under conditions of a typical diurnal temperature profile, reactions 45, 46, and 48 should have the effect of storing some quantity of $NO_2$ early in the day as PAN. As temperature increases, the equilibrium concentration of PAN decreases due to the increased rate of the decomposition reaction, causing a release of additional $NO_2$. This is the probable cause of most of the difference in the $NO_2$ profiles in Figure 87. This contributes to the $O_3$ concentration to the extent that it alters the $NO_2/NO$ ratio. At this time of day, however, this ratio is much more sensitive to changes in the NO concentration than changes in the $NO_2$ concentration. At lower temperatures, reactions 51 through 54 have the effect of converting $NO_2$ to NO, since reaction 54 can compete with 53 (at $77^o$ F, $k_{54}/k_{53}$ is about 1/12). As the temperature rises, the specific rate of 53 increases much more rapidly than the specific rate of 54 (at $93^o$ F, $k_{54}/k_{53}$ is about 1/25, and at $105^o$ F, it is about 1/60). Thus, the rate of conversion of $NO_2$ to NO by this pathway decreases with increasing temperature. This can greatly alter the $NO_2/NO$ ratio, which in turn changes the photostationary state $O_3$.

Jeffries et al. (52) presented three model runs for hydrocarbon mix using the same initial concentrations but different temperature profiles. The results are shown in Figure 87. It may be seen that morning temperature seems to have little effect but the afternoon temperature shows considerable effect on the $O_3$ concentrations produced. Note that the $NO_2$ and NO profiles are changed very little, but, since $O_3$ is a function of the ratio of $NO_2$ to NO, the $O_3$ profiles show a substantial temperature effect.

## DISCUSSION OF COMPARISONS

The direct comparison of the LARPP zero-gradient region concentrations with the simulation experiments of October 12 and 13 were presented in Figures 76 and 77. To evaluate how closely the chemistry in the chamber matched the chemistry in the atmosphere, the effects of

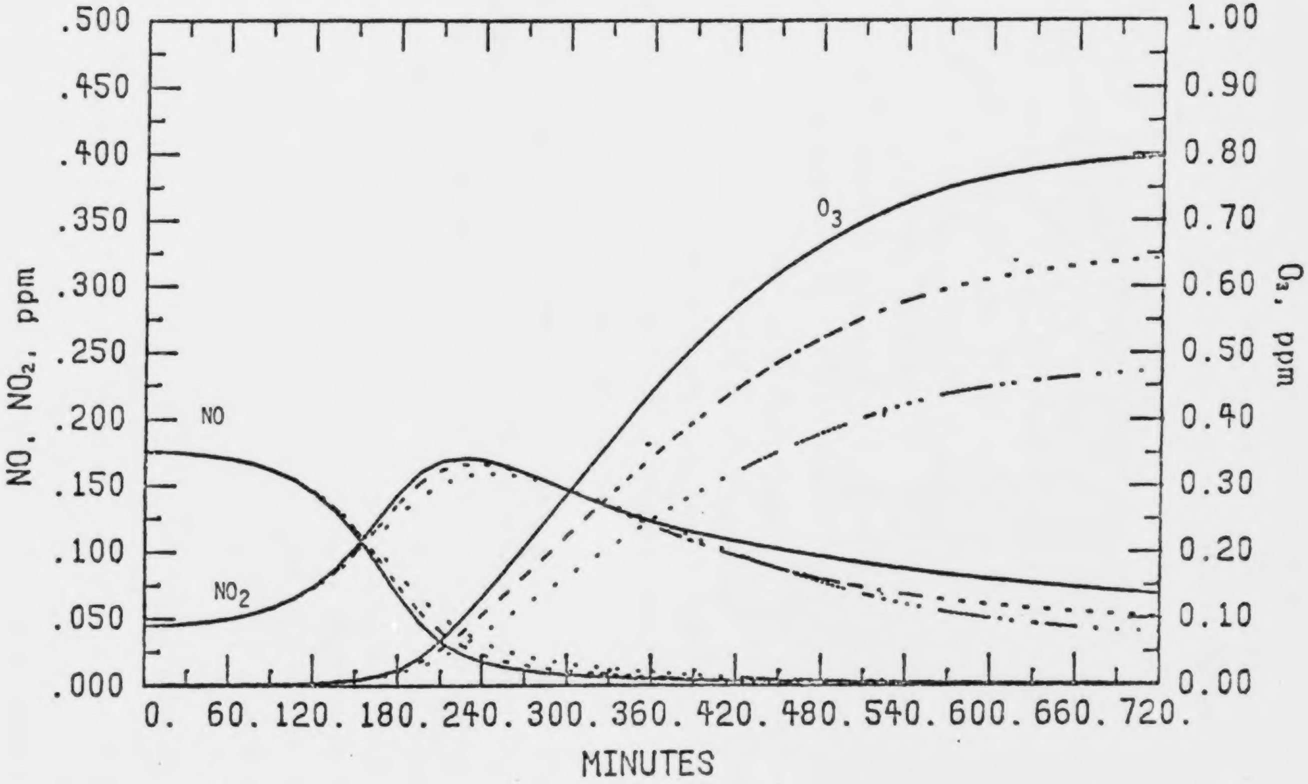

Figure 87. PKSS model of 0.22 ppm $NO_x$, 2.00 ppmC HC mix for three temperature profiles; (_____) 73° F to 105° F; (---) 73° F to 93° F; (....) constant 77° F.

variables not under experimental control must be quantified, and the magnitude of possible errors discussed.

It should first be pointed out that the lines representing the zero-gradient region profile in Figures 76 and 77 are smoothed representations of the zero-gradient region pattern averages as shown in Figure 88. The vertical deviations from these smooth lines is often 1 pphm and can be as high as 2 or 3 pphm. Thus, there is some small uncertainty as to the placement of the LARPP concentration profile lines. The NO profiles seem to have matched the NO profiles of the LARPP data extremely well. In the latter portion of the runs NO concentrations go quite low; small errors in measurements take on great importance. At this time, small changes in the NO concentration drastically affect the $NO_2$/NO ratio and, therefore, the $O_3$ concentration. Thus, it is difficult to ascertain the effect of small disagreements between the LARPP and chamber NO on the $O_3$ concentration comparison.

The $NO_2$ concentration in the simulations initially remained above the LARPP $NO_2$. In the October 12 experiment, the $NO_2$ concentration is quite close to the LAR[illegible] after 1230 PST. This is probably fortuitous since no attempt had been made to simulate the small rise in $NO_2$ observed at 1230 PST in the LARPP data. On October 13, the $NO_2$ remained above the LARPP values because simulation dilution was discontinued after 1200 PST. Also, the $NO_2$ measurements in LARPP and the simulations are performed with chemiluminescent instruments. These instruments are known to have interferences in the $NO_x$ mode such as PAN and nitric acid. It is not known how much the interfering species contributed to the $NO_2$ measurements in either LARPP or the simulations. In Los Angeles, PAN is thought to be roughly 10 percent of the total oxidant (24). This is not greatly different from the PAN to oxidant ratio from numerical models of the UNC hydrocarbon mix (99).

The assumption that hydrocarbon and $NO_x$ emissions remain in the same ratio for the entire operation is indeed a simplification, but was expedient in lieu of a reliable means of estimating $NO_2$ and NO emissions along the trajectory. This could be refined in further simulations, perhaps by use of emissions inventory information, at least to weight

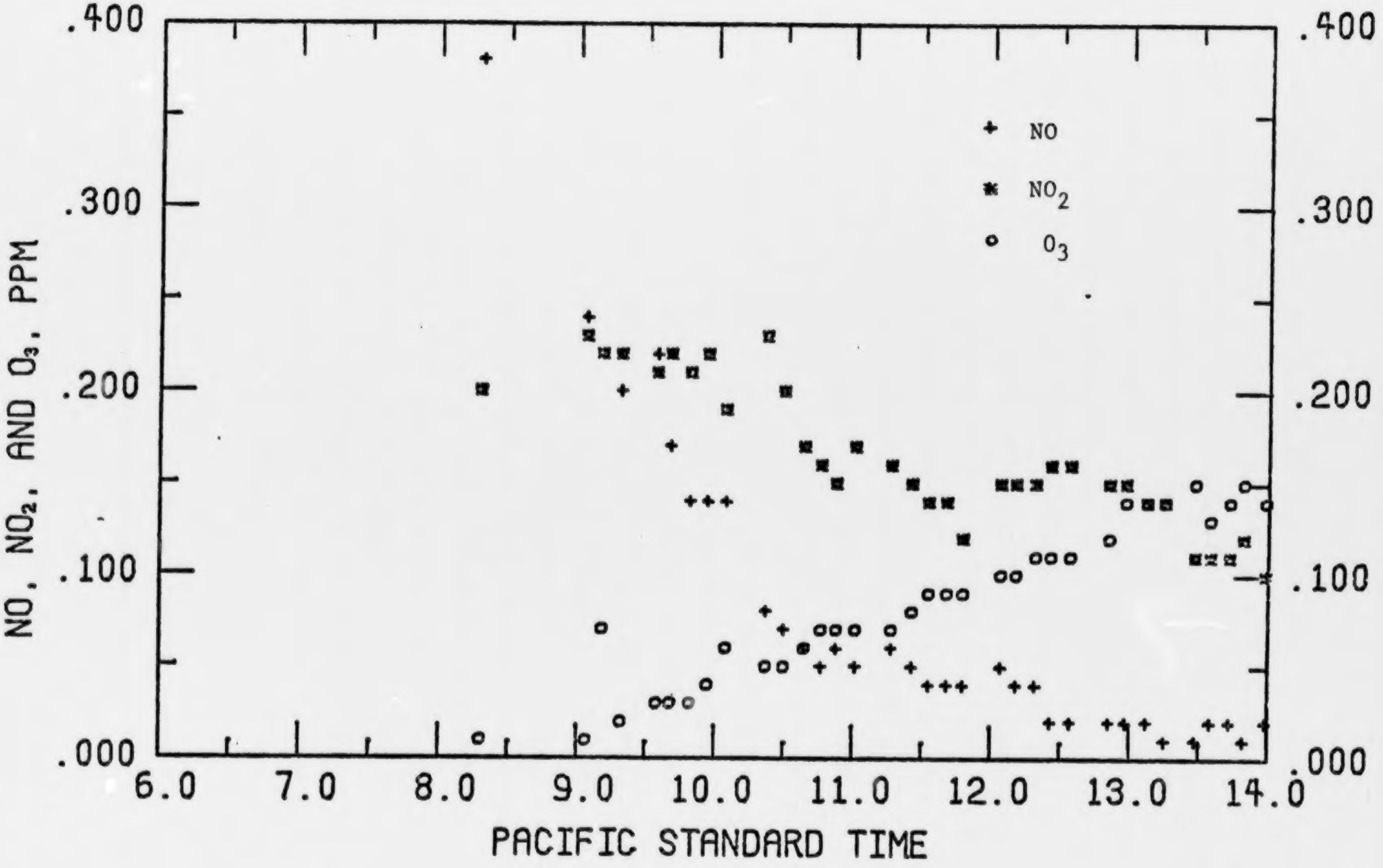

Figure 88. NO, $NO_2$, and $O_3$ helicopter pattern average concentrations from LARPP Operation 33.

the NMHC/$NO_x$ injection rate ratio differently at various times during the simulation.

One further consideration is that the measured concentrations of $O_3$, NO, and $NO_2$ are affected to some extent by dark reactions in the sampling manifold. A method was devised for correcting the data for the $O_3$-NO reaction as described in Appendix F. The correction is greatest around $O_3$-NO crossover since this is when the product of the $O_3$ and NO concentrations is greatest. Applying this correction to the data of October 12, it was found that the correction had a maximum value of 1 pphm, and decreases before and after crossover. This increases the agreement between the simulation and the atmosphere. (While the correction is small in considering concentration alone, it is quite important in comparing $[O_3][NO]/[NO_2]$ in the chamber with measured $k_1/k_3$.)

The difference in light intensity is another factor to be considered. Figure 89 shows the range of $k_1/k_3$ values calculated for the LARPP operation, as well as $k_1/k_3$ values from October 12 and 13. The $k_1$ chamber values are based on measurements taken inside the smog chamber (Figures 68 and 71). Since the $k_1$ sensor was sometimes shielded by structural components of the chamber it was necessary to fair a smooth line through the $k_1$ points to obtain the approximate average chamber $k_1$. $k_3$ was calculated as a function of chamber temperature as:

$$k_3 = 1330 \exp(-1200/T) \text{ ppm}^{-1} \text{ min}^{-1} .$$

$k_1/k_3$ was higher for both simulations than for the LARPP operations; however, it should be pointed out that there are discrepancies between $k_1/k_3$ determined from the $k_1$ sensor and temperature data and $k_1/k_3$ determined from Equation 17 using corrected concentrations. For October 12, the sensor yields $k_1/k_3$ values of 0.022 and 0.013 ppm at 1030 PST and 1430 PST versus corresponding concentration ratio values of 0.0144 and 0.00583 ppm. Thus, the disagreement was about 7 to 8 ppb for these two times; this is more important in a relative sense at the latter time since the absolute values of $k_1/k_3$ are smaller. Possible errors are present in both means of quantitating $k_1/k_3$. The following items may cause error in the evaluation of Equation 17.

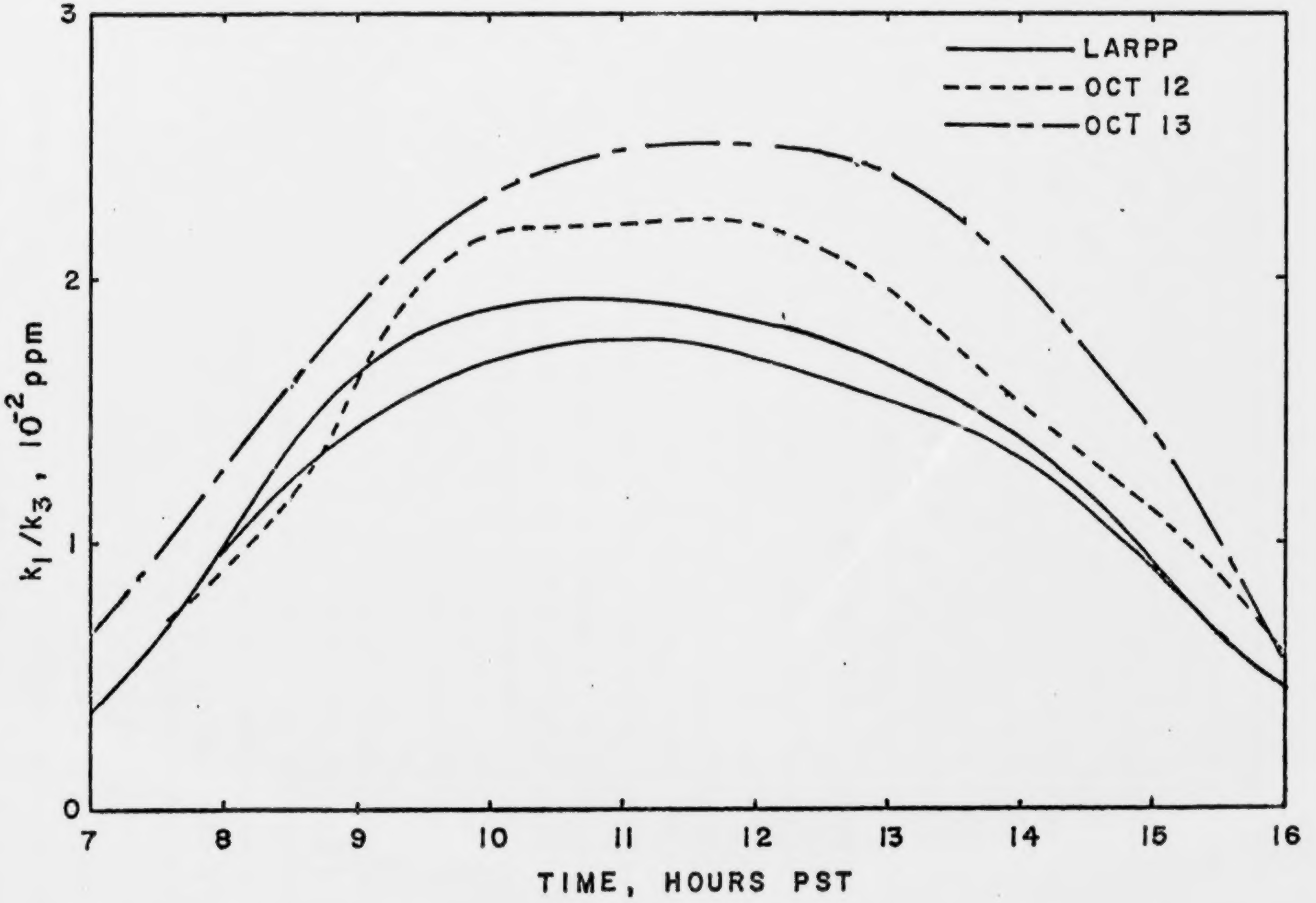

Figure 89. Comparison of ratio of $NO_2$ photolysis rate constant to $NO-O_3$ reaction rate constant, $k_1/k_3$, inside chamber on October 12 and 13, 1976, to the range of estimated $k_1/k_3$ values for altitudes from 200 feet to 800 feet in LARPP Operation 33.

(1) The concentration values were only corrected for reaction of $O_3$ and NO, when in reality other dark reactions are taking place, for instance, $O_3$ and $NO_2$, and $O_3$ and olefin. These reactions would result in a negative bias in estimating $k_1/k_3$.

(2) The interferences present in the $NO_2$ measurement would also produce lower $k_1/k_3$ estimates.

(3) The ratio is extremely sensitive to small errors in the NO concentration late in the day.

(4) Equation 17 itself is a simplification which does not account for reaction of $O_3$ with species other than NO. This, just as items (1) and (2) above, produces a negative bias in the $k_1/k_3$ estimate.

For the $k_1$ sensor, Sickles and Jeffries (85) considered the effect of normally distributed errors in all input variables. The 95 percent confidence interval at a measured $k_1$ of 0.5 $min^{-1}$ was ± 10%; at a measured $k_1$ of 0.1, it was ± 8.7%. Thus, it is likely that the $k_1/k_3$ estimate from the $k_1$ sensor is closer to the true value.

If the chamber $k_1/k_3$ had equaled the LARPP values, the $O_3$ simulation profiles would have been lower, thus increasing disagreement. At 1400 PST, the $O_3$ concentration of October 12 would be about 4 ppb lower and, on October 13, it would be about 2 pphm lower. This accounts only for the effect of light intensity on photostationary state, given the same NO and $NO_2$ concentration. It is not possible to take the effect of light intensity into account regarding the rate of conversion of NO to $NO_2$ in such a complex system short of modeling, however, it is not expected to be large compared with the effect on photostationary state (based on comparison of October 12 with October 13).

Atmospheric inhomogeneity, as discussed earlier, adds an average of 2 pphm to the LARPP $O_3$ profile. This accounts for about 13 percent of the LARPP $O_3$ concentration at 1400 PST and increasingly larger percentages earlier in the day. Recognition of this effect tends to increase agreement of the LARPP $O_3$ with the simulation $O_3$ profiles.

The differences in temperature between LARPP and the simulations of October 12 and 13 are shown in Figure 90. The small temperature difference between LARPP and October 12 is not expected to greatly influence $O_3$ concentration. The temperature difference in the afternoon of October 13 ranges from 8 to about 18 degrees. Judging from the Figure 87 the $O_3$ produced by this simulation may have been reduced by 20 to 30 percent if run under the temperature conditions of the LARPP operation.

In addition to the effect of variables just discussed, instrument errors add to the uncertainty of the comparison. Also, differences in calibration method may cause the comparison to be biased although this is very difficult to evaluate through retrospection.

To summarize, it may be stated that there are two classes of factors affecting the comparison: random and systematic. The random factors are the following:

(1) Errors in concentration measurements which are due to offsets in calibration. This could easily amount to $\pm$ 10% considering the sum of the errors in LARPP and chamber data for higher concentrations and much greater percentages for NO late in the day.

(2) Random errors in estimates of $k_1/k_3$ in the chamber have an approximate 95 percent interval of $\pm$ 10% and the estimates in the atmosphere may be in error by this amount also.

The systematic factors are the following:

(1) Differences in light intensity, accepting the estimates of $k_1/k_3$, add an additional 20 to 30 percent to the $O_3$ values for October 13, and somewhat less for October 12, thus decreasing the agreement.

(2) Dark reactions may add up to 16 to 20 percent to the $O_3$ concentration observed in the simulation at $O_3$-NO crossover, thus increasing agreement.

(3) Temperature differences probably plays little part in the comparison of October 12 with LARPP, but may be responsible for as much as 30% of ozone production of October 13, thus decreasing agreement.

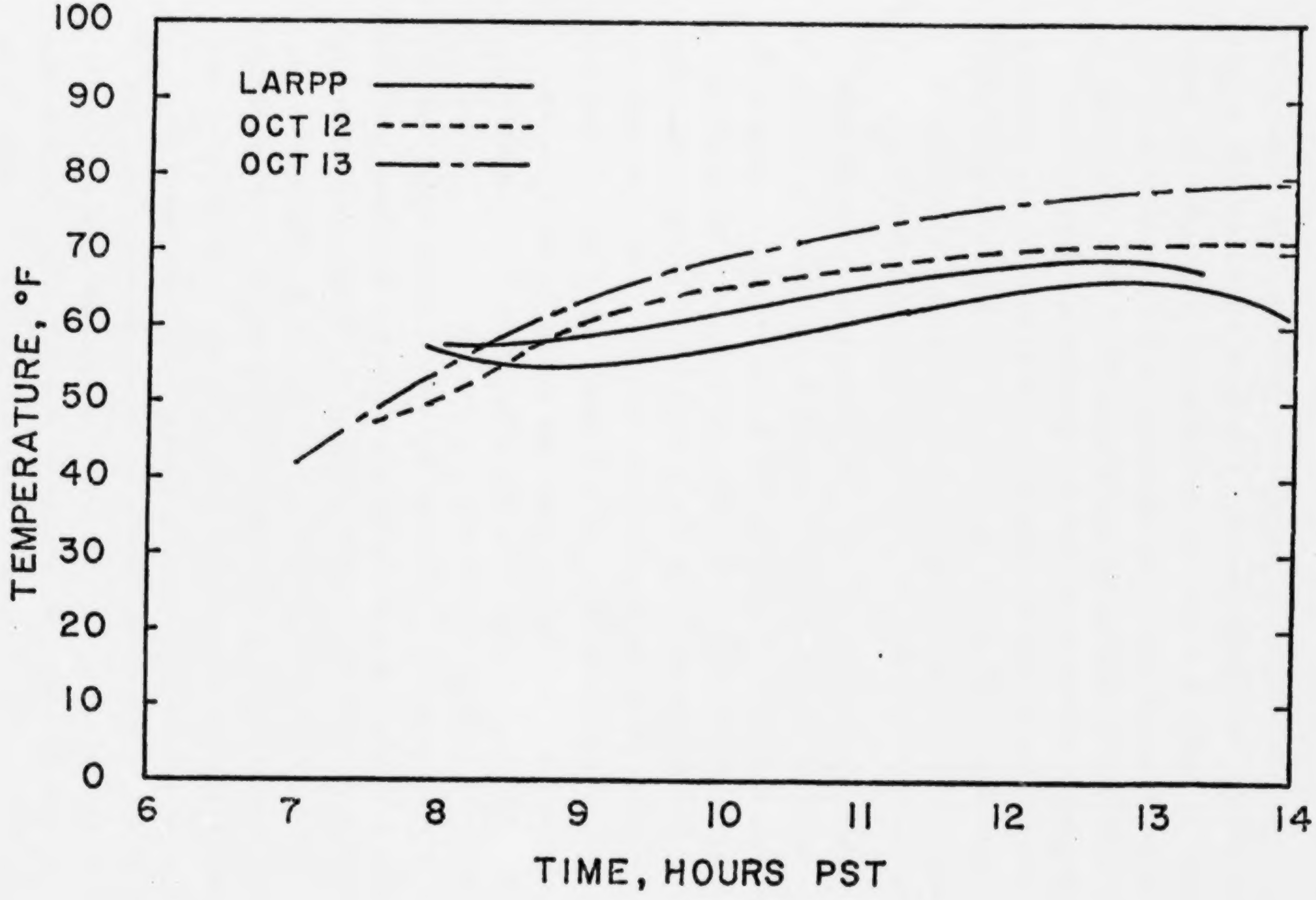

Figure 90. Comparison of the chamber temperatures on October 12 and 13 with range of helicopter pattern average temperatures from LARPP Operation 33.

(4) Atmospheric inhomogeneity accounted for about 2 pphm of the observed LARPP $O_3$, thus increasing agreement.

Considering the possible magnitudes of errors and the effects of light, temperature, and inhomogeneity, it may be concluded that agreement between the LARPP data for the zero-gradient region and the simulation results is quite good. The agreement is especially good if one considers some of the simplifying assumptions which were made in relating atmospheric processes to chamber injection and dilution, for example, (a) the use of constant NMHC/$NO_x$ injections; (b) the use of a constant composition hydrocarbon mix; (c) the straight-line approximation of source reconciliation results; and (d) the use of numerical computation to calculate NMHC flux values in the atmosphere.

The higher values of $k_1/k_3$ would have been expected to produce higher $O_3$ values in the simulation than in the atmosphere if the $NO_2$/NO ratio were the same as the average ratio in the atmosphere, even after correction for inhomogeneity to the $O_3$ concentration. The conclusion to be drawn is that the $NO_2$/NO ratio was in fact lower in the chamber than in the atmosphere. For reasons discussed earlier, it is very difficult to obtain good estimates of this ratio directly using typical chemiluminescent monitoring instruments. Since the values $O_3$ and $k_1/k_3$ are probably subject to less error than the nitrogen oxide concentrations, it is possible to estimate $NO_2$/NO ratio as the ratio of $O_3$ to $k_1/k_3$. Note that in the atmosphere, it is not the true average ratio, but the ratio if the atmosphere were homogeneous. This may be termed the effective $NO_2$/NO ratio. The ratios were compared for three times of day in Table 14. It is shown that the effective ratio in the atmosphere was greater than the simulation ratio, even when corrected for inhomogeneity by subtracting 0.02 ppm from the LARPP $O_3$ values. Differences of this magnitude could not result from differences in $NO_2$, but could more easily be caused by small differences in the NO concentration. For instance, if the $NO_2$ values are approximately correct, the difference in $NO_2$/NO ratio between LARPP and October 12 (corrected for dark reactions) can be explained by a difference in NO concentrations of 1 pphm. This

TABLE 14. ESTIMATES OF $NO_2$/NO RATIO FOR SIMULATIONS OF OCTOBER 12 AND 13 AND THE EFFECTIVE $NO_2$/NO RATIO FOR THE LARPP DATA CORRECTED AND UNCORRECTED FOR INHOMOGENEITY

| | $NO_2$/NO | | | |
|---|---|---|---|---|
| | LARPP | | | |
| Time, PST | Uncorrected | Corrected | October 12 | October 13 |
| 1000 | 2.33 | 1.2 | 1.0 | 1.0 |
| 1200 | 5.7 | 4.5 | 2.8 | 2.4 |
| 1400 | 10.9 | 9.4 | 4.6 | 6.3 |

indicates that the simulations had either a lower radical flux or more NO to be oxidized than the LARPP trajectory.

Recent experiments in the UNC outdoor smog chamber suggest a possible cause for lower chamber NO oxidation rates, and thus lower $O_3$. A static experiment was performed at a hydrocarbon mix concentration of 1 ppmC and an $NO_x$ concentration of 0.35 ppm with 20 percent $NO_2$ on both sides of the chamber. In addition, one side contained formaldehyde at a concentration equal to 10 percent of the total nonmethane carbon while the other side contained acetaldehyde at a concentration equal to 10 percent of the total nonmethane carbon. The formaldehyde side oxidized NO to $NO_2$ more rapidly and produced a maximum $O_3$ concentration of 0.24 ppm versus 0.08 ppm maximum $O_3$ in the acetaldehyde side. This indicates that the presence of formaldehyde could play a much greater role in the $O_3$ formation potential than was thought at the start of this experimental program. Thus, the rationale for the use of acetaldehyde only (presented in Section 6) was probably incorrect. Further simulations should use a mix of formaldehyde and acetaldehyde representative of the atmosphere.

Another factor was the convective entrainment of what appeared to be second-day material from above the inversion base. As results from October 16 indicate, the presence of second-day material can enhance the rate and extent of NO oxidation.

Another simplification is the assumption of no horizontal diffusion and the subsequent evaluation of NMHC vertical flux. After this work was completed, Crane, Panofsky, and Zeman (100) estimated vertical flux of CO after 9:15 PST by assuming values of the emission rates at the ground. The disagreement of their flux estimates with the estimates in this report lead Feigley and Jeffries (101) to conclude that some cross-wind diffusion of CO away from the trajectory had occurred. It is probable that some NMHC and $NO_x$ also diffused away from the trajectory, which would imply that both injection and dilution rates were somewhat underestimated. While the concentrations of nonreactive species injected into the chamber would not be changed, the concentration of reactive precursors would be increased by increased injection and dilution. It is difficult to determine how this would affect the ozone concentration since it would increase both the NO to be oxidized and the reactive hydrocarbon available for chain reactions which result in NO oxidation.

# REFERENCES

1. Haagen-Smith, A. J., C. E. Bradley, and M. M. Fox. Ozone Formation in Photochemical Oxidation of Organic Substances. Indus. Eng. Chem., 45(9):2080-2089, 1953.

2. Stephens, E. R., P. L. Hanst, R. C. Doerr, and W. E. Scott. Reactions of Nitrogen Dioxide and Organic Compounds in Air. Indus. Eng. Chem., 48:1498-1504, 1956.

3. Leighton, P. A. Photochemistry of Air Pollution. Academic Press, New York, 1961.

4. Wayne, L. G. The Chemistry of Urban Atmospheres. Los Angeles County Air Pollution Control District, 1962.

5. Haagen-Smit, A. J., and L. G. Wayne. Chapter 6. In: A. C. Stern, ed., Air Pollution, Vol. I, Academic Press, New York, 1968. p. 149.

6. Pitts, J. N., Jr. Adv. in Environ. Sci. Technol., 1:289, 1969.

7. Altshuller, A. P., and J. J. Bufalini. Environ. Sci. Technol., 5:39, 1976.

8. Demerjian, K. L., J. A. Kerr, and J. G. Calvert. Adv. Environ. Sci. Technol., 4:1, 1974.

9. Environmental Protection Agency. National Primary and Secondary Air Quality Standards and Air Pollution Control. Fed. Reg., 36(21): Part II, 1971.

10. Stephens, E. R. Chemistry of Atmospheric Oxidants. JAPCA, 19(3): 183, 1969.

11. Seinfeld, J. H. Air Pollution: Physical and Chemical Fundamentals. McGraw-Hill, New York, 1975. p. 151.

12. Seinfeld, J. H. Air Pollution: Physical and Chemical Fundamentals. McGraw-Hill, New York, 1975. p. 165.

13. Hampson, R. F., Jr., and D. Garvin. Chemical Kinetic and Photochemical Data for Modeling Atmospheric Chemistry. National Bureau of Standards Technical Note 866. U.S. Government Printing Office, Washington, DC, 1975. p. 59.

14. Jeffries, H. E. 1975. personal communication.

15. Gartrell, G., Jr., and S. K. Friedlander. Relating Particulate Formation to Sources: The 1972 California Aerosol Characterization Study. Atmos. Environ., 9:279, 1975.

16. McNelis, D. N. Aerosol Formation from Gas Phase Reactions of Ozone and Olefin in the Presence of Sulfur Dioxide. PhD Thesis, University of North Carolina, Chapel Hill, North Carolina, 1974. pp. 148-152.

17. Hasar, R. B., K. T. Whitley, and B. Y. H. Liu. Physical Mechanisms Governing the Los Angeles Smog Aerosol. J. Coll. Inter. Sci., 39:211-224, 1972.

18. Heisler, S. L. Gas-to-Particle Conversion in Photochemical Smog: Growth Laws and Mechanisms for Organics. PhD Thesis. California Institute of Technology, Pasadena, California, 1976.

19. Zeman, O., and H. Tennekes. Parameterization of the Turbulent Energy Budget at the Top of the Atmosheric Boundary Layer. J. Atmos. Sci., 1976. In press.

20. Edinger, J. G. Changes in the Depth of the Marine Layer Over the Los Angeles Basin. J. Appl. Meteorol., 16(3):219, 1959.

21. Edinger, J. G. Modification of the Marine Layer over Coastal Southern California. J. Appl. Meteorol., 2:706, 1963.

22. Roth, P. M., P. J. W. Roberts, M. -K Liu, S. D. Reynolds, and J. H. Seinfeld. Mathematical Modeling of Photochemical Air Pollution -- II. A Model and Inventory of Pollutant Emissions. Atmos. Environ., 8:97-130, 1974.

23. Eschenroeder, A. Q., and J. R. Martinez. Concepts and Applications of Photochemical Smog Models. Photochem. Smog Ozone React. R. F. Gould, ed., American Chemical Society, Washington, DC, 1972. pp. 101-168.

24. Air Quality Criteria for Photochemical Oxidants. National Air Pollution Control Administration, Pub. No. AP-63, Washington, DC, 1970.

25. Panofsky, H. A. 1976. personal communication.

26. Calvert, J. G. Test of the Theory of Ozone Generation in Los Angeles Atmosphere. Environ. Sci. Technol., 10(3):248-256, 1976.

27. Hecht, T. A., and J. H. Seinfeld. Development and Validation of a Generalized Mechanism for Photochemical Smog. Environ. Sci. Technol., 6:47, 1972.

28. Wayne, L. G., R. Danchick, M. Weisburd, A. Kokin, and A. Stein. Modeling Photochemical Smog and Computer for Decision Making. Pacific Conference on Chemistry and Spectroscopy, 6th Western Region Meeting, ACS, San Francisco, California, October 6-9, 1970.

29. Air Quality Criteria for Hydrocarbons. Ma, NAPCA Publication No. AP-64. U.S. Department of HEW, PHS, NAPCA, 1970. p. 5-4.

30. Huess, J. M., G. J. Nebel, and J. M. Colucci. National Air Quality Standards for Automotive Pollutants -- A Critical Review. J. Air Poll. Cont. Assoc., 21(9):535-544, 1970.

31. Altshuller, A. P. Relationships Among Pollutants Undergoing Atmospheric Reactions in CAMP Cities in the U.S. Presented at the 63rd Annual Meeting of the APCA, APCA Paper No. 70-113, June 14-18, St. Louis, Missouri, 1970.

32. Angell, J. K., C. R. Dickson, and W. H. Hoecker, Jr. Relative Dispersion Within Los Angeles Basin as Estimated from Tetroon Triads. Air Resources Laboratories, National Oceanic and Atmospheric Administration, Silver Spring, Maryland, November 1974.

33. National Academy of Sciences. Panel on Emission Standards and Atmospheric Chemistry. A Critique of the 1975-76 Federal Automobile Emission Standards for Hydrocarbons and Oxides of Nitrogen, May 22, 1973.

34. Dimitriades, B. Effects of Hydrocarbon and Nitrogen Oxides on Photochemical Smog Formation. Environ. Sci. Technol., 6(3):253-260, 1972.

35. Los Angeles Air Pollution Control District. Los Angeles County Air Pollution Control District Views on the Emission Control Strategy to Achieve the Oxidant Air Quality Standard. Los Angeles, California, April 5, 1974.

36. Los Angeles Air Pollution Control District. Answers to EPA Questions Posed in April 22, 1974 Letter (Covington to Lunche). Los Angeles, California, June 21, 1974.

37. Fox, D. L., R. M. Kamens, and H. E. Jeffries. Photochemical Smog Systems: Effect of Dilution on Ozone Formation. Sci., 188:1113, 1975.

38. Shuck, E. A., J. N. Pitts, and J. K. S. Wan. Relationship Between Certain Meteorological Factors and Photochemical Smog. Inter. J. Air Water Poll., 10:689-711, 1966.

39. Chock, D. P. and S. B. Levitt. A Space-Time Correlation Study of Oxidant and Carbon Monoxide in the Los Angeles Basin. Atmos. Environ., 10:107-113, 1976.

40. Paskind, J., and J. R. Kinosian. Hydrocarbon, Oxides of Nitrogen and Oxidant Pollutant Relationships in the Atmosphere Over California Cities. APCA Paper No. 74-31. Presented at the 67th Annual Meeting of the APCA, Denver, Colorado, June 9-13, 1974.

41. Edinger, J. G., M. H. McCutchan, P. R. Miller, B. C. Ryan, M. J. Schroeder, and J. V. Behar. Penetration and Duration of Oxidant Air Pollution in the South Coast Air Basin of California. J. Air Poll. Cont. Assoc., 22(11):882-886, 1972.

42. Barth, D. S. Federal Motor Vehicle Emission Goals for CO, HC, and $NO_x$ Based on Desired Air Quality Levels. Air Poll. Cont. Assoc., 20:519-523, 1970.

43. Larsen, R. I. A Mathematical Model of Air Pollution Concentration Averaging Time and Frequency. J. Air Poll. Cont. Assoc., 19:29, 1969.

44. Larsen, R. I. A Mathematical Model for Relating Air Quality Measurements to Air Quality Standards. Preliminary Publication No. AP-89. Environmental Protection Agency, Office of Air Programs, Research Triangle Park, North Carolina, 1971.

45. Hamming, W. J., R. L. Chass, J. E. Dickinson, and W. G. MacBeth. Motor Vehicle Control and Air Quality: The Path to Clean Air for Los Angeles. APCA Paper No. 73-73. Presented at the 66th Annual Meeting of the APCA., Chicago, Illinois, June 24-28, 1973.

46. Korth, M. W., A. H. Rose, Jr., and R. C. Stahman. Effects of Hydrocarbon to Oxides of Nitrogen Ratios on Irradiated Auto Exhaust. J. Air Poll. Cont. Assoc., 14:168, 1964.

47. Kamens, R. M., H. E. Jeffries, D. L. Fox, and L. Alexander. A Smog Chamber Study of the Potential Effects of Hydrocarbon Reductions on Nighttime $NO_2$ Concentrations. Atmos. Environ., 11:225-229, 1977.

48. Trijonis, J. C. Economic Air Pollution Control Model for Los Angeles County in 1975. Environ. Sci. Technol., 8(9):811-826, 1974.

49. Hamming, W. J., and J. E. Dickinson. Control of Photochemical Smog by Alteration of Initial Reactant Ratios. Presented at the 57th Annual Meeting of the APCA, APCA Paper No. 64-110, Houston, Texas, June 1964.

50. Myrabo, L. N., P. Schleifer, and K. Wilson. Oxidant Prediction Model for Land Use and Transportation Planning. Calif. Air Environ., 1974. In press.

51. Trijonis, J. C. Economic Air Pollution Control Model for Los Angeles County 1975. PhD Thesis, California Institute of Technology, Pasadena, California, 1972.

52. Jeffries, H. E., R. M. Kamens, and C. E. Feigley. Outdoor Simulations of Air Pollution Control Strategies. Progress Report, EPA Grant 800916. Department of Environmental Science and Engineering, School of Public Health, Univ. of North Carolina, Chapel Hill, North Carolina, 1977.

53. Stephens, E. R., and F. R. Burleson. Distribution of Light Hydrocarbons in Ambient Air. J. Air Poll. Cont. Assoc., 19(12):929-936, 1969.

54. Bailey, B. S., and K. H. Ludlum. Factors in Achieving the Oxidant Standard. Presented at 26th Southeastern Regional Meeting of American Chemical Society, Norfolk, Virginia, October 24, 1974.

55. Merz, P. H., L. J. Painter, and P. R. Ryason. Aerometric Data Analysis -- Time Series Analysis and Forecast and an Atmosphere Smog Diagram. Chevron Corporation, Los Angeles, California, 1970.

56. Dimitriades, B. An Alternative to the Appendix-J Method for Calculating Oxidant- and $NO_2$-Related Control Requirements. International Conference on Photochemical Oxidant Pollution and its Control Proceedings. Vol. II. EPA-600/3-77-001b. Raleigh, North Carolina, 1976. p. 871.

57. Dimitriades, B. On the Function of Hydrocarbon and Nitrogen Oxides in Photochemical Smog Formation. U.S. Bureau of Mines. Report of Investigations RI-7433, Bartlesville, Oklahoma, 1970.

58. Dodge, M. C. Combined Use of Modeling Techniques and Smog Chamber Data to Derive Ozone-Precursor Relationships. International Conference on Photochemical Smog Pollution and its Control Proceedings. Vol. II. EPA-600/3-77-001b. Raleigh, North Carolina, 1976. p. 88.

59. OAQPS, 1977.

60. Parker, R. O., and J. R. Martinez. Los Angeles Reactive Pollutant Program (LARPP) Data Archiving and Retrieval. ERT Document No. P-1464-W, Environmental Research and Technology, Inc., Concord, Massachusetts.

61. Shepard, D. A Two-Dimensional Interpolation Function for Irregularly-Spaced Data. Proceeding - 1968 ACM National Meeting, 1968.

62. Lea, D. A. Vertical Ozone Distribution in the Lower Troposphere near an Urban Pollution Complex. J. Appl. Meteorol., 1(2):252-267, 1968.

63. Edinger, J. G. Vertical Distribution of Photochemical Smog in Los Angeles Basin, Environ. Sci. Technol., 7(3):247-252, 1973.

64. Johnson, W. B., and H. B. Singh. Oxidant Layers Aloft: Their Origin and Significance. International Conference on Photochemical Oxidant Pollution and its Control. Raleigh, North Carolina, September 12-17, 1976.

65. Edinger, J. C. Preliminary Analysis of LARPP Data. Unpublished Report to the Coordinating Research Council, New York, New York, 1975.

66. Jeffries, H. E., J. E. Sickles, II, and L. A. Ripperton. Ozone Transport Phenomena: Observed and Simulated. APCA Paper No. 76-14.3. Presented at APCA Annual Meeting, Portland, Oregon, 1976.

67. Lumley, J. L., and H. A. Panofsky. The Structure of Atmospheric Turbulence. Interscience, New York, 1964.

68. Trijonis, J. C., and K. W. Arledge. Utility of Reactivity Criteria in Organic Emission Control Strategies for Los Angeles. Report for Contract No. 68-02-1735. Environmental Protection Agency, Research Triangle Park, North Carolina, 1975.

69. Panofsky, H. A. A Model for Vertical Diffusion Coefficients in a Growing Urban Boundary Layer. Boundary-Layer Meteorology, 9:235-244, 1975.

70. Deardorff, J. W., and G. E. Willis. Advances in Geophysics. 18b. Landsberg and Van Miegham, eds. Academic Press, New York, 1974, pp. 187-200.

71. Martinez, J. R. Comments on Dynamics and Kinetics in Environmental Problems -- Are They Separable? Proceedings of the Symposium on the Chemical Aspects of Air Quality Modeling. L. D. Kornreich, ed., University of North Carolina, Chapel Hill, North Carolina, April 17-19, 1974.

72. Donaldson, C. duP., and G. R. Hilst. Environ. Sci. and Technol., 6(9):312, 1972.

73. Hilst, G. R. Dynamics and Kinetics in Environmental Problems -- Are they Separable? Proceedings of the Symposium on Chemical Aspects of Air Quality Modeling. L. D. Kornreich, ed., University of North Carolina, Chapel Hill, North Carolina, 1974. p. 43.

74. Lamb, R. G. Continued Research In Mesoscale Air Pollution Simulation Modeling: Vol. III - Modeling of Microscale Phenomena. EPA-600/4-76-016c. U.S. Environmental Protection Agency, Research Triangle Park, North Carolina, 1976.

75. Mayrsohn, H., and J. H. Crabtree. Source Reconciliation of Atmospheric Hydrocarbons. Atmos. Environ., 10:137-143, 1976.

76. Mayrsohn, H., and J. H. Crabtree. Source Reconciliation of Atmospheric Hydrocarbons. personal communication to Basil Dimitriades. U.S. Environmental Protection Agency, Research Triangle Park, North Carolina, 1975.

77. Mayrsohn, H. personal communication to Basil Dimitriades, U.S. Environmental Protection Agency, Research Triangle Park, North Carolina, 1975.

78. Hurn, R. W. Mobile Combustion Sources. Chapter 33, Air Pollution, Vol. III, A. C. Stern, ed., 2nd edition, Academic Press, New York, New York, pp. 55-95, 1968.

79. Mayrsohn, H., J. H. Crabtree, M. Kuramoto, R. D. Southern, and S. H. Mano. Source Reconciliations of Atmospheric Hydrocarbons 1974. Atmos. Environ., 11:189-192, 1977.

80. Keith, R. 1976. personal communication. Los Angeles Air Pollution Control District.

81. Calvert, J. G. A Preliminary Analysis of the Data from LARPP Operation 33 of November 5, 1973. Report to Coordinating Research Council. New York, New York, 1973.

82. Geiger, R. The Climate Near the Ground. Howard University Press, Cambridge, Massachusetts, 1965.

83. Jeffries, H., D. Fox, and R. Kamens. Outdoor Smog Chamber Studies: Effect of Hydrocarbon Reduction on Nitrogen Dioxide. Publication No. EPA-650/3-75-011, U.S. Environmental Protection Agency, Raleigh, North Carolina, 1975.

84. Jeffries, H., D. Fox, and R. Kamens. Outdoor Smog Chamber Studies: Light Effects Relative to Indoor Chambers. Environ. Sci. Technol., 10:1006, 1976.

85. Sickles, J. E., and H. E. Jeffries. Development and Operation of a Device for the Continuous Measurement of $Ok_a$ for Nitrogen Dioxide. Publication No. 396. Department of Environmental Sciences and Engineering, School of Public Health, University of North Carolina, 1975.

86. Kamens, R. M., H. E. Jeffries, and T. Johns. An Automatic Chromatographic Method to Measure $C_1$-$C_8$ Ambient Hydrocarbons. Presented at ACS Meeting, New Orleans, Louisiana, March 17, 1977.

87. Methods of Determination of Velocity, Volume, Dust and Mist Content of Gases. Bulletin WP-50. Western Precipitator Division, Joy Manufacturing Company, Los Angeles, California, 1968.

88. Reynolds, S. D., M. -K. Liu, T. A. Hecht, P. M. Roth, and J. H. Seinfeld. Mathematical Modeling of Photochemical Air Pollution - III. Evaluation of the Model. Atmos. Environ., 8:563-596, 1974.

89. Lee, R. E., Jr., R. K. Patterson, W. L. Crider, and J. Wagman. Concentration and Particle Size Distribution of Particulate Emissions in Automobile Exhaust. Atmos. Environ., (5):225, 1971.

90. Crittenden, A. L. Analysis of Air Pollutants by Mass Spectroscopy. EPA-600/3-76-093. U.S. Environmental Protection Agency, Research Triangle Park, North Carolina, 1976.

91. Chan, W. H., R. J. Nordstrom, J. G. Calvert, and J. H. Shaw. Kinetic Study of HONO Formation and Decay Reactions in Gaseous Mixtures of HONO, NO, $NO_2$, $H_2O$ and $N_2$. Environ. Sci. Technol., 10(17):674-682, 1976.

92. Dimitriades, B., and T. C. Wesson. Reactivities of Exhaust Aldehydes. J. Air Poll. Cont. Assoc., 22(33):33-38, 1972.

93. Whitten, G. Z., and H. Hogo. Mathematical Modeling of Simulated Photochemical Smog. EPA-600/3-77-011. U.S. Environmental Protection Agency, Research Triangle Park, North Carolina, 1977.

94. Johnson, F. S. The Solar Constant. J. Meteorol., 11:431-439, 1954.

95. Ackerman, M. Ultraviolet Solar Radiation Related to Mesopheric Processes. Inst. Aeron. Spatials Belg. Brussels, A-77:149, 1970.

96. Peterson, J. T. Calculated Actinic Fluxes (290-700 nm) for Air Pollution Photochemistry Applications. EPA-600/4-76-025. U.S. Environmental Protection Agency, Research Triangle Park, North Carolina, 1976.

97. Danckwerts, P. V. The Definition and Measurement of Some Characteristics of Mixtures. Appl. Sci. Res., A3:279-296, 1952.

98. Hendry, D. G., J. E. Davenport, and R. A. Kenley. Quarterly Progress Report for Grant entitled "Reactions of Oxy Radicals in the Atmosphere." Stanford Research Institute, Menlo Park, California, 1976.

99. Jeffries, H. E. personal communication, 1976.

100. Crane, G., H. A. Panofsky, and O. Zeman. A Model for Dispersion from Area Sources in Convective Turbulance. Atmos. Environ., 11:893-900, 1977.

101. Feigley, C. E., and H. E. Jeffries. Analysis of Processes Affecting Oxidant and Precursors in the Los Angeles Reactive Pollutant Program (LARPP) Operation 33. submitted for publication, 1978.

102. Ostle, B. Statistics in Research. 2nd ed. Iowa State University Press, Ames, Iowa, 1963.

103. Milne, W. E. Numerical Solution of Differential Equations. Dover Publications, New York, 1970.

104. Ketter, R. L., and D. W. Prawel. Modern Methods of Engineering Computation. McGraw-Hill, New York, 1969.

105. Carnahan, B., H. A. Luther, and J. O. Wilkes. Applied Numerical Methods. John Wiley and Sons, Inc., New York, 1969.

# APPENDIX A

## FLAG FIELD MESSAGES FOR OPERATION 33

The flag field contained in the helicopter records for operation 33 was translated from EBCDIC to 7-track BCD and the messages were printed out using a program written for this purpose called FLAG. The messages for each helicopter were handled separately and are presented here in Tables A-1 and A-2.

TABLE A-1. SMOG 2 DATA FLAG MESSAGES FOR OPERATION 33

```
Approximate altitude correction applied
     from  72112 through 143620

Pots changed during flight.  Data suspect (zero drift)          :    NO        instrument
     from  72112 through 143620

No higher than NOx
     from  72112 through 143620

Poor cal data                                                   :    NO        instrument
     from  72504 through  74803
     from  84425 through  85159
     from  92400 through  93051
     from 100642 through 101135
     from 110451 through 111307
     from 115147 through 115822
     from 130322 through 131033
     from 142650 through 143253

Clogged plumbing                                                :    NO        instrument
     from  72112 through 143620
```

TABLE A-2. SMOG 3 DATA FLAG MESSAGES FOR OPERATION 33

| | | | |
|---|---|---|---|
| Instrument outage<br>from 124750 through 125006 | : | $CH_4$ | instrument |
| Instrument outage<br>from 124750 through 125006 | : | $O_3$ | instrument |
| Approximate altitude correction applied<br>from 84736 through 144549 | | | |
| Pots changed during flight. Data suspect (zero drift)<br>from 84736 through 144549 | : | NO | instrument |
| No higher than $NO_x$<br>from 84736 through 144549 | | | |
| Poor cal data<br>from 85331 through 90155<br>from 100930 through 101722<br>from 114831 through 115738<br>from 123817 through 124723 | : | NO | instrument |
| Scale change due to span pot no able to adjust inst to cal source<br>from 84736 through 144549 | : | $CH_4$ | instrument |
| Clogged plumbing<br>from 84736 through 144549 | : | NO | instrument |

# APPENDIX B

## SOURCE RECONCILIATION AND ASSOCIATED CALCULATIONS

The source reconciliation method itself has been described by Mayrsohn and Crabtree (75) and requires only brief discussion here. If $\underline{C}$ is a matrix of source weight fractions of m tracers from n sources ($m>n$), $\underline{A}$ is a column vector containing the n tracer concentrations observed in the atmosphere, and $\underline{B}$ is a matrix of m weighting coefficients, it is desired to find the best values of $\underline{B}$ for the overdetermined set of linear equations:

$$\underline{A} = \underline{C}\ \underline{B} \quad .$$

If the least square criterion is applied then the solution for the coefficients follows:

$$\underline{B} = (\underline{C}'C)^{-1}\ (\underline{C}'\underline{A}) \quad .$$

After the coefficients were calculated, the differences between the expected and observed values of tracer concentrations, $\underline{D}$, was calculated.

$$\underline{D} = \underline{C}\ \underline{B} - \underline{A}$$

Mayrsohn and Crabtree (75) calculate the standard error of estimate S:

$$S = (\underline{D}'\underline{D}/(n-1))^{1/2} \quad .$$

This form is incorrect; the sum of squares of the residuals $\underline{D}'\underline{D}$ should be divided by the number of degrees of freedom of the residuals which is the number of tracer species minus the number of coefficients estimated. Thus, the standard error was calculated as follows:

$$S = \underline{D}'\underline{D}/(m-n))^{1/2} \quad .$$

Mayrsohn and Crabtree (76) found that the fit could be improved by deleting certain sources from the $\underline{C}$ matrix. Thus, the calculations above were performed with all sources represented in $\underline{C}$ and then various smaller configurations were explored. The source combination with the lowest standard error was selected as the final result. Thirteen configurations were tried for each observation. Following the suggestions of Mayrsohn and Crabtree (76), auto exhaust was never deleted; either gasoline vaporization or gasoline evaporation were deleted but never both; either natural gas or LPG was always included.

For the best fitting configuration, the R-squared value for the regression was calculated by the following approach (102):

$$MSE = \underline{D}'\underline{D}/(n-m)$$

$$MSS = \left(\underline{A}'\underline{A} - \frac{(\overline{A_i})^2}{n}\right)/(n-1)$$

$$R^2 = 1 - \frac{MSE}{MSS}$$

The term $\overline{A_i}$ is the mean value of observed concentrations. $R^2$ provides a measure of how well the model fits.

Mayrsohn and Crabtree's (75) use of the chi-square goodness-of-fit test is not valid for this purpose. The chi-square test assumes an underlying multinomial distribution, i.e., frequency data.

The total concentration (weight/volume) of hydrocarbons emitted to produce the observed tracer concentrations may be calculated as follows:

$$\hat{a}_j = \sum_i C_{ji}\, b_i$$

or

$$\frac{\mu\text{g tracer } j}{m^3} = \sum_i \left( \frac{\mu\text{g tracer } j \text{ source } i}{\mu\text{g tracer norm. source } i} \cdot \frac{\mu\text{g tracer norm. source } i}{m^3} \right)$$

where "tracer norm" is the particular tracer species by which column i of $\underline{C}$ was normalized for computation of the transpose-product inverse. $\hat{a}_j$ is the value of a tracer species j predicted to be present in the air by the regression model. Because of the normalization of $\underline{C}$, the $b_i$'s have units of (μg tracer norm. source $i/m^3$). Since the source compositions are known for tracers as well as other species, the total expected concentrations of any of the emitted species in the absence of reaction may be calculated. The coefficients $b_i$'s are corrected for the effect of normalization by multiplying by the ratio of the total normalized tracer concentration over the "tracer norm" concentration.

$$\beta_i = b_i \frac{\sum_j C_{ji}}{C_{\text{norm } i}}$$

or

$$\frac{\mu\text{g total tracer source i}}{m^3} = \frac{\mu\text{g tracer norm. source i}}{m^3} \cdot \frac{\mu\text{g total tracer source i}}{\mu\text{g tracer norm. source i}} .$$

From the total source compositions, the ratio, $R_i$, of tracer species to total hydrocarbons is calculated. Thus, the total hydrocarbon concentration which would be present in the absence of reaction may then be determined.

$$\text{THC} = \sum_i \beta_i / R_i$$

or

$$\frac{\mu\text{g THC in air}}{m^3} = \sum_i \left(\frac{\mu\text{g total tracer source i}}{m^3}\right) \Bigg/ \left(\frac{\mu\text{g total tracer source i}}{\mu\text{g THC source i}}\right)$$

Also, the total nonmethane hydrocarbons contributed from each source may be calculated.

$$\text{NMHC}_i = \text{THC} \cdot \beta_i \cdot (1 - \text{FRMETH}_i)$$

where $\text{FRMETH}_i$ is the weight fraction of methane in source i.

$$\frac{\mu\text{g total NMHC in air}}{m^3} = \sum_i \text{NMHC}_i$$

# APPENDIX C

## NUMERICAL COMPUTATION OF VERTICAL FLUX ALONG A LARPP TRAJECTORY

Because the concentrations of pollutants was not measured up to the inversion base for much of the day, it was necessary to solve the equation

$$\frac{dc}{dt} = \frac{\partial}{\partial z} (K(z,t) \frac{\partial c}{\partial z}) \qquad (C-1)$$

numerically in an altitude-time space of variable dimensions. Such a solution estimates the concentration at each point in an altitude-time grid within the region of altitude from h to h/2 where h is the altitude of the inversion base at each time. Since h increases, the region in which solution takes place is the shaded region in Figure C-1.

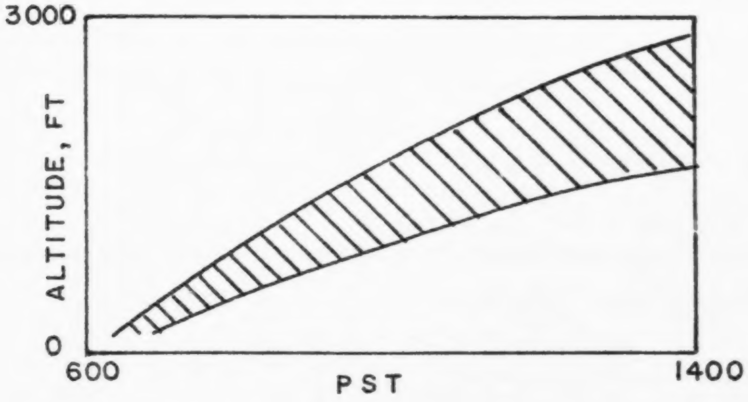

Figure C-1. Region of solution.

Equation C-1 may be written as

$$\frac{dc}{dt} = K(z,t)\,\frac{\partial^2 c}{\partial z^2} + K'(z,t)\,\frac{\partial c}{\partial z} \tag{C-2}$$

where K'(z,t) is the partial derivative of K(z,t) with respect to altitude. This is a parabolic partial differential equation according to the criteria of Milne (103).

To avoid stability problems, an implicit solution was derived analogous to the formulation of an implicit parabolic solution presented by Ketter and Prawel (104). The first and second spatial derivatives were replaced by first central-difference expressions. The first forward-difference expression was substituted for the time derivative yielding the following recurrence formula:

$$\begin{aligned}
C_{i+1,j} - C_{i,j} = (1-\theta)\Bigg\{ & \frac{\Delta t}{(\Delta z)^2}\,[K_{i,j+1/2}\,(C_{i,j+1} - C_{i,j}) \\
& + K_{i,j-1/2}\,(C_{i,j-1} - C_{i,j})] \\
& + \frac{1}{2\Delta z}\,[K'_{i,j}\,(C_{i,j+1} - C_{i,j-1})]\Bigg\} \\
+ \theta\Bigg\{ & \frac{\Delta t}{(\Delta z)^2}\,[K_{i+1,j+1/2}\,(C_{i+1,j+1} - C_{i+1,j}) \\
& + K_{i+1,j-1/2}\,(C_{i+1,j-1} - C_{i+1,j})] \\
& + \frac{1}{2\Delta z}\,[K'_{i+1,j}\,(C_{i+1,j+1} - C_{i+1,j-1})]\Bigg\} .
\end{aligned}$$

The term multiplied by $(1-\theta)$ is the contribution of concentrations on the $i^{th}$ time step and the term multiplied by $\theta$ is the contribution of concentrations on the $i+1^{th}$ time step. $C_{i+1,j}$, the concentration on the $i+1^{th}$ time step and the $j^{th}$ altitude level, is dependent upon the concentrations above and below it on the $i+1^{th}$ time step and the concentrations above, below and on the same altitude level on the $i^{th}$ time step. This dependence is shown in Figure C-2.

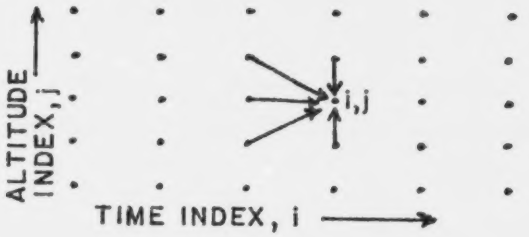

Figure C-2. Solution-space indexing.

The values of K and K' are average values across the altitude range to which they are applied. For instance, $K_{i,j+1/2}$ is the integral of K from $z_j$ to $z_{j+1}$ divided by $\Delta z$. The expressions for K and K' used here are:

$$K = -A' \ln \left(\frac{2z}{h} - 1\right) \tag{C-4}$$

and

$$K' \quad \frac{-A'}{z-h/2} \tag{C-5}$$

where z is altitude, $A' = 84{,}237 \text{ ft}^2 \text{ hr}^{-1}$ and h is the altitude of the inversion base. Special consideration must be made in evaluating K and K' near h/2. If z is nearly equal to h/2, absurdly high values of K and K' can result. Thus, if the difference between some z and h/2 was less than one foot the values of K and K' were computed based on a corrected z, $z_c$, such that

$$z_c = h/2 + 1 \quad . \tag{C-6}$$

Rearranging Equation C-3 so that the i+1th concentration terms are on the left side of the equation and the i terms on the right gives:

$$\begin{aligned} &- \theta\,(r\,K_{i+1,j+1/2} + sK'_{i+1,j})\,C_{i+1,j+1} \\ &+ [1 + \theta r\,(K_{i+1,j+1/2} + K_{i+1,j-1/2})]\,C_{i+1,j} \\ &- \theta\,(rK_{i+1,j-1/2} + sK'_{i+1,j})\,C_{i+1,j-1} \end{aligned} \tag{C-7}$$

$$= (1-\theta)\ (rK_{i,j+1/2} + sK'_{i,j})\ C_{i,j+1}$$

$$+ [1 + (1-\theta)\ r\ (K_{i,j+1/2} + K_{i,j-1/2})]\ C_{i,j}$$

$$+ (1-\theta)\ (rK_{i,j-1/2} + sK'_{i,j})\ C_{i,j-1}$$

where

$$r = \frac{\Delta t}{(\Delta z)^2} \quad \text{and} \quad s = \frac{1}{2\Delta Z} \quad .$$

Let

$$\alpha_j = -\theta(rK_{i+1,j+1/2} + sK'_{i+1,j}) \tag{C-8a}$$

$$\beta_j = 1 + \theta r(K_{i+1,j+1/2} + K_{i+1,j-1/2}) \tag{C-8b}$$

$$\gamma_j = -\theta(rK_{i+1,j+1/2} + sK'_{i+1,j}) \tag{C-8c}$$

and let $b_j$ equal the entire right-hand side of Equation C-7. Equation C-7 becomes

$$\alpha_j\ C_{i+1,j+1} + \beta_j\ C_{i+1,j} + \gamma_j\ C_{i+1,j-1} = b_j \quad . \tag{C-9}$$

This equation actually represents a set of equations from j equals 1 to n-2 where n is the number of altitude grid points inside the range $h \geq z \geq h/2$ plus 2 for the points just above and below the range. Since there are n concentrations and n-2 equations, the concentrations just above and below the region of solution must be specified. The system of linear equations is then:

$$\begin{bmatrix} \beta_1 & \gamma_1 & \cdots & \cdots & \cdots \\ \alpha_2 & \beta_2 & \gamma_2 & & \\ \vdots & \ddots & \ddots & \ddots & \\ \vdots & & \alpha_{n-3} & \beta_{n-3} & \gamma_{n-3} \\ \vdots & & & \alpha_{n-2} & \beta_{n-2} \end{bmatrix} \begin{bmatrix} C_{i+1,1} \\ C_{i+1,2} \\ \vdots \\ \vdots \\ C_{i+1,n-2} \end{bmatrix} = \begin{bmatrix} b_1 - \alpha_1 \\ b_2 \\ \vdots \\ b_{n-3} \\ b_{n-2} - \gamma_{n-2} \end{bmatrix}$$

or $$\underline{A}\ \underline{X} = \underline{B} \tag{C-10}$$

Matrix $\underline{A}$ is a tridiagonal matrix. A solution for $\underline{X}$ was obtained using a subroutine described by Carnahan, Luther and Wilks (105). The concentration just below h/2 is known from the helicopter data given the assumption that there is zero gradient of ground-source pollutants from about 50 m up to h/2; thus, the lower boundary condition is well established. The upper boundary condition, while not known from direct measurement, may be assumed to be quite low since this is characteristic of conservative pollutants emitted from the ground in the Los Angeles basin (65).

In order to initiate computation it is necessary to specify concentrations at all altitudes within the region of solution. These values were determined from helicopter data.

Since mixing depth, initial and boundary conditions were needed at the space-time grid points, it was necessary to interpolate the data between actual measurement points. A cubic spline interpolation subroutine from the International Mathematics and Statistics Library was used for this purpose. The computed vertical concentration profiles were saved in a buffer such that on any time step the profile from the previous step was available. For each time step, the temporal derivative at all altitude points was approximated by the first backward difference expression.

$$\frac{dC_{i,j}}{dt} \cong \frac{C_{i,j} - C_{i-1,j}}{\Delta} \tag{C-11}$$

These derivatives were then integrated between h and 150 feet. Both trapezoid rule integration and Simpsons rule were tested; there was very little difference between their results. Simpsons rule was used for the final results. The integral is the flux at j and was listed at time step i-1. Thus, the fluxes at time i-1 are those required to change the $C_{i-1,j}$ to the $C_{i,j}$ during the one time step for all j.

The initial grid spacing chosen was 0.10 hour and 25 feet. The effect of reducing both temporal and spatial steps was investigated by comparing the original estimated values of CO flux at various times during the run with those computed using one-half the altitude spacing and those using one-fourth the time steps. These comparisons in Table C-1 show that the differences are quite small and that the original choice of grid spacing was acceptable. Note that for the run with the shortened time step, the flux value obtained at a given time had to be averaged with the following three flux estimates before the comparison was made, since the flux at a particular time represents the average flux between that time and the next time.

TABLE C-1. COMPARISON OF FLUX CALCULATIONS USING DIFFERENT TIME AND ALTITUDE GRID SPACING

| Time, hours PST | Flux at h/2 $kg \cdot m^{-2} \cdot hr^{-1}$ | | | Flux at 150 ft $kg \cdot m^{-2} \cdot hr^{-1}$ | | |
|---|---|---|---|---|---|---|
| | $\Delta t$ = 0.1 hr<br>$\Delta h$ = 25 ft | $\Delta t$ = 0.1 hr<br>$\Delta h$ = 12.5 ft | $\Delta t$ = 0.025 hr<br>$\Delta h$ = 25 ft | $\Delta t$ = 0.1 hr<br>$\Delta h$ = 25 ft | $\Delta t$ = 0.1 hr<br>$\Delta h$ = 12.5 ft | $\Delta t$ = 0.025 hr<br>$\Delta h$ = 25 ft |
| 8.25- 8.35 | $6.02 \times 10^{-8}$ | $5.78 \times 10^{-8}$ | $5.91 \times 10^{-8}$ | $5.69 \times 10^{-8}$ | $5.46 \times 10^{-8}$ | $5.76 \times 10^{-8}$ |
| 10.05-10.15 | $6.29 \times 10^{-8}$ | $6.27 \times 10^{-8}$ | $6.33 \times 10^{-8}$ | $3.60 \times 10^{-8}$ | $3.60 \times 10^{-8}$ | $3.60 \times 10^{-8}$ |
| 12.05-12.15 | $6.09 \times 10^{-9}$ | $6.07 \times 10^{-9}$ | $6.40 \times 10^{-9}$ | $-4.60 \times 10^{-8}$ | $-4.60 \times 10^{-8}$ | $-4.60 \times 10^{-8}$ |
| 13.85-13.95 | $-1.33 \times 10^{-8}$ | $-1.36 \times 10^{-8}$ | $-1.33 \times 10^{-8}$ | $-7.18 \times 10^{-8}$ | $-7.18 \times 10^{-8}$ | $-7.18 \times 10^{-8}$ |

# APPENDIX D

## CALCULATION OF $k_1$ FROM THEORY

The calculation employed in this work is similar to that of Calvert (26) except that the actual mixing depth and $NO_2$ concentrations in the boundary layer were used instead of an empirical fit to ground station data. Also, $k_1$ was calculated directly taking into account reflection at the earth's surface rather than calculating $k_1$ without reflection and correcting afterward. The method generally uses the relations from Leighton (3) expanded to account for reflection.

### TRANSMISSION THROUGH THE ATMOSPHERE

Consider a point within the boundary layer at an altitude above the ground of $\ell$; at this time and location, the mixing depth is H and the solar zenith angle is z. The downward directed radiant flux on a horizontal surface for wavelength $\lambda$ just above the polluted layer has two components: $I'_{d\lambda}$, the direct beam irradiance, and $I'_{s\lambda}$, the sky irradiance which is some fraction of the light scattered from the direct beam. Leighton (3) gives the following relations:

$$I'_{d\lambda} = T_{s\lambda} T_{a\lambda} I_{o\lambda} \cos z \tag{D-1}$$

$$I'_{s\lambda} = g (1-T_{s\lambda}) T_{a\lambda} I_{o\lambda} \cos z \quad . \tag{D-2}$$

$T_{s\lambda}$ is the transmissivity resulting from molecular and particulate scattering. $T_{a\lambda}$ is the transmissivity resulting from $O_3$ absorption, $I_{o\lambda}$ is the solar constant, and g is the fraction of light scattered downward (taken as 1/2 here). The irradiances are summed over the wavelength interval $\Delta\lambda$ with a center wavelength $\lambda$, and the transmissivities are evaluated at $\lambda$. This analysis used 10 nm band widths. The solar constant data of Johnson (94) were used.

The transmissivities were determined as follows:

$$\log_{10} T_{a\lambda} = -\alpha_\lambda \, (O_3) \, m \tag{D-3}$$

where $\alpha_\lambda$ was interpolated from a table in Leighton (3), p. 19. $(O_3)$ is the ozone column and was taken to be 2.8 mm to agree with Calvert.

$$m \approx \sec z$$

$$T_{s\lambda} = T_{m\lambda} \, T_{p\lambda} \tag{D-4}$$

where $T_{m\lambda}$ is the molecular component; $T_{p\lambda}$ is the particulate component

$$\log_{10} T_{m\lambda} = -(S_{m\lambda})_o \frac{P}{Po} m \tag{D-5}$$

where $(S_{m\lambda})_o$ the theoretical attenuation coefficient is taken from Leighton (3).

$$\log_{10} T_{p\lambda} = -(3.75 \times 10^{-3} \, \lambda^{-2} \, w + 3.5 \times 10^{-2} \, \lambda^{-0.75} \, d) \, m \tag{D-6}$$

where w is the water factor; d is the dust factor. It was found that it was necessary to set w and d equal to 2 to fit UV radiometer values from Mt. Disappointment for LARPP operation 33. This fit is shown in Figure 82. This adjustment must be regarded as an empirical evaluation of w and d, bearing little relation to the actual water and dust content of the air measured by independent means.

## ATTENUATION OF DOWNWARD DIRECTED RADIATION

The downward directed radiation reaching an altitude, $\ell$, within the boundary layer is given by

$$I_{d\lambda} = I'_{d\lambda} \, 10^{-\alpha_\lambda C(H-\ell)\sec z} \tag{D-7}$$

$$I_{s\lambda} = I'_{s\lambda} 10^{-\alpha_\lambda Ci(H-\ell)} \tag{D-8}$$

which accounts for attenuation by $NO_2$ within the boundary layer. $\alpha_\lambda$ is the extinction coefficient for $NO_2$ at $\lambda$, C is the $NO_2$ concentration and i is a factor relating the average path length of diffuse sky radiation to the vertical thickness of the absorbing layer through which the beam must pass. Following Leighton's example, $i$ was set equal to 2. The molar absorption coefficient of $NO_2$ used by Calvert (26) were employed here. The concentration of $NO_2$ was determined from helicopter pattern averages constant up to the inversion base. It is believed that this method of calculating attenuation is more valid than Calvert's use of stationary, ground-level UV radiometers to estimate the appropriate concentration and path length for calculations. These stations may bear little relation to what happens along the trajectory, and Calvert's method has very poor temporal resolution in calculating attenuation.

## REFLECTED RADIATION

First the radiation reaching the ground was calculated by the following equations:

$$I_{dt\lambda} = I'_{d\lambda}\ 10^{-\alpha_\lambda CH \sec z} \qquad \text{(D-9)}$$

$$I_{st\lambda} = I'_{d\lambda}\ 10^{-\alpha_\lambda CiH} \qquad \text{(D-10)}$$

where $I_{dt\lambda}$ and $I_{st\lambda}$ are the portions of the direct and sky irradiance reaching the ground. Assuming that the radiation reflection at the ground is diffuse, the reflected irradiance at altitude $\ell$, $I_{r\lambda}$, after attenuation may be calculated (treating the path length problem similar to sky radiation path length).

$$I_{r\lambda} = (I_{dt\lambda} + I_{st\lambda})\ a_\lambda\ 10^{-\alpha_\lambda Ci\ell} \qquad \text{(D-11)}$$

where $a_\lambda$ is the albedo at $\lambda$.

The term $k_1$ may then be calculated by the addition of the reflection term and the quantum yield for $NO_2$ photolysis to Leighton's Equation (II-33) giving the following result:

$$k_1 = \sum_\lambda 2.303\ \Phi_\lambda\ \alpha_\lambda\ j^{-1}\ (I_{d\lambda} \sec z + i(I_{s\lambda} + I_{r\lambda})) \qquad \text{(D-12)}$$

where $\Phi_\lambda$ is the quantum yield at $\lambda$, and $j$ is a unit conversion factor.

The quantum yield was taken from Jones and Bayes as presented by Calvert (26).

Calvert's method of calculating $k_1$ differs somewhat from that presented here. He first calculated $k_1$ for the case of no attenuation in the zero gradient region and an albedo of zero. Then, the estimate was improved to give $k_1'$ by the following relationship:

$$k_1' = k_1 \frac{I_{dt} + I_{st} + I_r}{I_d + I_s} \quad . \tag{D-13}$$

The absence of subscript $\lambda$ indicates summation on $\lambda$. This correction is highly questionable for several reasons: (1) $I_{dt}$ and $I_{st}$ are the downward irradiances at the earth's surface, not at altitude $\ell$; (2) the dependence of $k_1$ on radiation direction has been removed in Equation D-12 by multiplying $I_d$ by sec z and $I_{s\lambda} + I_{r\lambda}$ by i, but this is ignored in D-13; (3) since $\Phi$ and $\alpha$ are functions of $\lambda$, the correction of $k_1$ using the irradiances summed on $\lambda$ is not correct -- the correction must be performed prior to summing on $\lambda$.

## APPENDIX E

## THE INTERACTIVE EFFECTS OF INHOMOGENEITY AND ATMOSPHERIC PROCESSES ON PHOTOSTATIONARY STATE OZONE

As shown by the example in Section 7, the inhomogeneous nature of the atmosphere can lead to average $O_3$ concentrations either greater or larger than one would expect based on $k_1$ and the average $NO_2/NO$ ratio. If the covariance of NO and $O_3$ is negative, the average $O_3$ will be higher than expected, and if the covariance is positive, the average $O_3$ will be less than expected, as may be seen from the equation:

$$[\hat{O_3}] = \frac{k_1}{k_3} \frac{[\hat{NO_2}]}{[\hat{NO}]} - \frac{\mathrm{cov}(NO,O_3)}{[\hat{NO}]} \quad . \tag{E-1}$$

The hats on the concentrations represent spatial averaging, either by composite sampling, or numerical averaging of point concentrations. The effects of various processes will be illustrated by means of simplified examples.

Example E-1. Averaging measurements of $NO_2$ and NO to calculate photostationary state $O_3$.

Consider the two air parcels from Section 7 as shown in Figure E-1. Each parcel is well mixed within itself to the molecular level. The $O_3$ concentration within each parcel obeys photostationary state at $k_1/k_3$ = 0.016 ppm.

$$[O_3] = \frac{k_1}{k_3} \frac{[NO_2]}{[NO]} \tag{E-2}$$

Instruments aboard a helicopter take a single measurement of NO, $NO_2$ and $O_3$ as the helicopter flys through the two parcels in such a way that each parcel contributes equally to the measurement. The measured quantities are then:

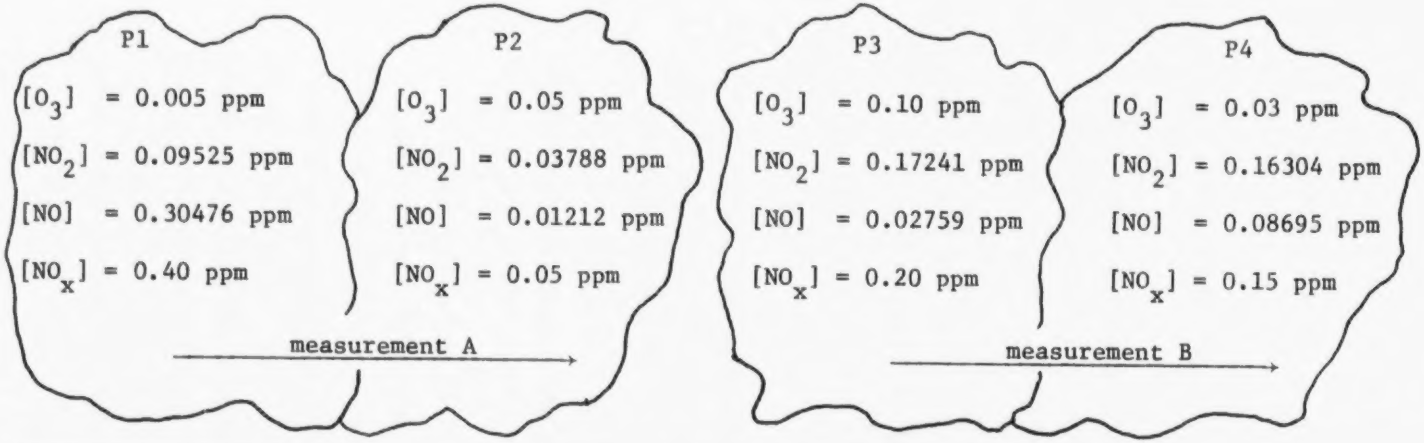

| Meas. | Parcel | $[NO_2]/[NO]$ | $[\hat{O}_3]$,ppm | $[\widehat{NO}_2]$,ppm | $[\widehat{NO}]$,ppm | $\frac{[\hat{O}_3]\,[\widehat{NO}]}{[\widehat{NO}_2]}$, ppm | cov,ppm$^2$ | cov/$[\widehat{NO}]$,ppm |
|---|---|---|---|---|---|---|---|---|
| A | 1 | 0.3125 | 0.02750 | 0.06657 | 0.15844 | 0.06545 | -0.00329 | -0.0208 |
|  | 2 | 3.1254 |  |  |  |  |  |  |
| B | 3 | 6.249 | 0.065 | 0.16773 | 0.05728 | 0.02220 | -0.00104 | -0.0182 |
|  | 4 | 1.8749 |  |  |  |  |  |  |
| Average of A & B |  |  | 0.04625 | 0.11715 | 0.10786 |  | -0.00217 | -0.01946 |

Figure E-1. Data for example E-1 and summary.

Measurement A:

$$[\hat{O}_3] = 0.02750 \text{ ppm}$$

$$[\hat{NO}_2] = 0.06657 \text{ ppm}$$

$$[\hat{NO}] = 0.15844 \text{ ppm}$$

as shown in Figure E-1.

The $k_1/k_3$ estimated from simple photostationary state is much too high

$$\frac{k_1}{k_3} = \frac{[\hat{O}_3][\hat{NO}]}{[\hat{NO}_2]} = 0.06545 \text{ ppm} \quad . \tag{E-3}$$

Thus, the photostationary state expressions such as E-2 and E-3 were rederived to take into account inhomogeneity (Section 7), yielding Equation E-1 and the following:

$$\frac{k_1}{k_3} = \frac{[\hat{NO}][\hat{O}_3] + \text{cov}(NO,\ O_3)}{[\hat{NO}_2]} \quad . \tag{E-4}$$

The covariance of the two parcels is calculated as follows:

$$\text{cov}(NO,O_3) = \frac{\sum_{i=1}^{2} (NO_i-\hat{NO})(O_{3i}-\hat{O}_3)}{2}$$

$$= -0.00329 \text{ ppm}^2 \quad .$$

This yields the correct value for $k_1/k_3$ in Equation E-4.

Now consider parcels 3 and 4 in Figure E-1, which were sampled in a manner similar to the previous two. They are subject to the same temperature and solar radiation as parcels 1 and 2.

Measurement B:

$$[\hat{O}_3] = 0.065 \text{ ppm}$$

$$[\hat{NO}_2] = 0.16773 \text{ ppm}$$

$$[\hat{NO}] = 0.05728 \text{ ppm}$$

$$\text{cov}(NO,O_3) = -0.00104 \text{ ppm}^2$$

If measurements A and B are averaged together mathematically,

$$\overline{[\hat{O_3}]} = 0.04625 \text{ ppm}$$

$$\overline{[\hat{NO_2}]} = 0.11715 \text{ ppm}$$

$$\overline{[\hat{NO}]} = 0.10786 \text{ ppm}$$

$$\overline{\text{cov}(NO,O_3)} = -0.00217 \text{ ppm}^2 \quad .$$

Putting these values in Equation E-3 gives too great a value,

$$\frac{k_1}{k_3} = 0.04258 \text{ ppm}$$

and in Equation E-2

$$[O_3] = \frac{(0.016)(0.11715)}{(0.10786)} = 0.01738 \text{ ppm}$$

the ozone concentration is underestimated.

If one attempts to calculate the average photostationary state ozone by entering the average of A and B in Equation E-1, the result is a little closer to the true average ozone.

$$[O_3] = \frac{(0.016)(0.11715)}{0.10786} - \frac{(-0.00217)}{(0.10786)}$$

$$= 0.03750 \text{ ppm} \quad .$$

Considering that the mean of a ratio is not necessarily equal to the ratio of the means, the following exact equation must be applied to estimate the average photostationary state $O_3$ from individual measurement values of $NO_2$ and NO.

$$\overline{[\hat{O_3}]} = \frac{k_1}{k_3}\left(\overline{\frac{[\hat{NO_2}]}{[\hat{NO}]}}\right) - \left(\overline{\frac{\text{cov}(NO,O_3)}{[\hat{NO}]}}\right) \qquad \text{(E-5)}$$

$$\overline{[\hat{O}_3]} = (0.016)(1.67423) - (-0.01946)$$

$$= 0.04625 \text{ ppm}$$

As may be seen from this Table E-1 if the photostationary state $O_3$ or $k_1/k_3$ are to be estimated from either composite sample measurements, or from averaged measurements, the effect of inhomogeneity must be considered unless the system is well mixed.

Example E-2. The Effect of Mixing.

If two air parcels containing $O_3$ in photostationary state are mixed together completely, the resulting concentrations of $O_3$, NO, and $NO_2$ may be determined from the constraint that the stationary state is maintained. Thus, letting X equal the amount of $O_3$ and NO that must be consumed to maintain stationary state:

$$\frac{k_1}{k_3} = \frac{([\hat{O}_3] - X)([\widehat{NO}] - X)}{([\widehat{NO}_2] + X)} \quad . \tag{E-6}$$

This is a quadratic equation in X whose solution is:

$$X = \frac{[\widehat{NO}]+[\hat{O}_3] + \frac{k_1}{k_3} - \sqrt{([\widehat{NO}]+[\hat{O}_3] + \frac{k_1}{k_3})^2 - 4([\widehat{NO}][\hat{O}_3] - \frac{k_1}{k_3}[\widehat{NO}_2])}}{2} \tag{E-7}$$

(The root formed by addition of the radical is extraneous.) From Equation E-4, it may be determined that

$$[\widehat{NO}][\hat{O}_3] - \frac{k_1}{k_3}[\widehat{NO}_2] = -\mathrm{cov}(NO,O_3) \quad .$$

Thus,

$$X = \frac{[\widehat{NO}]+[\hat{O}_3] + \frac{k_1}{k_3}}{2} - \sqrt{\frac{([\widehat{NO}]+[\hat{O}_3] + \frac{k_1}{k_3})^2}{4} + \mathrm{cov}(NO,O_3)} \quad . \tag{E-8}$$

## TABLE E-1. RESULTS OF VARIOUS APPROACHES TO ESTIMATE PHOTOSTATIONARY STATE $O_3$ AND $k_1/k_3$

| $\overline{O_3}$ (knowing $k_1/k_3$, $\hat{NO}_2$ and $\hat{NO}$) | |
|---|---|
| True average | 0.04625 ppm |
| Est. by $\frac{k_1}{k_3} \frac{\overline{[\hat{NO}_2]}}{\overline{[\hat{NO}]}}$ | 0.01738 |
| Est. by $\frac{k_1}{k_3} \frac{\overline{[\hat{NO}_2]}}{\overline{[\hat{NO}]}} - \frac{\overline{cov}}{\overline{[\hat{NO}]}}$ | 0.03750 |
| Est. by $\frac{k_1}{k_3} \left(\frac{\overline{[\hat{NO}_2]}}{\overline{[\hat{NO}]}}\right) - \left(\frac{\overline{cov}}{\overline{[\hat{NO}]}}\right)$ | 0.04625 |
| $k_1/k_3$ (knowing $O_3$, $NO_2$, $NO_2$) | |
| True value | 0.016 ppm |
| Est. by $\frac{\overline{[\hat{O}_3]}\ \overline{[\hat{NO}]}}{\overline{[\hat{NO}_2]}}$ | 0.04258 |

The $O_3$ after mixing, $[O_3]_m$ is given by:

$$[O_3]_m = [\hat{O}_3] - X \qquad \text{(E-9a)}$$

and similarly,

$$[NO]_m = [\hat{NO}] - X \quad \text{and} \quad [NO_2]_m = [\hat{NO}_2] + X \quad . \qquad \text{(E-9b,c)}$$

An alternate expression which emphasizes the effect on $O_3$ by alteration of the $NO_2/NO$ ratio follows:

$$[O_3]_m = \frac{k_1}{k_3} \; \frac{[\hat{NO}_2] + X}{[\hat{NO}] - X} \quad . \qquad \text{(E-10)}$$

The effect of the value of the original NO-$O_3$ covariance before mixing follows from Equations E-8 and E-9a.

$$\text{If } \mathrm{cov}(NO,O_3) < 0 \text{ then } [O_3]_m < [\hat{O}_3]$$

$$\text{If } \mathrm{cov}(NO,O_3) = 0 \text{ then } [O_3]_m = [\hat{O}_3]$$

$$\text{If } \mathrm{cov}(NO,O_3) > 0 \text{ then } [O_3]_m > [\hat{O}_3]$$

Consider the result of mixing parcels 1 and 2 from Example E-1 (Figure E-1).

$$X = 0.10097 - \sqrt{\frac{(0.20194)^2}{4} - 0.00329}$$

$$X = 0.01787 \text{ ppm}$$

Thus, the photostationary state $O_3$ has dropped from 0.02750 ppm to 0.00963 ppm. The ratio of $[\hat{NO}_2]/[\hat{NO}]$ has gone from 0.42016 to

$$\frac{[NO_2]_m}{[NO]_m} = \frac{([\hat{NO}_2] + X)}{([\hat{NO}] - X)} = \frac{0.08444}{0.14057} = 0.60070 \quad .$$

Thus, while the covariance/NO in Equation E-1 was raised to zero from -0.02076 ppm by mixing, the remaining term on the right-hand side increased by 0.00289 ppm to partially compensate for the loss of ozone by direct reaction with NO.

Example E-3. The Effect of Mixing on the Average of Measurements.

Consider the four air parcels from Example E-1. Measurement A spans parcels 1 and 2, and Measurement B spans parcels 3 and 4.

| A | B |
|---|---|
| $[\hat{O}_3] = 0.02750$ ppm | $[\hat{O}_3] = 0.06500$ ppm |
| $[\hat{NO}_2] = 0.06657$ ppm | $[\hat{NO}_2] = 0.16773$ ppm |
| $[\hat{NO}] = 0.15844$ ppm | $[\hat{NO}] = 0.05728$ ppm |
| $\mathrm{cov}(NO,O_3) = -0.00329\ \mathrm{ppm}^2$ | $\mathrm{cov}(NO,O_3) = -0.00104$ ppm |

When the two measurements were averaged, the following were obtained:

$$\overline{[O_3]} = 0.04625\ \mathrm{ppm},\quad \overline{[NO_2]} = 0.11715\ \mathrm{ppm}$$

$$\overline{[NO]} = 0.10786\ \mathrm{ppm},\quad \overline{\mathrm{cov}(NO,O_3)} = -0.00217\ \mathrm{ppm}^2$$

$$\frac{\overline{[\hat{NO}_2]}}{[\hat{NO}]} = 1.67423,\quad \frac{\overline{\mathrm{cov}(NO,O_3)}}{[\hat{NO}]} = -0.01946\ \mathrm{ppm}$$

If parcels 1 and 2 become well-mixed as in Example E-2

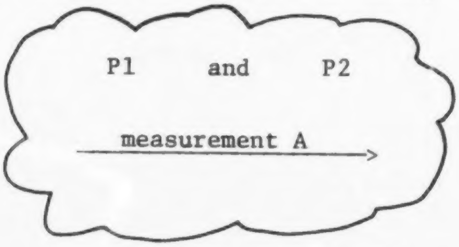

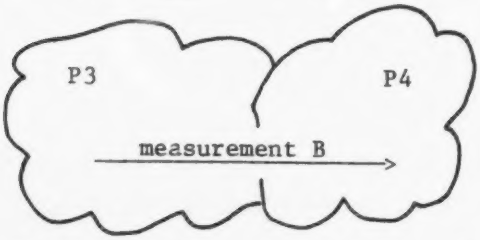

and the measurements were performed again, B would be the same but now A would be

A

$$[\hat{O}_3] = 0.00963 \text{ ppm}$$

$$[\hat{NO}_2] = 0.08444 \text{ ppm}$$

$$[\hat{NO}] = 0.14057 \text{ ppm}$$

$$\text{cov}(NO,O_3) = 0$$

The averaging of measurements A and B now yields:

$$\overline{[O_3]} = 0.03732 \text{ ppm}, \ \overline{[NO_2]} = 0.12609 \text{ ppm}$$

$$\overline{[NO]} = 0.09893 \text{ ppm}, \ \overline{\text{cov}(NO,O_3)} = -0.00052 \text{ ppm}^2$$

$$\left(\overline{\frac{[\hat{NO}_2]}{[\hat{NO}]}}\right) = 1.76447, \ \left(\overline{\frac{\text{cov}(NO,O_3)}{[\hat{NO}]}}\right) = -0.00908 \text{ ppm} \quad .$$

Prior to mixing Equation E-5 evaluates as follows:

$$\overline{[\hat{O}_3]} = \frac{k_1}{k_3}\left(\overline{\frac{[\hat{NO}_2]}{[\hat{NO}]}}\right) - \left(\overline{\frac{\text{cov}(NO,O_3)}{[\hat{NO}]}}\right)$$

$$\overline{[\hat{O}_3]} = 0.02679 + 0.01946 = 0.04625 \text{ ppm} \quad .$$

After mixing, it evaluates as:

$$\overline{[\hat{O}_3]} = 0.02823 + 0.00908 = 0.03731 \text{ ppm} \quad .$$

Thus, as was the case with the mixed parcel alone, the contribution of the cov/NO term to average ozone was reduced and the average $NO_2/NO$ ratio term partially compensates for the increased homogeneity.

Example E-4. The Effect of Photochemical Oxidation of NO to $NO_2$ on the Covariance of NO and $O_3$.

The effect of oxidation of NO to $NO_2$ is more difficult to handle mathematically. Such oxidation increases $[\hat{O}_3]$. Solving Equation E-1 for the covariance

$$\mathrm{cov}(NO,O_3) = \frac{k_1}{k_3}\,[\hat{NO_2}] - [\hat{O_3}][\hat{NO}] \quad .$$

Also,
$$[\hat{O_3}] = \frac{k_1}{k_3}\quad \overline{\frac{[NO_2]}{[NO]}} \quad .$$

Thus,
$$\mathrm{cov}(NO,O_3) = \frac{k_1}{k_3}\left([\hat{NO_2}] - \overline{\frac{[NO_2]}{[NO]}}\quad [\hat{NO}]\right) \quad . \qquad \text{(E-11)}$$

It is not readily apparent whether NO conversion increases or decreases covariance from this form since it depends upon the joint probability distribution of NO, $NO_2$, and some variable representing the amount of NO oxidized within each parcel. To get an idea of the possibilities, a condition close to those in the atmosphere will be considered.

Three parcels of air maintain photostationary state $O_3$ at a $k_1/k_3$ of 0.016.

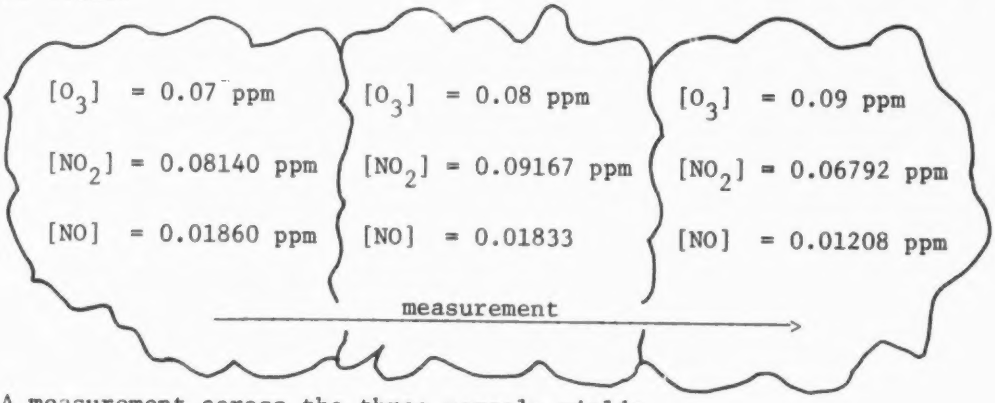

A measurement across the three parcels yields

$$[\hat{O_3}] = 0.08 \text{ ppm}$$

$$[\hat{NO_2}] = 0.08033 \text{ ppm}$$

$$[\hat{NO}] = 0.01634 \text{ ppm} \quad .$$

Also,
$$\mathrm{cov}(NO,O_3) = -2.2000 \times 10^{-5}\ \text{ppm}^2$$

$$\overline{\frac{[NO_2]}{[NO]}} = 5.00000, \qquad \frac{[\hat{NO_2}]}{[\hat{NO}]} = 4.91616$$

$$\frac{\mathrm{cov}(\mathrm{NO},\mathrm{O}_3)}{[\widehat{\mathrm{NO}}]} = -1.3464 \times 10^{-3}\ \mathrm{ppm}\quad .$$

If 10 percent of the NO in each parcel is oxidized the concentrations below result.

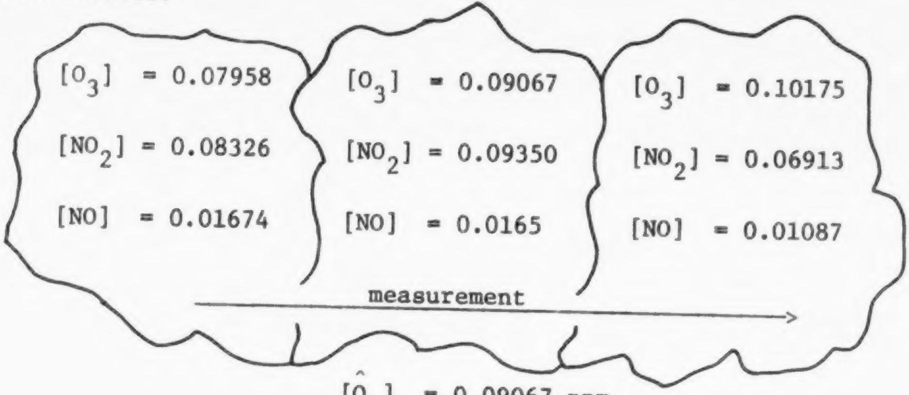

$$[\widehat{\mathrm{O}_3}] = 0.09067\ \mathrm{ppm}$$

$$[\widehat{\mathrm{NO}_2}] = 0.08196\ \mathrm{ppm}$$

$$[\widehat{\mathrm{NO}}] = 0.01470\ \mathrm{ppm}$$

$$\mathrm{cov}(\mathrm{NO},\mathrm{O}_3) = -2.1433 \times 10^{-5}\ \mathrm{ppm}^2$$

$$\frac{\mathrm{cov}(\mathrm{NO},\mathrm{O}_3)}{[\widehat{\mathrm{NO}}]} = -1.4581 \times 10^{-3}\ \mathrm{ppm}$$

$$\frac{\overline{[\mathrm{NO}_2]}}{[\mathrm{NO}]} = 5.66670, \qquad \frac{[\widehat{\mathrm{NO}_2}]}{[\widehat{\mathrm{NO}}]} = 5.57551$$

Thus, in this example, oxidation of NO to $NO_2$ has increased the measured $O_3$ by about 1 pphm. The covariance of NO and $O_3$ was raised slightly, but the cov/$[\widehat{\mathrm{NO}}]$ was slightly lowered indicating increased effect of inhomogeneity on $O_3$. Other numerical examples have shown that when the concentrations in the parcels are greatly different, a great change in the covariance can result from oxidation with very little change in $O_3$.

Example E-5. Emission of $NO_2$.

Consider air parcels 1 and 2 from Example E-1 (Figure E-1). The $NO_2$ is injected into both parcels. The resulting concentrations in each parcel may be determined by Equation E-7 where $[\hat{NO_2}]$ is replaced by the initial $NO_2$ concentration in a parcel plus the increase in $NO_2$ concentration caused by the emission in the absence of reaction.

If emission produced an additional 0.01 ppm of $NO_2$ in each parcel, then

parcel 1

$$X = \frac{0.32576 - \sqrt{(0.32576)^2 - 4(1.5238 - 1.68 \times 10^{-3})}}{2}$$

$$X = \frac{0.32576 - 0.32674}{2} = -0.00049 \text{ ppm}$$

parcel 2

$$X = \frac{0.07812 - \sqrt{(0.07812)^2 - 4(6.0600 \times 10^{-4} - 7.6603 \times 10^{-4})}}{2}$$

$$X = \frac{0.07812 - 0.08212}{2} = -0.00200 \text{ ppm}$$

Thus, the new concentrations are:

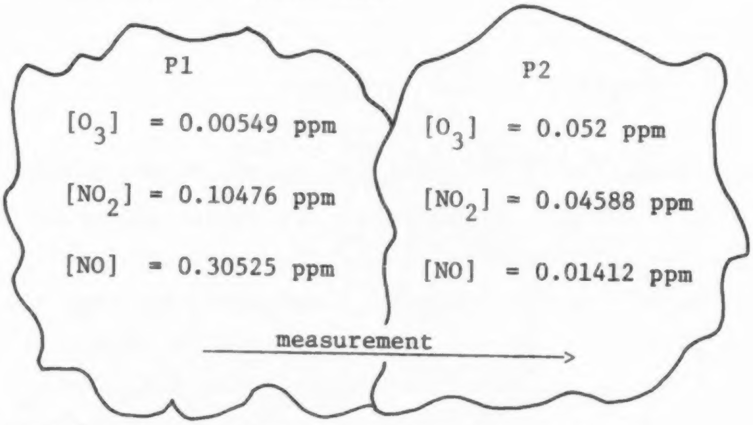

The measured concentration, as shown above would be:

$$[\hat{O_3}] = 0.02875 \text{ ppm}$$

$$[\hat{NO_2}] = 0.07532 \text{ ppm}$$

$$[\hat{NO}] = 0.15969 \text{ ppm} \quad .$$

Also,

$$\text{cov}(NO,O_3) = -0.00339 \text{ ppm}^2$$

$$\frac{\text{cov}(NO,O_3)}{[\hat{NO}]} = -0.02120 \text{ ppm}$$

$$\frac{[\hat{NO_2}]}{[\hat{NO}]} = 0.47166$$

Thus, emission of $NO_2$ has had the effect of increasing the measured $O_3$ while decreasing the covariance of NO and $O_3$. This may be seen by comparing the above values with those from Example E-1. The terms in Equation E-1 have been changed by emission of $NO_2$ as follows:

| | $[\hat{O_3}]$ | $\frac{k_1}{k_3}\frac{[\hat{NO_2}]}{[\hat{NO}]}$ | $\frac{\text{cov}(NO,O_3)}{[\hat{NO}]}$ |
|---|---|---|---|
| before | 0.02750 ppm | 0.00672 ppm | -0.02076 ppm |
| after | 0.02875 ppm | 0.00755 ppm | -0.02120 ppm |

It may be seen that the effect of addition of $NO_2$ is to increase the $O_3$ concentration by raising the $NO_2$/NO ratio as well as the increased effect of inhomogeneity (i.e., the cov/NO term).

# APPENDIX F

## CORRECTION OF DATA FOR THE DARK REACTION OF NO AND $O_3$ DURING SAMPLING

For most purposes correction of smog chamber data for the loss of NO and $O_3$ and gain of $NO_2$ is not worthwhile. Generally, the corrections are not much more than 1 pphm, however, in the simulation experiments the maximum ozone concentration only reached about 10 to 15 pphm. Thus, a method was developed for correcting NO, $O_3$, and $NO_2$ data for the NO - $O_3$ reaction.

Given the measured concentration [NO], $[O_3]$, and $[NO_2]$, it is desired to determine the original concentrations at some time, t, in the past. The rate expression for the reaction may be written in terms of the decrease of reactant concentrations, x.

$$\frac{dx}{dt} = k_3 \, [NO][O_3] \tag{F-1}$$

$$= k_3 \, ([NO]-x)([O_3]-x)$$

$$\frac{dx}{([NO]-x)([O_3]-x)} = kdt$$

The left-hand side of the equation may be integrated by use of partial fractions.

$$\frac{1}{[NO]-[O_3]} \int_0^{x_f} \left( - \frac{dx}{[NO]-x} + \frac{dx}{[O_3]-x} \right) = \int_{t_f}^{0} k_3 dt$$

Note that the limits of integration on t have been reversed so that the reaction will be run in reverse (x is negative).

$$\frac{1}{[NO]-[O_3]} \left(\ln([NO]-x) - \ln([O_3]-x)\right) \Big|_0^{x_f} = -k_3 t_f \tag{F-2}$$

$$\frac{1}{[NO]-[O_3]} \ln \left( \frac{([NO]-x_f)[O_3]}{([O_3]-x_f)[NO]} \right) = -k_3 t_f$$

Rearranging Equation F-2 yields an expression for the initial reactant ratio.

$$\frac{([NO]-x_f)}{([O_3]-x_f)} = \frac{[NO]}{[O_3]} \exp\left(-k_3([NO]-[O_3])t_f\right) \tag{F-3}$$

Let
$$\frac{[NO]}{[O_3]} \exp\left(-k_3([NO]-[O_3])t_f\right) = R \quad . \tag{F-4}$$

Solving for $x_f$ gives

$$x_f = \frac{[NO]-R[O_3]}{(1-R)} \quad . \tag{F-5}$$

Then the concentrations prior to reaction are given by

$$[NO]_o = [NO] - x_f \tag{F-6}$$

$$[O_3]_o = [O_3] - x_f$$

$$[NO_2]_o = [NO_2] + x_f \quad .$$

Selected sets of measurements from the October 12 simulation were corrected. The original data and corrected data for $O_3$, NO, and $NO_2$ were plotted versus time as shown in Figures F-1, F-2, and F-3. The correction is greatest between 0900 and 1000 (corrected to PST) reaching values just above 1 pphm.

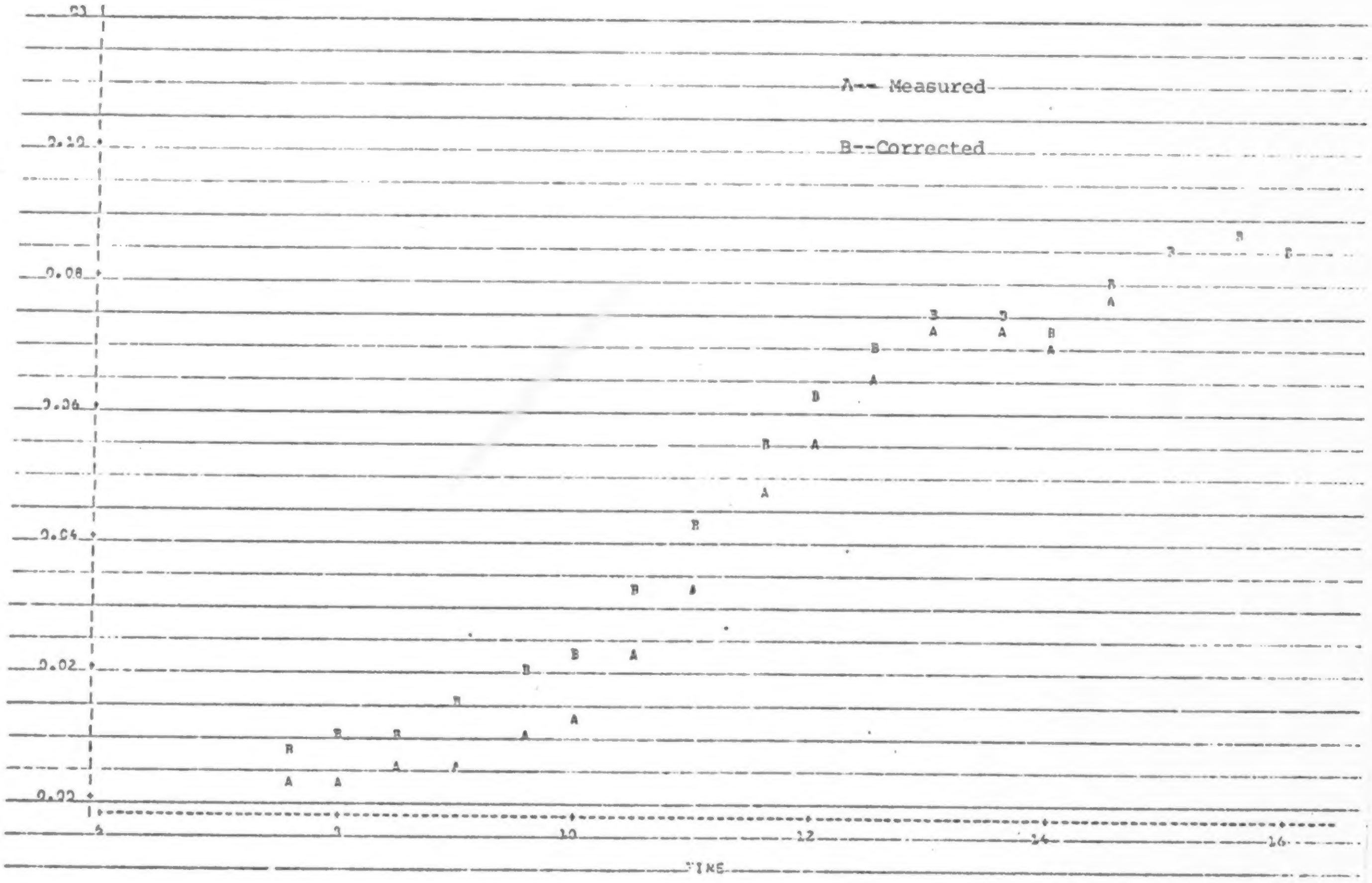

Figure F-1. Measured and corrected ozone for October 12 simulation.

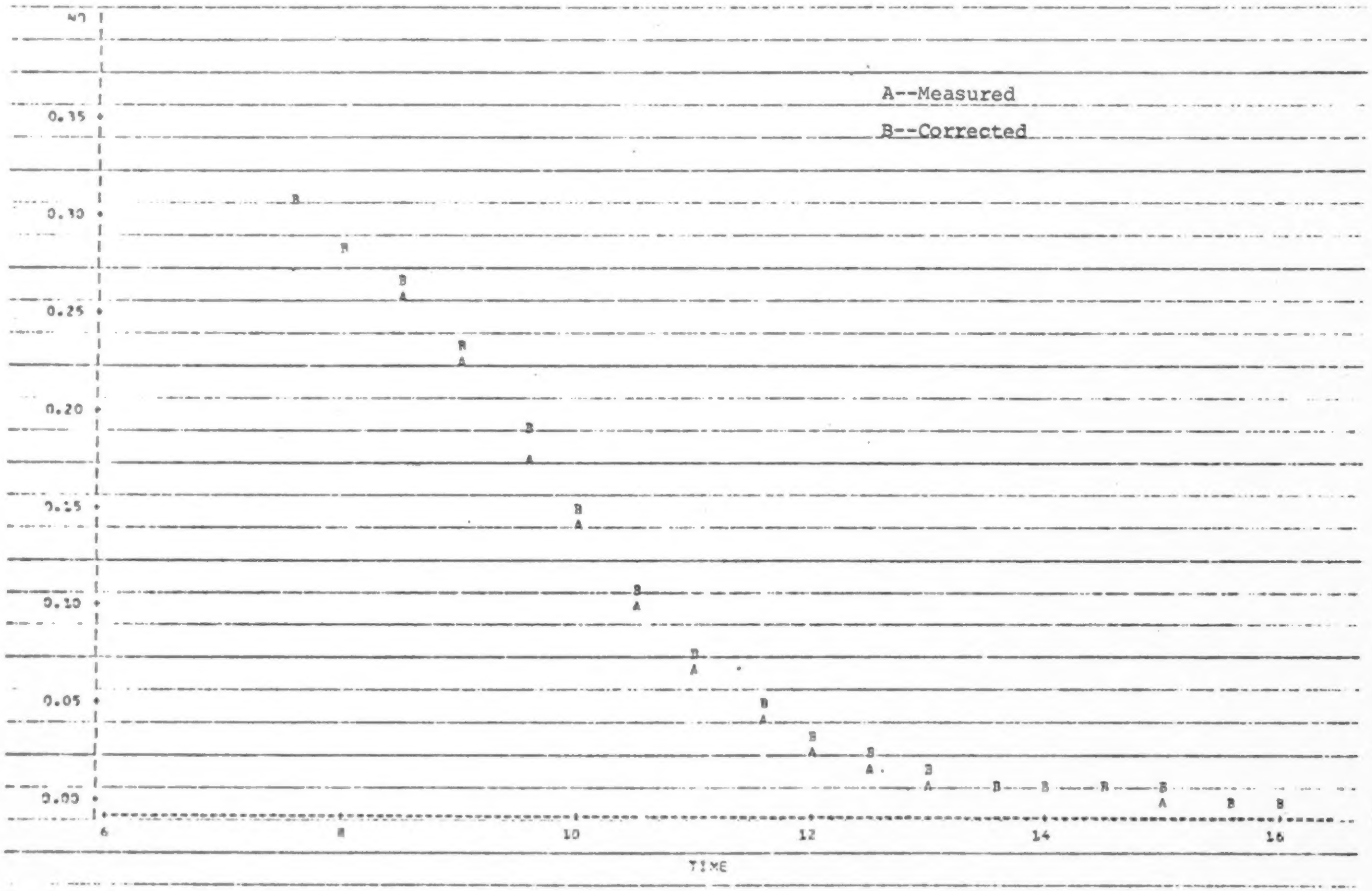

Figure F-2. Measured and corrected NO for simulation of October 12.

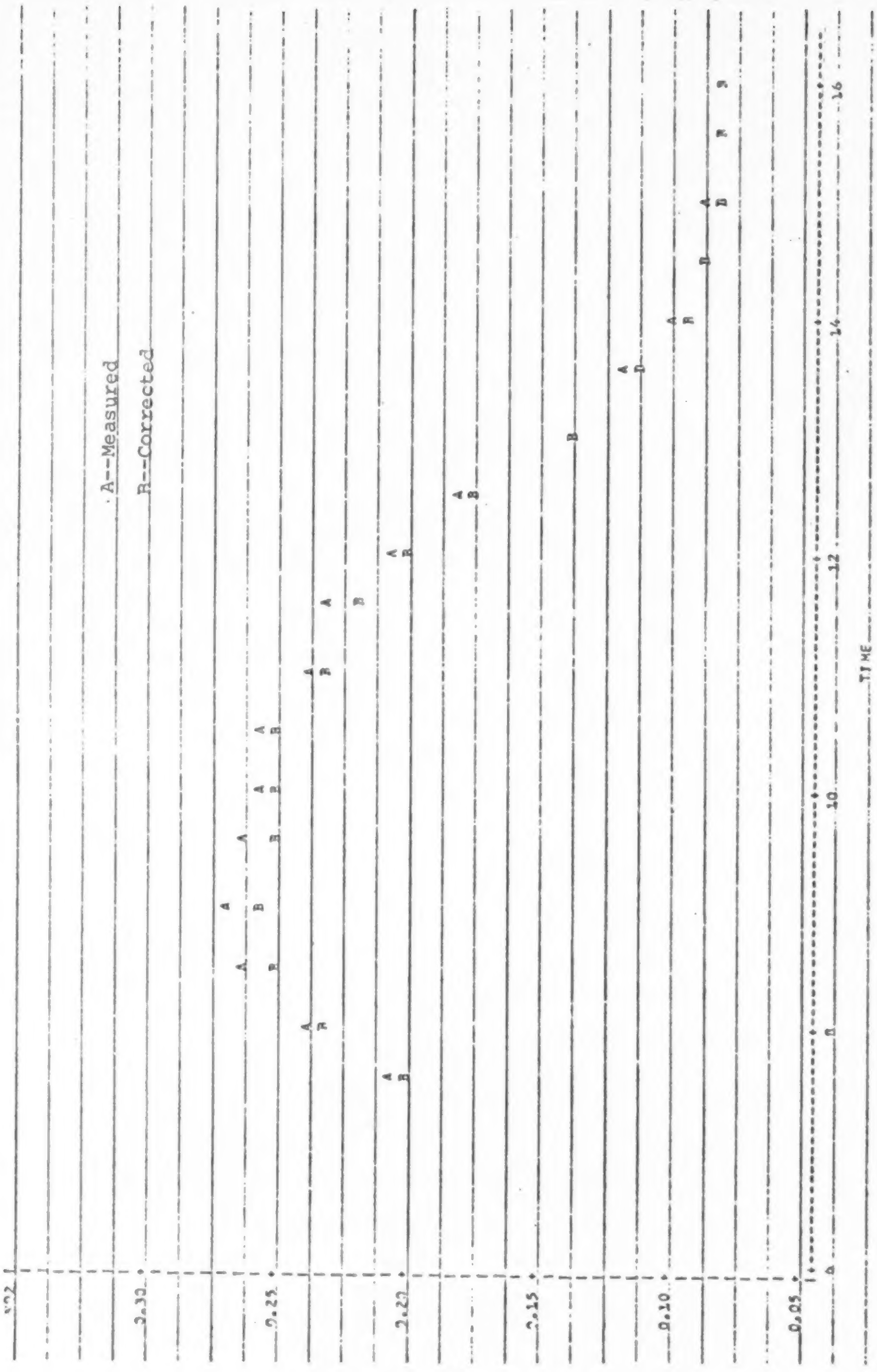

Figure F-3. Measured and corrected $NO_2$ for October 12 simulation.